'Coupling Between Electromagnetic Waves and Wires Using Transmission-Line Modelling.'

by Phillip Naylor, B.Sc., M.Sc.

Thesis submitted to the University of Nottingham

for the degree of Doctor of Philosophy,

October, 1986.

ABSTRACT

Three techniques are used to introduce wire models into Transmission Line Matrix (TLM) Electromagnetic field solvers. The first involves the setting up of a one-dimensional time-domain transmission-line model of a pair of wires. Voltages and currents coupled into the wires can be obtained from the incident fields. The differentials of these fields are used as source terms of the one-dimensional model. Results obtained by this model were compared with frequency domain results and good agreement was found. Non-linear loads can easily be modelled, and the response of a simple non-linear device is presented.

Wires of realistic radii can only be modelled in 2- or 3-dimensional TLM by using a fine mesh. Using progressively finer meshes the modelled radius converges to an unexpected result. The problem lies with the two forms of the TLM mesh, each giving a different modelled radius. This can lead to velocity of propagation errors of up to 10%.

A short-circuit node was developed but this has poor propagational characteristics and a radius equal to half the mesh spacing.

Diakoptics was re-examined and some operating conditions suggested. Frequency Domain Diakoptics was also introduced and tested.

Time Domain Diakoptics was used to create blocks of space containing wires which could be pre-solved for future use. Since a very fine mesh was used to describe the wire, but a coarse mesh was used for the remainder of the geometry there is a very crude approximation between the two meshes. This effect meant that long wires could not be constructed out of a multitude of pre-solved short-wires. A longer wire could be pre-solved as a single element and a reasonable modelled radius obtained. The technique became unstable after about 750 iterations.

Comparisons between the wire models developed show reasonable agreement. The one-dimensional method was the easiest technique to use.

Acknowledgements

I would like to thank Professor P. B. Johns and Dr C. Christopoulos for their helpful advice and support during the course of this work.

I would also like to thank Dr J. M. Thomson, Miss C. Smerdon and Mr M. Galvin of the Royal Aircraft Establishment, Farnborough for their continued interest in this work.

Special thanks to Penny Kelham who had the difficult task of translating the draft text into the typewritten form.

This work was supported by the UK Ministry of Defence (Procurement Executive) under contract D/ER1/9/4/2024/075/XR-FS.

Contents

Chapter 1 Introduction

1.1 Objective

The objective of this work is to investigate the use of wire models within the Transmission Line Matrix (TLM) electromagnetic field solvers.

Three separate techniques will be developed which allow wires to be modelled within TLM procedures.

Firstly, a one-dimensional approach, based on a numerical, time-domain solution of the transmission-line equations will be investigated.

Secondly, wires will be modelled directly in two and three dimensional TLM electromagnetic field solvers by the use of a fine mesh description.

Diakoptics will be discussed, in both the time and frequency domain, as a precursor to the use of pre-solved wire elements. Here an elemental length of wire will be pre-solved, on a fine mesh using the diakoptic techniques. The rest of the field problem will be solved on a coarse mesh and the wire element response will be obtained from a joining of the two mesh results. Finally, the various TLM methods will be compared with each other for simple geometries.

1.2 The Importance of Electromagnetic Compatibility and Wire Coupling

As more and more sophisticated and low voltage computer and allied equipment is installed in land, sea and air vehicles so the interest in Electromagnetic Compatibility (EMC) has grown. Many of the research and experimental topics in this field have developed as a result of military interests in the effects of the Electromagnetic Pulse (EMP) both from Nuclear (NEMP) and Lightning (LEMP) sources. As stated in (1) it is "... difficult to compile even a brief history of EMP ... (because) ... early work was never written down or documented in readily available sources ... (or) ... much of the work was classified ..." This is especially true as much of the work is connected with the development and maintenance of nuclear weapons and the protection of equipment from the effects of the EMP released by them.

The earliest interests in wire coupling problems was probably around 1830 when, according to COOK, (2), "Oersted, Ampere and Faraday were demonstrating the experimental relationships between magnetism, electric currents and induction effects". Later, around 1870, Maxwell argued the existence of electromagnetic radiation from mathematical considerations. Around 1900 the first effects of external coupling were observed when interference from one of Marconi's generators was detected on the other side of the Atlantic. At the same time COOK states that a Dr. Hoyt Taylor first heard ignition noise (from a motor vehicle) "... on his receiver." Indeed these are the obvious forms of Electromagnetic Incompatibility with which most of us are familiar - the 'noise' from a neighbour's electric drill or lawn mower which can be seen on a television picture; the 'clicks' heard on the radio when there is lightning nearby. The effects of electromagnetic interference can have far more damaging effects, though.

It is reported in (1) that around 1952, during the first British atomic tests, equipment failed due to "radio flash" (an early name for EMP). In 1959 the first interest in EMP coupling into underground cables (of the Minuteman missile) was recorded. The first EMP system tests were carried out by the Air Force Weapons Laboratory (AFWL) in 1963/4.

GIBBONS (3) has shown that a motor vehicle containing sophisticated computer equipment for engine management was easily susceptible to low power UHF radio transmissions. Under certain circumstances this required a complete re-boot of the computer to clear the fault (by switching the ignition off and on).

In (4) LITTLE describes how lightning close to an aircraft often couples into internal cables. The large currents and voltages induced can damage or destroy the connected equipment perhaps leading to premature launch of a missile or even the destruction of the aircraft.

Other researchers (e.g. SCHARFMAN et al. (5)) have shown interest in how lightning and EMP may couple into Power Transmission Lines and the effect this may have.

The importance of the subject is reflected in the number of conferences in the recent past dedicated to EMC (e.g. 6th Symposium and Technical Exhibition on Electromagnetic Compatibility, Zurich 1975; International Conference on Electromagnetic Compatibility, The University of Surrey, September 1984).

As pointed out by TAYLOR (6) and ABRAHAM and PAUL (7) experimental results in EMC/EMP type problems are either not generally available in the open literature or are difficult to obtain (although it is worth noting that SCHARFMAN et al. (5) do present experimental data from a scale model to complement their theoretical work).

Apart from experimental results there are a number of numerical and analytical techniques used for predicting the currents coupled into wires by an incident field, and these will be discussed in the next section.

1.3 Methods Used for Predicting the Coupling into Wires

From PERALA et al. (8) , BEVENSEE et al. (9) and EMP Interaction (1) there would seem to be four main techniques used to model wire coupling. These are:

i) Integral methods (method of moments/finite elements)
ii) Singularity Expansion Method (SEM)
iii) Transmission-line methods
iv) Finite Differences (FD)

1.3.1 Integral Methods

The majority of techniques which can be included under this heading stem from the method of moments developed by HARRINGTON (10,11,12). According to SILVESTER and FERRARI (13) the method of moments is just a specialised form of what is now known as finite elements.

The method of moments formulation proposed by Harrington can be used to compute the currents flowing in thin wires. This can usually be achieved by writing down the equations describing the problem (generally Maxwell's equations) and the boundary conditions. The required solution is then expressed as a product of the sum of expansion functions (basis functions) and the sum of weighting functions (testing functions). By writing a set of matrix equations describing the connection between the coefficient of the expansion functions, the weighting functions and the known parts of the original equation the coefficients can be determined. Hence it is possible to obtain the required solution.

The testing functions are often chosen to enforce the boundary conditions whilst the choice of expansion function really depends on the expected result. If the testing and expansion functions are the same then the technique is usually referred to as Galerkin's method. Depending on the type of code used (and the intended application) the testing function might be delta functions for point-matching problems or a more complicated formulation (7).

The Integral-Equation (EFIE/MFIE) approach described in (1,8,9,14) results in the solution of the same set of equations (the Pocklington equations (13)). In these references a number of distinct equations have been derived namely the Electric Field Integral Equation, the Magnetic Field Integral Equation and the Thin Wire Integral Equation, all in the time and frequency domains.

All these equations can be put into a form suitable for solution by computer, but as stated in (7) whilst the method of moments can give very accurate results it is very expensive in the use of computer resources.

1.3.2 Singularity Expansion Method

This technique has its origins in the classical analysis of the transient response of lumped networks using Laplace Transforms. The Laplace Transform of the equations characterising the field problem plus the sources are required along with the boundary conditions. The desired function (e.g. current) can then be expressed as a multiple of the known terms. This function is then re-expressed in a form with the complex poles of the system in the denominator of the equation. The method of residues (15) then allows the inverse Laplace Transform to be obtained readily yielding the time domain response.

In many problems (1,16,17) the equations describing the electromagnetic system are too complicated for the poles (and residues) to be determined analytically. Often the poles are found by using the method of moments described above. Other methods exist for the derivation of the complex poles and residues from time domain data (18). These numerical techniques are usually only approximate but are generally adequate to obtain good results.

1.3.3 Transmission-Line Methods

One of the most popular methods used for wire modelling are the variations on the transmission-line model. In this the ordinary transmission-line equations (19) are used to model the propagation of the induced voltages and currents. The actual induction terms are obtained from Maxwell's equations and amount to voltage and current sources on the transmission-line defined in terms of the incident flux and voltage.

The standard derivation of the transmission-line equations and the associated source terms for two conductor wires is given by LEE (20), but a simpler derivation - and one which will be modified later in this work-is given by ABRAHAM and PAUL (7).

Other versions of the response of a transmission-line are given by SMITH (21), SCHLESSINGER (22) and BATES and HAWLEY (23).

This transmission-line form of electromagnetic coupling has been extended to multiconductor wires by BETCHTOLD and KOZAKOFF (24), MARX (25), PAUL(26-32), HARRISON (33), TAYLOR and CASTILLO (34), AGRAWAL et al. (35-38), GIRI et al. (39) and ter HASEBORG et al. (40). Further developments have been made which allow the modelling of twisted, skewed and interconnected cables (41-43).

Most of these versions involve the writing down of the transmission-line equations in the frequency domain and in matrix form. The solution is then obtained using chain parameter matrices (7).

The main disadvantages with most forms of the transmission-line approach are:

i) The thin wire assumption implicit from the derivation
ii) Only differential mode currents are calculated
iii) Most forms operate in the frequency domain, making the inclusion of non-linearities difficult
iv) Re-radiation from the wires is not taken into account.

The main advantage is that it is a very simple and computationally efficient model.

1.3.4 Finite Differences

In Finite Differences Maxwell's equations are differenced both in time and space usually in the way first shown by YEE (44). Later MEREWETHER (45) extended the method to incorporate metal bodies of revolution. In 1977 HOLLAND (46) described the computer code THREDE which allows the modelling of an aircraft in a finite-difference routine. Lossy structures were also modelled by HOLLAND et al. (47).

In two similar papers (48,49) HOLLAND and SIMPSON have shown how thin-struts and wires may be incorporated into finite-differences. An in-cell inductance is derived and this is used in the differencing of a current-E-field equation as well as Maxwell's equations. ZIMMERMAN (50) has generalised the finite-difference code to allow the inclusion of circuit elements within the space. Here the equations describing the time domain response of a network element are differenced along with Maxwell's equations.

The main difficulties in using finite differences arise from the separation in space of electric and magnetic field points. This limits the positions of conducting boundaries within the routine to the points where an electric field is defined (44). MEREWETHER (45) and WILLIFORD and HERBERT (51) point out that the external boundaries of the finite difference routine can be chosen such that any electromagnetic radiation is absorbed.

JOHNS (52) has shown that the TLM method and the finite difference method are equivalent in certain circumstances but there are fundamental differences. The finite-difference method differences the electric and magnetic field operations of Maxwell (i.e. a mathematical model). TLM is a physical model using transmission-lines which can be solved exactly using a computer.

1.3.5 Remarks

The above brief resume has suggested that each of the methods exists as a separate, distinct routine. This is not the case.

PALADIAN et al. (53) use both the method of moments and finite difference to derive their response of a single conductor wire.

THIELE and NEWHOUSE (54) and THIELE and CHAN (55) have combined the method of moments with the Geometric Theory of Diffraction to obtain the currents induced into wire antennae.

In (8) Perala et al. point out that the singularity Expansion Method is "... not so much an alternate method for solving boundary value problems but one which should be used in conjunction with other methods ...".

1.4 Transmission-Line Modelling (TLM)

The seeds of TLM were sown by KRON (56) in 1944. He derived equivalent circuit representations of Maxwell's equations. The two-dimensional networks which Kron obtained in (56) are identical to the series and shunt nodes in TLM. In 1971 JOHNS and BEURLE (57) used the TLM method (in the shunt node form) to compute the H modes in a waveguide. Both homogeneous and inhomogeneous waveguides have been modelled (58,59). Series nodes are described by AKHTARZAD and JOHNS (60) and their use in an expanded asymmetrical 3D node developed in (61,62). (It is this form of the TLM method which Johns likens to finite-differences in (52)). A general summary of the development of TLM up to 1978 is given by BREWITT-TAYLOR and JOHNS in (63). JOHNS and O'BRIEN described how non-linear loads could be modelled in (64). The diakoptic techniques, first introduced for the steady-state in (63) were developed into time varying field solutions by JOHNS and AKHTARZAD (65,66).

In recent years TLM has been in use commercially to model carbon fibre materials (67) and aircraft (68,69).

A review of TLM in 1985 is given by HOEFER (70). The most recent development in TLM has been the construction and implementation of a 3D symmetrical condensed TLM node (71,72,73).

It is the use of TLM to compute fields and surface currents in aircraft which has led to the work described here. A technique is required in TLM which allows wires or wire looms in an aircraft (for example) to be modelled.

Chapter 2 A One-Dimensional TLM Method for Predicting the Differential Mode Current Induced into a Pair of Wires

2.1 Introduction

The transmission-line model described by LEE (20) ABRAHAM and PAUL (7) and in E.M.P. Interaction (1) is widely used for computing the differential mode currents induced into a pair of wires.

The indicent electric and magnetic fields in the vicinity of the wires are used to excite the one-dimensional transmission-line model. The resulting current is usually obtained in the frequency domain.

Since the model is a frequency domain one, there are difficulties in incorporating non-linearities into the wire or its terminations. Most modern equipment contains non-linear devices so this is a serious deficiency of the model.

TLM is a time domain numerical modelling technique which has already been used to model non-linear devices (64).

What is required is a one-dimensional transmission-line model, solved in the time domain (TLM), in which the non-linearities of a problem can be included. The first part of the derivation, for the transmission-line equations, is a modified form of the derivation produced by ABRAHAM and PAUL in (7).

This is followed by the derivation of the one-dimensional TLM model.

Then the TLM model is compared with (7). (For brevity the results in (7) will be referred to as the RADC method - after Rome Air Development Center). Finally a simple non-linear problem is investigated

2.2 The Derivation of the Transmission-Line Equations

2.2.1 Voltage Equation

Consider the two parallel wires shown in figure 2.1a. It is assumed that the wires are perfectly conducting non-insulated and immersed in an homogeneous medium.

Applying the integral form of Maxwell's Curl $\underline{E}$ equation (Faraday's law) over the closed path indicated by the dotted line:

$$\oint_{\ell} \underline{E} \cdot d\underline{\ell} = -\frac{\partial}{\partial t} \int_S \underline{B} \cdot d\underline{S} \qquad (2.1)$$

Substituting $\underline{B} = \mu \underline{H}$ (2.2)

gives

$$\oint_{\ell} \underline{E} \cdot d\underline{\ell} = -\mu \frac{\partial}{\partial t} \int_S \underline{H} \cdot d\underline{S} \qquad (2.3)$$

The left hand integral can be rewritten as the sum of four other integrals : (figure 2.1b)

$$\oint_{\ell} \underline{E} \cdot d\underline{\ell} = \int_x^{x+\Delta x} E_x(x,o)\,dx + \int_o^d E_y(x+\Delta x,y)\,dy$$

$$- \int_x^{x+\Delta x} E_x(x,d)\,dx - \int_o^d E_y(x,y)\,dy \qquad (2.4)$$

Figure 2·1 Two parallel wires

a) Geometry

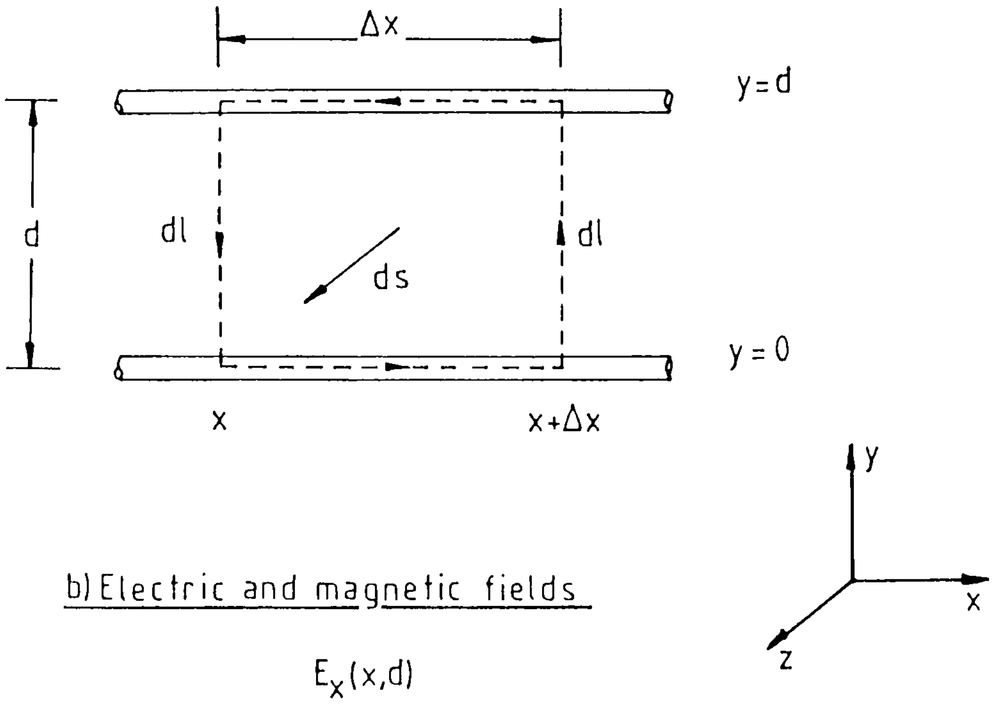

b) Electric and magnetic fields

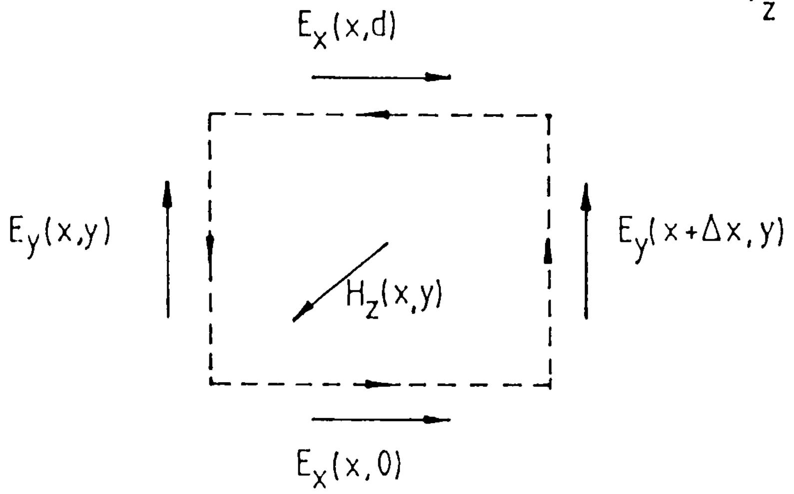

c) Magnetic field, flux and current directions

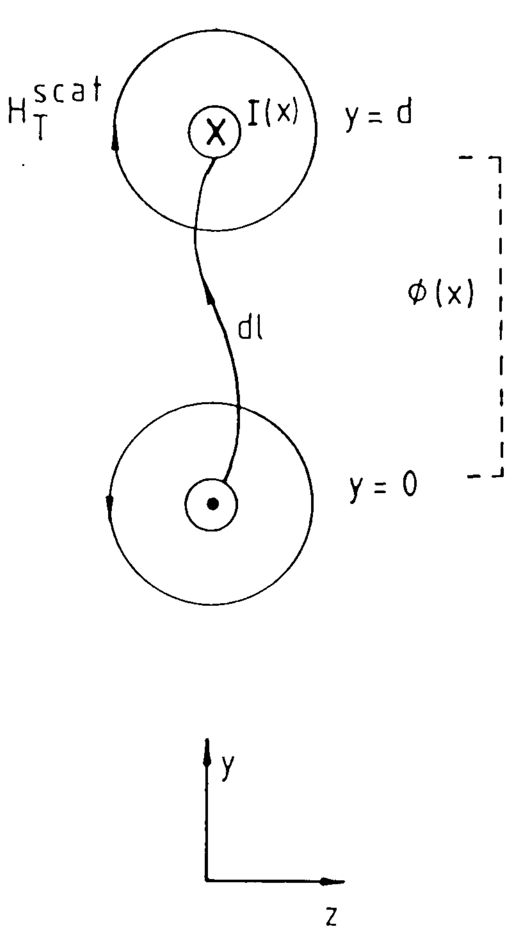

Since the wire is perfectly conducting the E_x field at the wire surface must be zero, giving:

$$\oint_{\ell} \underline{E}.d\underline{\ell} = \int_0^d E_y(x+\Delta x,y)dy - \int_0^d E_y(x,y)dy \qquad (2.5)$$

The right hand term of equation (2.3) can also be rewritten:

$$-\mu\frac{\partial}{\partial t} \int_S \underline{H}.d\underline{S} = -\mu\frac{\partial}{\partial t} \int_x^{x+\Delta x}\int_{y=o}^{d} H_z(x,y)dydx \qquad (2.6)$$

The voltage between the two wires at any point x is given by:

$$V(x) = -\int_o^d E_y(x,y)dy \qquad (2.7)$$

and similarly for a point (x + Δx):

$$V(x+\Delta x) = -\int_o^d E_y(x + \Delta x, y)dy \qquad (2.8)$$

From (2.5), (2.7) and (2.8):

$$\oint_{\ell} \underline{E}.d\underline{\ell} = V(x) - V(x + \Delta x) \qquad (2.9)$$

and from (2.3), (2.6) and (2.9) this gives:

$$V(x)-V(x+\Delta x) = -\mu\frac{\partial}{\partial t} \int_x^{x+\Delta x} \int_o^d H_z(x,y)dydx \qquad (2.10)$$

Assuming the magnetic field (H_z) remains constant over the interval Δx allows dx to be replaced by Δx, thus:

$$V(x)-V(x+\Delta x) = -\mu\frac{\partial}{\partial t}\left[\int_o^d H_z(x,y)dy\right].\Delta x \qquad (2.11)$$

Then

$$\lim_{\Delta x \to o} \left(\frac{V(x)-V(x+\Delta x)}{\Delta x}\right) = -\mu\frac{\partial}{\partial t} \int_o^d H_z(x,y)\,dy \qquad (2.12)$$

which is:

$$\frac{\partial V(x)}{\partial x} = \mu\frac{\partial}{\partial t} \int_o^d H_z(x,y)\,dy \qquad (2.13)$$

H_z is the total magnetic field. This can be split into two parts - an incident and a scattered field. The incident field is the field which would appear with no wires present. The scattered field is the field due to the wire being present (i.e. due to a current flowing in the wire).

By definition the relationship:

$$\oint \underline{H}.d\underline{\ell} = I(x) + \int \frac{\partial \underline{D}}{\partial t}.\ d\underline{S} \qquad (2.14)$$

becomes:

$$\oint \underline{H}^{scat}.d\underline{\ell} = I(x) \qquad (2.15)$$

since the scattered field is dependent only on the current flowing in a thin wire.

From PAUL (30) and ABRAHAM and PAUL (7) the per-unit-length flux linkage is:

$$\Phi(x) = -\int_\ell \mu \underline{H}_T^{scat}.d\underline{\ell} \quad \text{(see figure 2.1c)} \qquad (2.16)$$

The per-unit length inductance, L_d, is:

$$L_d = \frac{\Phi(x)}{I(x)} \qquad (2.17)$$

From (2.13):

$$\frac{\partial V(x)}{\partial x} = \mu\frac{\partial}{\partial t}\int_0^d H_z^{inc}(x,y)\,dy + \mu\frac{\partial}{\partial t}\int_0^d H_z^{scat}(x,y)\,dy \qquad (2.18)$$

Equation (2.16) becomes:

$$-L_d I(x) = \mu\int_0^d H_z^{scat}dy \qquad (2.19)$$

Substituting (2.19) into (2.18) gives:

$$\frac{\partial V(x)}{\partial x} + L_d\,\frac{\partial I(x)}{\partial t} = \mu\frac{\partial}{\partial t}\int_0^d H_z^{inc}\,(x,y)\,dy \qquad (2.20)$$

Replacing

$$\mu\frac{\partial}{\partial t}\int_0^d H_z^{inc}\,(x,y)\,dy = V_s(x) \qquad (2.21)$$

in (2.20) gives

$$\frac{\partial V(x)}{\partial x} + L_d\,\frac{\partial I(x)}{\partial t} = V_s(x) \qquad (2.22)$$

which is the first transmission-line equation.

2.2.2 Current Equation

Conservation of charge on an elemental wire requires:

$$\oint_S \underline{J}.d\underline{S} = -\frac{\partial}{\partial t}\int_V \rho dV \qquad (2.23)$$

From figure 2.2a the left hand term can be replaced by two surface integrals, representing end (S_e) and circumferential (S_c) current densities, thus:

$$\oint_S \underline{J}.d\underline{S} = \int_{S_e} \underline{J}.d\underline{S}_e + \int_{S_c} \underline{J}.d\underline{S}_c \qquad (2.24)$$

For perfect conductors there will be no current flow circumferentially ($\int_{S_c} \underline{J}.d\underline{S}_c = 0$). Hence

$$\oint_S \underline{J}.d\underline{S} = \int_{S_e} \underline{J}.d\underline{S}_e \qquad (2.25)$$

From figure 2.2b this can now be replaced by:

$$\int_{S_e} \underline{J}.d\underline{S}_e = \int_{S_e} \underline{J}(x+\Delta x)\,d\underline{S}_e(x+\Delta x) - \int_{S_e} \underline{J}(x)\,d\underline{S}_e(x) \qquad (2.26)$$

which is

$$\int_{S_e} \underline{J}.d\underline{S}_e = I(x+\Delta x) - I(x) \qquad (2.27)$$

If ρ in equation (2.23) is charge density, then the charge, Q, is:

$$Q = \int_V \rho dV \qquad (2.28)$$

Figure 2·2 Current and charge on the lines

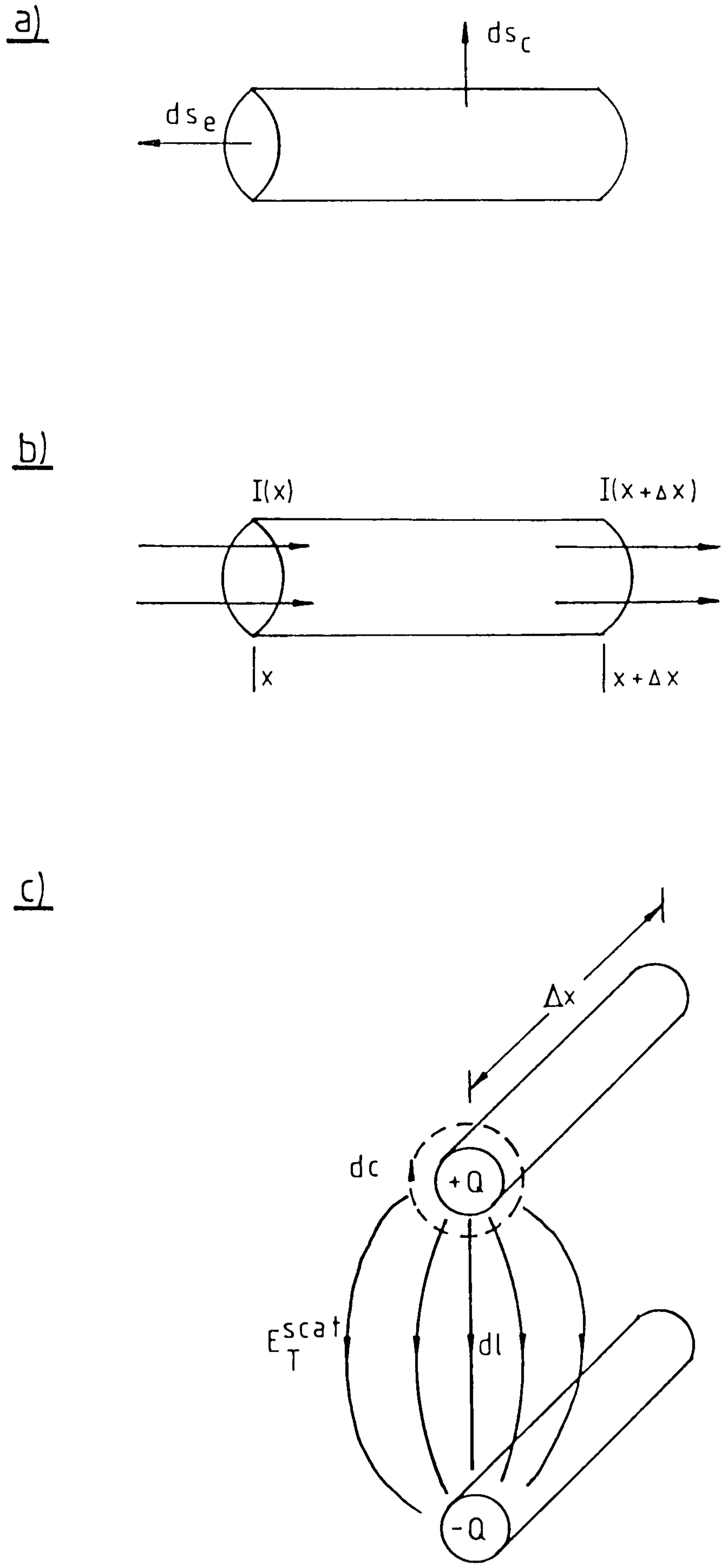

From Maxwell's $\nabla.\underline{D}$ equation in integral form:

$$\oint_S \underline{D}.d\underline{S} = \int_V \rho dV \qquad (2.29)$$

for a thin wire in free space:

$$\oint_S \underline{D}^{inc}.d\underline{S} = 0 \qquad (2.30)$$

giving

$$\oint_S \underline{D}^{scat}.d\underline{S} = Q \qquad (2.31)$$

or

$$\varepsilon\oint_S \underline{E}_T^{scat}.d\underline{S} = Q \qquad (2.32)$$

Where $\underline{E}_T^{scat}$ is the scattered tangential magnetic field as defined in figure 2.2c. This becomes:

$$Q = \varepsilon\int_x^{x+\Delta x} \int_C \underline{E}_T^{scat} \; d\underline{c}.d\underline{x} \qquad (2.33)$$

The scattered field form of equation (2.7) is:

$$\overset{scat}{V(x)} = -\int_o^d \underline{E}_T^{scat} \; d\underline{\ell} \qquad (2.34)$$

By definition $Q = C_d \Delta x V$ (2.35)

where C_d is capacitance per metre.

Equations (2.35), (2.27) and (2.23) combine to give:

$$I(x+\Delta x) - I(x) = -\frac{\partial}{\partial t} \; C_d\overset{scat}{V(x)} \; \Delta x \qquad (2.36)$$

Dividing both sides of (2.36) by Δx and taking

$$\lim_{\Delta x \to 0} \left(\frac{I(x+\Delta x) - I(x)}{\Delta x} \right)$$ leaves:

$$\frac{dI(x)}{dx} = - C_d \frac{\partial \overset{scat}{V(x)}}{\partial t} \qquad (2.37)$$

Note also that from (2.35)

$$C_d = \frac{-\Delta x\, \varepsilon \int_c \underline{E}_T^{scat}\, d\underline{c}}{\int_0^d \underline{E}_T^{scat}\, d\underline{\ell}} \qquad (2.38)$$

Since $\overset{scat}{V(x)} = V(x) - \overset{inc}{V(x)}$ (2.39)

and from (2.7) that

$$\overset{inc}{V(x)} = -\int_0^d E_y^{inc}\,(x,y)\,dy \qquad (2.40)$$

then

$$\frac{\partial I(x)}{\partial x} = - C_d \frac{\partial V(x)}{\partial t} - C_d \frac{\partial}{\partial t} \int_0^d E_y^{inc}(x,y)\,dy \qquad (2.41)$$

Setting

$$I_S(x) = - C_d \frac{\partial}{\partial t} \int_0^d E_y^{inc}(x,y)\,dy \qquad (2.42)$$

gives

$$\frac{\partial I(x)}{\partial x} + C_d \frac{\partial V(x)}{\partial t} = I_S(x) \qquad (2.43)$$

(with $\frac{\partial V(x)}{\partial x} + L_d \frac{\partial I(x)}{\partial t} = V_S(x)$ (2.22))

These are the two transmission-line equations which define the voltages and currents on the lines plus the coupling from external electric and magnetic fields.

ABRAHAM and PAUL (7) then solve these two equations (replacing $\frac{d}{dt}$ by jw) to give:

$$V(x) = \cos(\beta x)V(o) - jcL_d\sin(\beta x)I(o) + V_s^1(x) \qquad (2.44)$$

$$I(x) = -jcC_d\sin(\beta x)V(o) + \cos(\beta x)I(o) + I_s^1(x) \qquad (2.45)$$

where $\beta = \frac{2\pi}{\lambda}$, c = velocity of light and

$$V_s^1(x) = \int_o^x [\cos(\beta(x-\tau))V_s(\tau) - jcL_d\sin(\beta(x-\tau))I_s(\tau)]\,d\tau \qquad (2.46)$$

$$I_s^1(x) = \int_o^x [-jcC_d\sin(\beta(x-\tau))V_s(\tau) + \cos(\beta(x-\tau))I_s(\tau)]\,d\tau \qquad (2.47)$$

In (7) ABRAHAM and PAUL have presented a FORTRAN program which computes the solutions to equations (2.44) to (2.47) for various frequencies. Later results obtained using the TLM method developed below will be compared with those obtained in (7).

2.3 Development of a One-Dimensional TLM Model

By recognising that V and I vary with time and space equations (2.22) and (2.43) become:

$$\frac{\partial}{\partial x}I(x,t) + C_d\frac{\partial}{\partial t}V(x,t) = I_s(x,t) \qquad (2.48)$$

$$\frac{\partial}{\partial x}V(x,t) + L_d\frac{\partial}{\partial t}I(x,t) = V_s(x,t) \qquad (2.49)$$

2.3.1 Ignoring Source Terms

Setting $V_S(x,t) = I_S(x,t) = 0$ initially and combining (2.48 and 2.49) to give the wave equations:

$$\frac{\partial^2}{\partial x^2} V(x,t) = L_d C_d \frac{\partial^2}{\partial t^2} V(x,t) \qquad (2.50)$$

$$\frac{\partial^2}{\partial x^2} I(x,t) = L_d C_d \frac{\partial^2}{\partial t^2} I(x,t) \qquad (2.51)$$

These have solutions of the form, for a loss-less line (KRAUS (74)):

$$V(x,t) = Ae^{j(wt+\beta x)} + Be^{j(wt-\beta x)} \qquad (2.52)$$

$$I(x,t) = \frac{Ae^{j(wt+\beta x)} - Be^{j(wt-\beta x)}}{Z_o} \qquad (2.53)$$

In equations (2.52) and (2.53) $e^{j(wt-\beta x)}$ corresponds to a wave travelling in the positive x-direction and $e^{j(wt+\beta x)}$ to a wave travelling in the negative x-direction on the transmission line.

In the time discrete TLM form this can be written as:

$$V(x,t) = V(x,k\Delta t) = {}_kV(x) = {}_kV_1^i(x) + {}_kV_2^i(x) \qquad (2.54)$$

$$I(x,t) = I(x,k\Delta t) = {}_kI(x) = \frac{{}_kV_1^i(x) - {}_kV_2^i(x)}{Z_o} \qquad (2.55)$$

where ${}_kV_1^i(x)$ means the voltage of a wave incident on the x^{th} node in the direction 1 at the k^{th} time step (= $k\Delta t$). (See figure 2.3). Δt is the time step of the iterative process.

The node of a problem can be considered as a scattering area converting the incident pulses of figure 2.3a into the reflected pulses of figure 2.3b.

From the fundamental TLM equation (JOHNS and BEURLE (57))

$$V = V^i + V^r \tag{2.56}$$

it is possible to write:

$${}_kV_1^r(x) = {}_kV(x) - {}_kV_1^i(x) \tag{2.57}$$

and

$${}_kV_2^r(x) = {}_kV(x) - {}_kV_2^i(x) \tag{2.58}$$

From (2.54), (2.57) and (2.58)

$${}_kV_1^r(x) = {}_kV_2^i(x) \tag{2.59}$$

$${}_kV_2^r(x) = {}_kV_1^i(x) \tag{2.60}$$

These equations apply only to a uniform line. If the impedance changes at the node, as suggested by figure 2.4a then equation (2.54) becomes:

Figure 2·3 Incident and reflected pulses

a) Incident

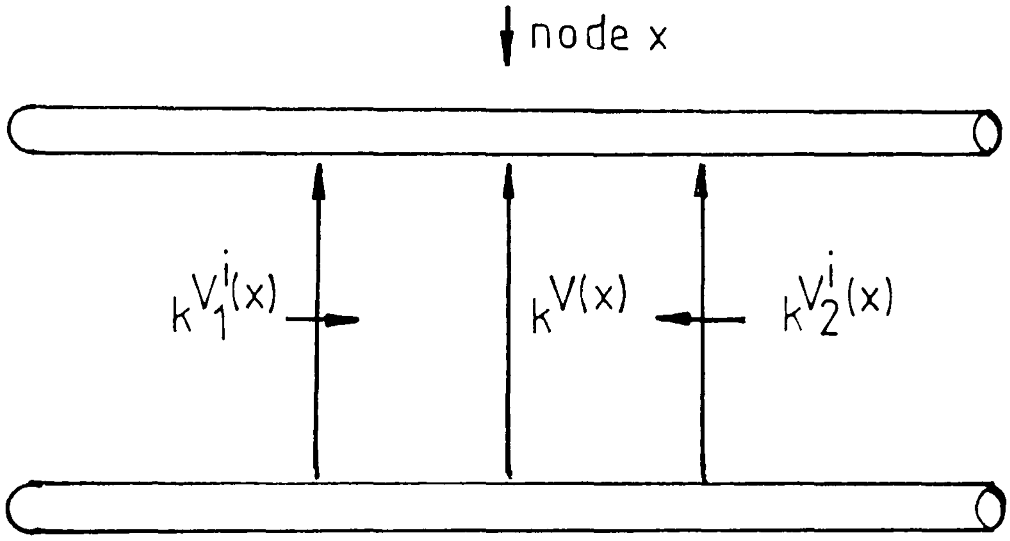

b) Reflected

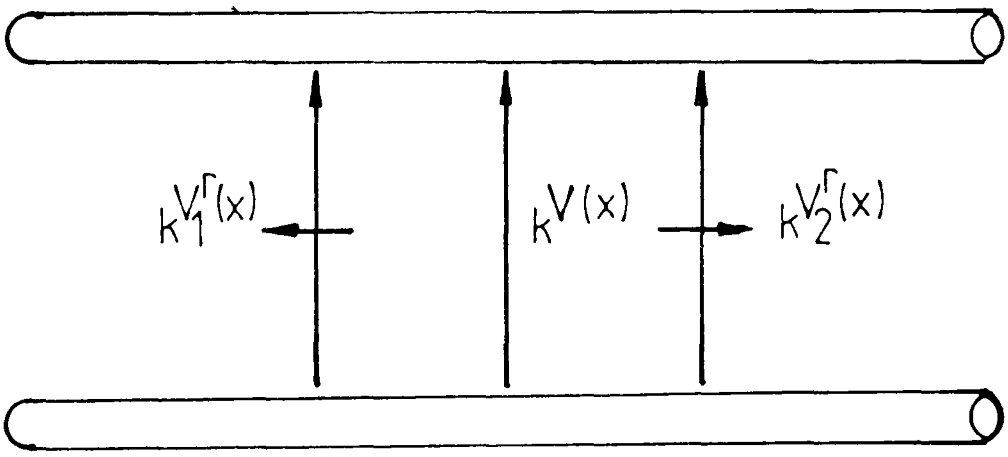

Figure 2·4 Line discontinuities

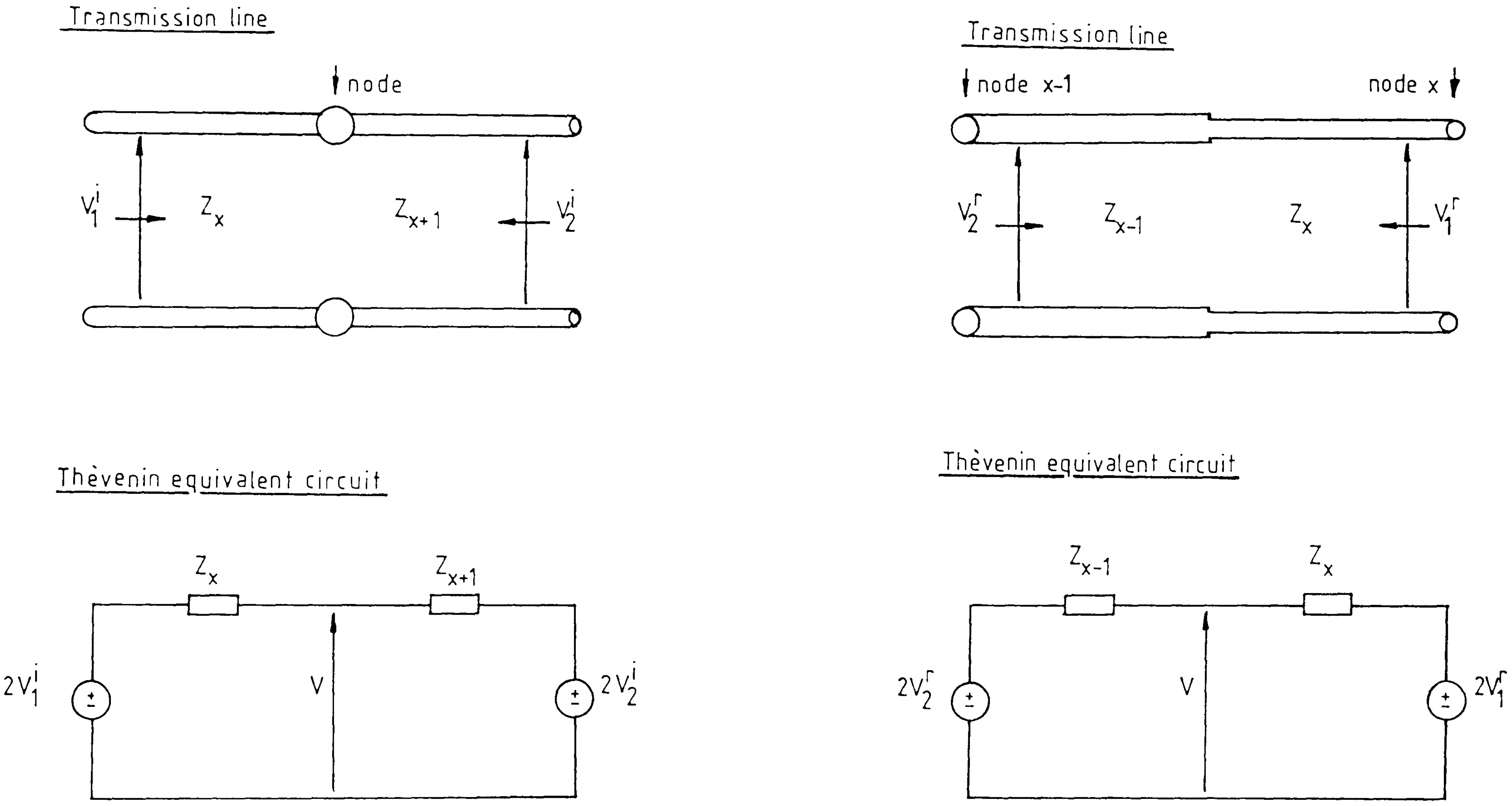

a) at the node

b) between nodes

$$ {}_kV(x) = \frac{2({}_kV_1^i(x)Z_{x+1} + {}_kV_2^i(x)Z_x)}{Z_x + Z_{x+1}} \tag{2.61} $$

and V^r can be calculated from equations (2.57) and (2.58).

Reflected pulses from each node become incident on the adjacent nodes according to the formulae:

$$ {}_{k+1}V_1^i(x) = {}_kV_2^r(x-1) \tag{2.62} $$

$$ {}_{k+1}V_2^i(x) = {}_kV_1^r(x+1) \tag{2.63} $$

Again this applies only to a uniform transmission line between x and x+1 (or x-1).

If the impedance discontinuity is between nodes as in figure 2.4b then:

$$ {}_{k+1}V_1^i(x) = \frac{2({}_kV_1^r(x)Z_{x-1} + {}_kV_2^r(x-1)Z_x)}{Z_{x-1} + Z_x} - {}_kV_1^r $$

$$ = \frac{(Z_x - Z_{x-1})}{(Z_{x-1} + Z_x)} {}_kV_1^r(x) + \frac{2{}_kV_2^r(x-1)Z_x}{Z_{x-1} + Z_x} \tag{2.64} $$

$$ = \rho_{11}\ {}_kV_1^r(x) + \tau_{21}\ {}_kV_2^r(x-1) \tag{2.65} $$

where ρ_{11} and τ_{21} are reflection and transmission coefficients. Similarly for

$$ {}_{k+1}V_2^i(x) = \rho_{22}\ {}_kV_2^r(x) + \tau_{12}\ {}_kV_1^r(x+1) \tag{2.66} $$

where

$$\rho_{11} = \frac{(Z_x - Z_{x-1})}{(Z_x + Z_{x-1})}, \quad \rho_{22} = \frac{(Z_x - Z_{x+1})}{(Z_x + Z_{x+1})}$$

$$\tau_{12} = \frac{2Z_x}{Z_x + Z_{x+1}}, \quad \tau_{21} = \frac{2Z_x}{Z_x + Z_{x-1}} \qquad (2.67)$$

Thus for no source terms the iterative process is defined by equations (2.61), (2.57), (2.58), (2.65), (2.66) and (2.67).

2.3.2 Adding in the Source Terms

From PAUL (30) and figure 2.5 it can be seen that the source terms add to the voltages and currents already on the transmission line.

Consider the voltage source term, $V_S(x)$, first. From figure 2.6a it is clear that the excitation can be separated into two equal parts. This gives $V^i \pm \frac{V_S}{2} \Delta \ell$ incident on the node.

Thus, the total voltage of the incident wave ${}^T V^i$ can be defined as:

$$ {}^T_k V^i_1(x) = {}_k V^i_1(x) + \tfrac{1}{2} {}_k V_S(x) \Delta \ell \qquad (2.68)$$

$$ {}^T_k V^i_2(x) = {}_k V^i_2(x) - \tfrac{1}{2} {}_k V_S(x) \Delta \ell \qquad (2.69)$$

Figure 2·5 Source terms

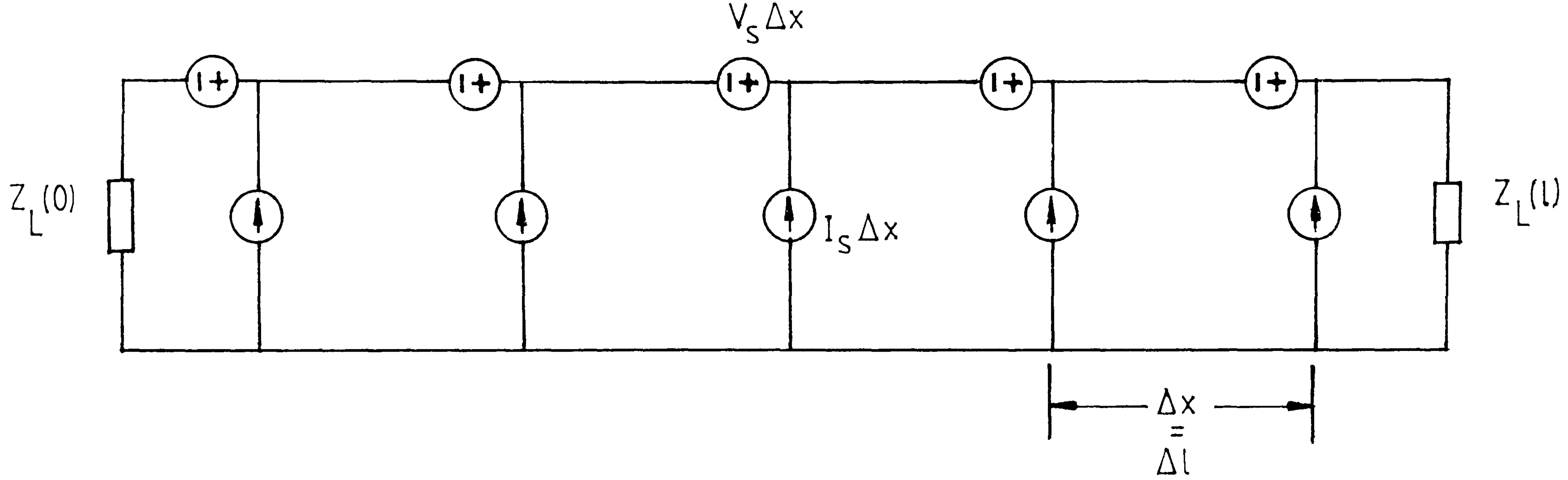

Figure 2·6 Source terms

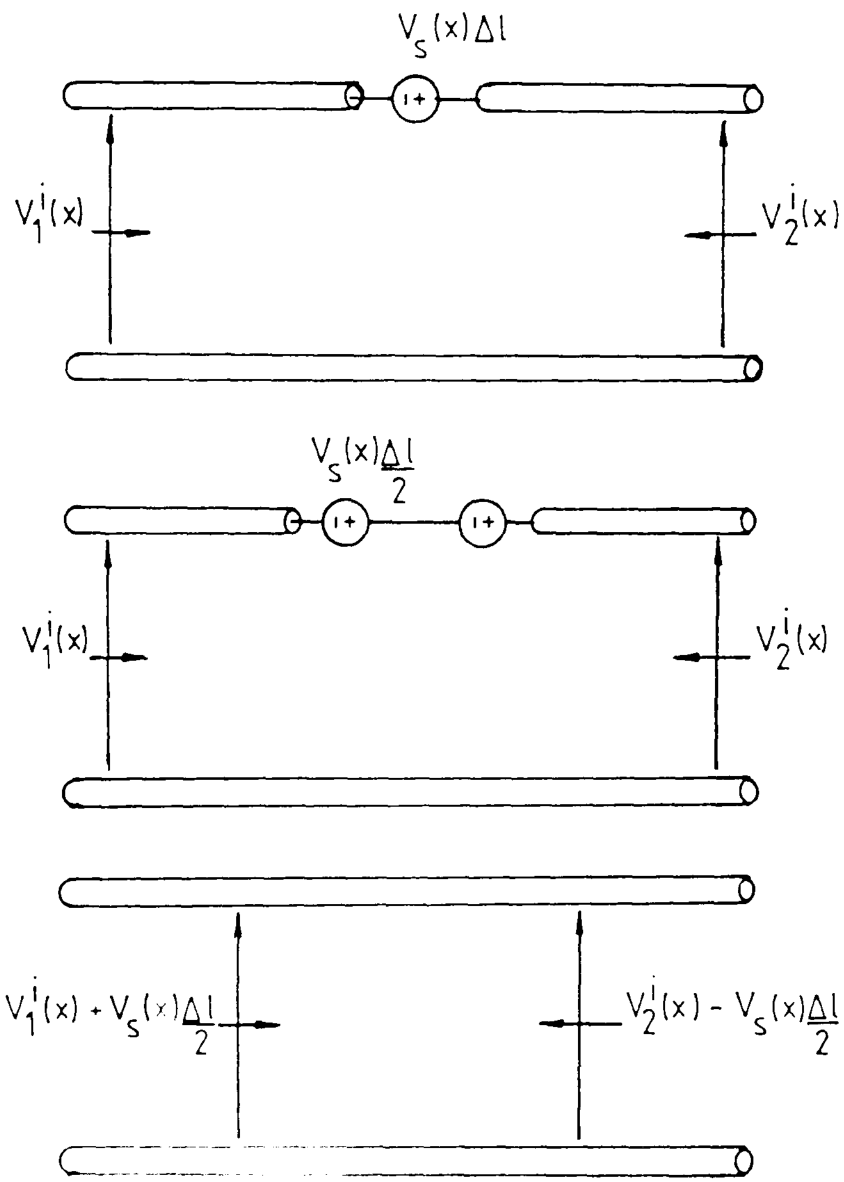
a) Voltage source term

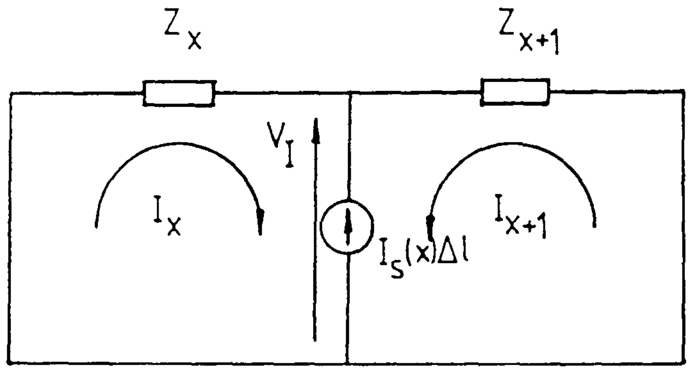
b) Current source term

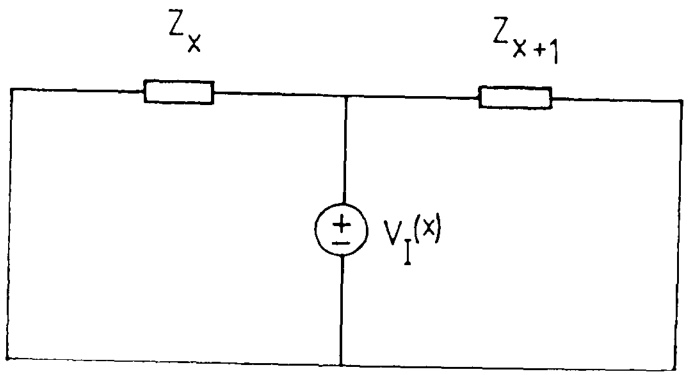
Equivalent voltage source

The current source is shown in figure 2.6b. The equivalent voltage source configuration is preferable since such a voltage would add directly to the nodal voltage.

To achieve this:

$$V_I(x) = -I_x Z_x = -I_{x+1} Z_{x+1} \tag{2.70}$$

where $I_S(x)\Delta\ell = -(I_x + I_{x+1})$ (2.71)

Multiplying (2.71) by Z_x gives:

$$I_S(x)\Delta\ell Z_x = -(I_x Z_x + I_{x+1} Z_x) \tag{2.72}$$

Substituting for I_x:

$$I_S(x)\Delta\ell\, Z_x = -I_{x+1}(Z_x + Z_{x+1}) \tag{2.73}$$

and using (2.70) this becomes:

$$I_S(x)\Delta\ell\, Z_x = \frac{V_I(x)}{Z_{x+1}}(Z_x + Z_{x+1}) \tag{2.74}$$

Rearranging:

$$V_I(x) = \frac{I_S(x) Z_x Z_{x+1} \Delta\ell}{Z_x + Z_{x+1}} \tag{2.75}$$

Now the nodal voltage equation (2.61) can be re-expressed:

$${}_kV(x) = \frac{(2\,{}_kV_1^i(x) + {}_kV_S(x)\frac{\Delta\ell}{2}) Z_{x+1} + (2\,{}_kV_2^i(x) - {}_kV_S(x)\frac{\Delta\ell}{2}) Z_x + {}_kI_S(x) Z_x Z_{x+1} \Delta\ell}{Z_x + Z_{x+1}} \tag{2.76}$$

Hence the complete iterative process for an infinite line with sources and discontinuities is (in order) equations (2.68), (2.69), (2.76), ((2.57) with ${}^{T}V_1^i$ replacing V_1^i) ((2.58) with ${}^{T}V_2^i$ replacing V_2^i), (2.66) and (2.67).

2.3.3 End Conditions and Load Currents

Figure 2.7 shows a terminated line. To model the loads, a reflection coefficient is required which defines what proportion of the pulse incident on the load is reflected back into the problem. The current flowing in the loads may also be required.

The voltage across the load $Z_L(0)$ as given by:

$$ {}_kV_o = \frac{2\,{}_kV_1^r(1)\,Z_L(0)}{Z_1+Z_L(0)} \tag{2.77} $$

Then $$ {}_{k+1}V_1^i(1) = {}_kV_0 - {}_kV_1^r(1) \tag{2.78} $$

giving

$$ {}_{k+1}V_1^i(1) = \frac{2\,{}_kV_1^r(1)\,Z_L(0)}{Z_1+Z_L(0)} - {}_kV_1^r(1) \tag{2.79} $$

i.e. $$ {}_{k+1}V_1^i(1) = \frac{Z_L(0) - Z_1}{Z_L(0) + Z_1}\;{}_kV_1^r(1) \tag{2.80} $$

Putting ${}_{k+1}V_1^i(1) = \rho_0 \cdot {}_kV_1^r(1)$ yields

$$ \rho_0 = \frac{Z_L(0) - Z_1}{Z_L(0) + Z_1} \tag{2.81} $$

Figure 2·7 Terminated line

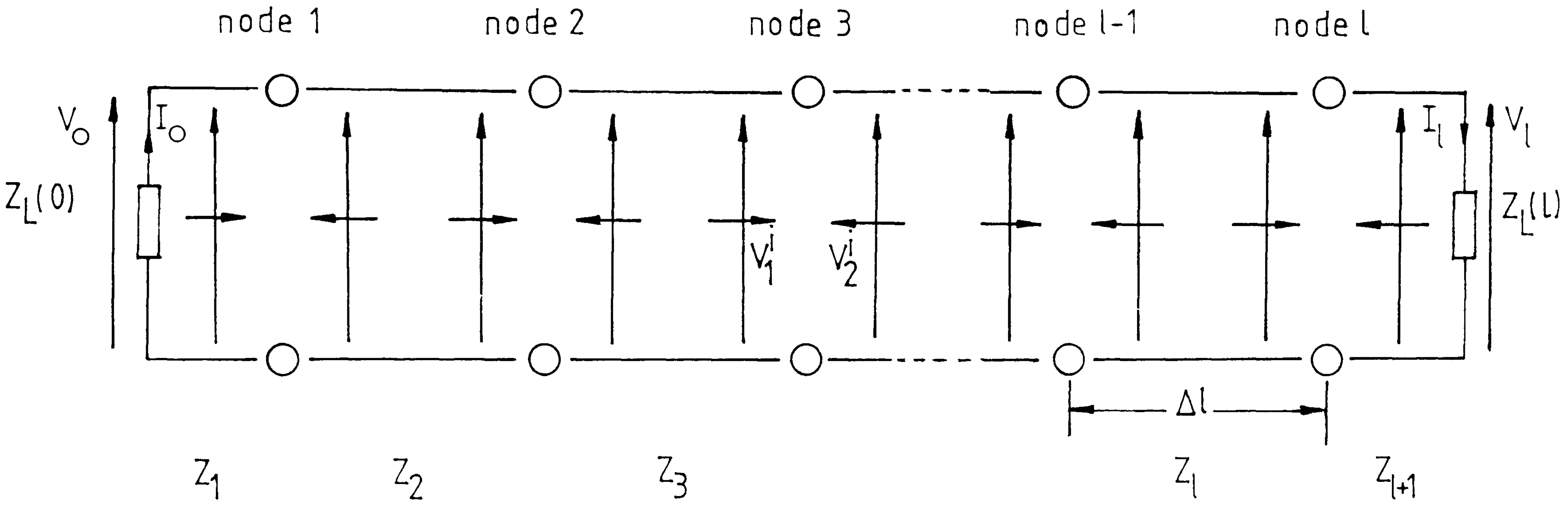

Similarly

$$ {}_{k+1}V_2^i(\ell) = \rho_\ell \; {}_kV_2^r(\ell) \tag{2.82} $$

and

$$ \rho_\ell = \frac{Z_L(\ell) - Z_{\ell+1}}{Z_L(\ell) + Z_{\ell+1}} \tag{2.83} $$

From (2.77) and

$$ {}_kI_0 = -\frac{{}_kV_0}{Z_L(0)} \tag{2.84} $$

$$ {}_kI_0 = \frac{-2\,{}_kV_1^r(1)}{Z_1+Z_L(0)} \tag{2.85} $$

Similarly

$$ {}_kI_\ell = \frac{2\,{}_kV_2^r(\ell)}{Z_{\ell+1}+Z_L(\ell)} \tag{2.86} $$

Note

The source voltage and current equations (2.68) to (2.76) apply only to a pair of wires parallel to the x-axis. For wires parallel to the other axes the signs of the equations change.

2.4 Comparison with the RADC Method

In (7) ABRAHAM and PAUL have provided comparisons between their formulation of the Transmission Line equations (the "RADC" method) and the method of moments. They also provided a FORTRAN program which reproduces their results.

The one-dimensional TLM method derived above was compared with the RADC method for the simple problem shown in figure 2.8. The physical parameters in 2.8a are modelled in both the RADC and TLM methods by the geometry shown in figure 2.8b.

Three different plane-wave excitation conditions were modelled: Sidefire, Endfire and Broadside, as shown in figure 2.9.

Applying equations (2.21) and (2.42) to the plane wave condition results in the excitations shown in figure 2.9a-f.

Since the TLM model is time discrete these excitations cannot be modelled exactly. If the excitations are shorter (in time) than one time step, Δt, (where $\Delta t = \frac{\Delta \ell}{c} = \frac{0.1}{c} = 3.3356 \times 10^{-10}$s in this case) then the TLM excitations have to be those shown in figure 2.9g,h.

For endfire excitation the wave propagates in the direction of the wire and so the TLM excitation must do the same. A suitable TLM excitation is depicted in figure 2.9i.

Three termination conditions were compared: low impedance (50Ω), matched (552.23Ω) and high impedance (10000Ω).

Figures 2.10, 2.11 and 2.12 show the resulting comparisons between the TLM and the RADC models.

Figure 2·8 Simple wire problem

a) Physical parameters

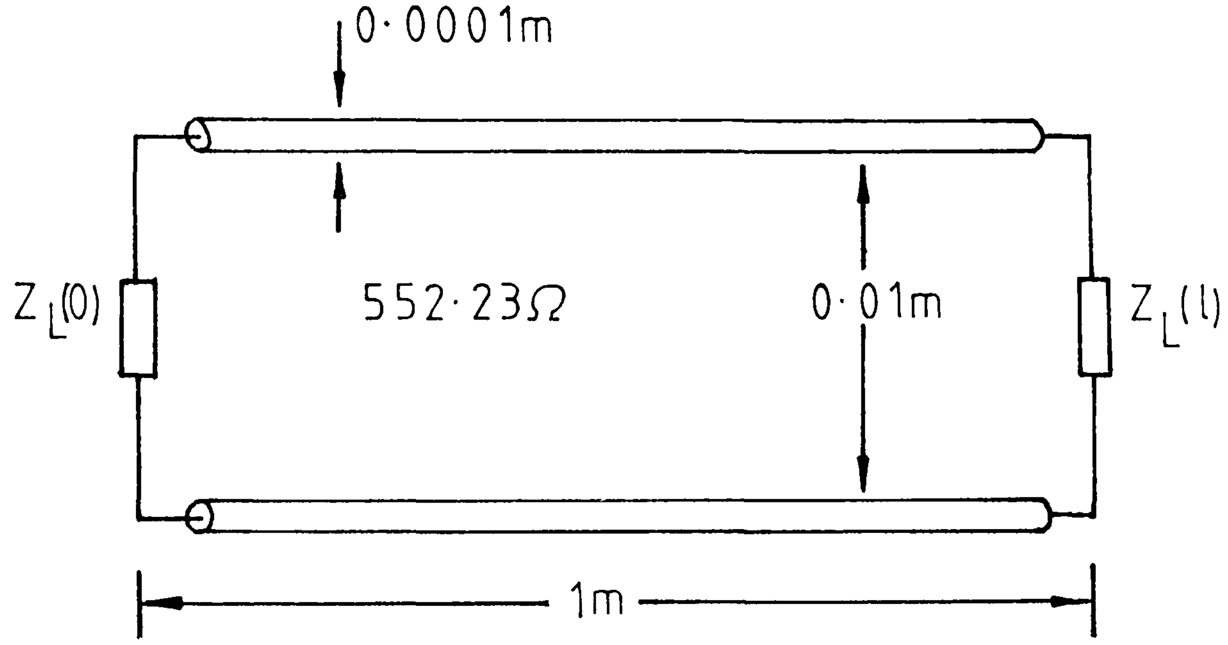

b) Model

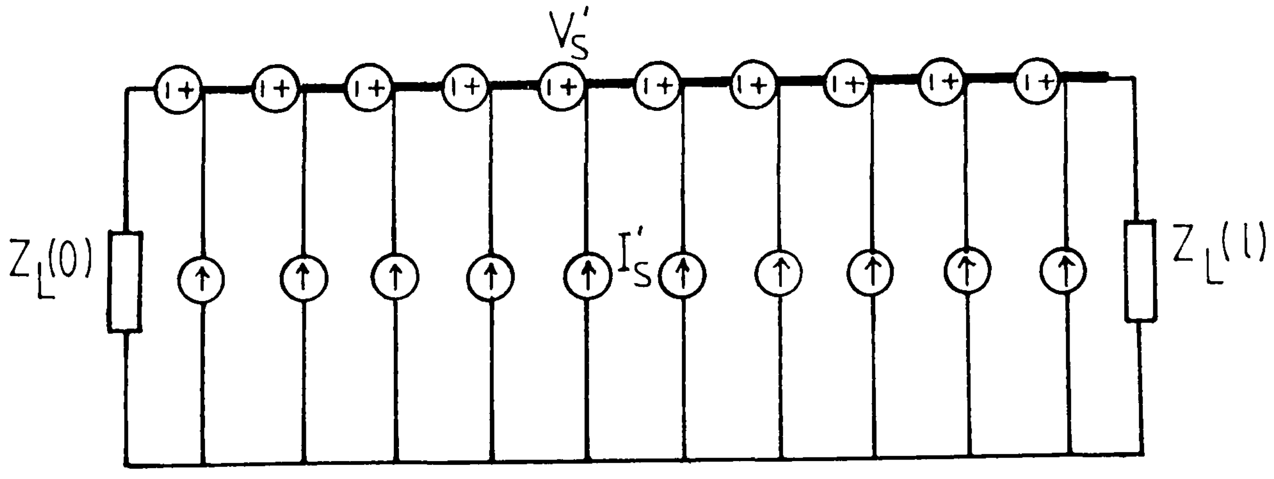

$$V_s' = V_s \Delta l$$
$$I_s' = I_s \Delta l$$

Figure 2·9 Excitation conditions

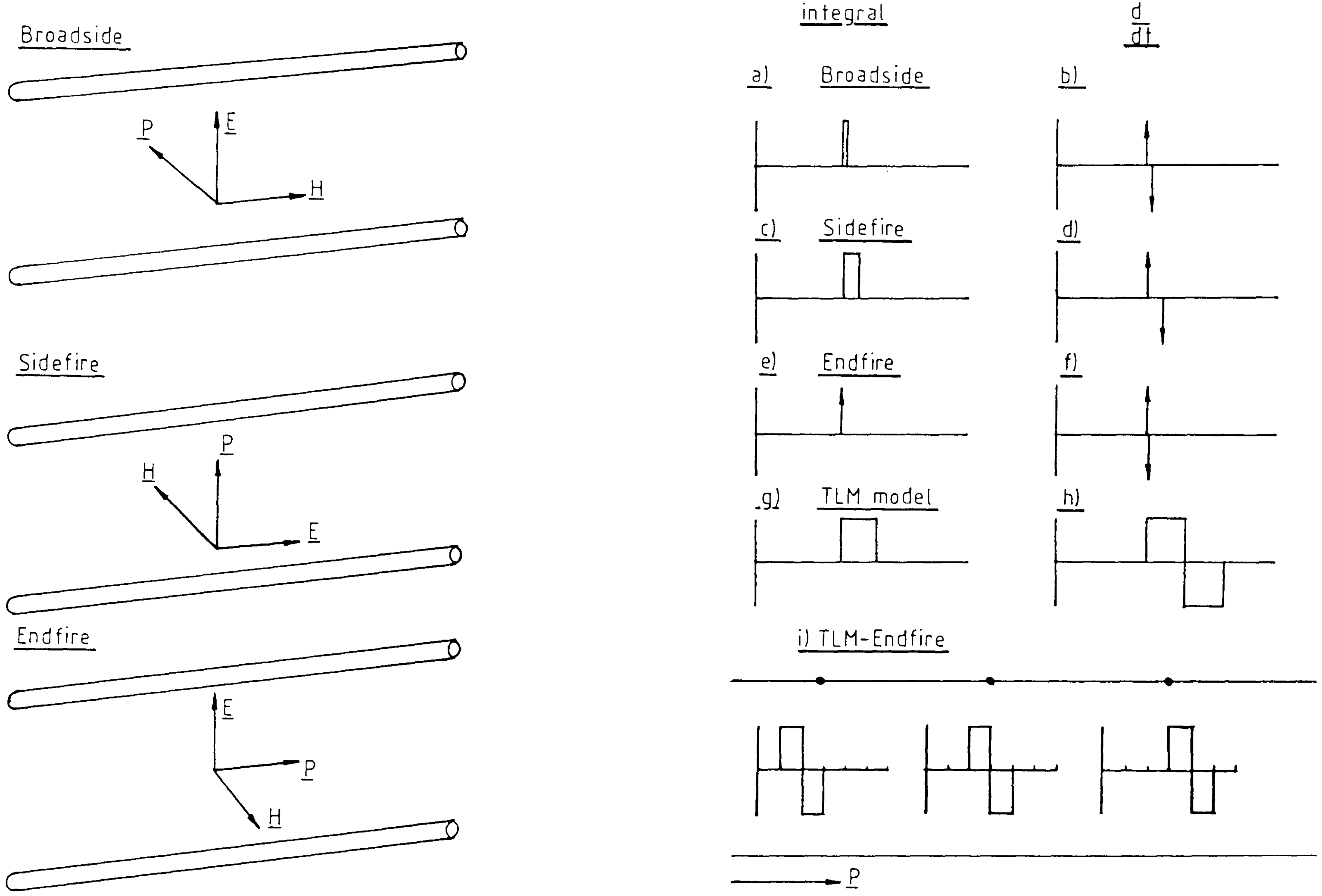

The TLM model used ten nodes and the time domain output was Fourier transformed.

The Sidefire and Broadside results (figures 2.10 and 2.11 respectively) show good agreement. The Endfire result (figure 2.12) is less convincing. Referring back to figure 2.9i it can be seen that an excitation of frequency $\frac{1}{2\Delta t}$ is applied at each node. It was found that the results in figure 2.12 were affected by a very high resonance at $\frac{1}{2\Delta t}$. By changing the model to one with 20 nodes (halving the time step) the results of figure 2.13 were obtained. These results show a good match at low frequencies, although the high frequencies are still affected by the resonance at $\frac{1}{2\Delta t}$.

2.5 A Simple Non-Linear Problem

One of the benefits of using TLM is that discontinuities and non-linearities can be modelled easily. Figure 2.14a shows a simple problem. The line contains two discontinuities and is terminated by a resistor plus diode combination. The TLM mesh spacing is 0.1m, hence there are 100 nodes. The modelling of the discontinuities is as described above (Section 2.3).

The resistor plus diode can be modelled using the techniques in (64).

Hence the voltage, V, across the resistor (R_L) plus diode is:

Figure 2·10 Comparison between TLM and RADC for Sidefire excitation

a) Low impedance (50Ω) loads

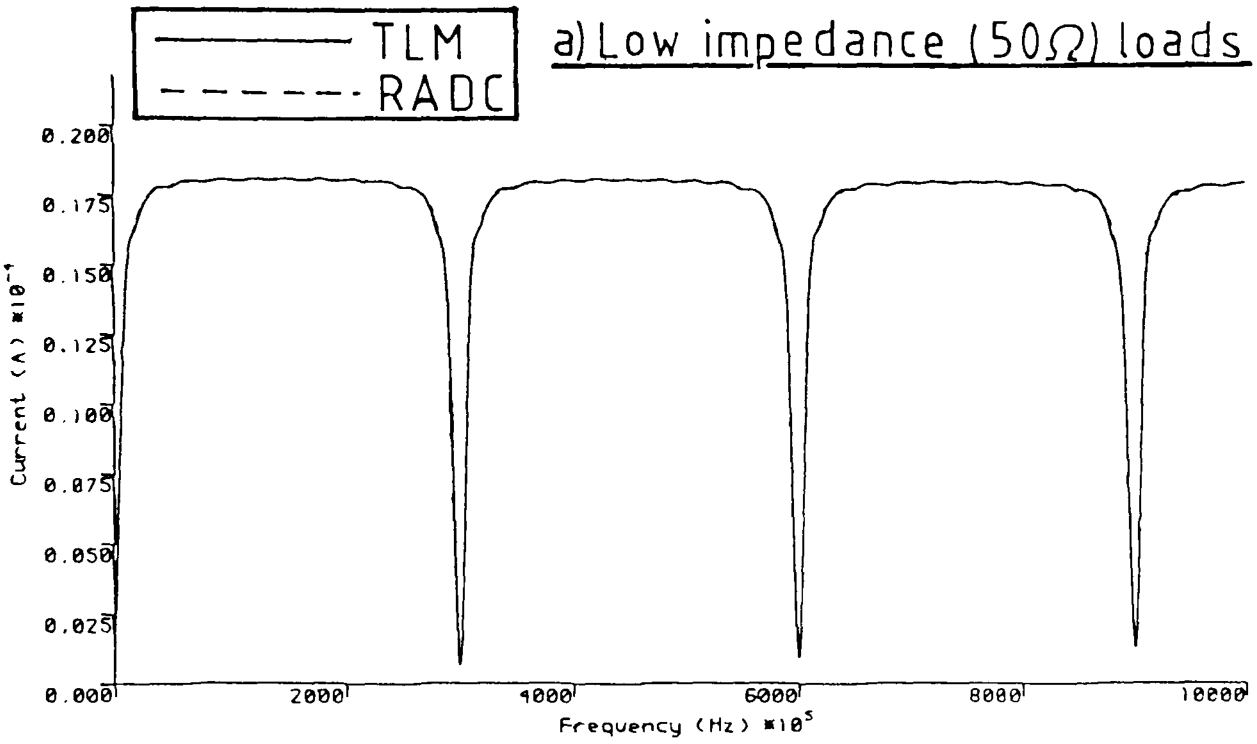

b) Matched (552·23Ω) loads

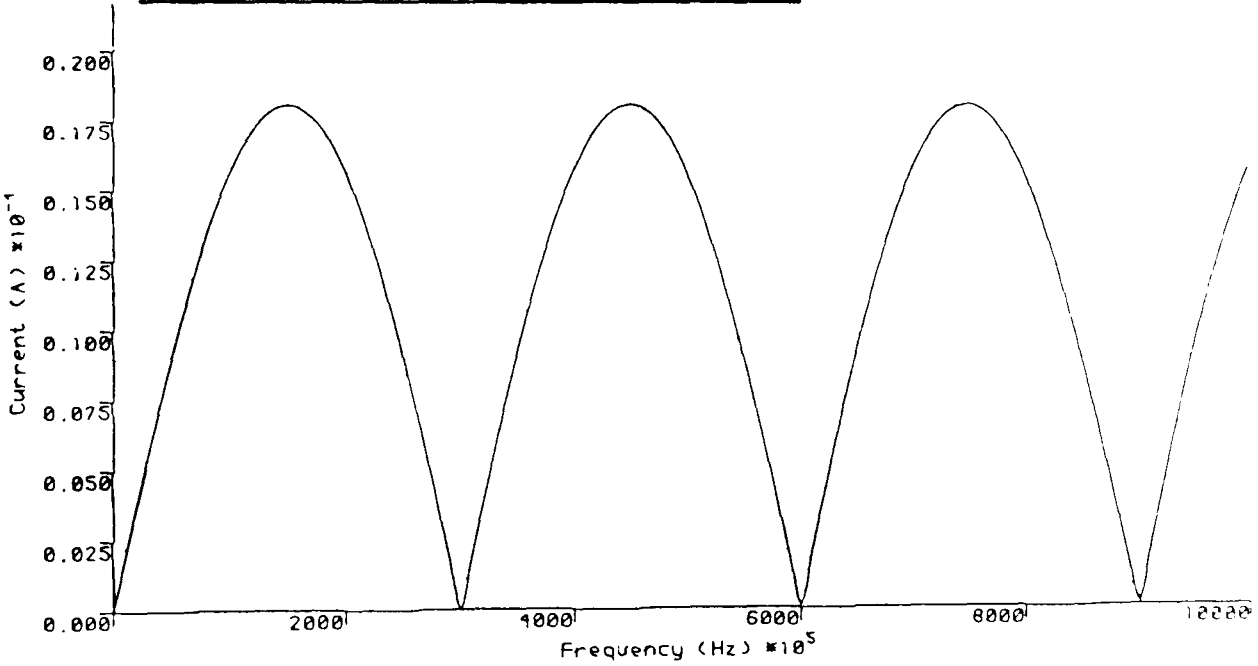

c) High impedance (10 000Ω) loads

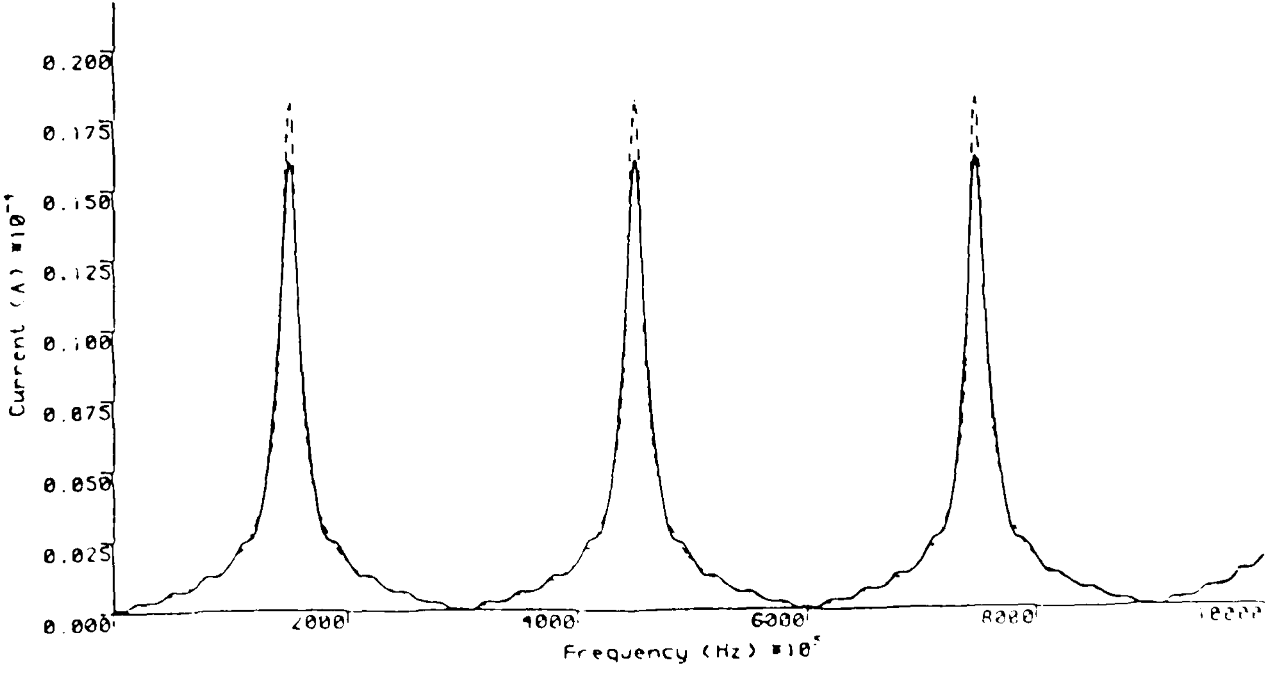

Figure 2·11 Comparison between TLM and RADC for Broadside excitation

a) Low impedance (50Ω) loads

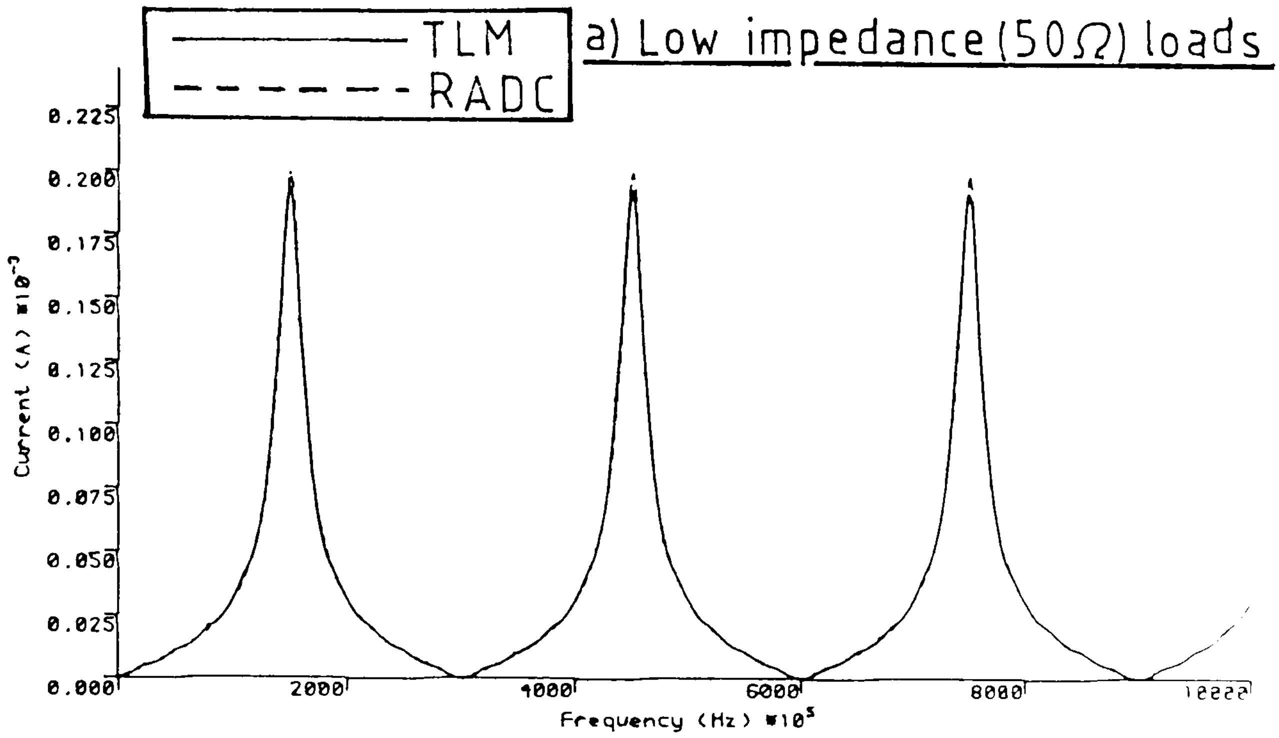

b) Matched (552·23Ω) loads

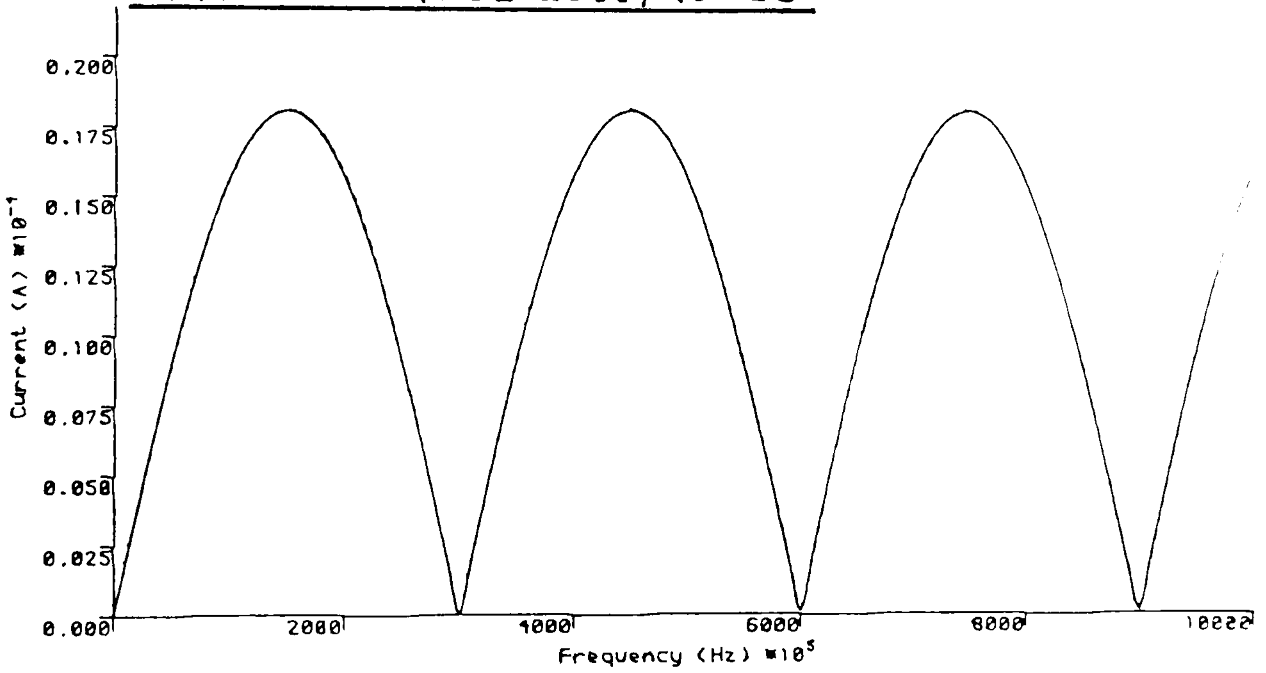

c) High impedance (10 000Ω) loads

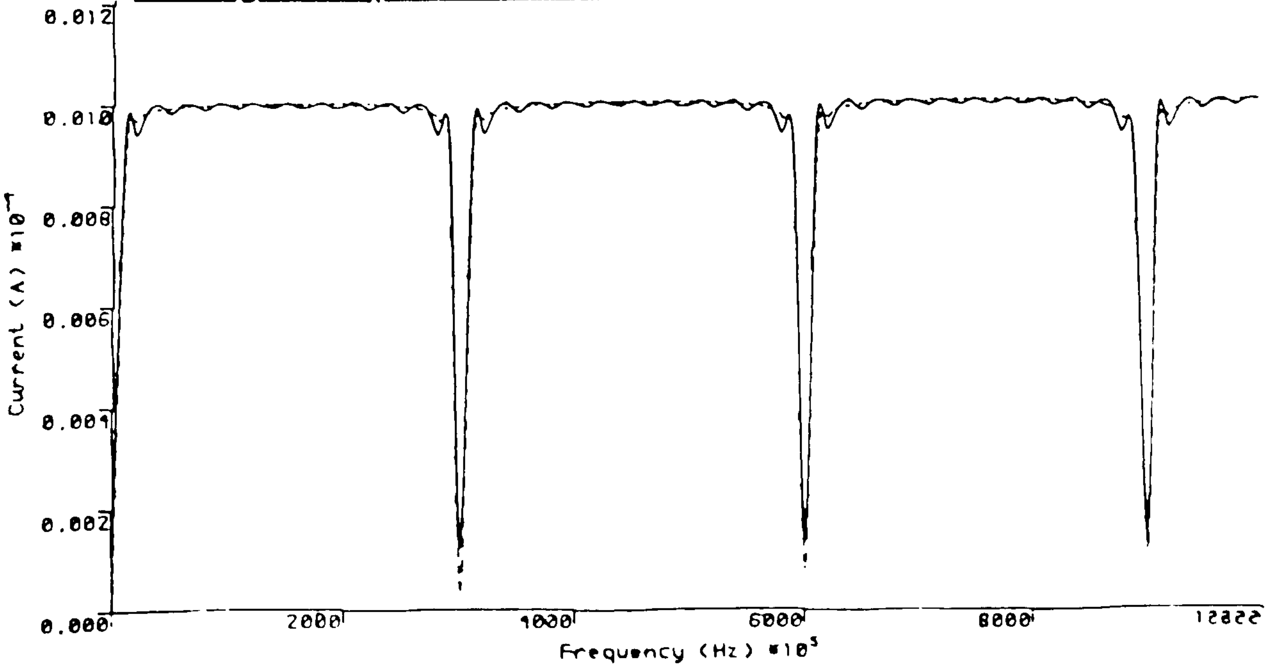

Figure 2·12 Comparison between TLM and RADC for Endfire excitation - 10 nodes

a) Low impedance (50Ω) loads

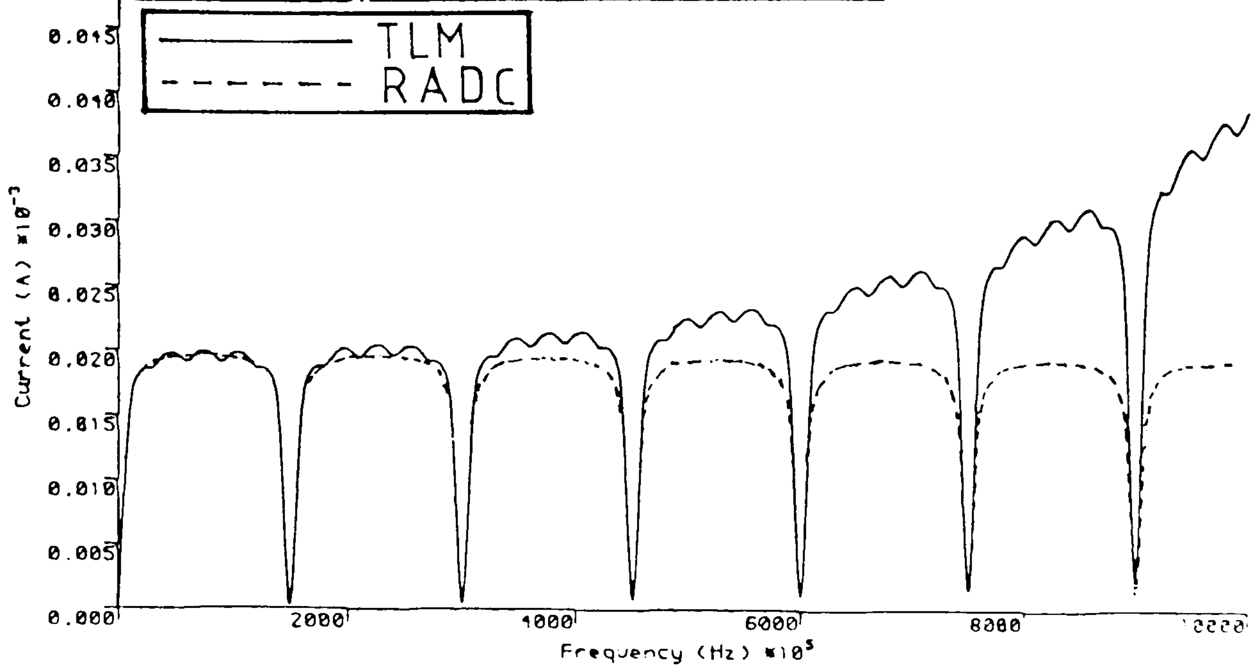

b) Matched (552•23Ω) loads

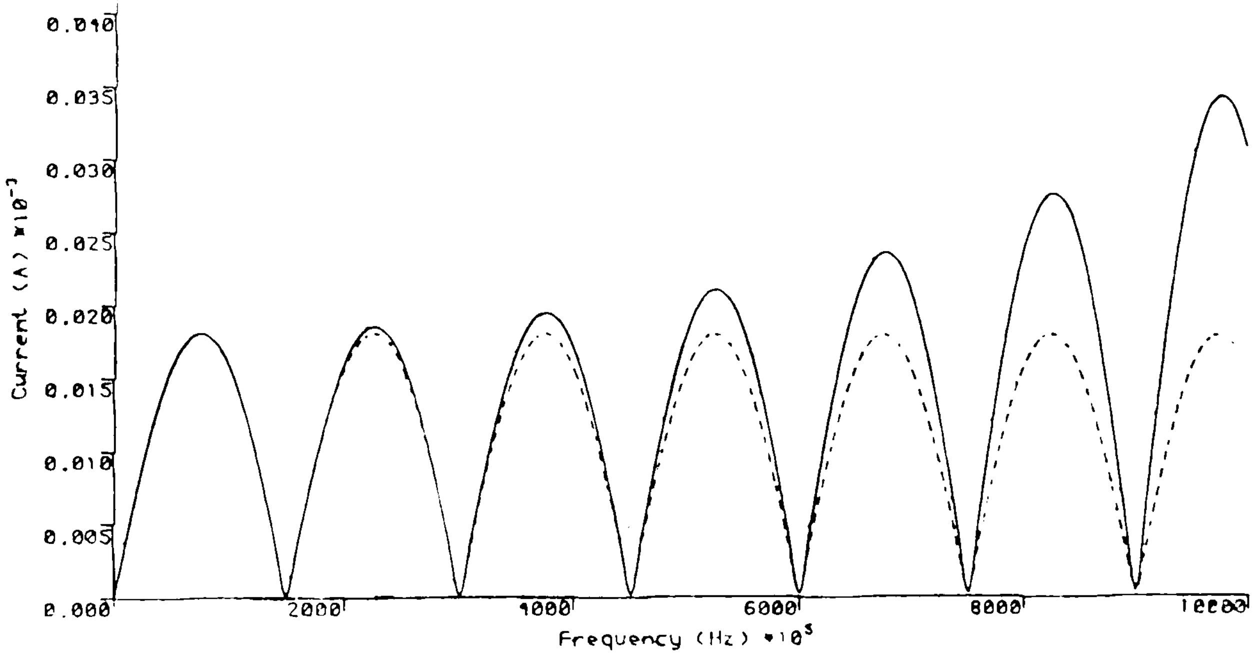

c) High impedance (10 000Ω) loads

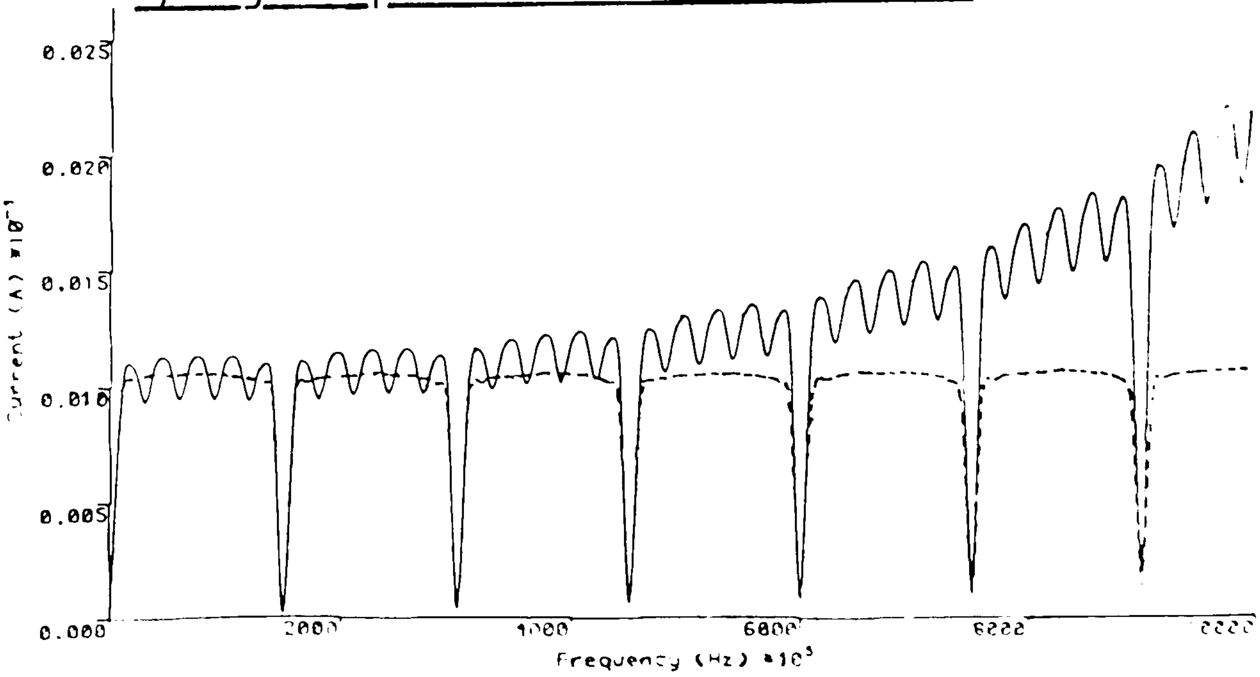

Figure 2·13 Comparison between TLM and RADC for Endfire excitation - 20 nodes

a) Low impedance (50Ω) loads

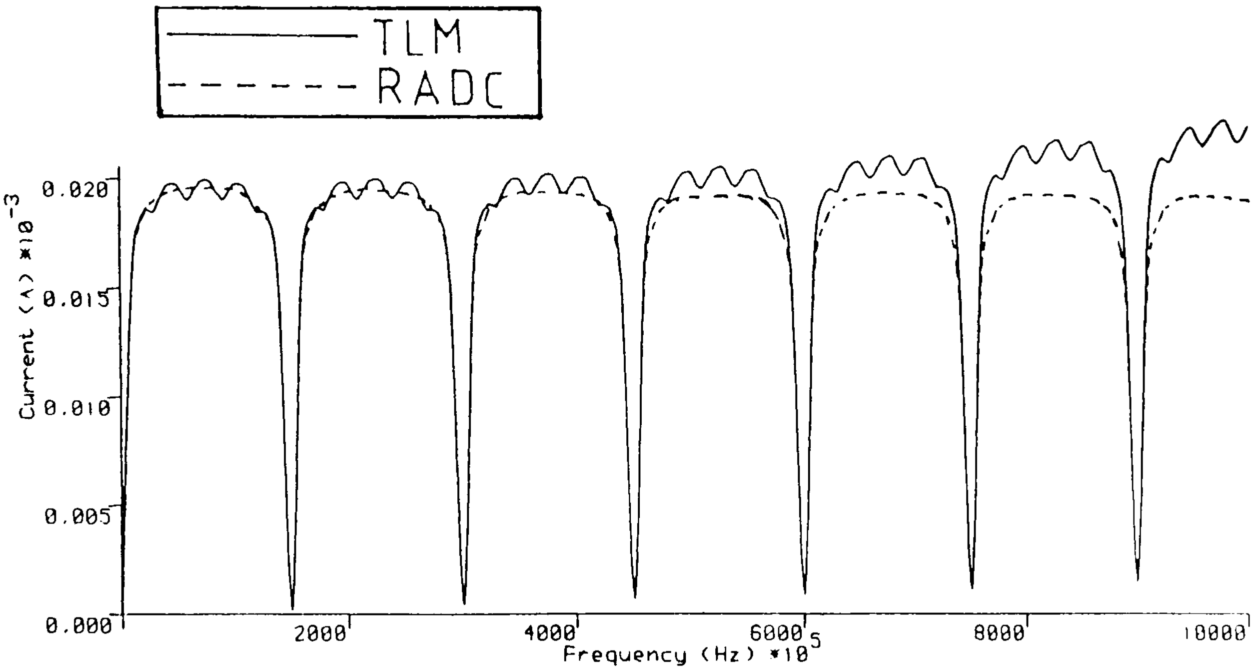

b) Matched (552·23Ω) loads

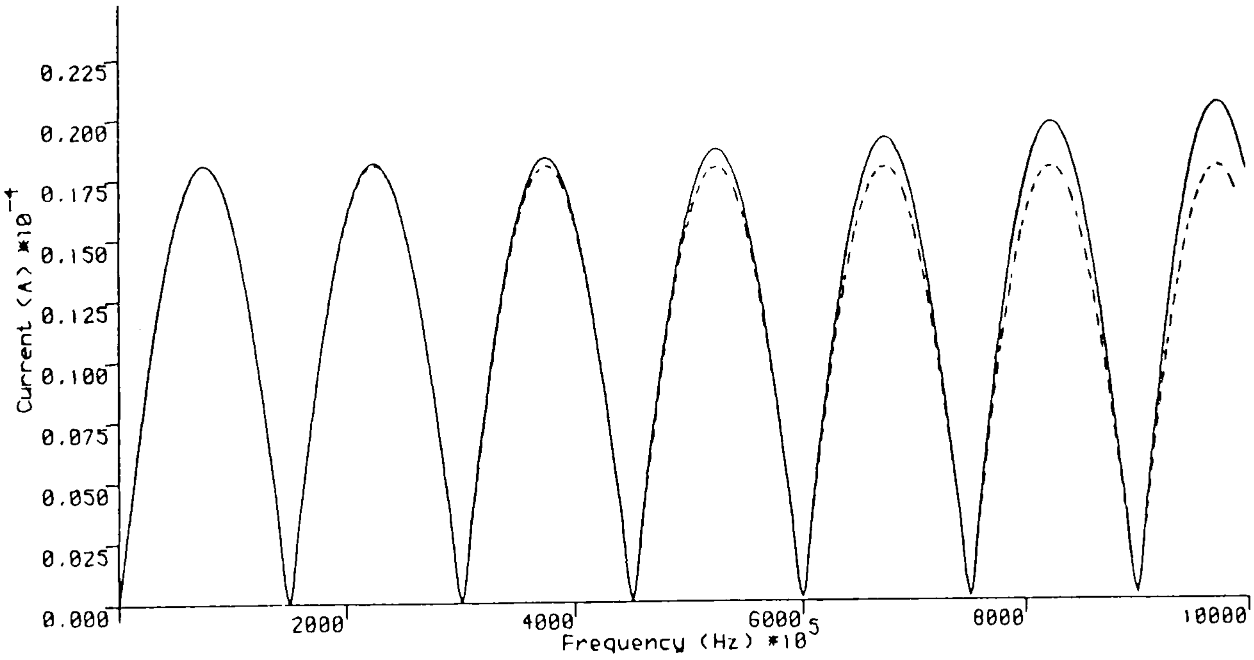

c) High impedance (10 000Ω) loads

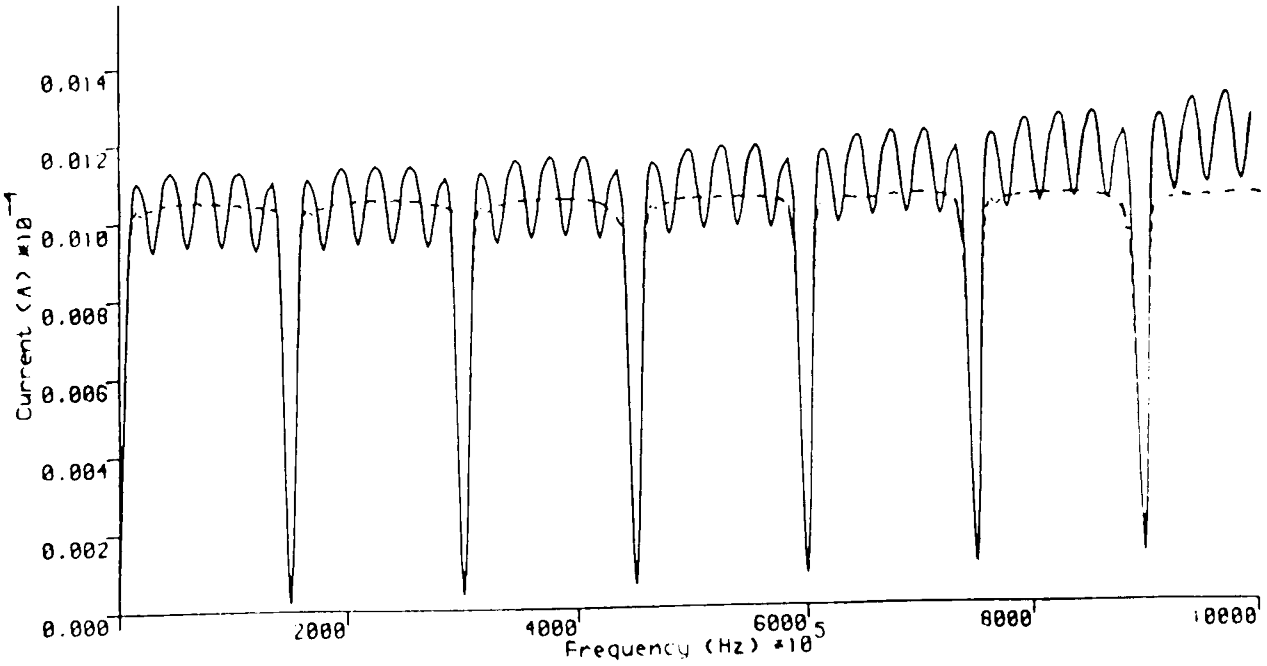

Figure 2·14 Simple non-linear problem geometry and results

a) Circuit diagram

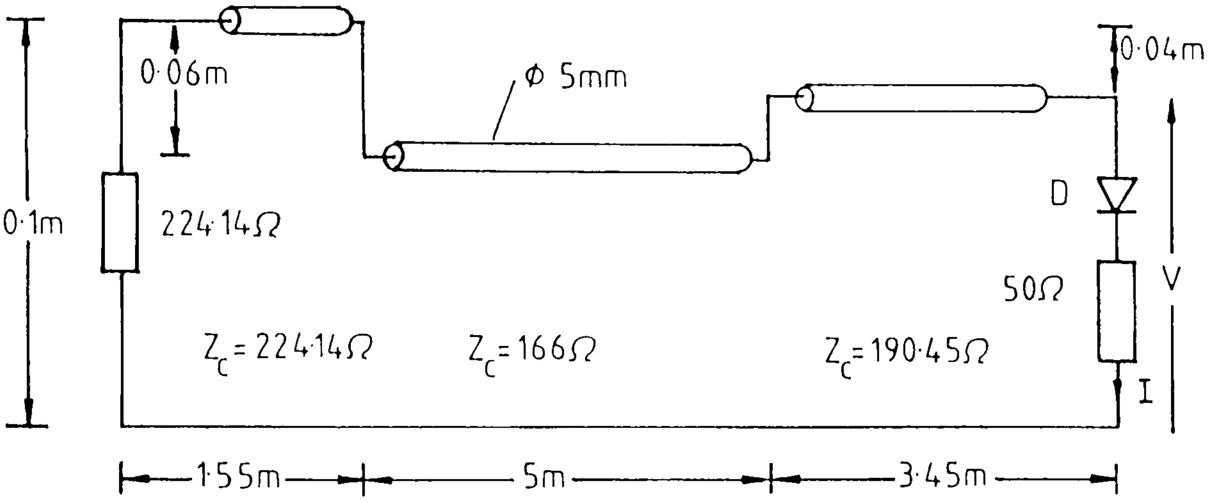

b) Voltage across (50Ω + D)

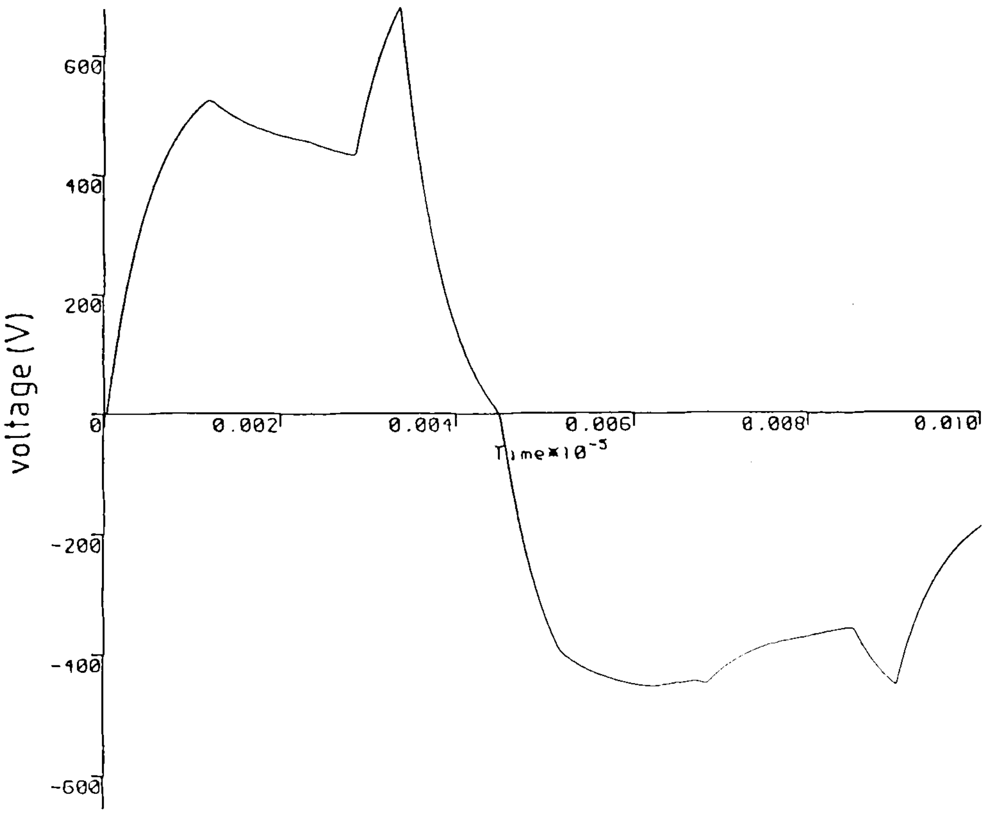

c) Current through diode

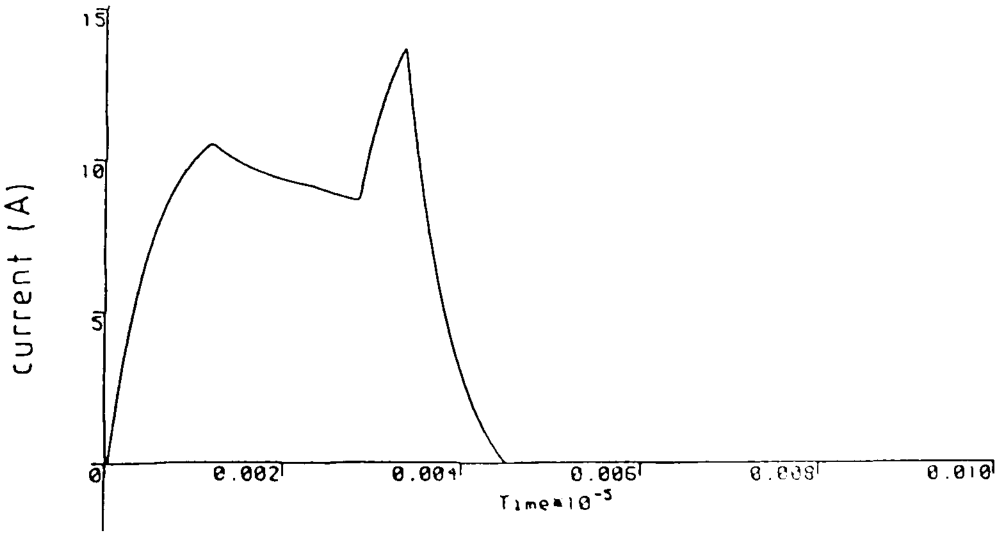

$$V = V^i + V^r \tag{2.87}$$

The current through the diode, I_d, is:

$$I_d = \frac{V^i - V^r}{Z_c} \tag{2.88}$$

The voltage across the diode only, V_d, is:

$$V_d = V - I_d R_L \tag{2.89}$$

and a typical equation characterising the diode:

$$I_d = 10^{-6}(\exp(40V_d) - 1) \tag{2.90}$$

Using equations (2.87) to (2.90) I_d can be expressed in terms of V^i:

$$\frac{\log_e \left[10^6 I_d + 1\right]}{40} = 2V^i - I_d(R_L + Z_o) \tag{2.91}$$

I_d can be found for a particular V^i by using the Newton-Raphson method (75).

Then

$$V^r = V^i - I_d Z_o \tag{2.92}$$

Thus, for a given excitation, the voltage V and the current I_d can be computed.

The excitation condition chosen was a sidefire electromagnetic pulse (EMP). From figure 2.9 it can be seen that only the magnetic field couples into the wire.

The EMP is characterised by; (76):

$$H(t) = \frac{E_o}{Z_o} (\exp(-t/\tau_f) - \exp(-t/\tau_r)) \qquad (2.93)$$

where

$E_o = 5 \times 10^4 \mathrm{Vm}^{-1}$

$Z_o = 376.73\Omega$

$\tau_f = 3.252 \times 10^{-7}\mathrm{s}$

$\tau_r = 5.400 \times 10^{-9}\mathrm{s}$

If the height, h, of the wire is small compared with the length then H(t) remains approximately constant over h and the distributed flux per metre, Φ_d^i, is:

$$\Phi_d^i \approx \mu_o H(t) h \qquad (2.94)$$

giving a source voltage:

$$V_S(x,t) \approx \mu_o h \frac{dH(t)}{dt} \qquad (2.95)$$

Figures 2.14b,c show the resulting voltage and current for the non-linear problem assuming that the diode does not breakdown.

In figure 2.14b the first peak at 12ns is caused by the smaller excitation on the middle section of wire arriving at the diode. The second maximum occurs when the larger excitation from the matched end arrives at the diode. The large decrease after 33.7ns occurs when a negative excitation on the matched end has travelled down the line to the diode. After 45ns the diode no longer conducts.

However the large negative voltage would cause the diode to breakdown giving a large negative current.

2.6 Conclusions

A one-dimensional TLM model for the coupling of electromagnetic radiation into a pair of wires has been derived. The comparisons with the RADC method show very good agreement.

Since TLM is a time domain modelling technique it is possible to include non-linearities which are difficult to model using frequency domain techniques. An example of a non-linear problem was presented and results obtained.

In Chapter 7 the one-dimensional model described here will be compared with a three-dimensional (TLM) field solution.

Chapter 3 Discrete Models of Wires Using TLM

3.1 Introduction

In Chapter 2 TLM was used to solve a transmission-line problem. TLM is often used to model Maxwell's equations (that is, to solve field problems). (57,58,59). Recently TLM has been used to obtain the fields close to, and surface currents on, aircraft (68,77,78). A logical progression from this is to model the actual wires contained within the aircraft.

A wire could be modelled as shown in figure 3.1a. By short-circuiting the transmission-lines mid-way between nodes or by short-circuiting a node (Chapter 4) a discrete model of a wire can be formed. If the wire is perfectly conducting - an assumption that will be made throughout this work - then the current flowing in the wire at each of the short-circuits will be (from figure 3.1b):

$$I = \frac{-2V^r}{Z_o} \quad \text{(between nodes)} \qquad (3.1)$$

By summing all such currents around the wire, the total current flowing can be computed.

3.2 The Radius of the Wire Model

The effective (or modelled) radius of the discrete wire (as in figure 3.1a) can be computed in several ways. The two methods chosen were: a wire-above-ground and a

Figure 3·1 TLM wire model

a) 2D shunt mesh

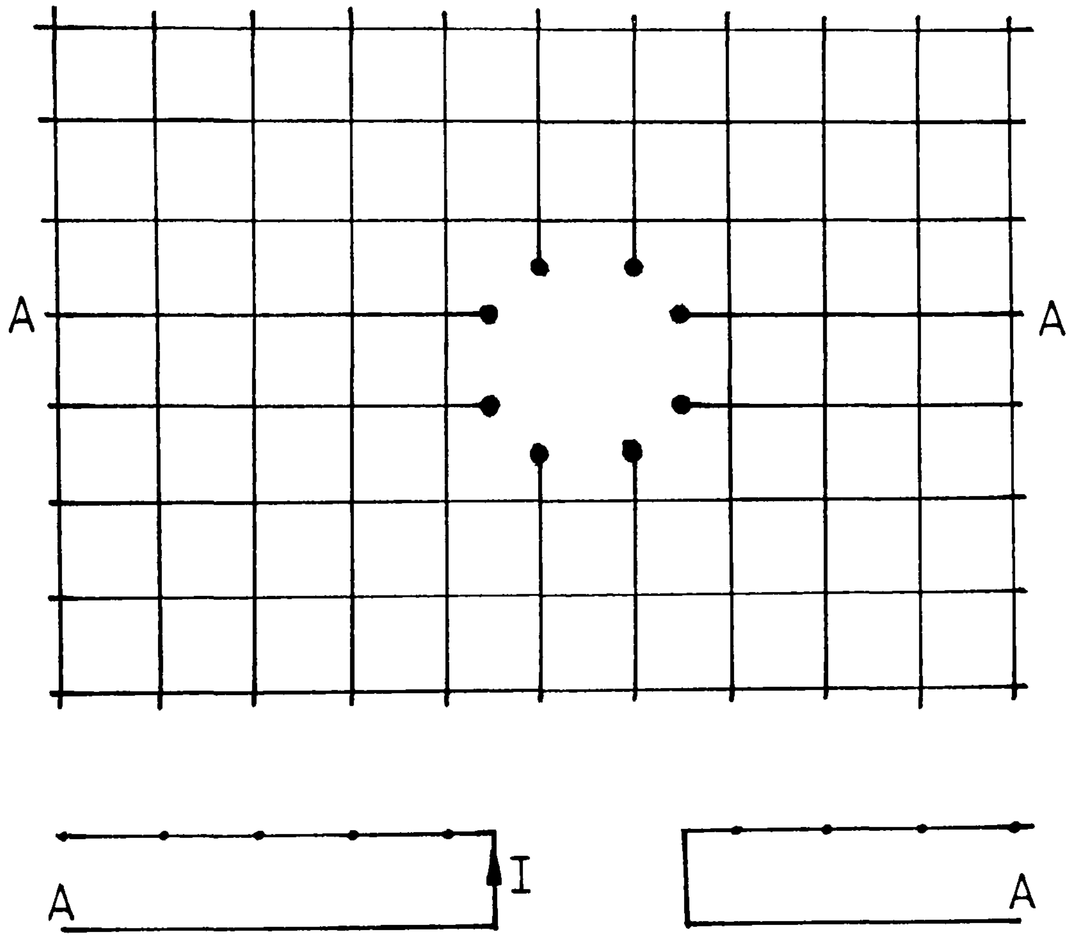

b) Current in short-circuit

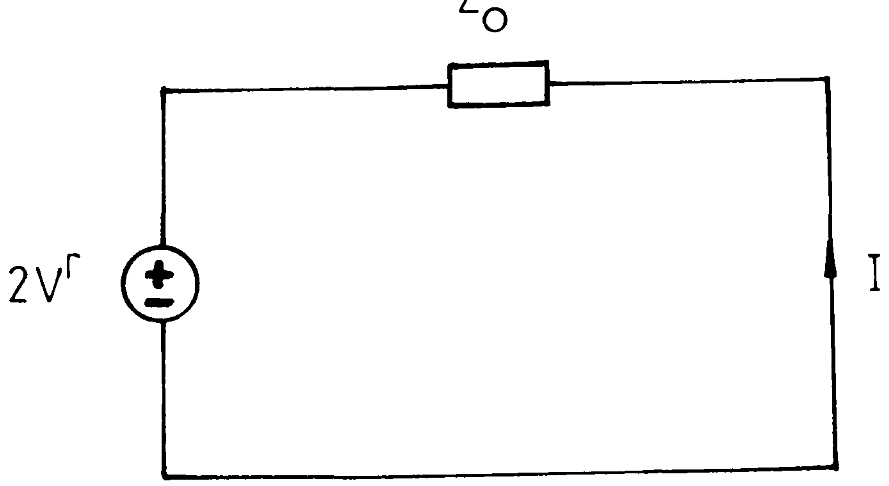

wire in a resonant cavity geometries.

For a wire-above-ground the inductance and capacitance to ground are available from standard formulae (79,80). These can also be computed from the zero frequency (of the Fourier Transform) of the field values computed using a 2D or 3D TLM routine (Appendices A, B).

In the resonant cavity the voltages and currents can be obtained at a resonant frequency in the TLM model. The characteristic impedance can then be computed and compared with known formulae (80).

3.2.1 Wire Above Ground

Figure 3.2a shows a typical wire above ground geometry. The analytical formulae for the distributed inductance and capacitance (L_d, C_d) are (74,79):

$$L_d = \frac{\mu_o}{2\pi} \cosh^{-1} \left(\frac{h}{r}\right) \quad Hm^{-1} \tag{3.2}$$

$$C_d = \frac{2\pi\varepsilon_o}{\cosh^{-1} \left(\frac{h}{r}\right)} \quad Fm^{-1} \tag{3.3}$$

The current flowing in the wire is related to the distributed inductance by (Chapter 2):

$$\Phi_d = L_d I \tag{3.4}$$

where Φ_d is the distributed flux linkage.

$$\Phi = \int_S \underline{B} . d\underline{S} \tag{3.5}$$

Figure 3·2 Wire above ground

a) geometry

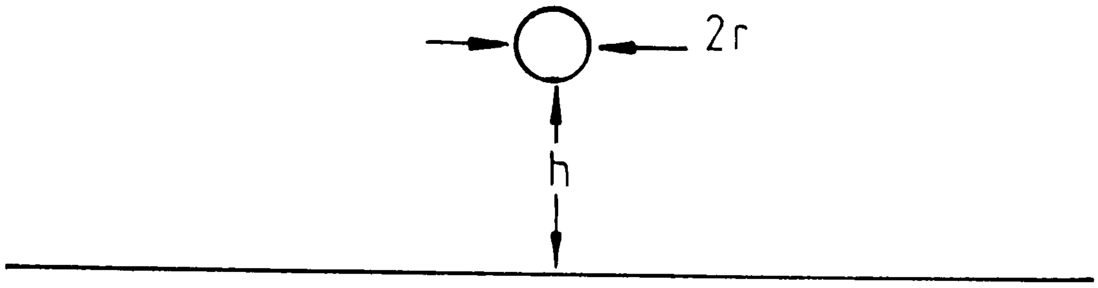

b) TLM shunt mesh

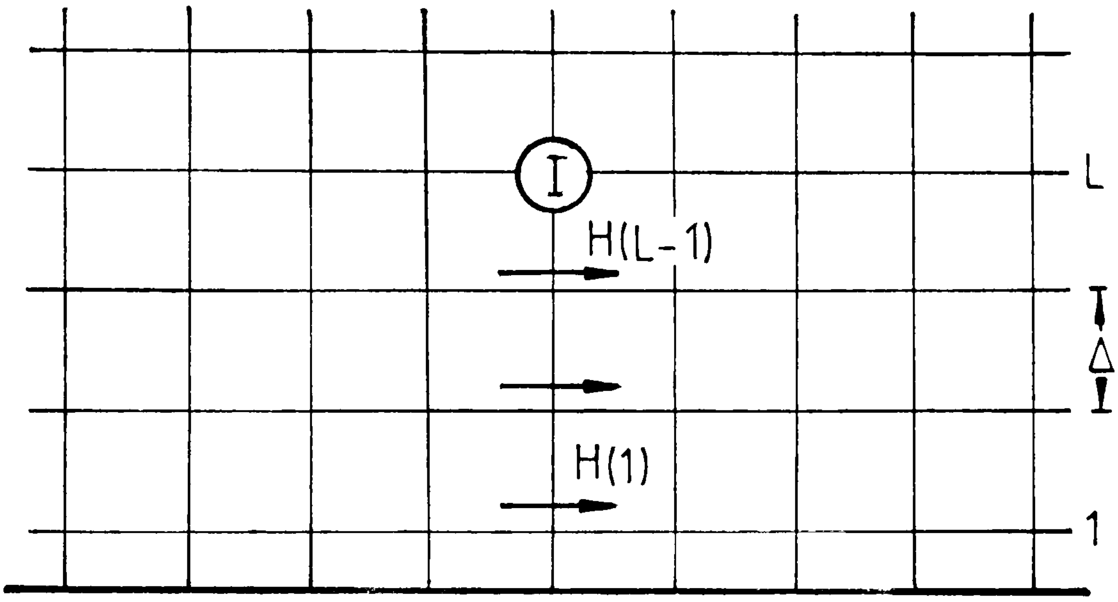

c) TLM series mesh

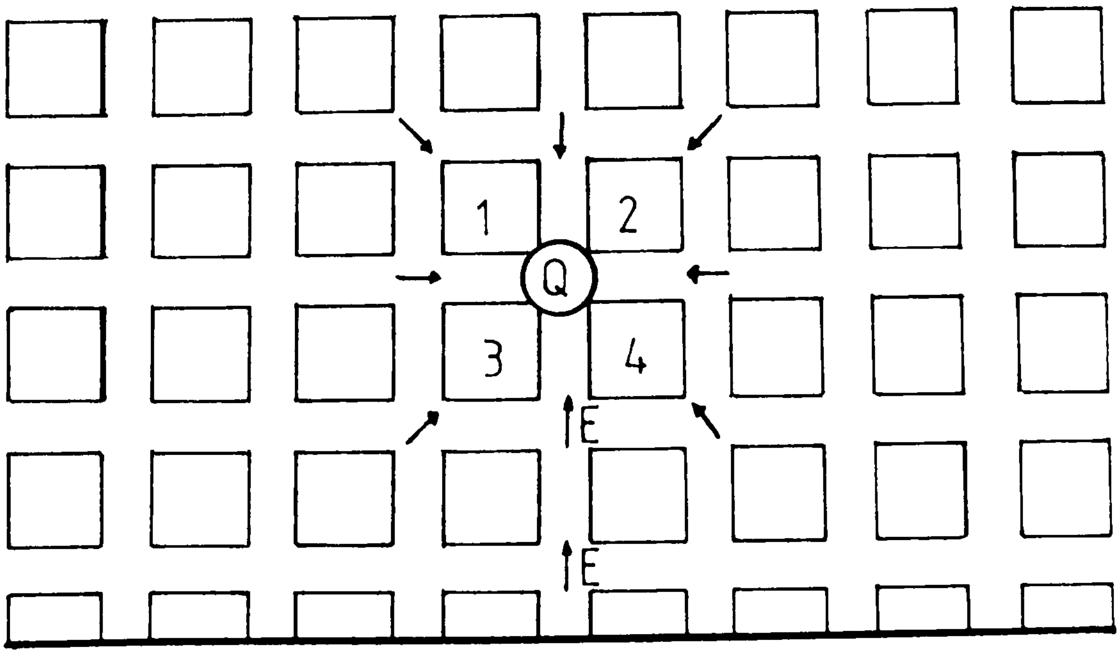

$$\therefore \quad \Phi_d = \int \underline{B}.d\underline{\ell} \tag{3.6}$$

and since $\underline{B} = \mu\underline{H}$ then

$$\Phi_d = \mu \int \underline{H}.d\underline{\ell} \tag{3.7}$$

In TLM, equation (3.7) becomes (see figure 3.2b)

$$\Phi_d = \mu \sum_{\ell=1}^{L-1} H(\ell)\Delta\ell \tag{3.8}$$

Both H and I can be obtained from the zero frequency term of the Fourier Transform of the TLM time-domain response, giving L_d. This can be substituted into equation (3.2) and the radius, r, obtained.

Since L_d is a self inductance a current has to be forced through the wire to obtain the required solution. This can be achieved in one of three ways - all of which produce identical results:

i) Inject a current into the wire;
ii) Inject a current into the whole ground plane;
iii) Excite $\oint \underline{H}.d\underline{\ell}$ around the wire.

Similarly for the distributed capacitance, C_d:

$$Q_d = C_d V \tag{3.9}$$

From equations (2.37) and (2.38):

$$Q = \oint_S \underline{D}.d\underline{S} \tag{3.10}$$

with $\underline{D} = \varepsilon\underline{E}$ giving:

$$Q_d = \varepsilon \int \underline{E}.d\underline{\ell} \tag{3.11}$$

In the TLM solution this becomes:

$$Q_d = \varepsilon \sum^{\text{loop}} E\Delta\ell \tag{3.12}$$

The voltage between the wire and the ground plane is

$$V = -\sum_{\ell=1}^{L-1} E(\ell)\Delta\ell \tag{3.13}$$

E and V are obtained from the zero frequency term of the Fourier Transform of the TLM time-domain electric field and voltage outputs. The radius of the wire can then be evaluated using equations (3.9) and (3.3). To find the capacitance the TLM model has to be excited with a voltage between the wire and ground.

3.2.2 Wire in Resonant Cavity

The wire in cavity geometry is shown in figure 3.3. In (80) the characteristic impedance of a coaxial wire in such a geometry is shown to be:

$$Z_o = \frac{60}{\sqrt{\varepsilon_r}} \log_e (1.08 \frac{h}{d}) \tag{3.14}$$

and from (19):

$$Z_x = \frac{Z_o(Z_L + Z_o \tanh\gamma x)}{Z_o + Z_L \tanh\gamma x} \tag{3.15}$$

where: Z_L is the load impedance;

Z_x is $\frac{V}{I}$ at a point x metres along the wire;

γ is the propagation constant $= \alpha + j\beta$.

Figure 3·3 Wire in cavity geometry

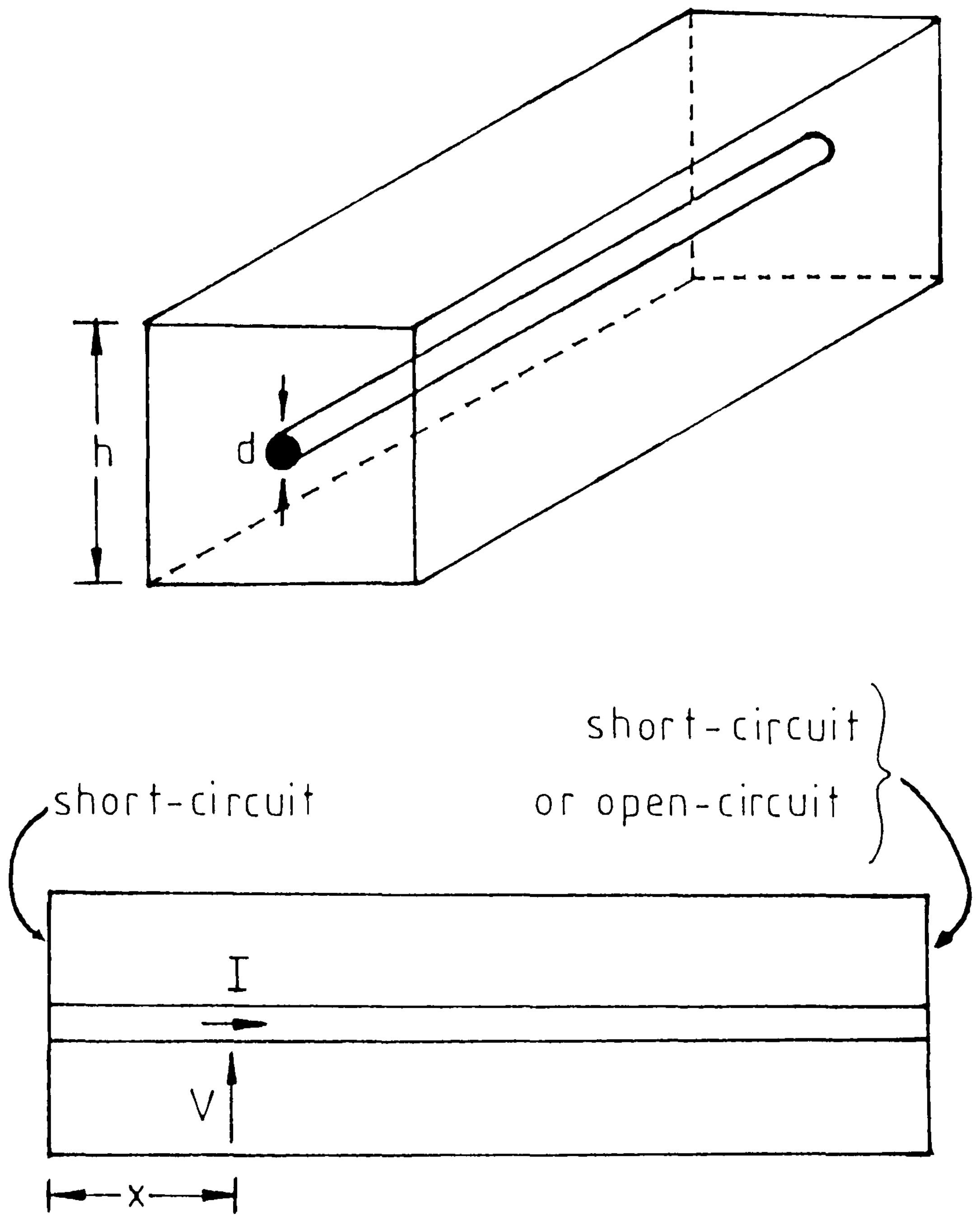

Excitation

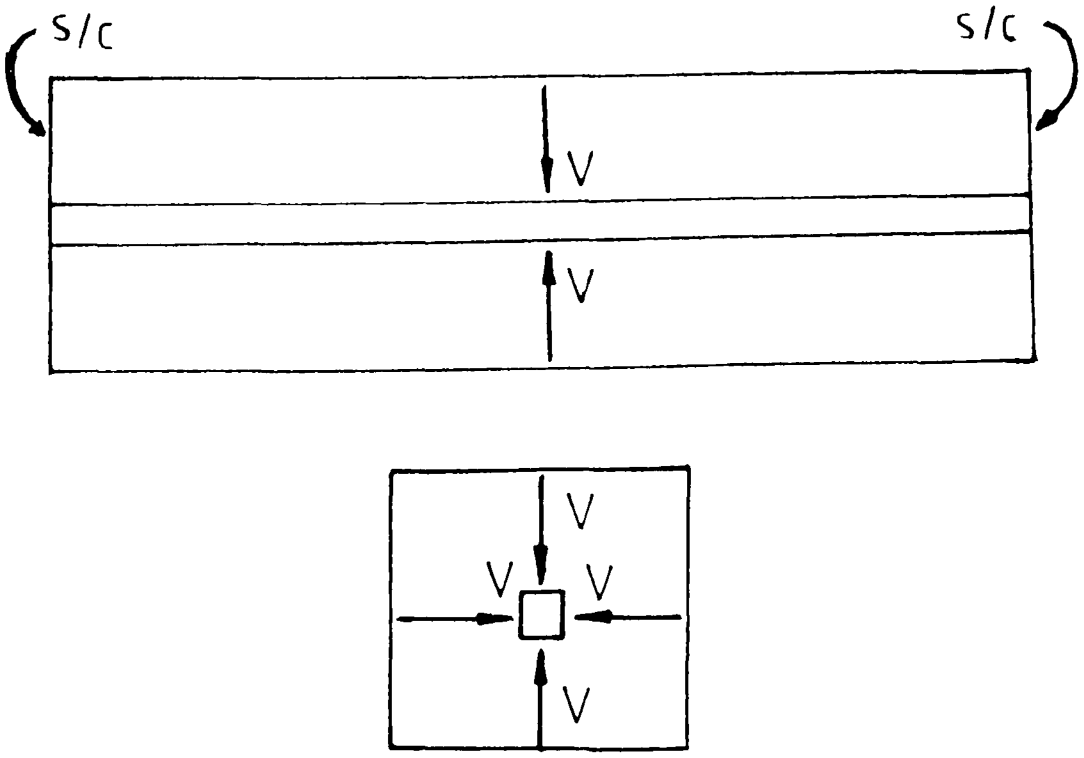

For lossless lines with short-circuit (perfectly conducting) loads:

$$Z_x = jZ_o \tan \beta x \tag{3.16}$$

where $\beta = \frac{2\pi}{\lambda}$ and λ is the wavelength.

In the TLM model the time-varying voltage (V) and current (I) can be observed at any TLM node along the wire due to an initial excitation. For the geometries considered here, where both ends of the wire are terminated in conducting boundaries, this was a voltage applied symmetrically to the mid-point of the wire as shown in figure 3.3. After Fourier Transformation the resonant frequencies of the voltage and current waveforms can be obtained.

Taking the wavelength, λ, to be twice the wire length (the longest wavelength) the voltage and current amplitudes at the corresponding (the lowest) frequency can be found. By substituting these values into equations (3.16) and (3.14) the diameter of the wire (and hence the radius) can also be computed. The velocity of propagation, ν, is also available

since $\nu = f\lambda$ (3.17)

3.3 Numerical Simulation

3.3.1 Wire Above Ground

Figure 3.4 shows four 2D TLM models of a wire mesh radius 0.5m, 1.5m above ground.

Figure 3·4 Wire above ground, $r = 0{\cdot}5\text{m}$, $h = 1{\cdot}5\text{m}$

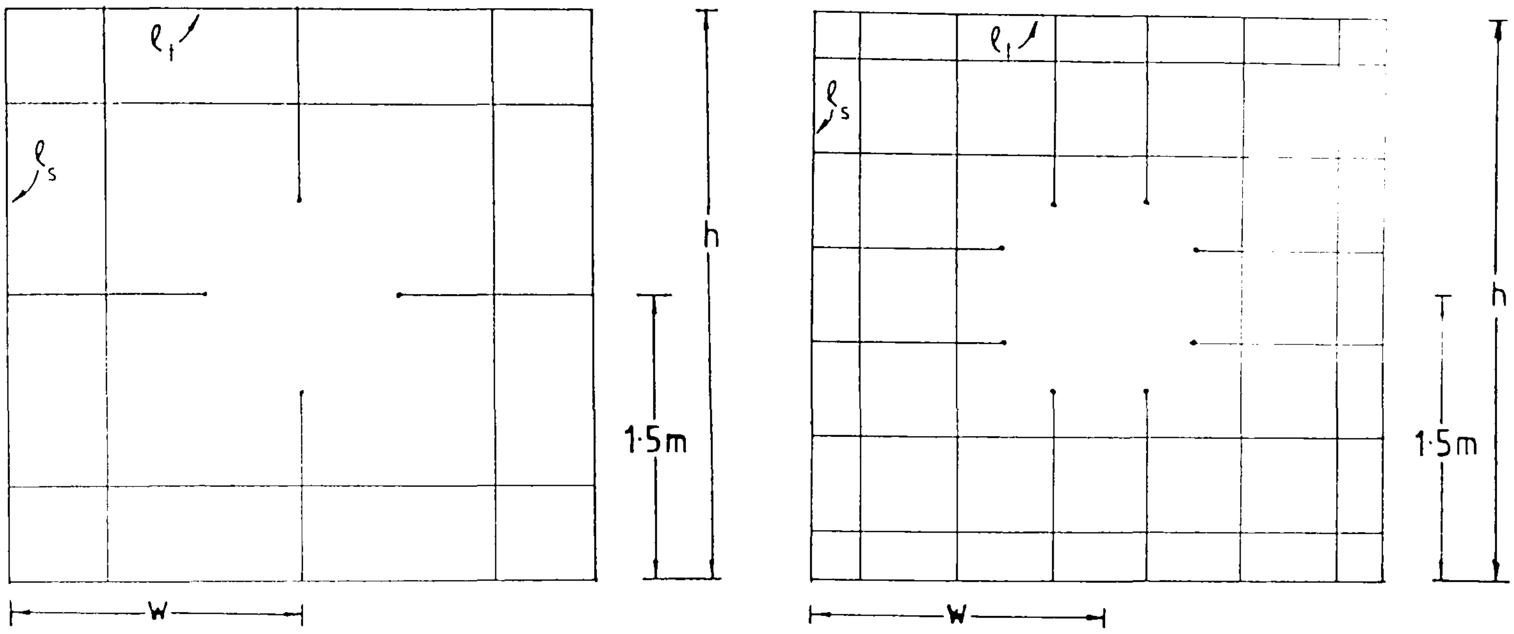

a) $\Delta l = 1\text{m}$

b) $\Delta l = 0{\cdot}5\text{m}$

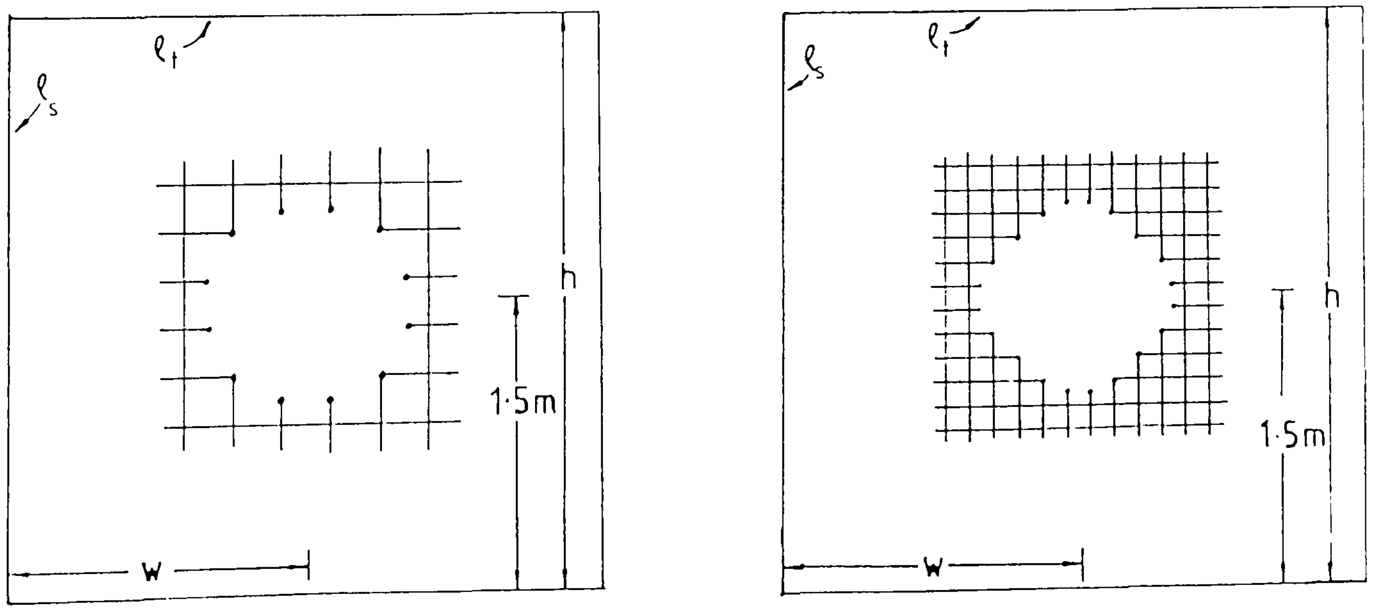

c) $\Delta l = 0{\cdot}25\text{m}$

d) $\Delta l = 0{\cdot}125\text{m}$

Using equations (3.2) and (3.3) the theoretical inductance and capacitance were calculated to be:

$$L_d = 3.525 \times 10^{-7} \ \mathrm{Hm}^{-1}$$

$$C_d = 3.156 \times 10^{-11} \mathrm{Fm}^{-1}$$

The technique described in section 3.2.1 was applied to each of the geometries and the inductance and capacitance were obtained numerically. Table 3.1 shows the results obtained for a width, w, of 1.5m and a height, h, of 3m. Clearly there are large errors in modelling the inductance and capacitance.

The main problem is that an infinite ground plane cannot be modelled accurately using the TLM technique. This is because the numerical model has to be terminated with some boundary since only a finite volume can be modelled. If a matched boundary is used at the sides of figure 3.4 then the ground plane effectively stops at this point.

By moving the boundaries away from the wire and changing the boundary conditions the effective size of the ground plane can be enlarged.

Table 3.2 shows how the resulting inductance and capacitance improve in accuracy as the size of the ground plane was increased.

The difference in accuracy between the inductance and capacitance models can be explained by referring back to

Table 3.1 Variation in Inductance and Capacitance with two dimensional mesh description.

w = 1.5m, h = 3.5m, r = 0.5m, d = 1.5m

$L_d = 3.525\text{x}10^{-7}\ \text{Hm}^{-1}$, $C_d = 3.156\text{x}10^{-11}\ \text{Fm}^{-1}$

Δl (m)	Its	L_d x10^{-7} (Hm^{-1})	%error in L_d	C_d x10^{-11} (Fm^{-1})	%error in C_d
1.000	50	6.123	73.7	-	-
1.000	100	6.061	71.9	-	-
1.000	300	6.010	70.5	6.945	120.1
0.500	400	5.496	55.9	5.924	87.7
0.250	200	5.650	60.2	5.107	61.8
0.250	400	5.615	59.3	5.483	73.7
0.125	800	5.838	65.6	4.859	54.0

Table 3.2 Two dimensional wire above ground results.

$r = 0.5\text{m},\ h = 1.5\text{m}$

$L_d = 3.525\text{x}10^{-7}\ \text{Hm}^{-1},\ C_d = 3.156\text{x}10^{-11}\ \text{Fm}^{-1}$

Δl (m)	ρ_t	ρ_s	h (m)	w (m)	its	L_d x10^{-7} (Hm^{-1})	error in L	C_d x10^{-11} (Fm^{-1})	error in C
0.125	0	0	3.00	1.50	800	5.838	65.6	-	-
0.125	0	0	2.38	1.50	1600	5.834	65.5	-	-
0.125	0	0	3.00	1.13	1600	7.017	99.1	-	-
0.125	0	0	3.00	3.00	1600	4.367	23.9	-	-
0.125	0	0	3.00	4.50	1600	4.118	16.8	-	-
0.125	0	0	3.00	4.50	2400	4.109	16.6	-	-
0.250	0	0	6.00	6.00	2000	3.657	3.7	3.808	20.5
0.250	0	1	6.00	6.00	2000	3.653	3.6	3.415	8.1
0.250	0	-0.5	6.00	6.00	2000	3.665	4.0	-	-
0.250	0	-1	6.00	6.00	2000	4.282	21.5	-	-
0.250	1	1	6.00	6.00	2000	3.648	3.5	3.348	6.0
0.500	0	0	6.00	6.00	1000	3.582	1.6	3.954	25.1
0.500	0	0	6.00	6.00	2000	3.576	1.5	-	-
0.500	0	1	6.00	6.00	1000	3.578	1.5	3.539	12.0
0.500	1	0	6.00	6.00	1000	3.576	1.5	3.712	17.5
0.500	1	1	6.00	6.00	1000	3.577	1.5	3.519	11.4
0.500	0	0	6.00	3.00	1000	4.042	14.7	-	-
0.500	0	0	6.00	1.50	1000	5.483	55.6	-	-
0.500	0	0	4.50	6.00	1000	3.616	2.6	-	-
0.500	0	0	3.00	6.00	1000	3.801	7.8	-	-

figure 3.2. In the inductance case the wire area is defined by the position of the short-circuits introduced to model the wire. In the capacitance case, (figure 3.2c) although the short-circuits may be between the nodes, the structure of the mesh adds the whole of the transmission line loops (1, 2, 3, 4) onto the wire geometry. This effectively rounds up the wire radius and increases the capacitance to ground. From Table 3.2 the optimum boundary condition was found to be an open-circuit ($\rho = 1$). With a non-matched boundary, the boundary actually changes the problem being modelled. An open-circuit boundary models a multiple wire-above-ground geometry as shown in figure 3.5.

The above method can also be used in a 3D TLM routine (Appendix B). Figure 3.6 and Table 3.3 show the geometry and results for a simple wire model in a single-slice of a 3D TLM routine. Again, if open-circuit boundaries are used a reasonably accurate radius and velocity are obtained.

Thus, using TLM, it is possible to find the inductance and capacitance per metre and hence the radius. However, this problem is not well defined because a non-physical external boundary has to be introduced. To separate out any non-physical boundary conditions it is necessary to model a closed geometry. The wire in a resonant cavity is such a closed geometry and the results obtained from this model should be considered as a more reliable indicator of the wire radius.

Figure 3·5 Actual problem modelled when open-circuit boundaries are used

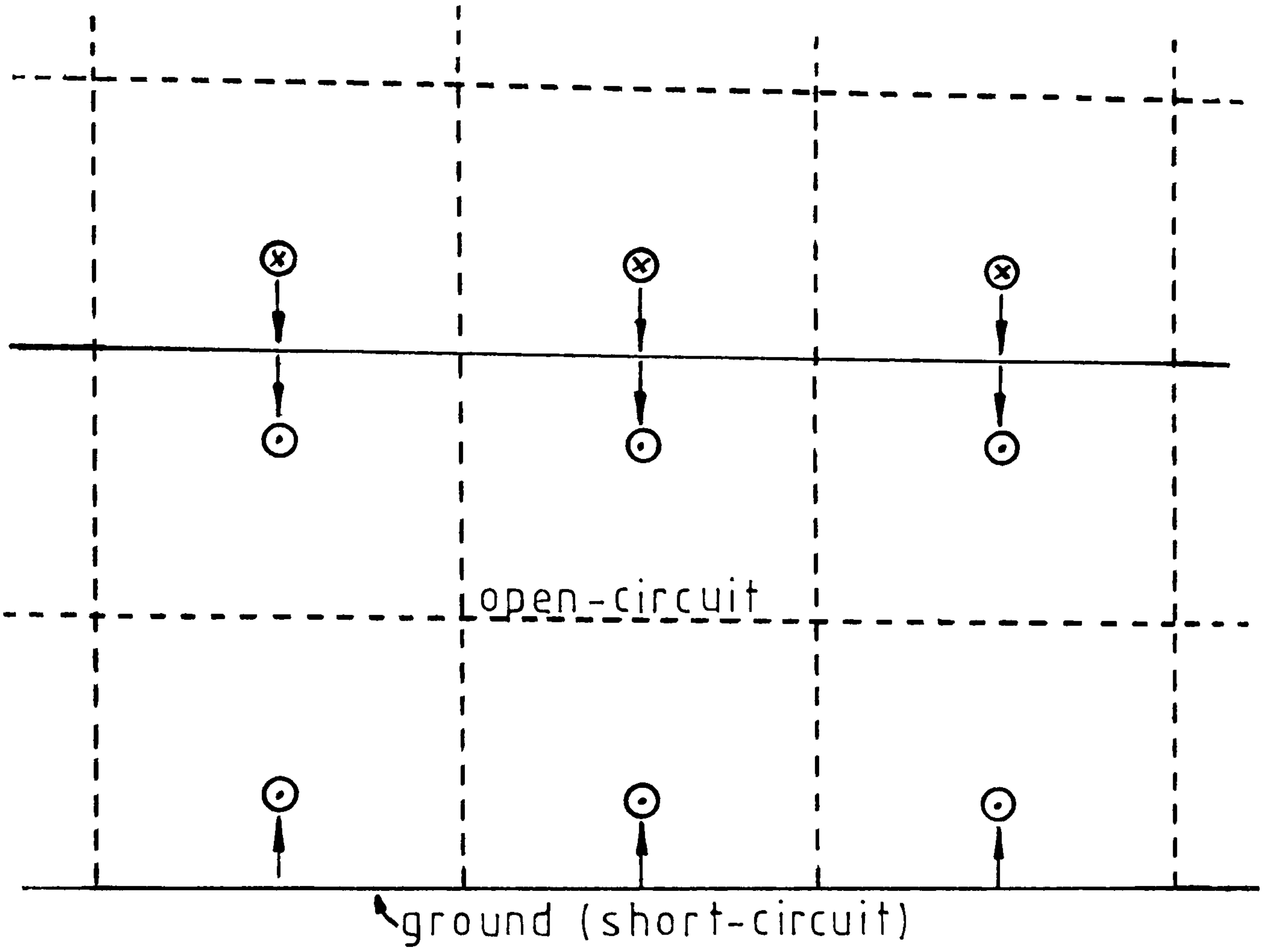

Figure 3·6 3D wire above ground geometry

Third dimension boundaries o/c for capacitance

s/c for inductance

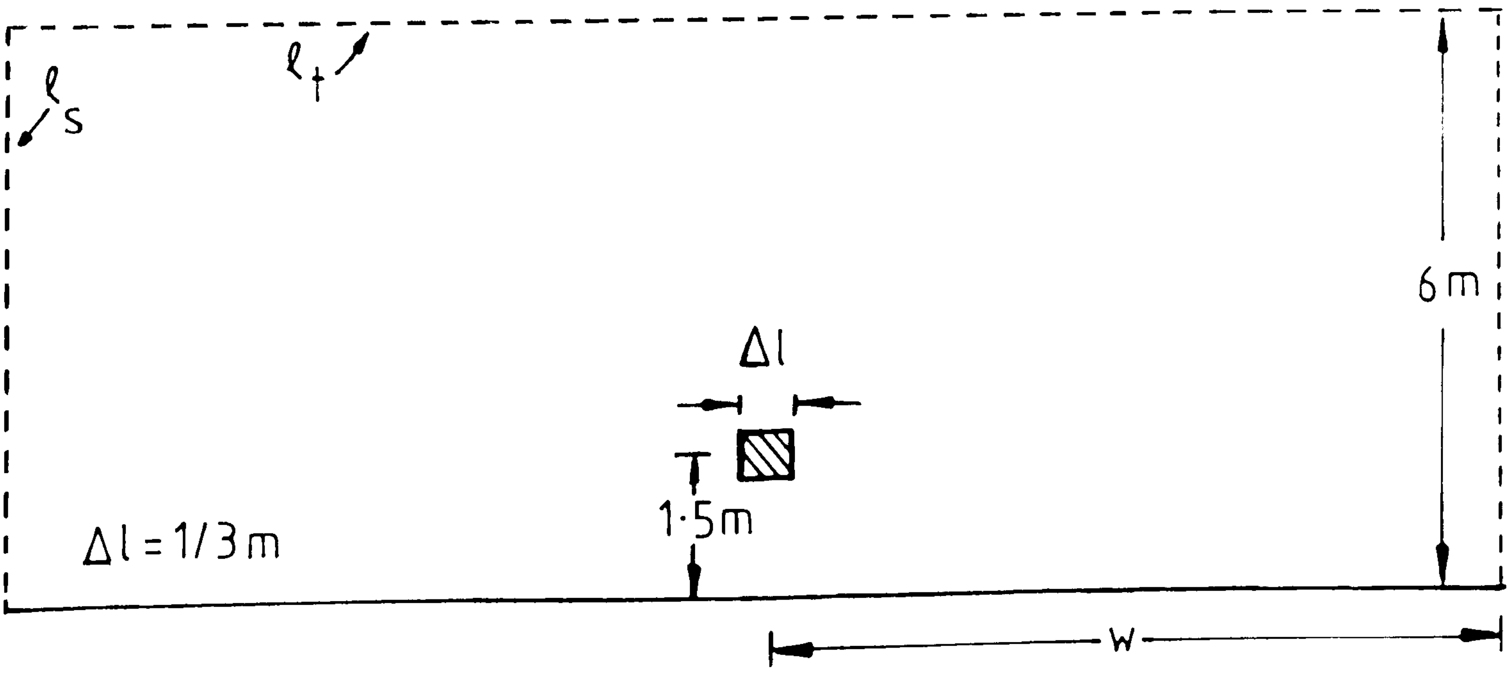

Table 3.3 Variation of wire radii with boundaries in three dimensions.

$w = 5.833$, 2000 iterations, $\Delta l = 1/3$m.

ρ_s	L_d $\times 10^{-7}$ (Hm^{-1})	r_L (m)	C_d $\times 10^{-11}$ (Fm^{-1})	r_C (m)	$\frac{r_L}{r_C}$	$(L_d C_d)^{-1/2}$ $\times 10^{8}$ (ms^{-1})
0	5.999	0.149	2.023	0.191	0.780	2.870
1	5.947	0.153	1.862	0.151	1.014	3.005

Table 3.4 Wire in 23m high box, 16m long. results for $\lambda = 32$m, 500 iterations & output 4.5m from end.

Description	radius (m)	velocity TLM $\times 10^{8}$ (ms^{-1})	velocity analytic $\times 10^{8}$ (ms^{-1})
one node square	0.665	2.82	2.83
1.5m	1.778	2.88	2.90
□ 1.5m	1.890	2.94	2.90
3.5m	3.870	2.94	2.91
□ 3.5m	4.200	2.94	2.91

Figure 3·7 Coaxial wire geometries

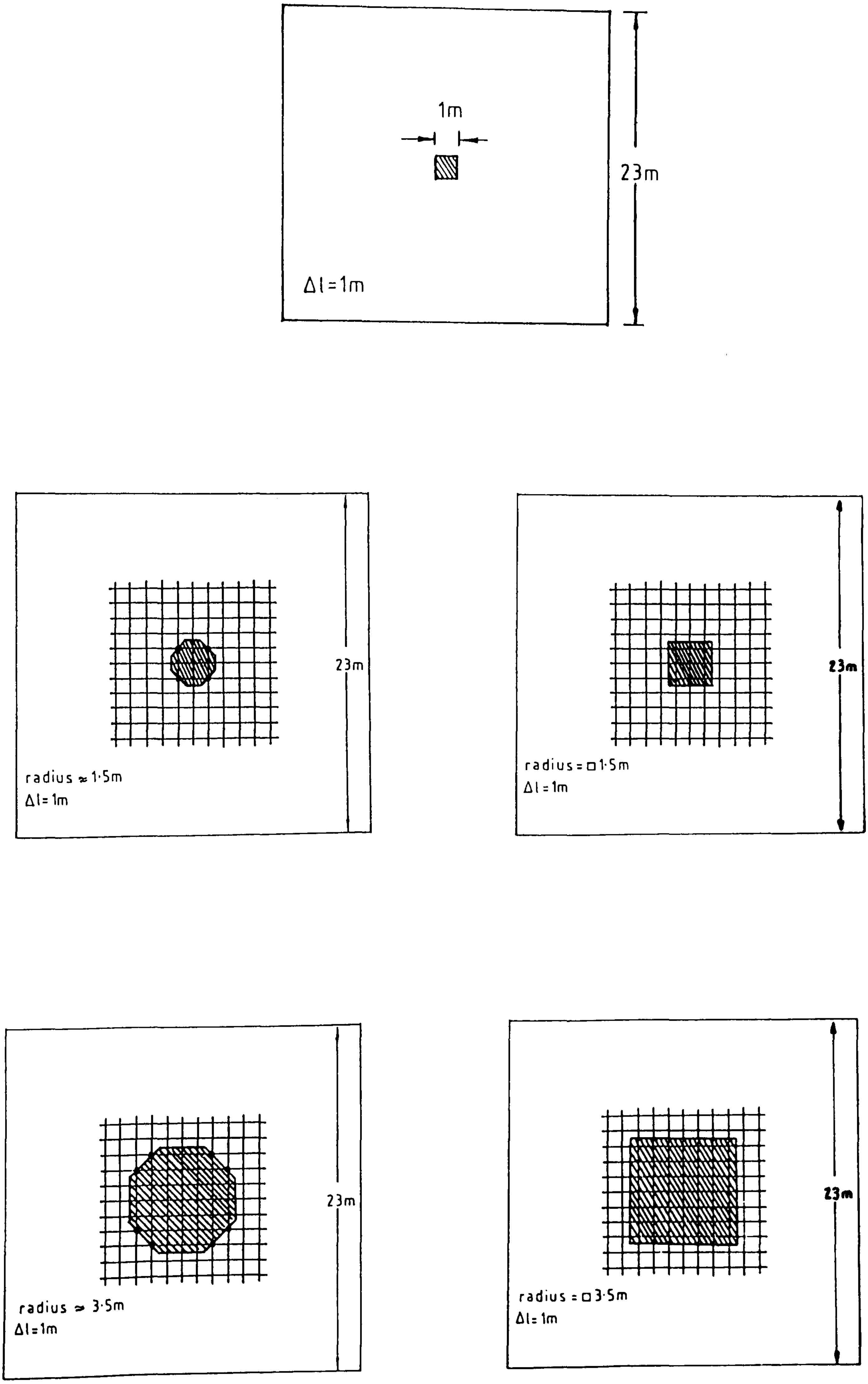

3.3.2 Wire in Resonant Cavity

Figure 3.7 shows five coaxial wire geometries using a $16\Delta\ell$ long and $23\Delta\ell$ high cavity of square cross-section, containing various wire models. The frequency domain voltage and current responses were obtained at a point $4.5\Delta\ell$ from one end of the cavity.

Table 3.4 shows the velocity and radius obtained after 500 iterations of the TLM routine had been performed and the equations of section 3.2.2 applied to the resulting voltage and current.

Clearly the finer the wire description the more accurate the velocity of propagation is. The most likely cause of this is as follows:

In section 3.3.1 it was seen that the 2D inductance and capacitance wire above ground models computed different radii. If the same condition applies to a 3D wire in a resonant cavity, then figure 3.8 shows what will happen.

For a wave propagating in the direction of the wire the magnetic field component sees the conducting boundaries as correctly located. This is because the calculation of the magnetic field involves TLM voltages which are reflected from the boundary (as in figure 3,8a,b).

For the electric field the TLM voltages are always perpendicular to the boundary and there is an uncertainty of δ in the location of the boundaries (figure 3.8c and d),

Figure 3·8 Difference between electric and magnetic fields on the mesh

wave in the cavity

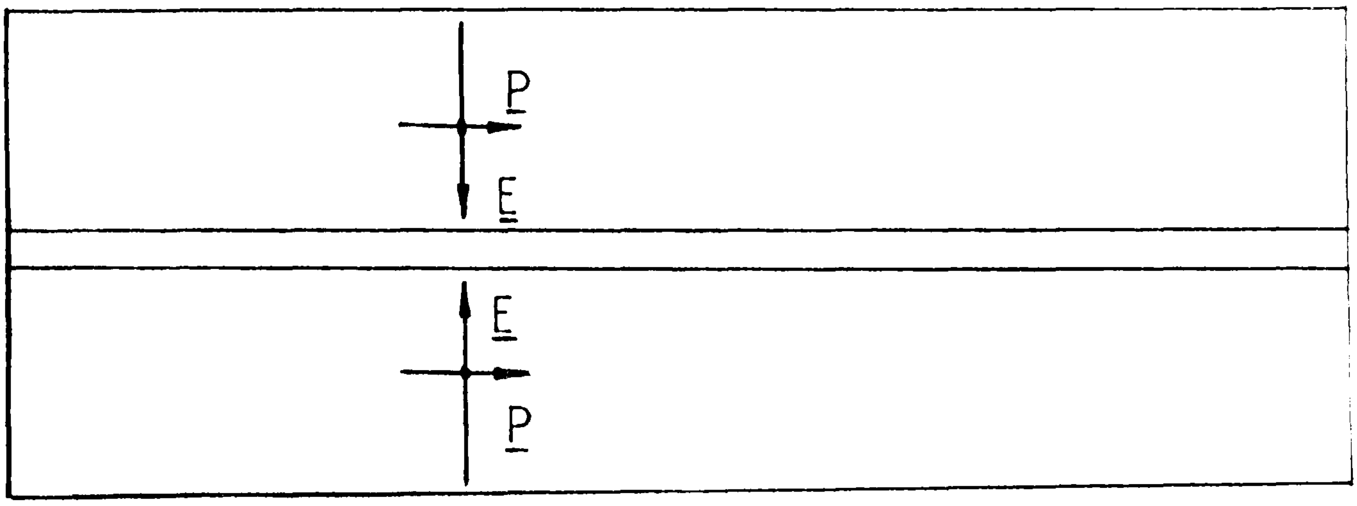

a) Magnetic field

c) Electric field

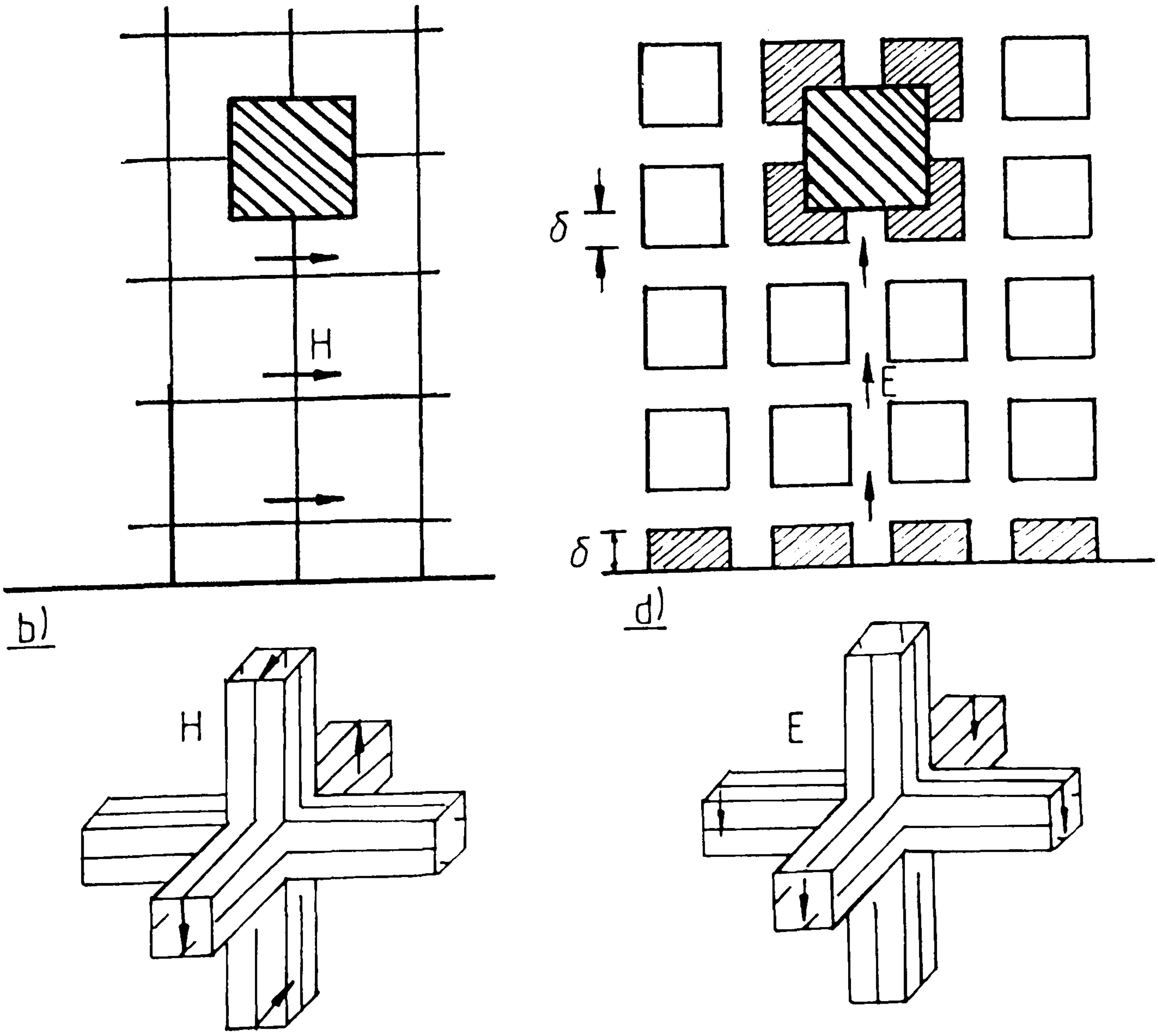

since the electric field calculation involves no TLM voltages which have interacted directly with the boundary.

Equation 3.14 can be manipulated to provide the inductance and capacitance per metre:

$$L_d = \frac{Z_o}{c} = 60 \log_e \left(1.08 \frac{h_L}{d_L}\right) \qquad (3.18)$$

where $\sqrt{\varepsilon_r}$ is defined as 1 and h_L and d_L are the height and diameter for an inductance model.

$$C_d = \frac{1}{cZ_o} = \frac{1}{c60 \log_e(1.08\ h_c/d_c)} \qquad (3.19)$$

Where h_c and d_c are defined for the capacitance model.

The velocity of propagation is then:

$$\nu = \frac{1}{\sqrt{L_d C_d}} \qquad (3.20)$$

Thus

$$\nu = c\sqrt{\frac{\log_e(1.08h_c/d_c)}{\log_e(1.08h_L d_L)}} \qquad (3.21)$$

$$\text{In general} \quad \left.\begin{aligned} h_c &= h_L - 2\delta \\ d_c &= d_L + 2\delta \end{aligned}\right\} \qquad (3.22)$$

When δ was chosen to be 0.2m (by trial and error) the analytical velocities obtained were those shown in Table 3.4. These are within the range of velocities computed from the TLM model.

This is only an approximate analysis because by changing the output point for the voltage and current and the number of iterations of the model different radii could be obtained.

To confirm how the radius varies with position and number of iterations a finer description of the wire was investigated.

The coaxial wire geometry of figure 3.9 is a TLM model of a wire, radius 3.5m, in a coaxial cavity of height 23m. The length of the wire is 16m and all the cavity boundaries are perfectly conducting.

Table 3.5 shows the resulting radii at four output points (measured from the wire termination). As can be seen the radius varies with position along the line and with the number of iterations. There are two likely causes of this:

i) Figure 3.10 shows a wave propagating along the wire. At some time $n\Delta t$ it has reached $x = L$ for the $(\rho - 1)$th time (3.10a). This means that the wave has passed all points on the wire an equal number of times. In (3.10b) the wave has propagated to another point on the line. Some parts of the wire had now 'seen' the wave more times than others. If the solution is obtained at this point, the Fourier Transform of voltage and current in region (p) is bound to be different from

Figure 3·9 Wire of radius 3·5m in a 16m long coaxial cavity

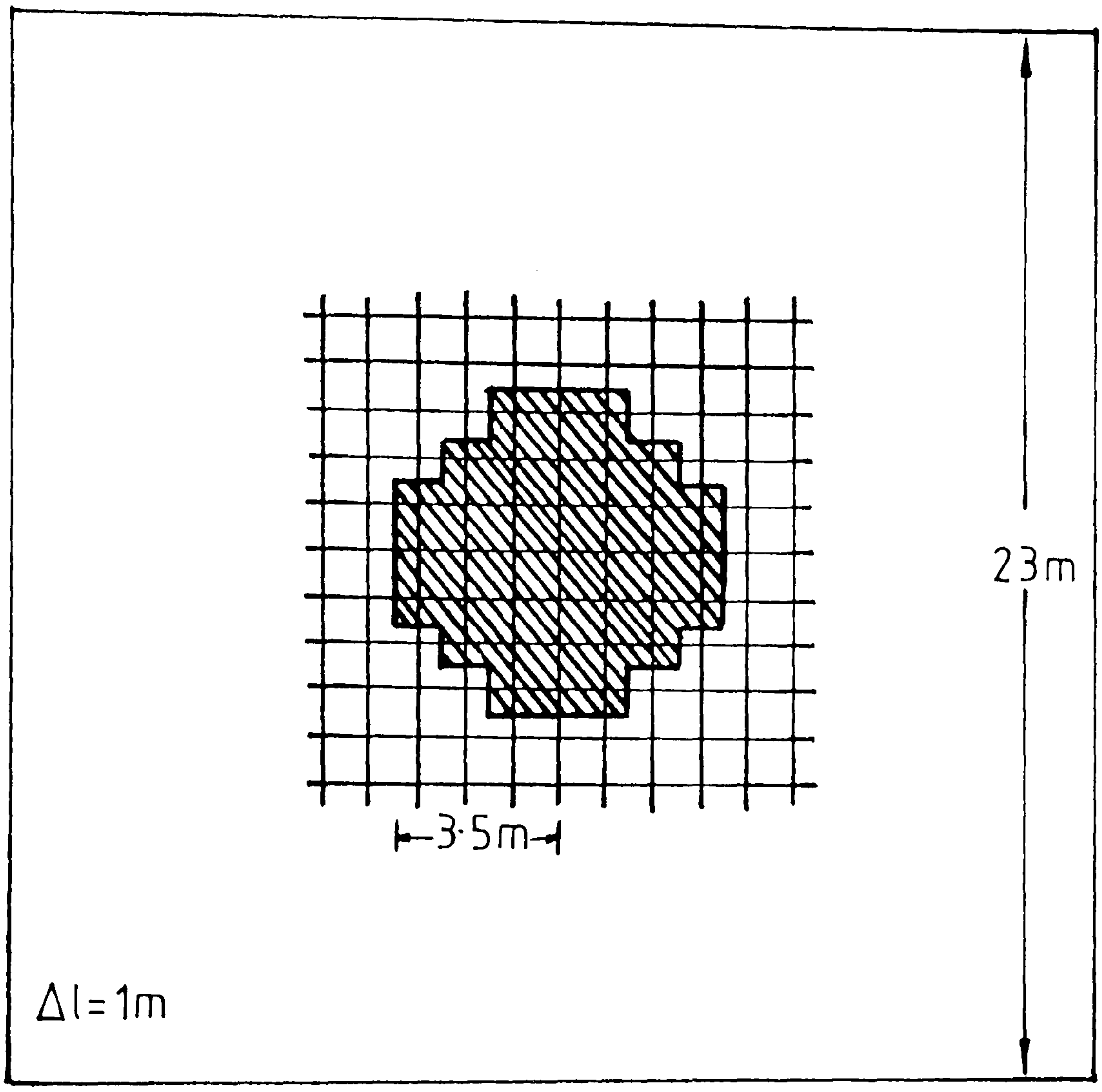

Table 3·5 Radii obtained for λ=32m in above geometry

Number of Iterations	radii			
	x = 2.5m	x = 3.5m	x = 4.5m	x = 6.5m
1010	3.519	3.302	3.581	3.677
1000	3.714	3.449	3.675	3.636
990	3.619	3.381	3.642	3.702
510	3.674	3.395	3.577	3.598
500	3.736	3.417	3.610	3.725
490	3.391	3.227	3.574	3.817
Average	3.609	3.362	3.610	3.693
		Overall average		3.568

Figure 3·10 Wave propagating along the wire

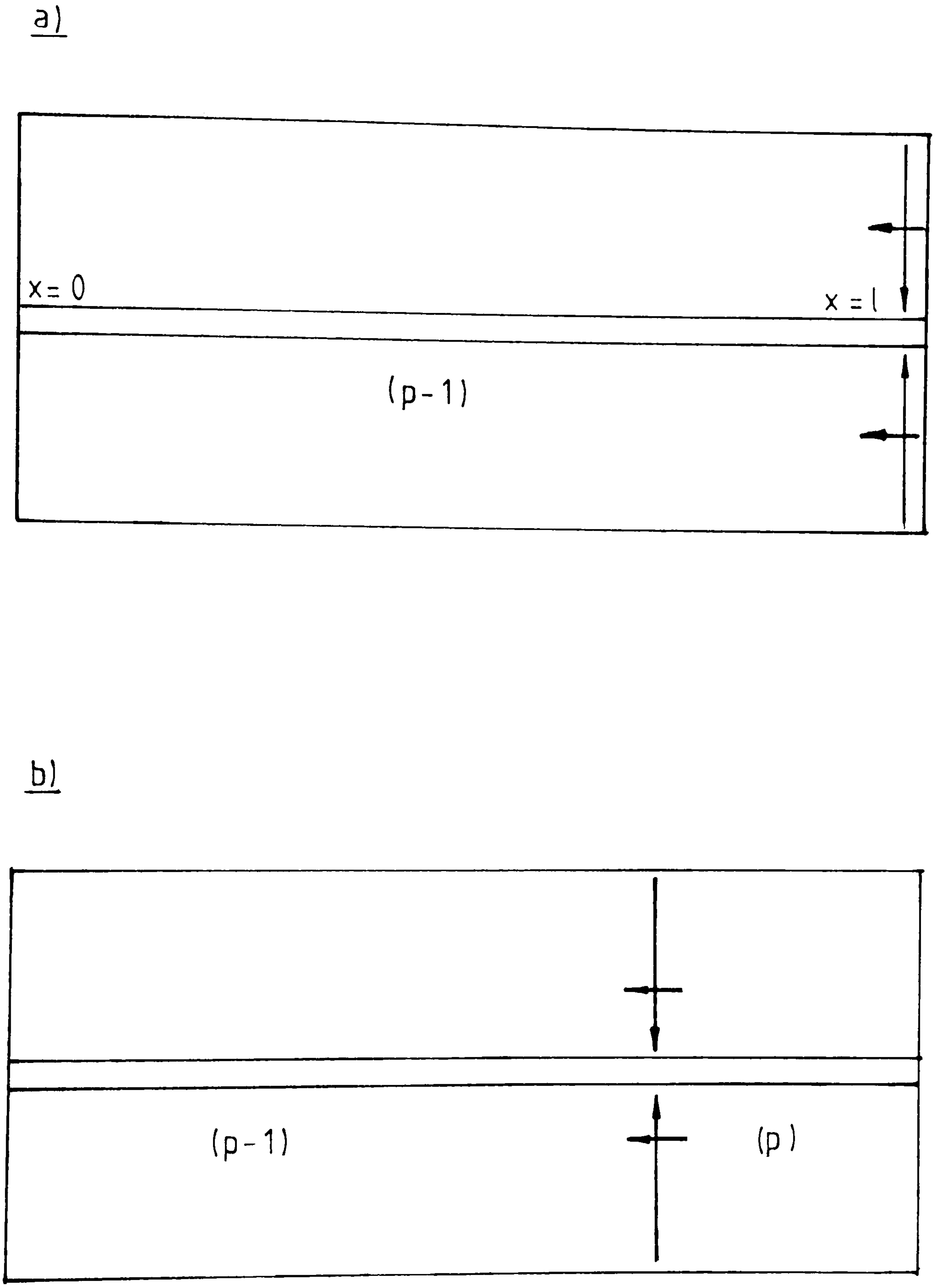

$(\rho - 1)$ because there is more information present.

ii) The differences in inductance and capacitance radii described above are likely to cause dispersion of the wave propagating along the wire.

The combination of these two effects leads to a variation of the observed radius with time and position.

Taking the average radius calculated by the model gives r = 3.567m - a modelling error of 2%. The resonant frequency at which the voltages and currents were obtained was 9.2 MHz. This gives a velocity of propagation of 2.94×10^8 ms^{-1} which is also an error of 2%.

The radius of the simple square ($\Delta\ell \times \Delta\ell$) wire shown in figure 3.11 was also obtained using the same technique. Table 3.6 shows that the average radius was 0.636m and since the resonant frequency was 8.8 MHz, the velocity of propagation was 2.82×10^8 ms^{-1}.

3.3.3 Convergence of the TLM Radius

To validate the TLM model the description of the wire was made progressively finer. The objective was to show that, as the description of the wire is made more accurate, the modelled radius converges to correct radius.

Figure 3.12 shows the geometry of a wire radius 0.5m in a 3m x 3m resonant cavity. Two tests were performed:

Figure 3·11 Simple square wire in 16m long coaxial cavity

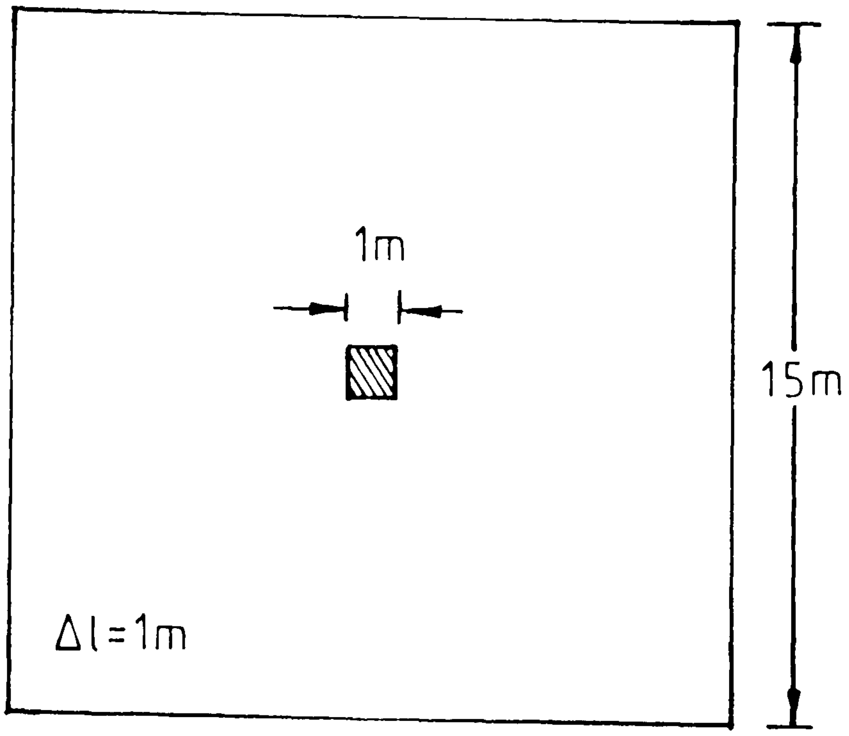

Table 3·6 Radii obtained for λ=32m in above geometry

Number of Iterations	radii			
	x = 2.5m	x = 3.5m	x = 4.5m	x = 6.5m
2000	0.623	0.621	0.620	0.620
1010	0.656	0.652	0.653	0.640
1000	0.647	0.662	0.663	0.620
990	0.618	0.618	0.613	0.576
510	0.566	0.570	0.574	0.560
500	0.714	0.678	0.657	0.686
490	0.659	0.679	0.687	0.671
Average	0.640	0.640	0.638	0.625
		Overall average		0.636

Figure 3·12 Excitations used for single-slice wire section

a) Inductance

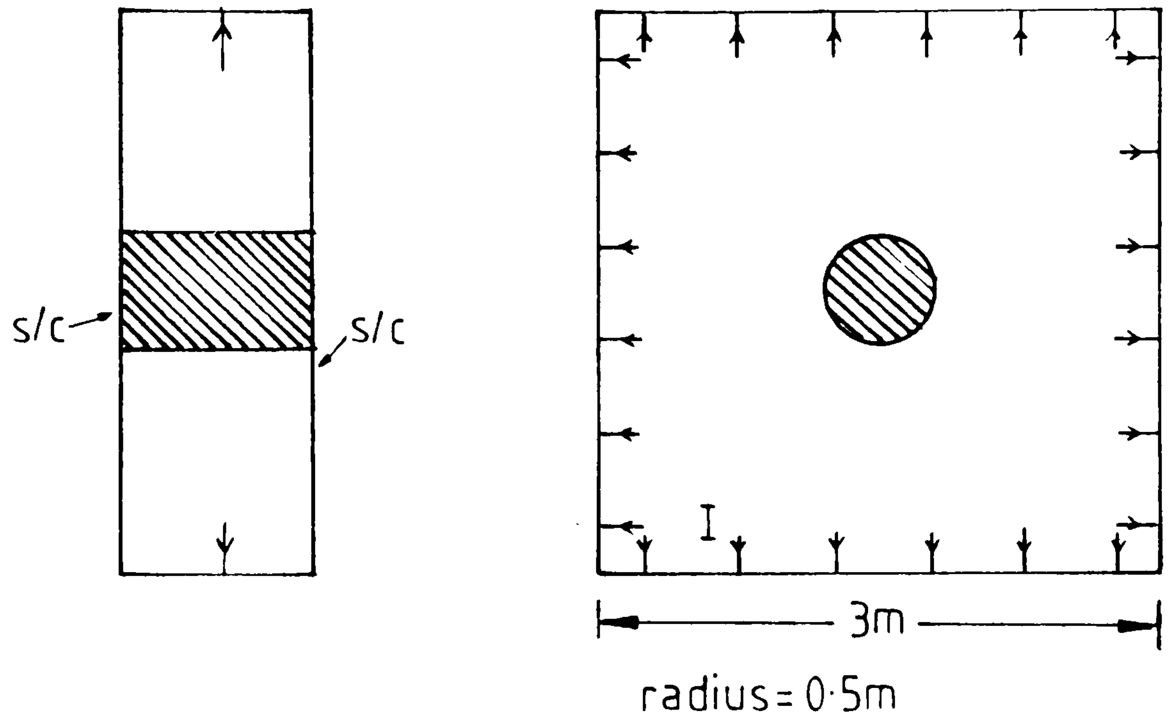

b) Capacitance

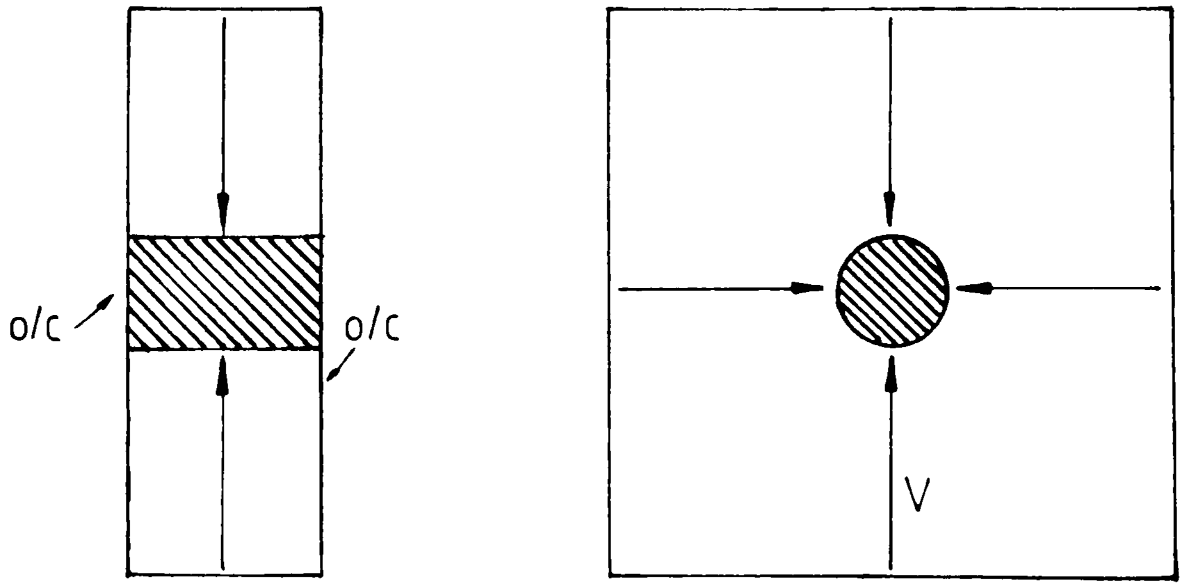

an inductance calculation (3.12a) and a capacitance calculation (3.12b). The excitations for the separate tests are also shown in the figure. The zero frequency (dc) current, voltage, flux and charge were computed in a similar way to the wire-above-ground (sections 3.2.1 and 3.3.1).

The various TLM models of this geometry are shown in figure 3.13. The resulting inductance, capacitance and radii are tabulated in Table 3.7. The convergence of the inductance and capacitance are detailed in figure 3.14.

What is clear is that increasing the accuracy of the wire description does give convergence both for the inductance and capacitance of the wire. The fact that convergence is not to the analytic answer is due to an error in choosing the wire description. In figures 3.13 (f and h), the discrete model has a radius slightly larger than 0.5m. Also, as previously shown, the capacitance model actually models a slightly different problem. Analytically this gives a smaller inductance and larger capacitance, which is what was observed. Convergence was found to be quicker if no short-circuit nodes (Chapter 4) were used in the wire description.

3.4 Conclusions

Wires can be modelled using a field-solution technique (TLM). The transmission-lines of the TLM mesh can be short-circuited on or between nodes and a discrete model of a wire formed.

Figure 3·13 Wire descriptions for various mesh sizes

a) Whole geometry for Δl=1m

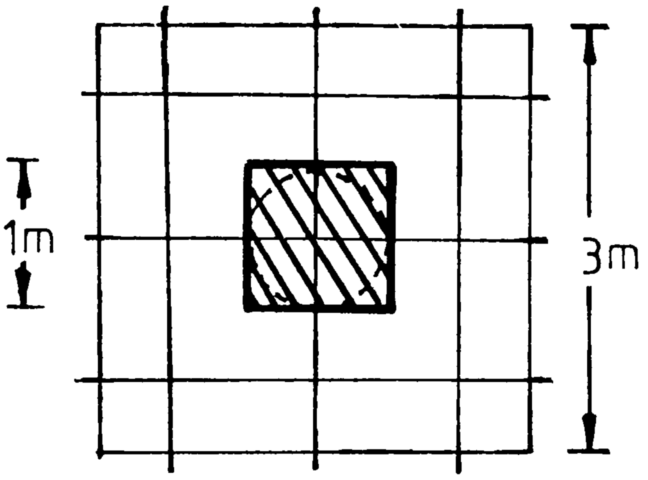

Quarter wire geometry

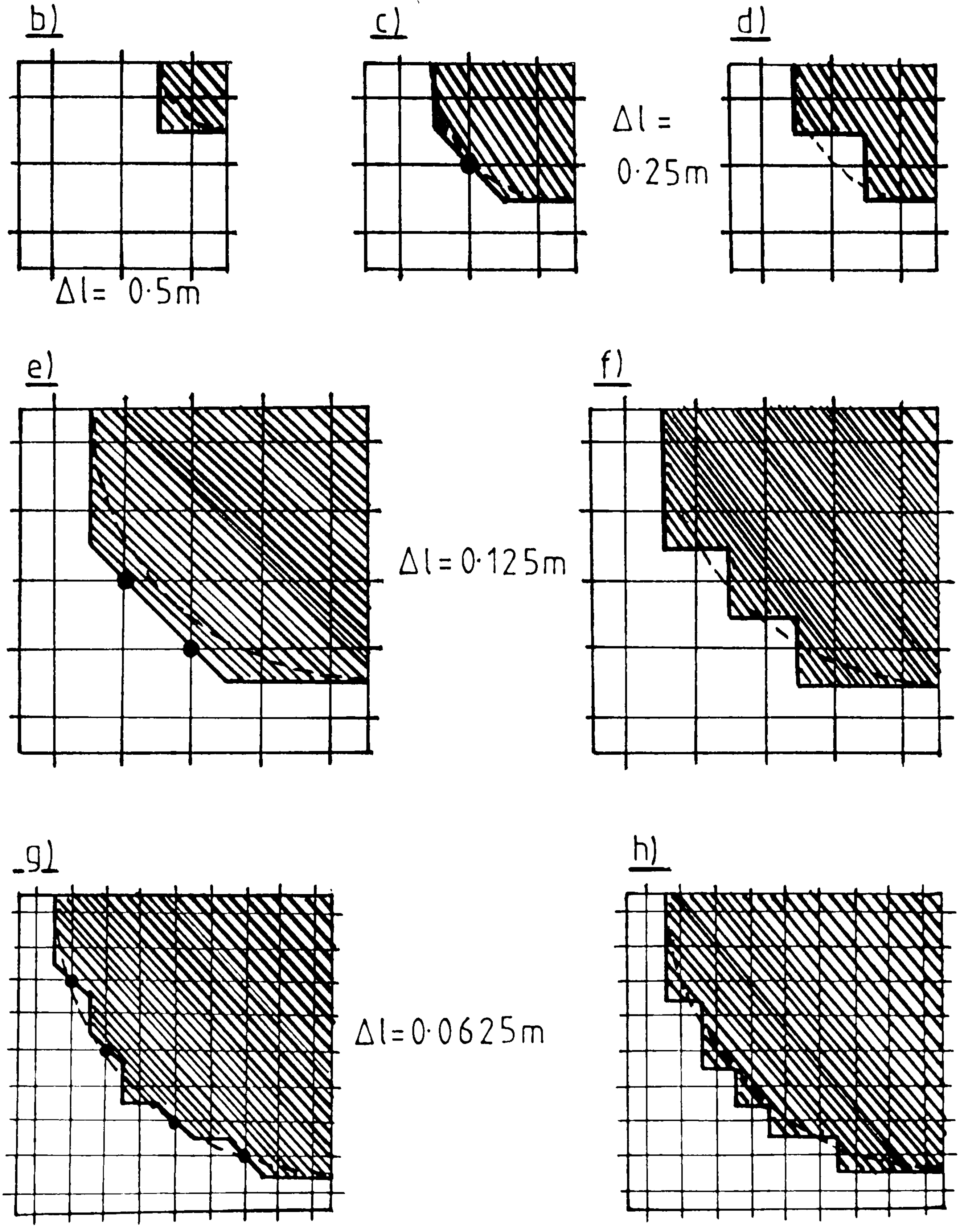

Table 3.7 Inductances and Capacitances found by TLM for the wires depicted in figure 3.13.

Δl (m)	figure	Its.	Inductance $(x10^{-7}Hm^{-1})$	Capacitance $(x10^{-11}Fm^{-1})$	%error		Velocity $(x10^{8}ms^{-1})$
					L	C	
1.0000	a	300	2.353	5.313	0.12	-12.46	2.83
0.5000	b	600	2.140	5.604	9.16	-18.63	2.89
0.2500	c	1200	2.188	5.543	7.09	-17.34	2.87
0.2500	d	1200	2.372	4.963	-0.69	-5.06	3.00
0.1250	e	2400	2.358	4.963	-0.11	-5.06	2.92
0.1250	f	2400	2.312	4.970	1.88	-5.21	2.95
0.0625	g	4800	2.319	4.885	1.54	-3.41	2.97
0.0625	h	4800	2.308	-	2.00	-	-
Analytical			2.353	4.729			3.00

Figure 3·14 Variation of inductance and capacitance with increasing mesh fineness

a) Inductance

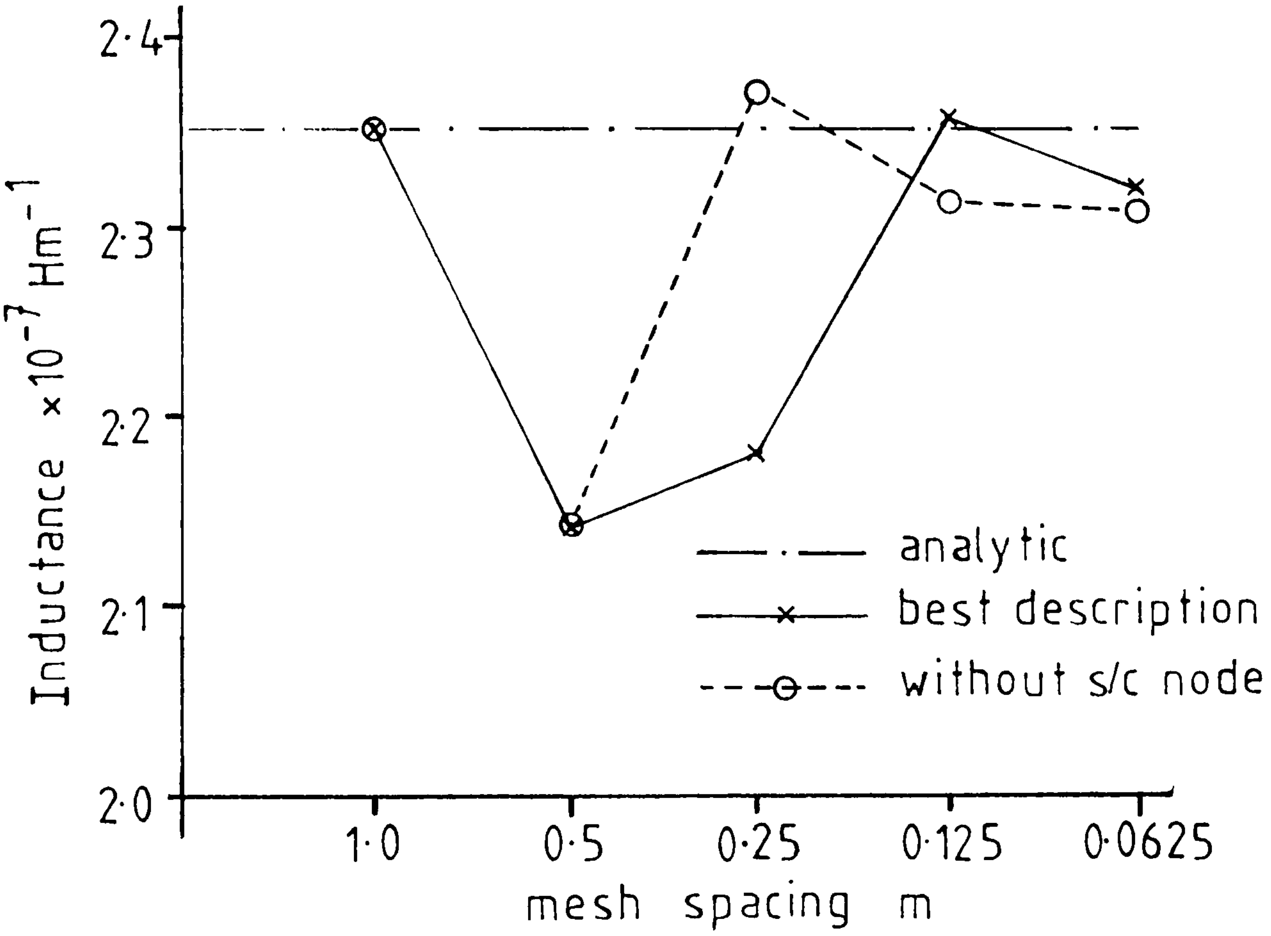

b) Capacitance

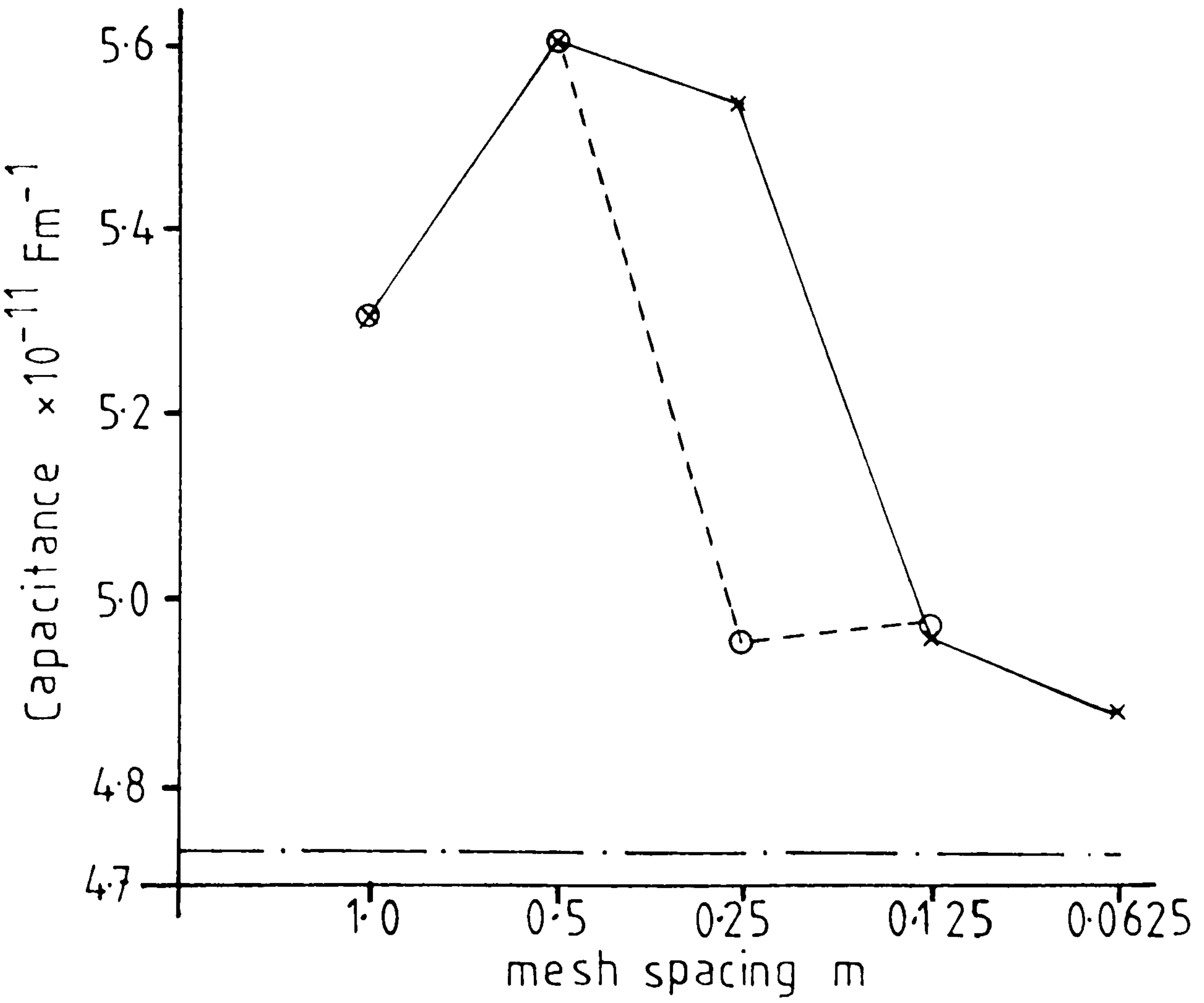

The modelled radius of the wire was investigated by two geometries: wire-above-ground and wire in a resonant cavity.

Strictly speaking, the wire-above-ground geometry requires an infinite ground plane. Such an infinite boundary condition cannot be modelled accurately in the computer. Thus there is an inherent error in the results obtained using the geometry.

The resonant cavity method was found to be a more successful way of obtaining the modelled radius. For a 3.5m radius wire, the modelled radius and velocity of propagation were accurate to with 2%.

With increased mesh fineness the radius, capacitance and inductance could be modelled with increasing accuracy.

Chapter 4 Single Time Level Scatterers

4.1 Introduction

In Chapter 3 the radius of a wire modelled as described in figure 4.1a was found. The main problem with such a model is that the radius of the wire (approximately $0.6\Delta\ell$) determines the mesh spacing. Clearly this can give a very large workspace for the problem if the wire is small compared with the surrounding geometry.

What is required is a method of replacing the ordinary 2D or 3D nodes by a node which models a wire of radius less than $\Delta\ell/2$. In the interests of computational economy it would be preferable if the relationship between incident and reflected pulses on the TLM mesh is simple. A free space node (Appendices A, B) has a simple one-time-level scattering matrix where the reflected pulses are dependent only on the currently incident pulses and not on any previous incident pulses. Such a relationship is derived for a simple wire model, the short-circuit node, which is also only dependent on the currently incident pulses.

The radius that this short-circuit node models will be determined later in this chapter. It will be found to be invariable and (relatively) large. In an attempt to vary the effective (or modelled) radius a node containing an extra transmission-line stub at the node, rather than a short-circuit, will be introduced and the

Figure 4·1

a) crude wire model

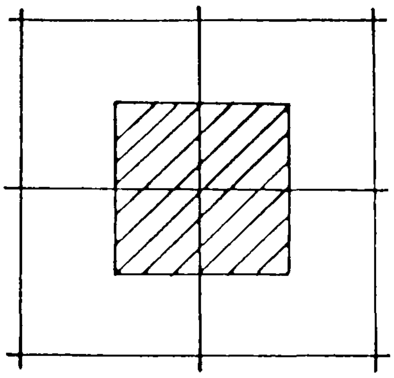

b) 2-D shunt node

c) 2-D series node

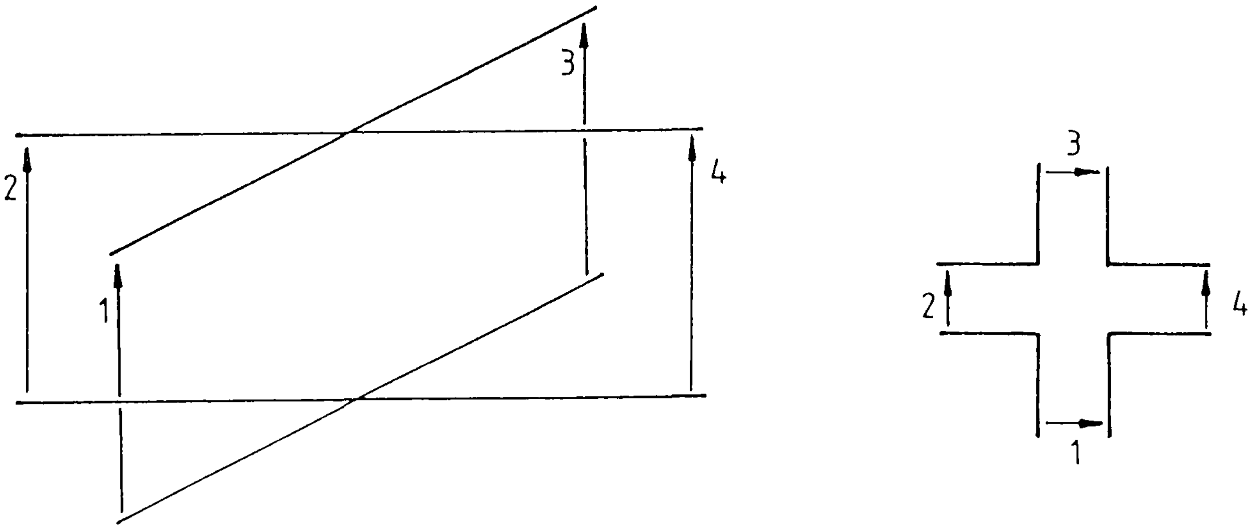

d) 3-D symmetrical condensed node

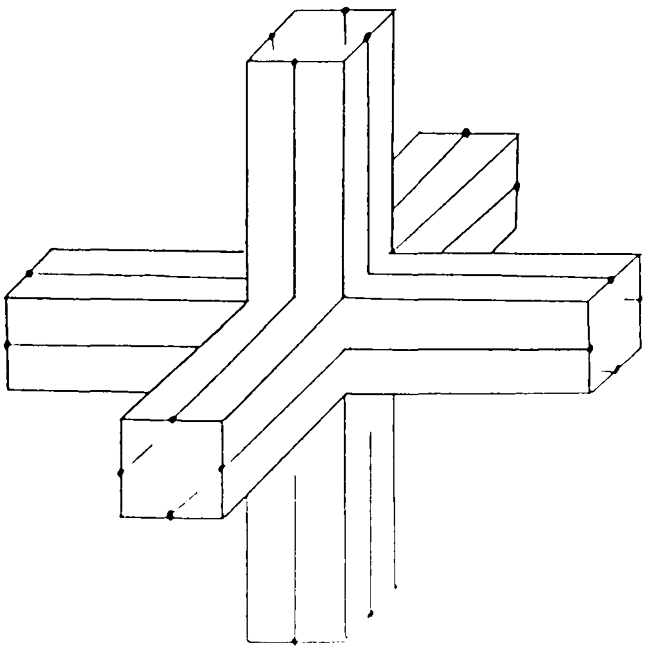

modelled radius determined. This model does not, strictly, have a one-time-level scattering matrix but is included here because the scattering is simply described. Various other wire models incorporating transmission-line stubs will also be investigated.

4.2 The Short-Circuit Node

In this section the scattering matrix of the short-circuit node will be derived. Later the modelled radius will be evaluated using the two geometries detailed in the previous chapter, namely the wire-above-ground and resonant cavity geometries.

4.2.1 Numerical Solution

One way of finding the scattering matrix of a particular block of space, whether containing a wire or not, is to consider the space in isolation. In a simple case, such as figure 4.2a, the time domain scattering matrix can be obtained for the block by impulsing the structure in some way and observing how the pulses are reflected. A detailed description of this method is left until Chapters 5 and 6 where the techniques of diakoptics will be discussed.

For the purposes of this chapter, consider the space shown in figure 4.2a as a finer model of a space usually modelled by a single (2D) node. Each pair of transmission lines emerging from block (those contained within the braces in the figure) represent one transmission line in the

Figure 4·2 Diakoptic approach

a) 2 × 2 free-space block

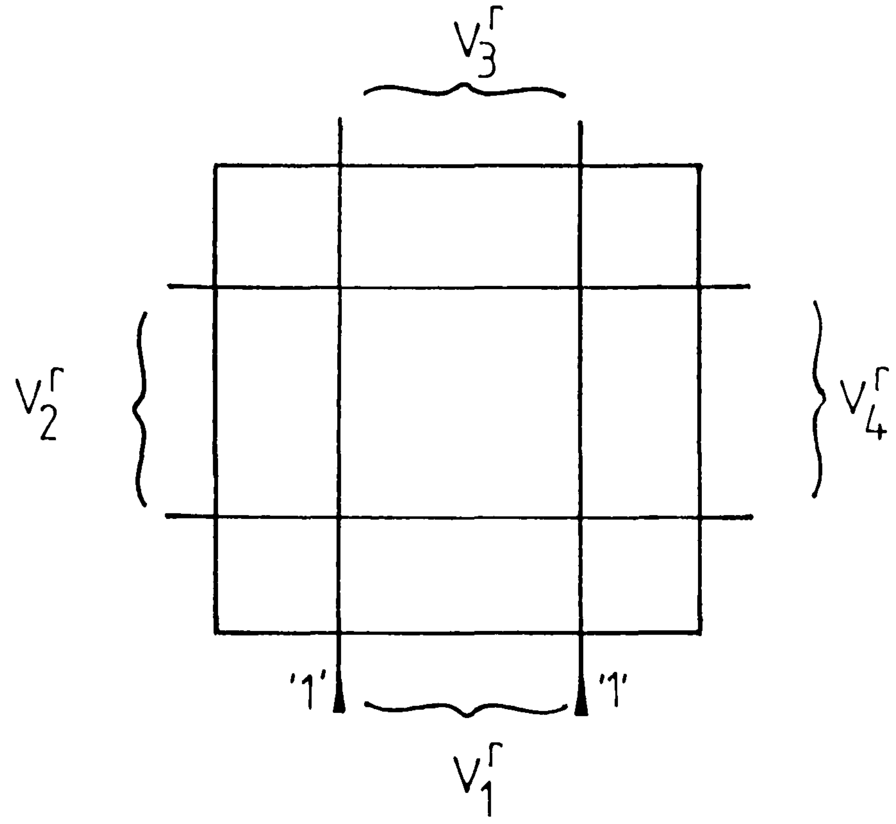

b) Reflected pulses

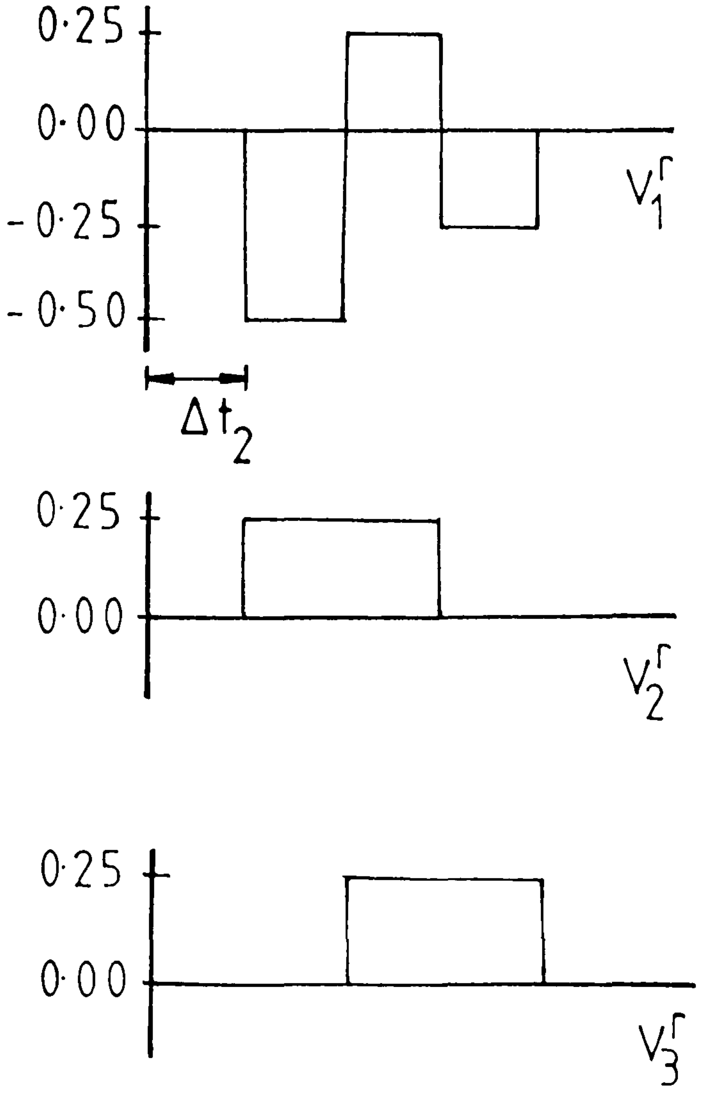

standard description. To find the impulse response, and hence the scattering matrix, each pair of lines is impulsed in turn and the (spatial) average of the pulses returned on each pair is recorded. These are shown in figure 4.2b. This type of response is a three-time-level matrix in that (ignoring the first, $t = 0$, term) the scattering is defined over $3\Delta t$. For free space geometries larger than 2 x 2 the scattering matrix is infinite - with decaying terms. If this scattering matrix is to be used in place of an ordinary node then these pulses are at the wrong time step ($\Delta t_2 = \Delta t/2$). Thus the pulses need to be resampled at the correct time step, Δt. The usual technique is to "Filter and Resample" - but for reasons which will be explained in Chapter 5, this will not usually provide a one-time-level matrix from a multi-time-level one.

If the reflected voltage pulses are Fourier Transformed for a single node and for three other free-space geometries then the results of figure 4.3 are obtained. The results show that the zero frequency term is the same in all models. This implies that the charge is equal in all models. Also the finer mesh models and the single node correspond up to 40 MHz. The finer meshes are, of course, more accurate, but they require more time levels to be computed so that energy is conserved.

What these results suggest is that a one-time-level matrix can be determined from the zero frequency of the Fourier Transformed impulse response.

Figure 4·3 Geometry and Fourier transforms of free-space blocks

F(V) is the spatial average on each boundary

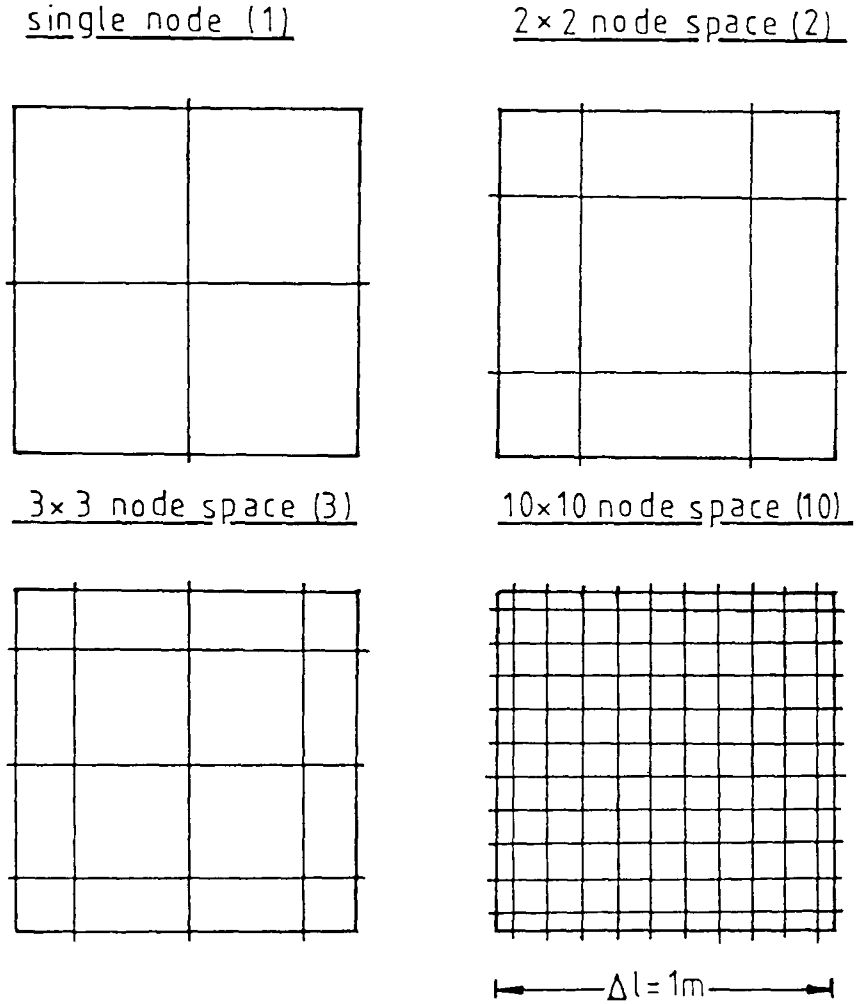
single node (1)

2 × 2 node space (2)

3 × 3 node space (3)

10×10 node space (10)

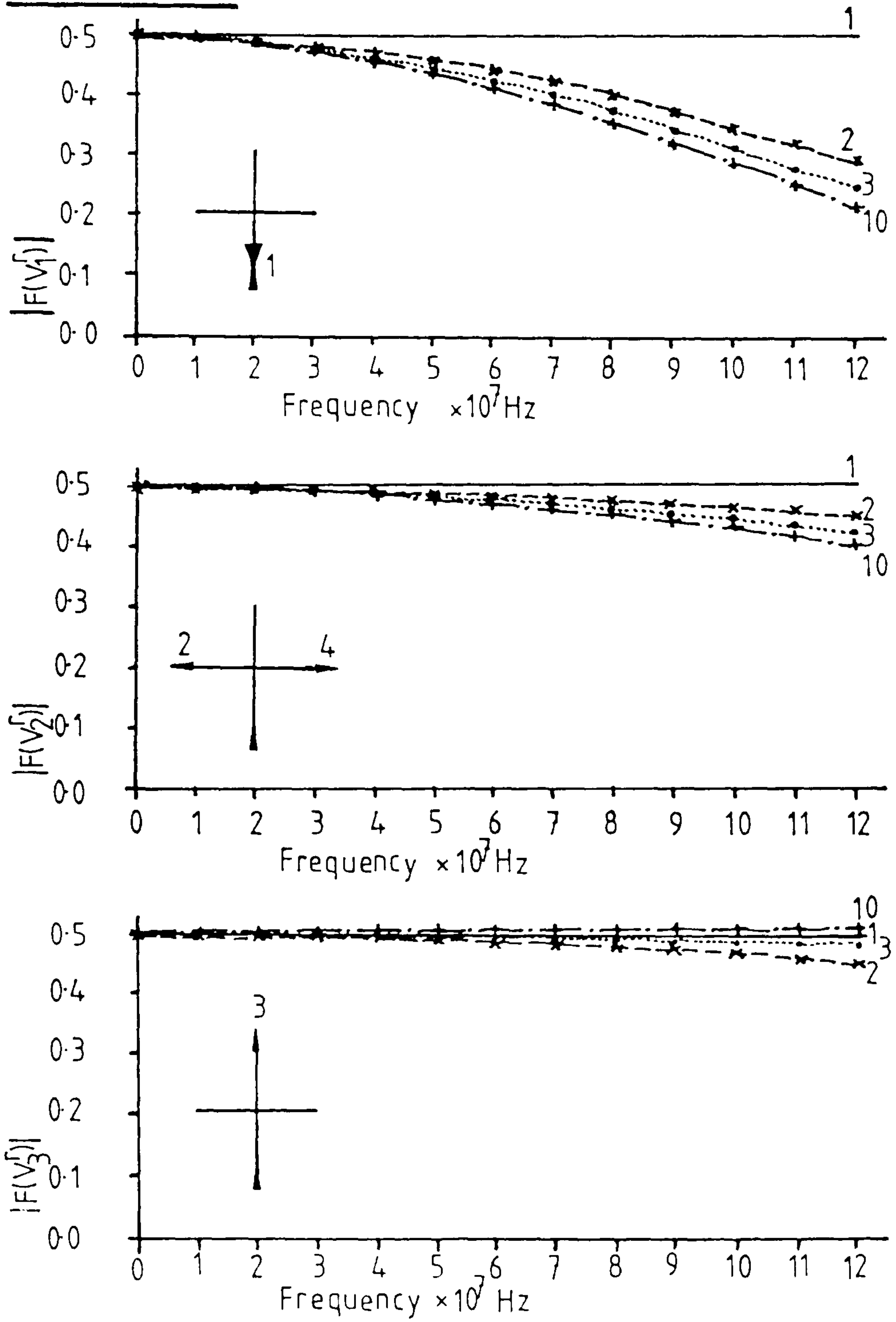

If a conductor is placed in free-space the wire geometries shown in figure 4.4 can be modelled. If the impulse response is obtained as before (in a multi-time-level form) and then the Fourier Transform is taken, the frequency responses shown in the figure are obtained. It can be seen that the zero frequency terms correspond to a scattering matrix equal to that of a short-circuit node.

In order to model wires of differing radii the whole frequency response, not just zero frequency, has to be considered. This requires a more than one-time-level scattering matrix, which is beyond the scope of this chapter and will be considered in Chapter 6.

4.2.2 Analytical Solution

The scattering matrix of the short-circuit node can be derived by purely analytical considerations.

Collin (81) has shown that a valid scattering matrix $\underline{S}$ obeys the following condition:

$$\underline{S}.\underline{S}^{*T} = \underline{U} \qquad (4.1)$$

where $\underline{S}^{*T}$ is the transpose and complex conjugate of matrix $\underline{S}$. $\underline{U}$ is the unit, or identity, matrix.

All the conventional free-space TLM nodes detailed in figure 4.1b, c, d meet this condition. For a two-dimensional node excited by an impulse the shunt mesh scattering matrix is of the form:

Figure 4·4 Geometry and Fourier transforms of blocks containing wires

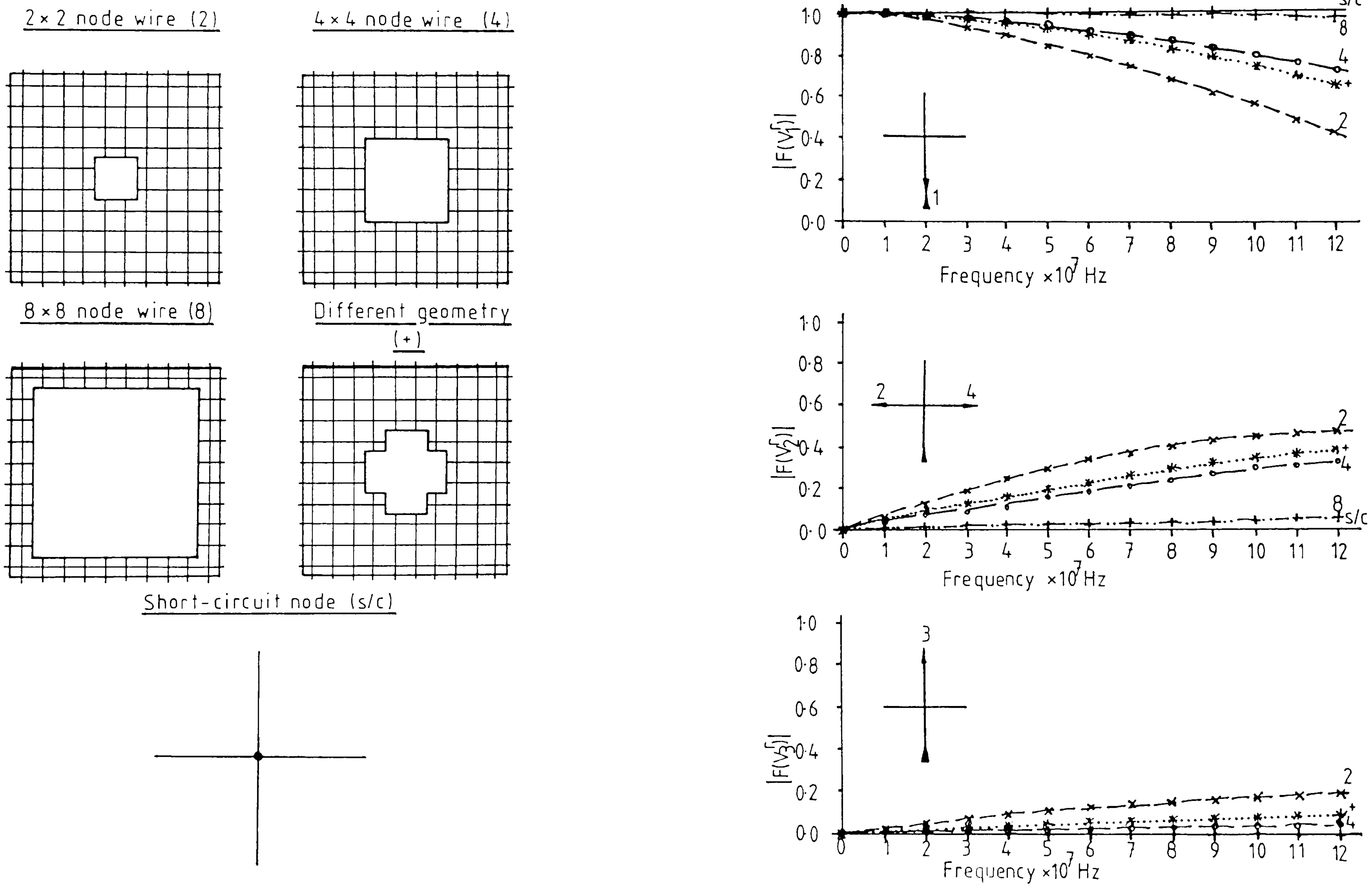

2 × 2 node wire (2)

4 × 4 node wire (4)

8 × 8 node wire (8)

Different geometry (+)

Short-circuit node (s/c)

$$\begin{bmatrix} V_1^r \\ V_2^r \\ V_3^r \\ V_4^r \end{bmatrix} = \begin{bmatrix} a & b & c & b \\ b & a & b & c \\ c & b & a & b \\ b & c & b & a \end{bmatrix} . \begin{bmatrix} V_1^i \\ V_2^i \\ V_3^i \\ V_4^i \end{bmatrix} \tag{4.2}$$

assuming a left-right symmetry.

$\underline{S}.\underline{S}^{*T}$ gives:

$$a^2 + 2b^2 + c^2 = 1 \text{ (four times)} \tag{4.3}$$

$$2b(a + c) = 0 \text{ (eight times)} \tag{4.4}$$

$$2ac + 2b^2 = 0 \text{ (four times)} \tag{4.5}$$

If in equation (4.4), $a = -c$ then the solution is the usual shunt scattering matrix (57, Appendix A). If $b = 0$ in equation (4.4), the only other solution, then the following short-circuit node scattering matrix is obtained, viz:

$$\begin{bmatrix} V_1^r \\ V_2^r \\ V_3^r \\ V_4^r \end{bmatrix} = \begin{bmatrix} -1 & 0 & 0 & 0 \\ 0 & -1 & 0 & 0 \\ 0 & 0 & -1 & 0 \\ 0 & 0 & 0 & -1 \end{bmatrix} . \begin{bmatrix} V_1^i \\ V_2^i \\ V_3^i \\ V_4^i \end{bmatrix} \tag{4.6}$$

A similar matrix can be obtained for the two-dimensional series node and for the 3D node.

This corresponds to the case when the centre of the node is short-circuited as shown in figure 4.5. Thus a one-time-level wire model has been obtained, the scattering matrix of which is:

$$\underline{S} = -\underline{U} \qquad (4.7)$$

The current in this short-circuit node is given by the equivalent circuits of figure 4.6:

$$I = \frac{-2}{Z_o} \sum_{d=1}^{4} V_d^i \qquad (4.8)$$

for the 2D shunt node (Appendix A)

and

$$I_x = \frac{-2(V_1^i + V_2^i + V_9^i + V_{12}^i)}{Z_o} \qquad (4.9)$$

$$I_y = \frac{-2(V_3^i + V_4^i + V_8^i + V_{11}^i)}{Z_o} \qquad (4.10)$$

$$I_z = \frac{-2(V_5^i + V_6^i + V_7^i + V_{10}^i)}{Z_o} \qquad (4.11)$$

for the 3D node (Appendix B).

Using the wire-above-ground and resonant cavity geometries of Chapter 3 it is possible to calculate the radius modelled by the short-circuit node.

Figure 4·5 2D short-circuit nodes

a) Series

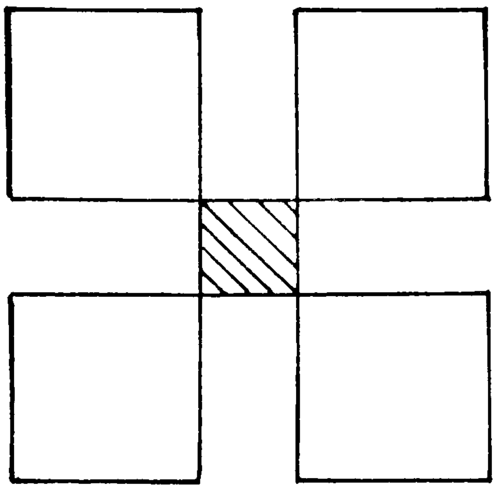

b) Shunt

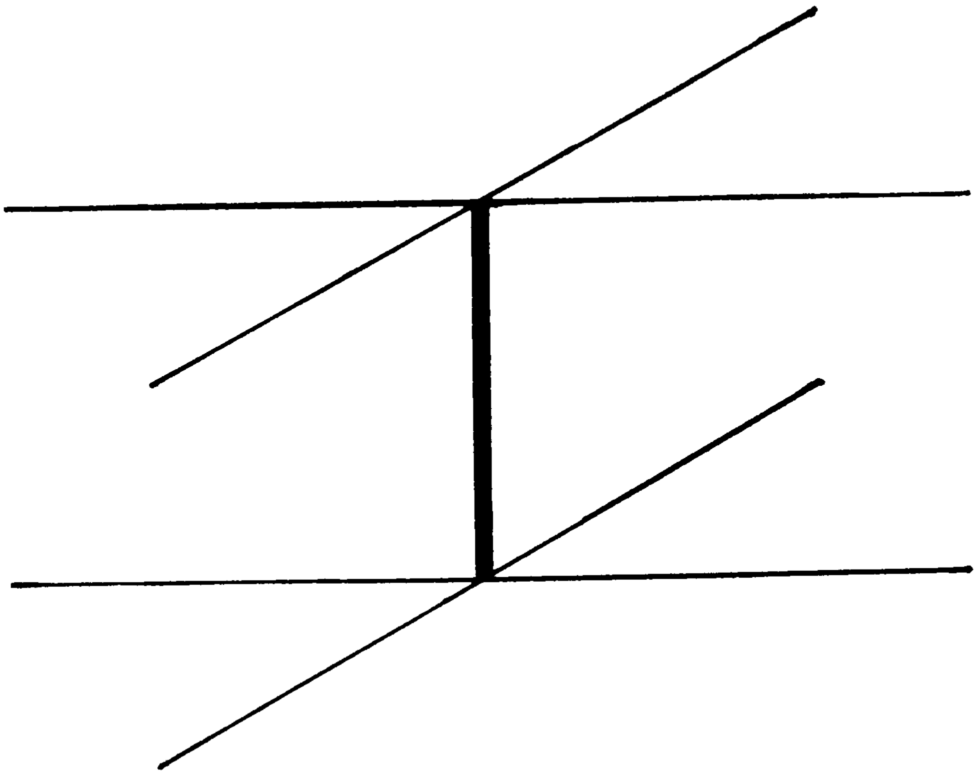

c) Scattering matrix

$$\begin{bmatrix} V_1^r \\ V_2^r \\ V_3^r \\ V_4^r \end{bmatrix} = \begin{bmatrix} -1 & 0 & 0 & 0 \\ 0 & -1 & 0 & 0 \\ 0 & 0 & -1 & 0 \\ 0 & 0 & 0 & -1 \end{bmatrix} \cdot \begin{bmatrix} V_1^i \\ V_2^i \\ V_3^i \\ V_4^i \end{bmatrix}$$

Figure 4·6 Current in the short-circuit node

a) 2D

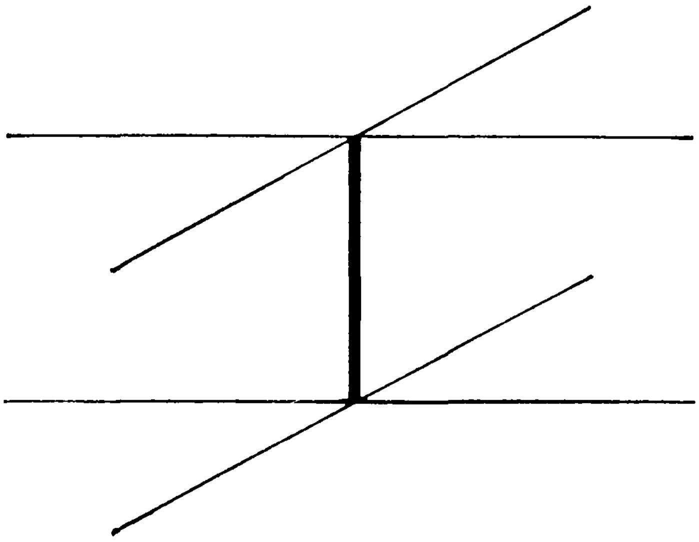

b) 3D

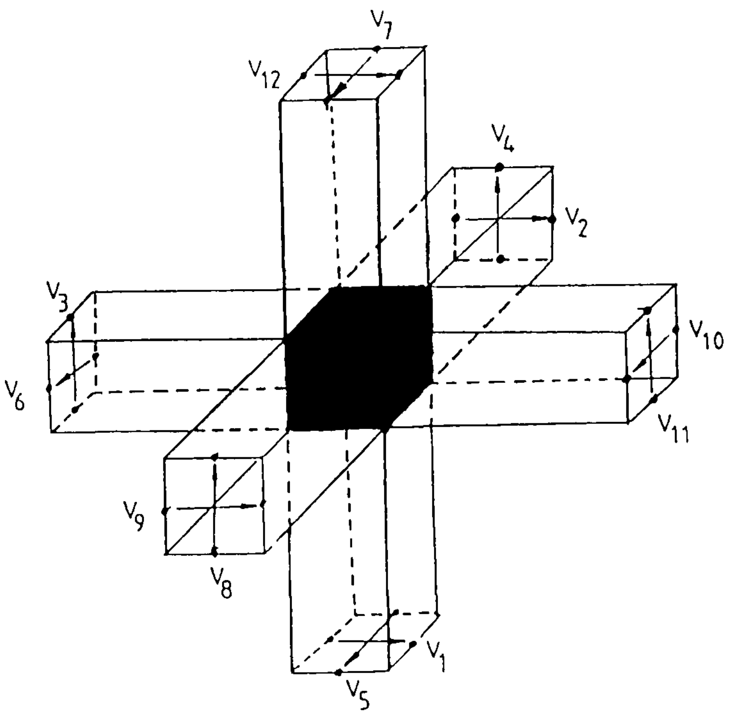

c) Equivalent circuit

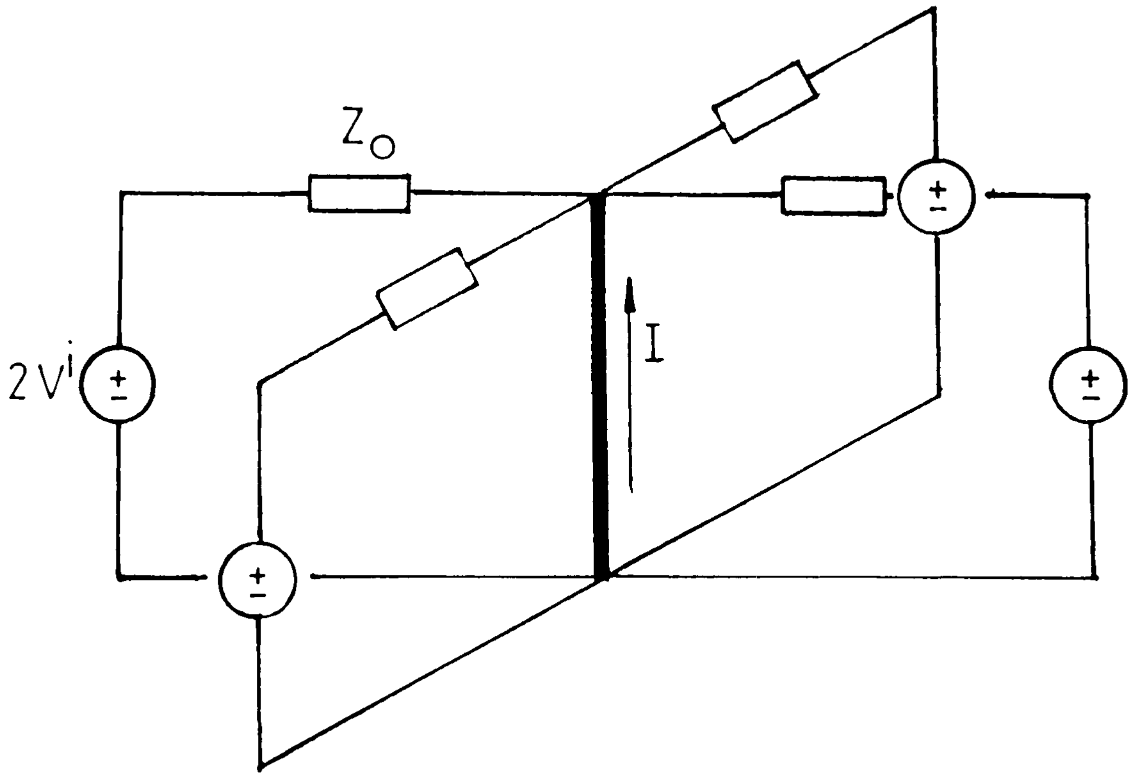

4.2.3 Radius of the Short-Circuit Node

4.2.3.1 Wire-Above-Ground

The wire-above-ground geometries shown in figure 4.7 were used in 2D and 3D TLM models.

In two dimensions the inductance, capacitance, velocity and radii (r_L and r_C) were computed using the technique described in section 3.2.1. Various boundary conditions were tested. The results obtained are shown in Table 4.1.

In three dimensions the same parameters were computed, using the same technique, for different boundary placements, w, and conditions. These results are shown in Table 4.2.

In both cases the inductance radii (r_L) and the capacitance radii (r_C) are quite different. This again points to the difference between the inductance and capacitance forms of the TLM mesh (shunt and series meshes in 2D) as described in Chapter 3.

Further evidence for the nature of the capacitance (or series) form of the mesh can be found by comparing Table 4.2 with Table 3.3 (Chapter 3). In both tables the entry for the capacitance radius r_C is very similar for $w = 5.83$m and 2000 iterations, yet the wire descriptions are quite different. The inductance radii (r_L) are not similar.

Figure 4·7 Wire above ground geometry

a) 2D

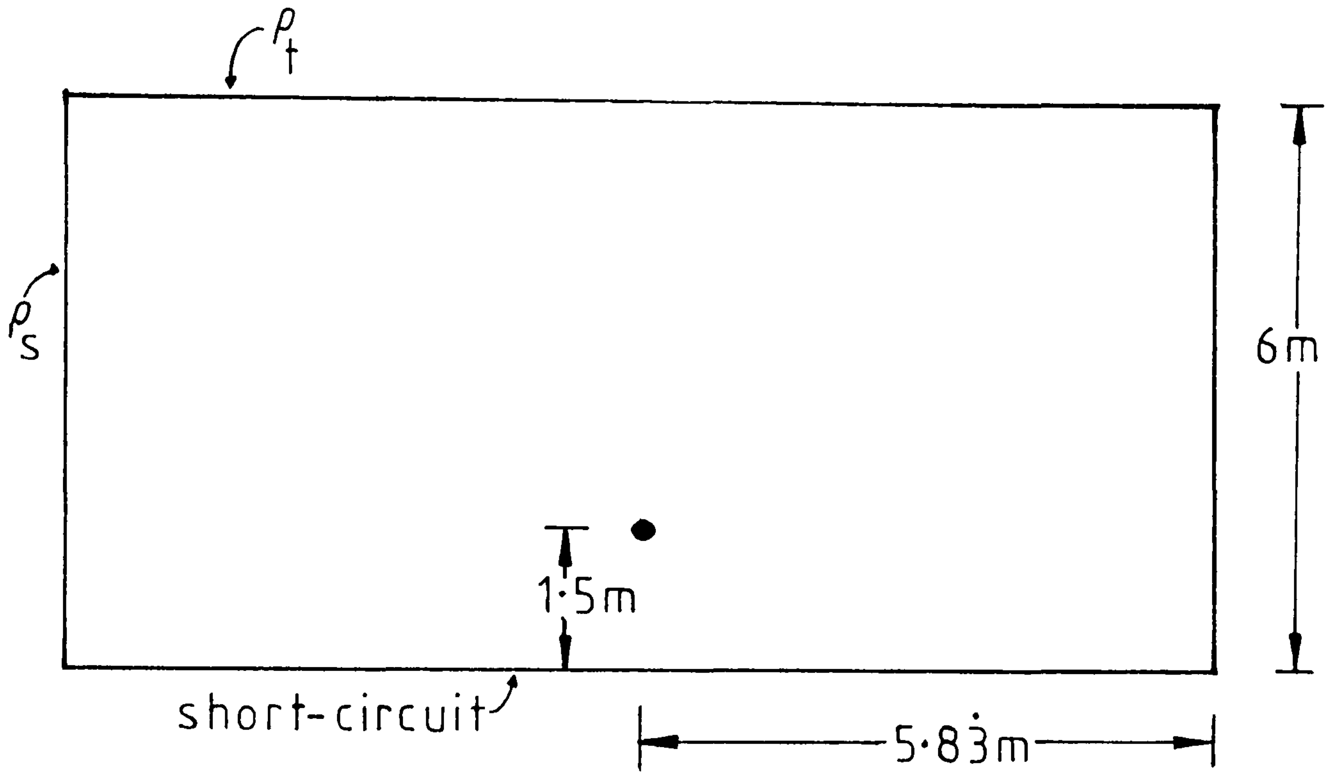

b) 3D

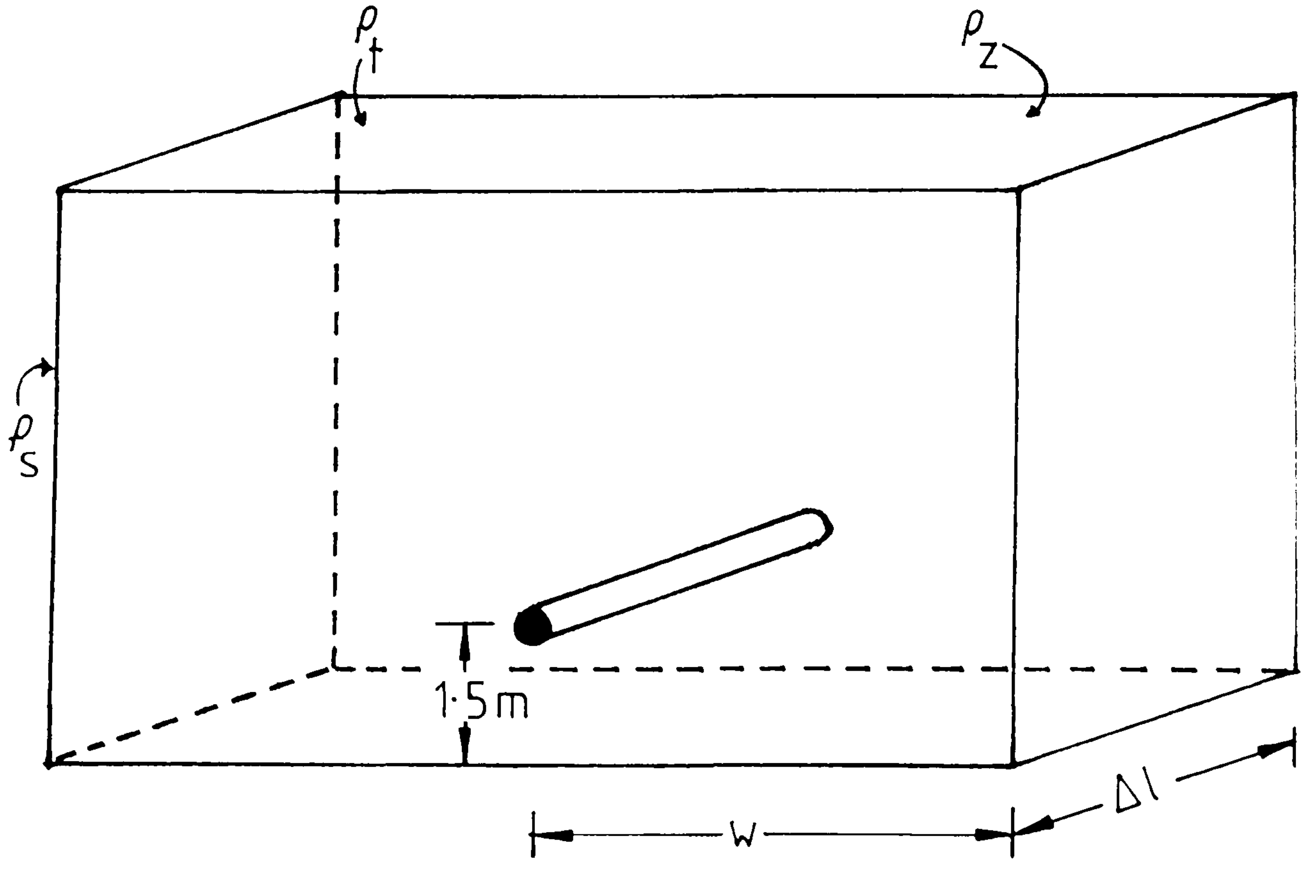

$\Delta l = 1/3$m

Table 4.1 Variation of modelled radii with external boundaries for a short-circuit node wire, 1.5m above ground in two-dimensions.

w = 5.83m, 2000 iterations, Δl = 1/3m.

reflection		inductance		capacitance		velocity
ρ_t	ρ_s	L_d x10^{-7} (Hm^{-1})	r_L (m)	C_d x10^{-11} (Fm^{-1})	r_C (m)	$(L_dC_d)^{-1/2}$ x10^{8} (ms^{-1})
0	0	7.870	0.059	2.299	0.265	2.351
0	1	7.862	0.059	2.121	0.217	2.449
1	0	7.858	0.059	2.203	0.247	2.403
1	1	7.834	0.060	2.112	0.214	2.458

Table 4.2 Variation of modelled radii with boundary type and positions for a short-circuit node wire in three-dimensions.

Δl = 1/3m.

ρ_s	w	Its.	inductance		capacitance		velocity
	(m)		L_d x10^{-7} (Hm^{-1})	r_L (m)	C_d x10^{-11} (Fm^{-1})	r_C (m)	$(L_dC_d)^{-1/2}$ x10^{8} (ms^{-1})
0	3.167	2000	7.269	0.079	2.079	0.208	2.572
1	3.167	2000	7.218	0.081	1.726	0.119	2.833
1	4.833	3000	6.863	0.097	-	-	-
0	5.833	2000	6.794	0.100	2.023	0.191	2.697
1	5.833	2000	6.722	0.104	1.865	0.152	2.824
0	5.833	4000	6.775	0.101	2.032	0.193	2.695
1	5.833	4000	6.765	0.102	1.869	0.152	2.813

The two wire geometries being compared here are the short-circuit node and a $\Delta\ell$ x $\Delta\ell$ coarse wire description. These are shown in figure 4.8. The short-circuit node is where only the node containing the wire is short-circuited. For a $\Delta\ell$ x $\Delta\ell$ wire each transmission-line leading to the node is short-circuited half way between nodes. Thus quite different geometries should be modelled.

The capacitance model effectively rounds the radius up to a larger value irrespective of the short-circuit position, as suggested by figure 4.8. Since the inductance radii are different for the two models (the short-circuit node having r_L smaller than the $\Delta\ell$ x $\Delta\ell$ wire) the velocity of propagation will be less on the short-circuit-node wire than on the $\Delta\ell$ x $\Delta\ell$ wire. This is confirmed by examining Tables 4.2 and 3.3. Also, as was found in Chapter 3, the wire-above-ground geometry was not well defined because of the non-physical external boundary conditions ρ_s and ρ_t which were introduced. For this reason the resonant cavity geometry was used for further tests.

4.2.3.2 Resonant Cavity

The resonant cavity geometry introduced in Chapter 3 was also applied to a short-circuit node wire model. The cavity geometry is shown in figure 4.9. Various wire terminations were investigated. They were $0.1Z_o$, $0.25Z_o$, $0.5Z_o$ and short-circuit, where Z_o is the (unknown) characteristic impedance of the wire to its coaxial surroundings.

Figure 4·8 Series mesh radii

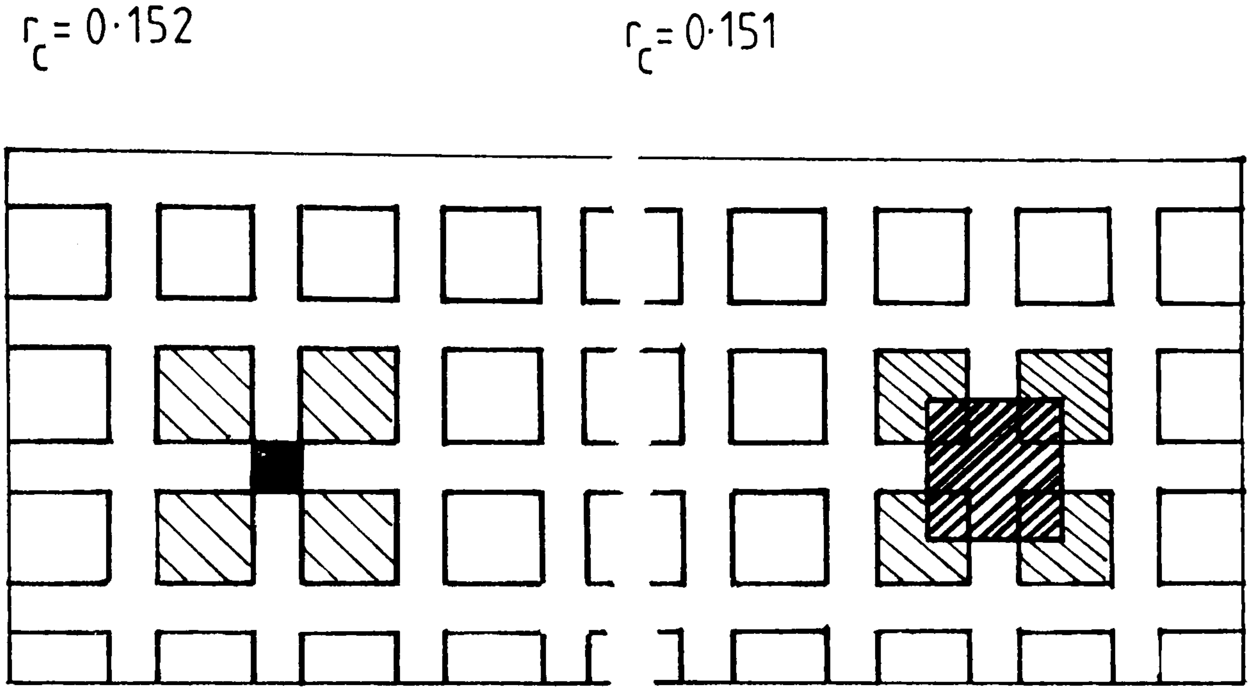

Figure 4·9 Cavity geometry

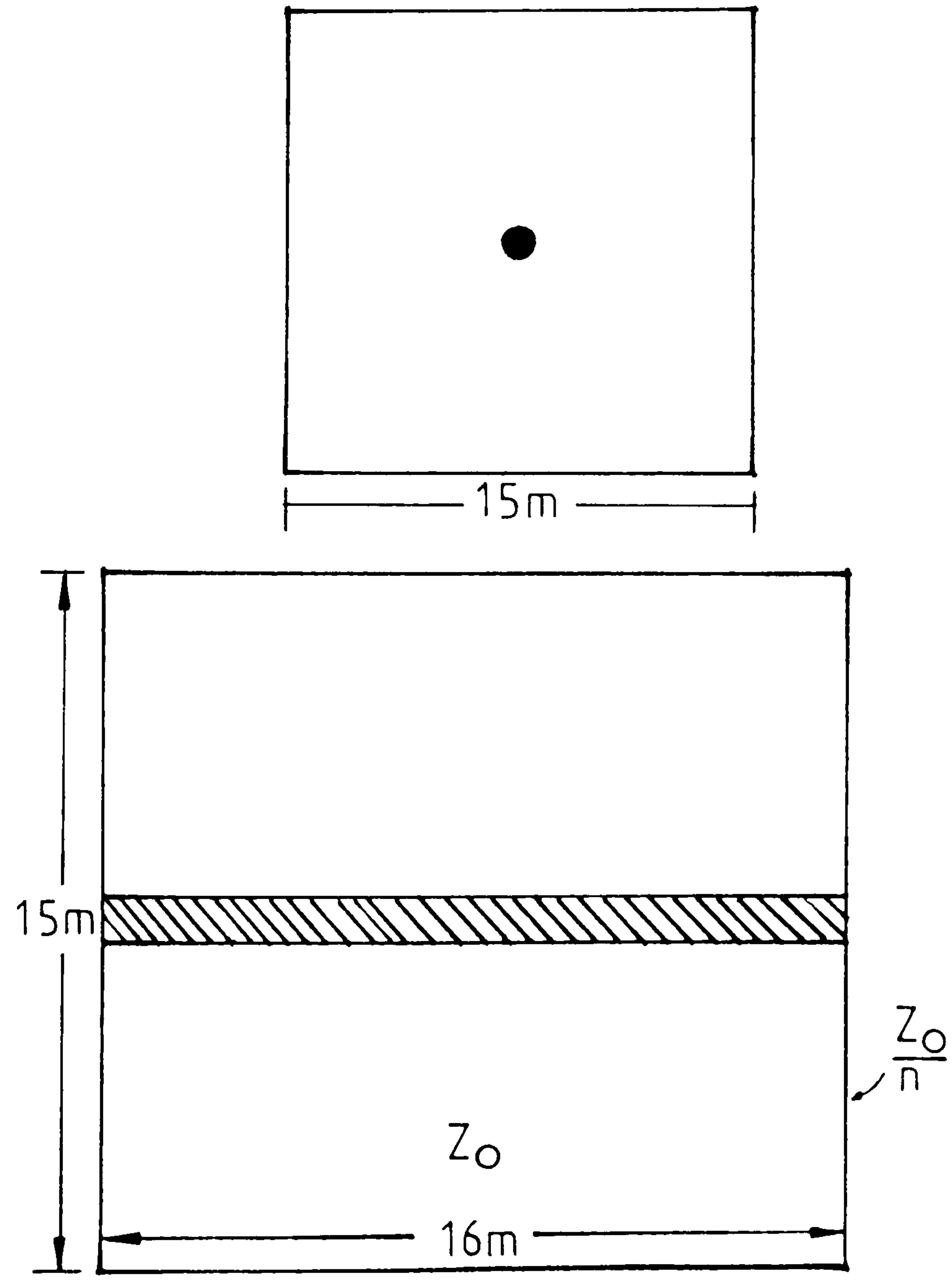

From equation (3.15):

$$Z_x = Z_o \frac{(\frac{Z_o}{n} + Z_o \tanh\gamma x)}{(Z_o + \frac{Z_o}{n} \tanh\gamma x)} \qquad (4.12)$$

where n is 10, 4, 2 or ∞ (to give the values above) which for a lossless line becomes:

$$Z_x = Z_o \frac{(1 + jn \tan\beta x)}{(n + j \tan\beta x)} \qquad (4.13)$$

To model these boundaries in the TLM workspace the ends of the cavity were terminated by an imperfect conductor.

The reflection coefficient, ρ, of this boundary is then given by

$$\rho = \frac{Z_o/n - Z_o}{Z_o/n + Z_o} \qquad (4.14)$$

Using this formula, the above terminations were modelled. Table 4.3 shows the radii obtained for differing positions, iterations and loads. The radii obtained place the modelled radius in the range $0.415 \leqslant r \leqslant 0.681$ ($\Delta\ell$ or metres in this case). The average radius was $0.564\Delta\ell$ and the velocity of propagation was 2.7×10^8 ms^{-1}.

Table 4.4 shows how the radii and velocity of propagation vary with length of the wire. Although the velocity is fairly constant (but slower than the velocity of light) the measured radii vary from $0.475 \leqslant r \leqslant 0.702$.

Table 4.3 Variation in modelled radius with differing number of iterations and load type for short-circuit node wire 16m long in a 15m x 15m coaxial description.

Δl = 1m. Velocity = 2.7×10^8 ms^{-1}.

Number of iterations	Load Type xZ_0	radii at			
		2.5m	3.5m	4.5m	6.5m
490	0.00	0.558	0.538	0.511	0.494
	0.10	0.558	0.549	0.538	0.595
	0.25	0.546	0.550	0.545	0.489
	0.50	0.542	0.548	0.552	0.504
500	0.00	0.564	0.591	0.599	0.681
	0.10	0.556	0.556	0.565	0.589
	0.25	0.570	0.544	0.536	0.489
	0.50	0.556	0.583	0.570	0.493
510	0.00	0.635	0.620	0.602	0.585
	0.10	0.597	0.596	0.594	0.573
	0.25	0.612	0.601	0.592	0.515
	0.50	0.565	0.567	0.543	0.415
990	0.00	0.528	0.536	0.534	0.567
	0.10	0.575	0.566	0.569	0.587
	0.25	0.554	0.627	0.550	0.644
1000	0.00	0.569	0.566	0.551	0.551
	0.10	0.551	0.550	0.555	0.582
	0.25	0.557	0.554	0.554	0.545
1010	0.00	0.581	0.590	0.605	0.631
	0.10	0.559	0.562	0.570	0.555
	0.25	0.559	0.566	0.576	0.611
2000	0.00	0.558	0.563	0.568	0.584
	0.10	0.560	0.557	0.552	0.577
	0.25	0.561	0.559	0.551	0.624
Average		0.565	0.568	0.562	0.562
Overall Average					0.564

The likely cause of this difference was investigated in Chapter 3. An observer at a point 4.5m along the wire will have seen the plane wave pass more times for a short wire than for a long wire. Thus there is effectively less information used in obtaining the longer wire results (compared with the short wires).

Both results suggest that the short-circuit node is a worse model of a wire than the simple ($\Delta\ell$ x $\Delta\ell$) wire introduced in Chapter 3. The radius is, on average, of the same order as those modelled in Chapter 3 and therefore the modelling of thin wires is still a problem. The velocity of propagation is 10% less than the velocity of light and so there may be considerable errors in modelling any wire using the short-circuit node.

4.3 Stub Models of Wires

4.3.1 Introduction

The short-circuit node developed above does model a wire of radius approximately half the mesh spacing. The radius modelled is not variable and the velocity of propagation is less than the velocity of light.

If this short-circuit node is replaced by a short-circuited transmission line stub, as shown in figure 4.10a, then is the effective radius made variable by changing the impedance of the stub? The purpose of this section is to answer the above question and to investigate two other stub wire models (also shown in figure 4.10).

Table 4.4 Variation of short-circuit wire radius with length of wire.

Radii evaluated at 4.5m from termination.

Length (m)	Iterations	radius (m)	velocity ($\times 10^8$ ms^{-1})
11	1000	0.622	2.63
	500	0.702	2.61
16	1000	0.551	2.64
	500	0.599	2.64
25	1000	0.556	2.65
	500	0.551	2.65
40	1000	0.475	2.66
	500	0.561	2.62

Table 4.5 Effect of stub impedance on modelled radius.

2000 iterations $\rho_s = \rho_t = 0$, $\Delta l = 1/3$m.

Relative impedance of stub (wrt Z_0)	Inductance ($\times 10^{-7}$ Hm^{-1})	radius (m)	$\frac{\int B.dS}{\Delta l}$ ($/Z_0$)
0	7.872	0.059	1.0000
1	7.896	0.058	0.5569
2	7.920	0.057	-
10	8.111	0.052	0.1143
100	10.258	0.018	0.0161

Figure 4·10 Stub models of wires

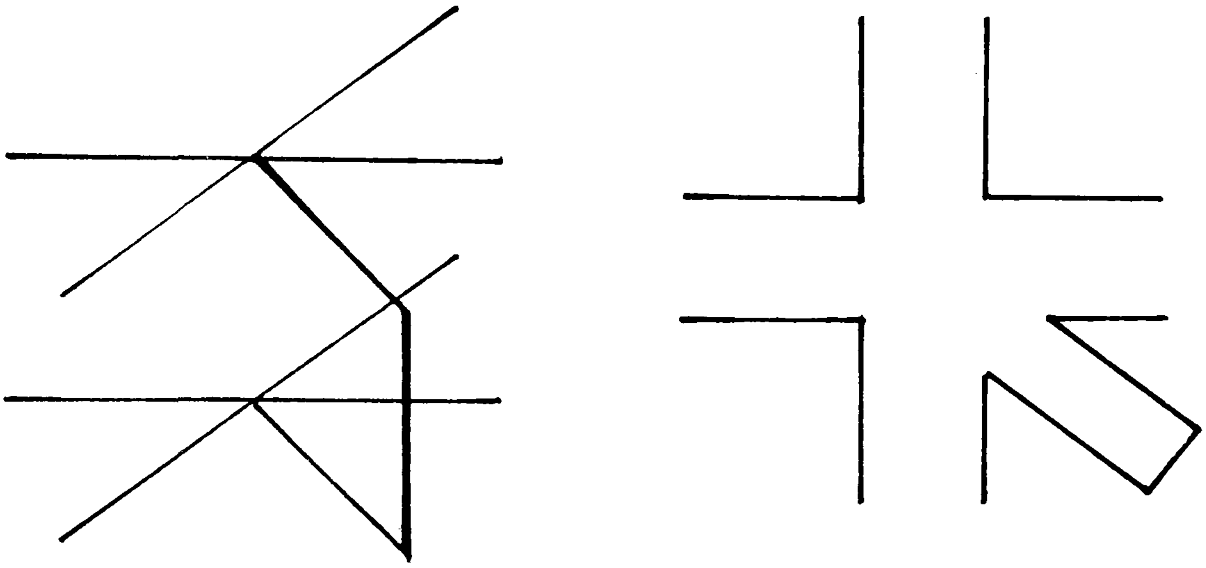

a) shunt

b) series

c) terminated transmission line

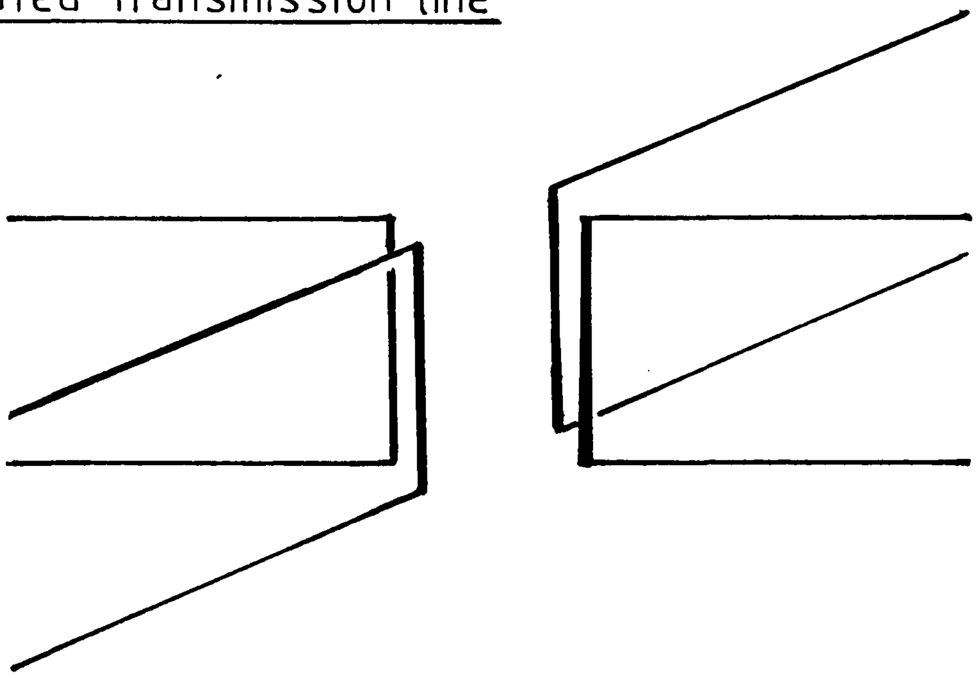

d) alternative series model

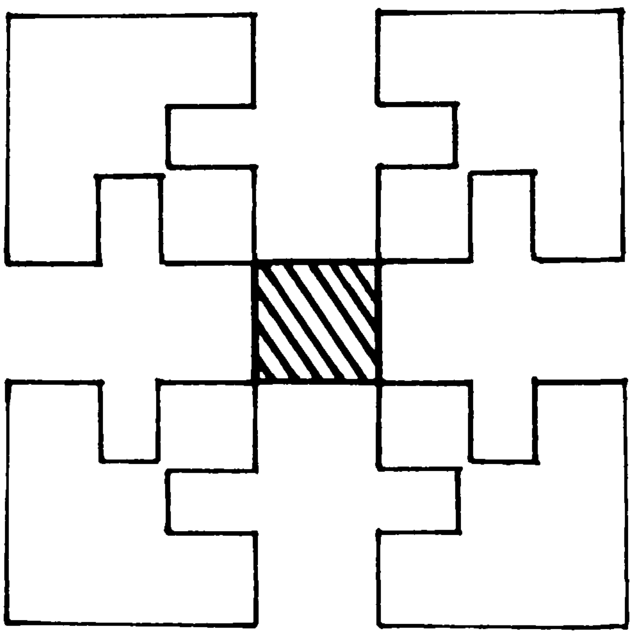

4.3.2 Simple Short-Circuit Stub

The simple short-circuit stub in a 2D mesh shown in figure 4.10a has been shown to have a scattering matrix as follows (62):

$$\begin{bmatrix} V_1 \\ V_2 \\ V_3 \\ V_4 \\ V_5 \end{bmatrix}^{r}_{k+1} = \frac{1}{1+4Z_s} \begin{bmatrix} -(1+2Z_s) & 2Z_s & 2Z_s & 2Z_s & 2 \\ 2Z_s & -(1+2Z_s) & 2Z_s & 2Z_s & 2 \\ 2Z_s & 2Z_s & -(1+2Z_s) & 2Z_s & 2 \\ 2Z_s & 2Z_s & 2Z_s & -(1+2Z_s) & 2 \\ 2Z_s & 2Z_s & 2Z_s & 2Z_s & (1+4Z_s) \end{bmatrix} \cdot {}_{k}\begin{bmatrix} V_1 \\ V_2 \\ V_3 \\ V_4 \\ V_5 \end{bmatrix}^{i}$$

(4.15)

where $Z_s = \frac{Z_{stub}}{Z_o}$

and $Z_{stub} = \frac{2L_{stub}}{\Delta t}$

and Z_o = characteristic impedance of the surrounding medium.

When this stub was used in place of the short-circuit node in the geometry of figure 4.7 the radii in Table 4.5 were obtained for various Z_s. (Note that if $Z_s = 0$ the scattering matrix of equation 4.15 becomes a short-circuit node). The results shown in the table suggest that it is possible to vary the radius of the wire.

The initial excitation, described in section 3.2.1, establishes an initial flux between the wire and ground.

For lossless wires this flux remains constant. In the previous wire-above-ground models this flux was found to be constant and independent of wire radius, because the wires had no losses. For wires composed of stubs the flux does not maintain the constant value but decreases with increasing stub impedance. This indicates that the wire or the surrounding media is lossy. There is one further problem with this model of a wire. The above results only apply to the radius calculated from the inductance (2D-shunt) model.

A short circuit stub applied to the 2D-series TLM mesh, as in figure 4.10b, does not model a wire at all. It only changes the permittivity of the medium as shown in (59). It would also be difficult to model a wire in three-dimensions using this technique.

4.3.3 Short-Circuit Stubs Terminating the Transmission Lines

Short-circuit stubs can be used to replace a short-circuit node as shown in figure 4.11. The impedances of such stubs are given by (82)

$$Z_s = \frac{2L_{stub}}{\Delta t} \qquad (4.16)$$

putting $L_{stub} = L_d \Delta \ell$ suggests a way that the modelled radius can be varied.

When the radius, r, in figure 4.11 is zero then

$Z_s = Z_o$,

$$\text{i.e.:} \quad Z_o = 2L_d \frac{\Delta \ell / 2}{\Delta t} \qquad (4.17)$$

Figure 4·11 Stub termination wire model

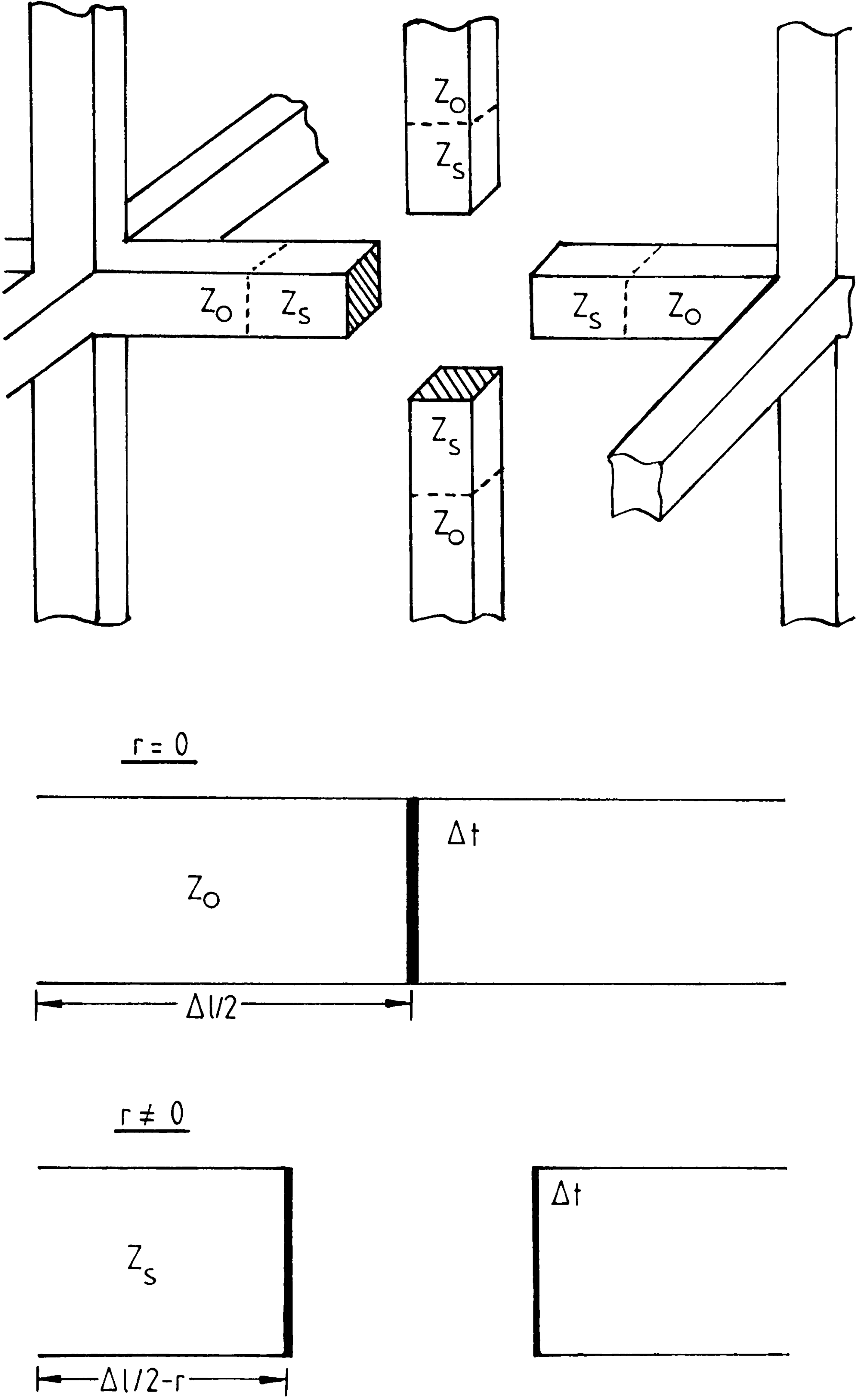

when $r \neq 0$ then :

$$Z_s = 2L_d \frac{\Delta\ell/2 - r}{\Delta t} \tag{4.18}$$

giving

$$Z_s(r) = Z_o(1 - \frac{2r}{\Delta\ell}) \tag{4.19}$$

or, in general:

$$Z_s(r) = Z_o(1 - \alpha) \tag{4.20}$$

The stub model was used in a wire-above-ground (3D) geometry shown in figure 4.12 and the wire radius was evaluated for various α. Figure 4.13 shows that it was possible to vary the (inductance) radius quite widely. Above $\alpha = 0.04$ errors occur in the modelling which lead to current flowing in and out of the wire as shown in the figure. This model again makes no change to the capacitance radius obtained. This adds further weight to the arguments, expounded in sections 4.2.3.1 and 3.3.1, that suggest the radius is rounded up to the same larger radius irrespective of the model used.

In an attempt to reduce the radius modelled in the capacitance model, stubs were introduced mid-way between the short-circuit node and the adjacent nodes, as shown in figure 4.14. The 2D capacitance (series) model of figure 4.12 was then solved for various values of Z_s and the resulting radii evaluated.

Figure 4.15 shows how the modelled radius varies with stub impedance Z_s (all stubs taking the same value).

Figure 4·12 Stub wire geometry

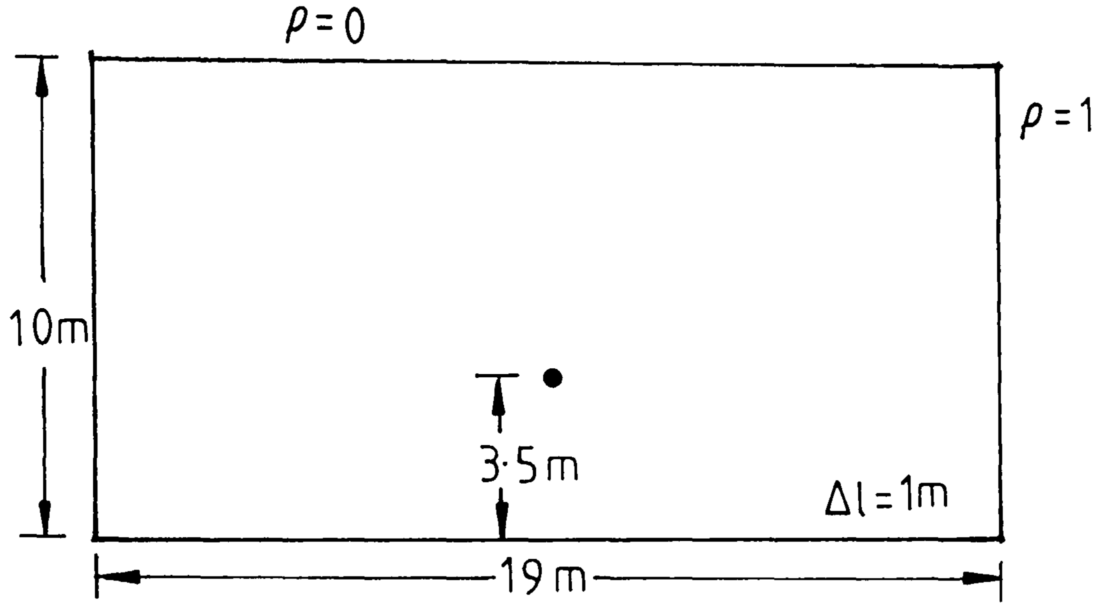

Figure 4·13 Inductance radii

$Z_s(r) = Z_O(1-\alpha)$

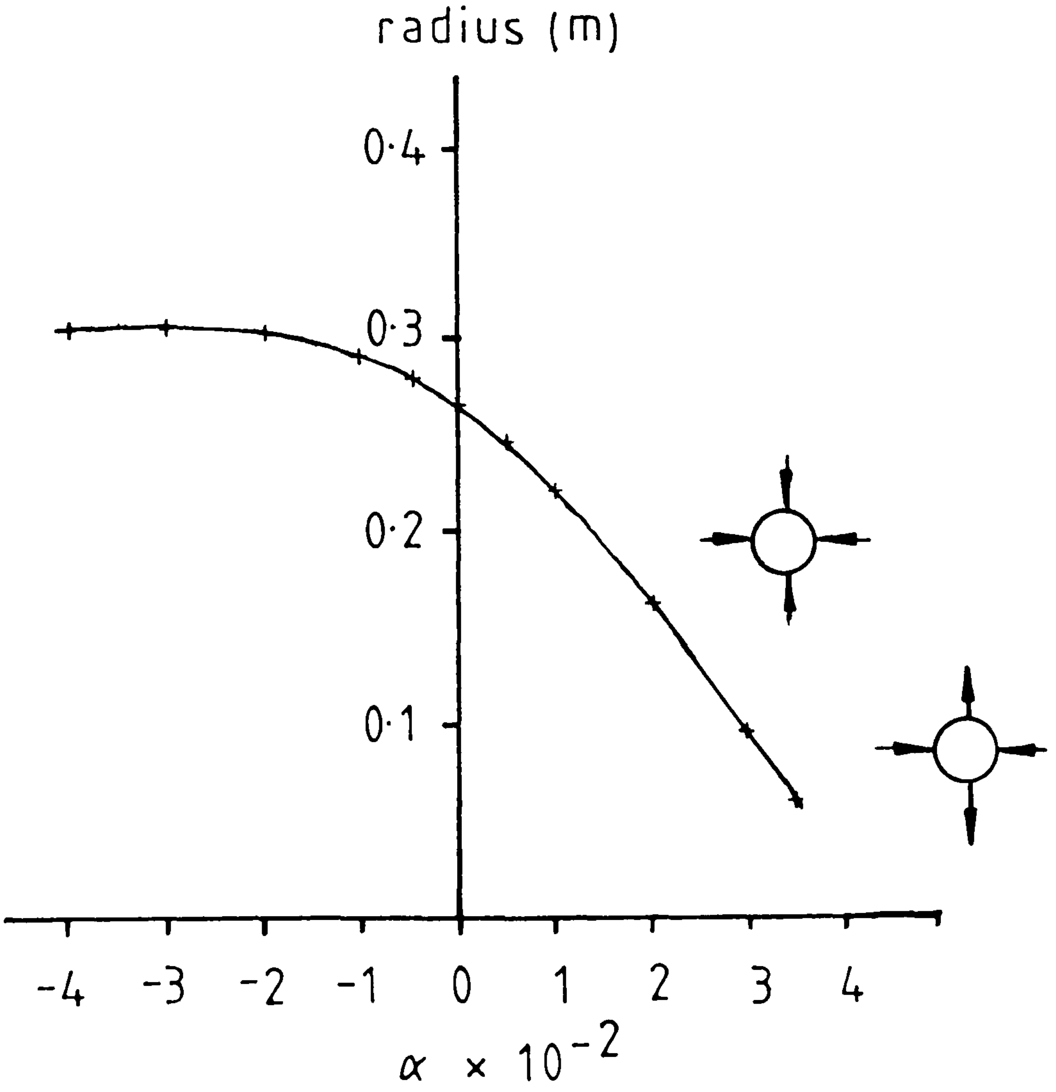

Figure 4·14 Series mesh with stubs

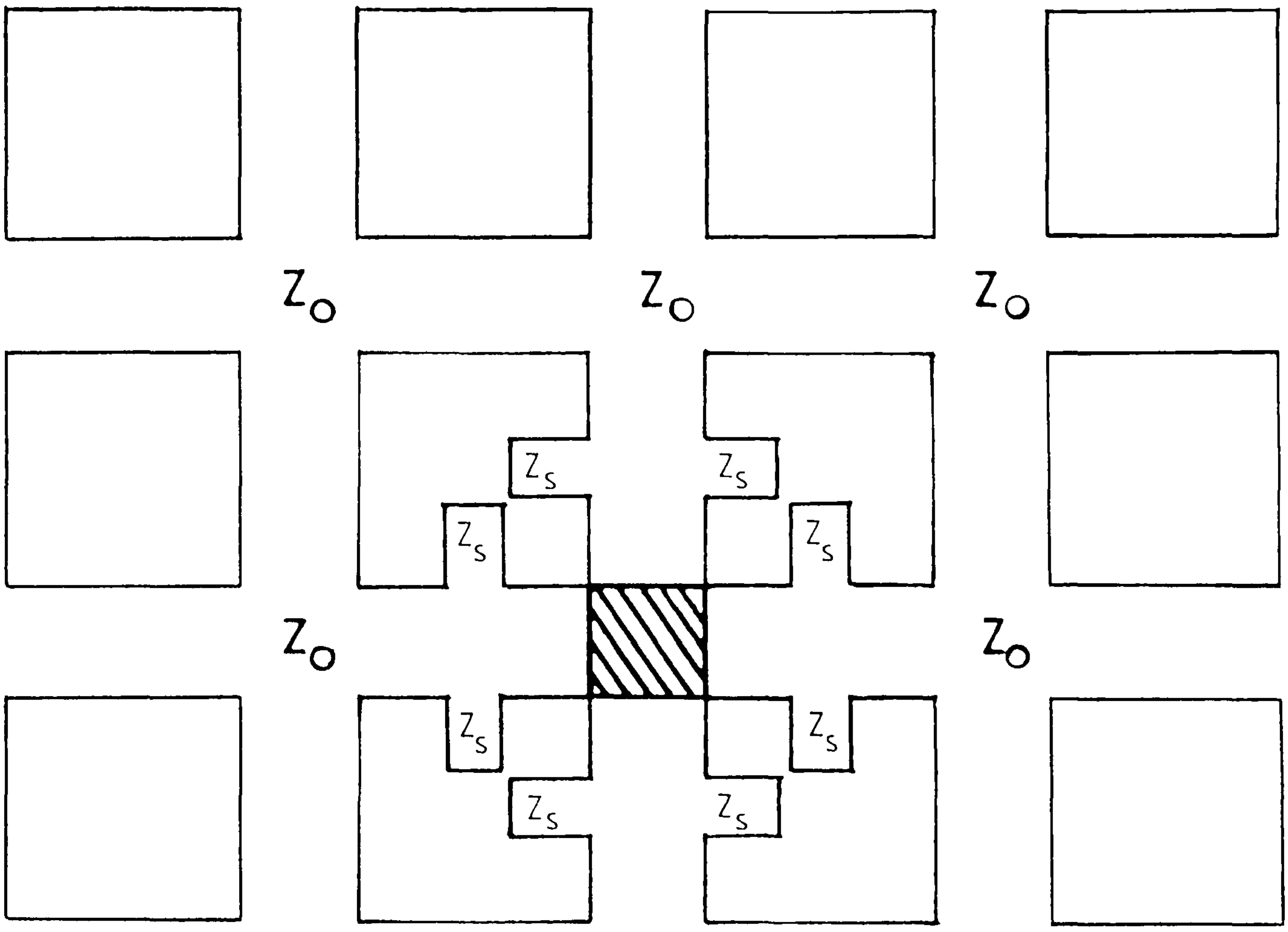

Figure 4·15 Capacitance radii

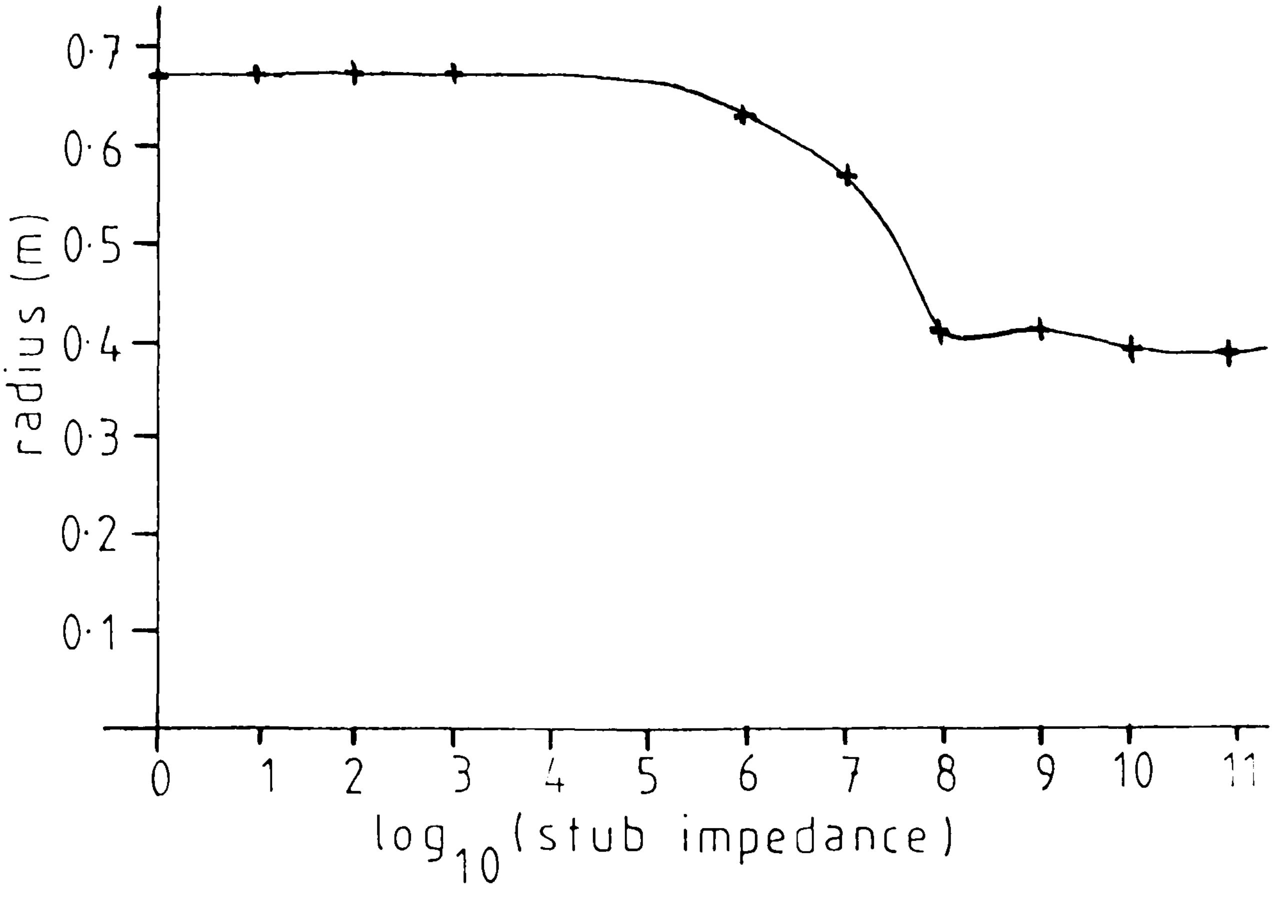

Only large stubs $10^4 \leqslant Z_s \leqslant 10^8$ cause variation in the radius between $0.4\Delta\ell \leqslant r \leqslant 0.675\Delta\ell$. This range of radii does not overlap the range available to the inductance model.

This means the inductance radii and capacitance radii cannot be made equal by use of the stub models derived here. Consequently the velocity of propagation of any wave on the model is expected to be less than the velocity of light.

4.4 Comparison Between Two of the Wire Models

The ultimate aim of this work is to be able to calculate the current induced into a wire. Two of the wire models described in this chapter, namely the short-circuit node and the short-circuit stub modelling a radius of 0.2m (as defined in section 4.3.3), were compared. The two wire models were illuminated by an electromagnetic pulse as shown in figure 4.16. The induced currents obtained are shown in figure 4.17. Since the wire radii are supposed to be different (approximately 0.267m and 0.2m) the two waveforms are too similar. Based on the (approximate) impedances of the wires to the ground plane (196Ω and 213Ω), the currents should differ by 9%. Clearly this is not so. It has already been shown that the effective (or modelled) radius, as determined by the inductance calculation, is variable whilst the capacitance radius is almost constant. What the above results suggest is that the radius modelled in a coupling

Figure 4.16 Comparison between two wire models

a) EMP excitation

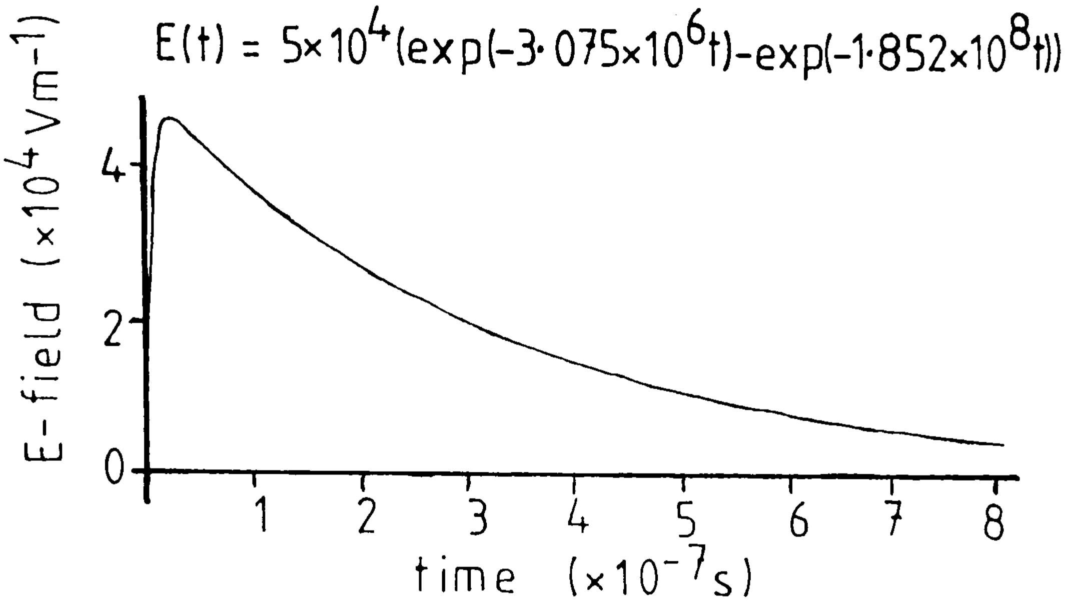

b) Geometry

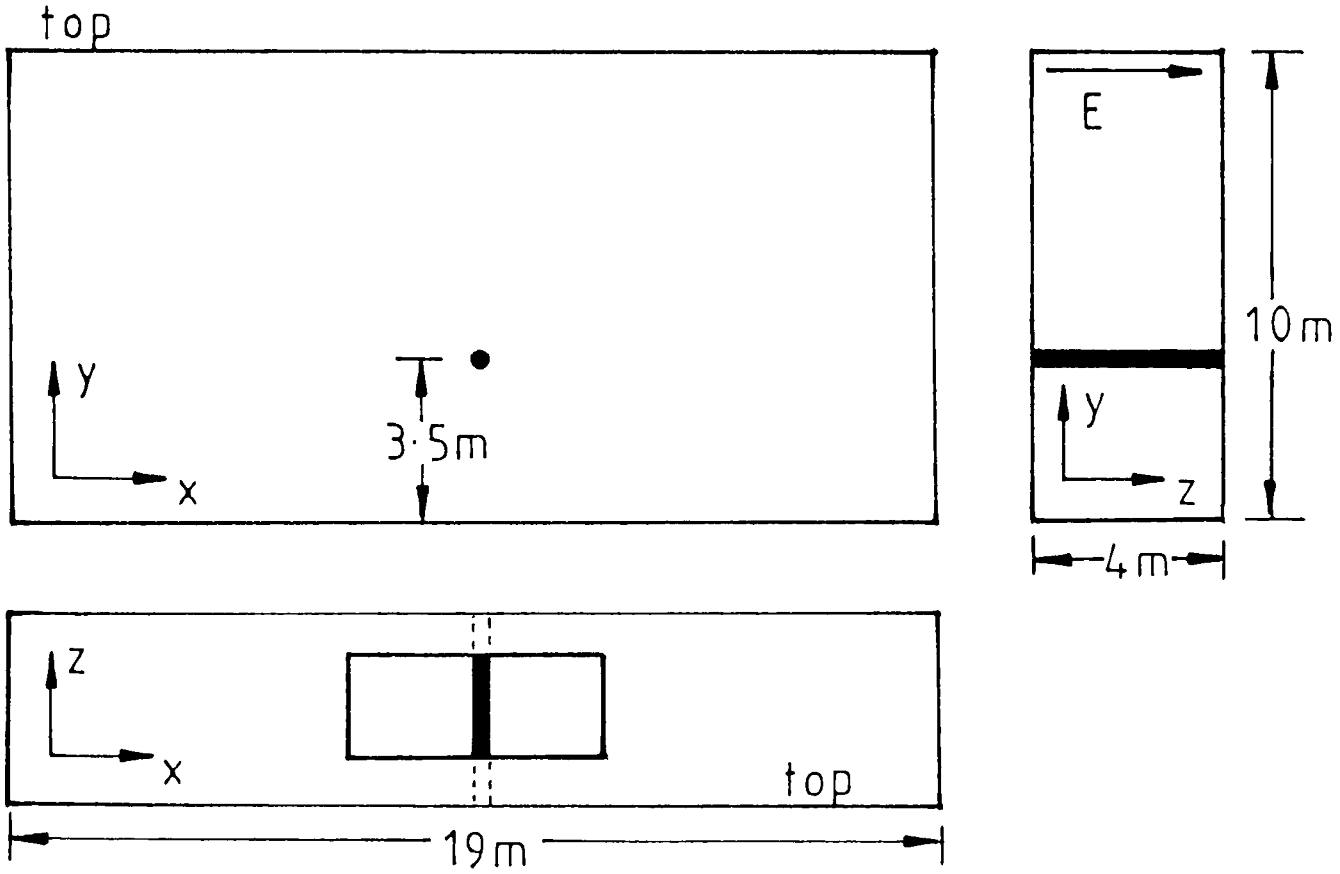

Figure 4.17 Currents induced

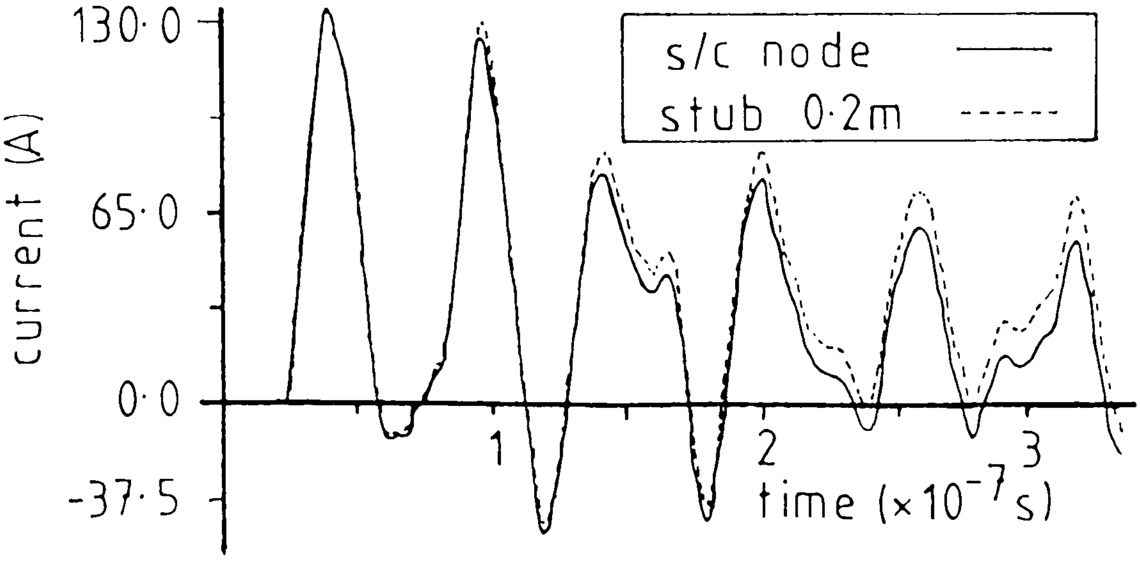

geometry is changed very little by the introduction of stubs. In fact, the actual geometry of the node, whether short-circuit or containing stub(s), does not seem to affect the current induced into the wire, although the electric and magnetic fields surrounding the wire are changed.

Thus to model a thin wire a fine mesh must be used, either over the whole geometry of the problem (Chapter 3) or in the region of the wire (Chapter 6). In either case this increases the computational time and storage required to solve the problem.

4.5 Conclusions

Single-time-level scatterers (short-circuit nodes) have been used to model wires. The radius modelled by such a node was found to be $0.564\Delta\ell$ in a resonant cavity geometry. The velocity of propagation was found to be 10% less than the velocity of light. This is due to 'rounding up' effects in the capacitance evaluation.

The use of stub transmission-lines in the wire models was investigated. This did not have the desired effect of reducing the modelled radius. The stub configurations do not make alterations to both the inductance and capacitance radii. It was not possible to obtain stub values which modelled the same radii for both inductances and capacitance calculations. Thus the velocity of propagation of waves on a stub model is less than the velocity of light.

When the induced currents in two wire models (short-circuit node and stub), modelling different radii, were compared, there was very little difference in the currents, implying no change in the radius or the velocity of propagation.

Chapter 5 TLM-Diakoptics

5.1 Introduction

The technique of diakoptics (83,84) is used to tear electrical networks into smaller and, usually, easier to solve sub-networks. These sub-networks (or substructures as they are called in TLM-Diakoptics) are solved in isolation. The resulting solutions can then be joined together to give the complete network response. Diakoptics in its network solution form is exact and does not involve an iterative process (84). Such a technique is useful if the network to be solved is large and complicated or if many solutions to the network are required with only small, localised changes made.

In TLM field solutions it is quite often the case that there is a very complicated structure contained within an otherwise empty and homogeneous space. Rather than solve the whole space using a very fine TLM mesh it is possible using TLM-Diakoptics to solve only the complicated geometry on a fine mesh. The rest of the geometry can be solved on a coarse mesh (63,65,66). TLM-Diakoptics when used in this way is an iterative process and is therefore not exact.

In this chapter TLM-Diakoptics will be briefly summarised by means of a simple example. The use of the 'filtering and resampling' technique in approximating the time domain data of the fine mesh will also be investigated. Finally, Frequency Domain Diakoptics will be introduced.

5.2 Summary of TLM-Diakoptics (Time Domain Diakoptics (TDD))

Probably the easiest way of summarising diakoptics is by means of a simple example.

Consider the simple one-dimensional transmission-line shown in figure 5.1. If the line is excited by an impulse as indicated then the time-domain output waveform is as shown in the figure.

Suppose that the line is now split into two substructures as in figure 5.2, and assume that the cut branches are terminated in a matched impedance. Four separate impulse responses will totally define the way each substructure interacts with the outside world. These are :

1) Source to port (cut-branch) response, $\underline{V}_{ex}$; how the given excitation emerges at the cut branch.
2) Source to output point, $\underline{V}_{op}$; how the excitation is observed at the output point.
3) Port to port, $\underline{S}$; the scattering matrix which describes the response of the substructure to an impulse.
4) Port to output-point, $\underline{O}$; how an impulse incident on the cut-branch is viewed at the output-point.

Each substructure must have a scattering matrix, $\underline{S}$, (otherwise it would not be a substructure) but it need not be described by the other matrices. (i.e. a substructure

Figure 5·1 1D Transmission line

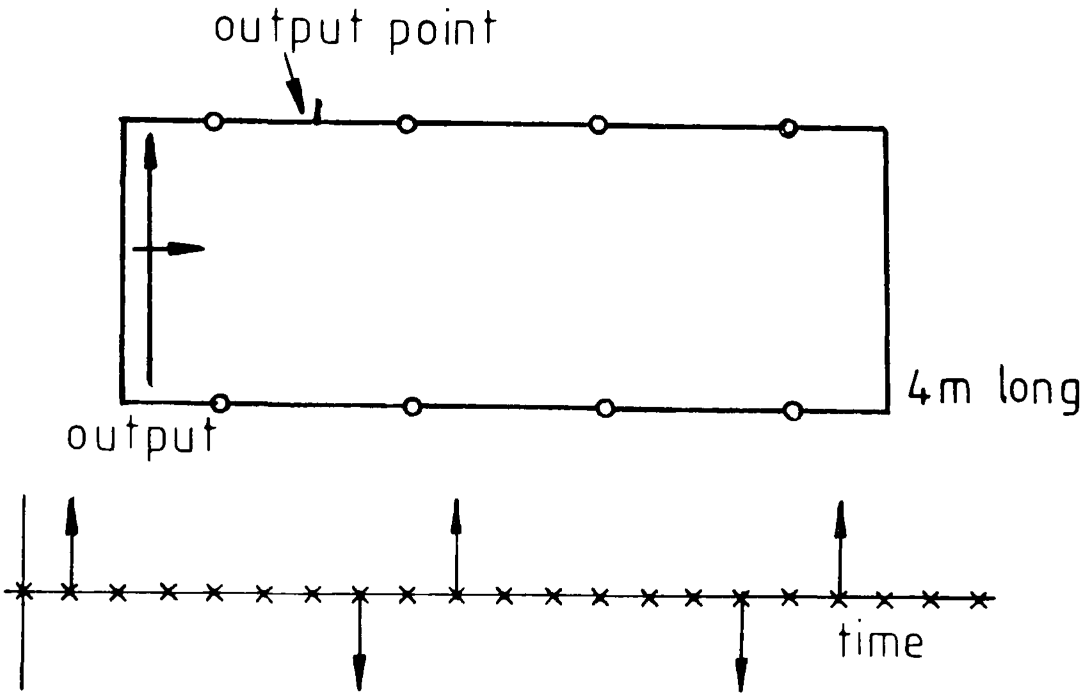

Figure 5·2 Substructure responses

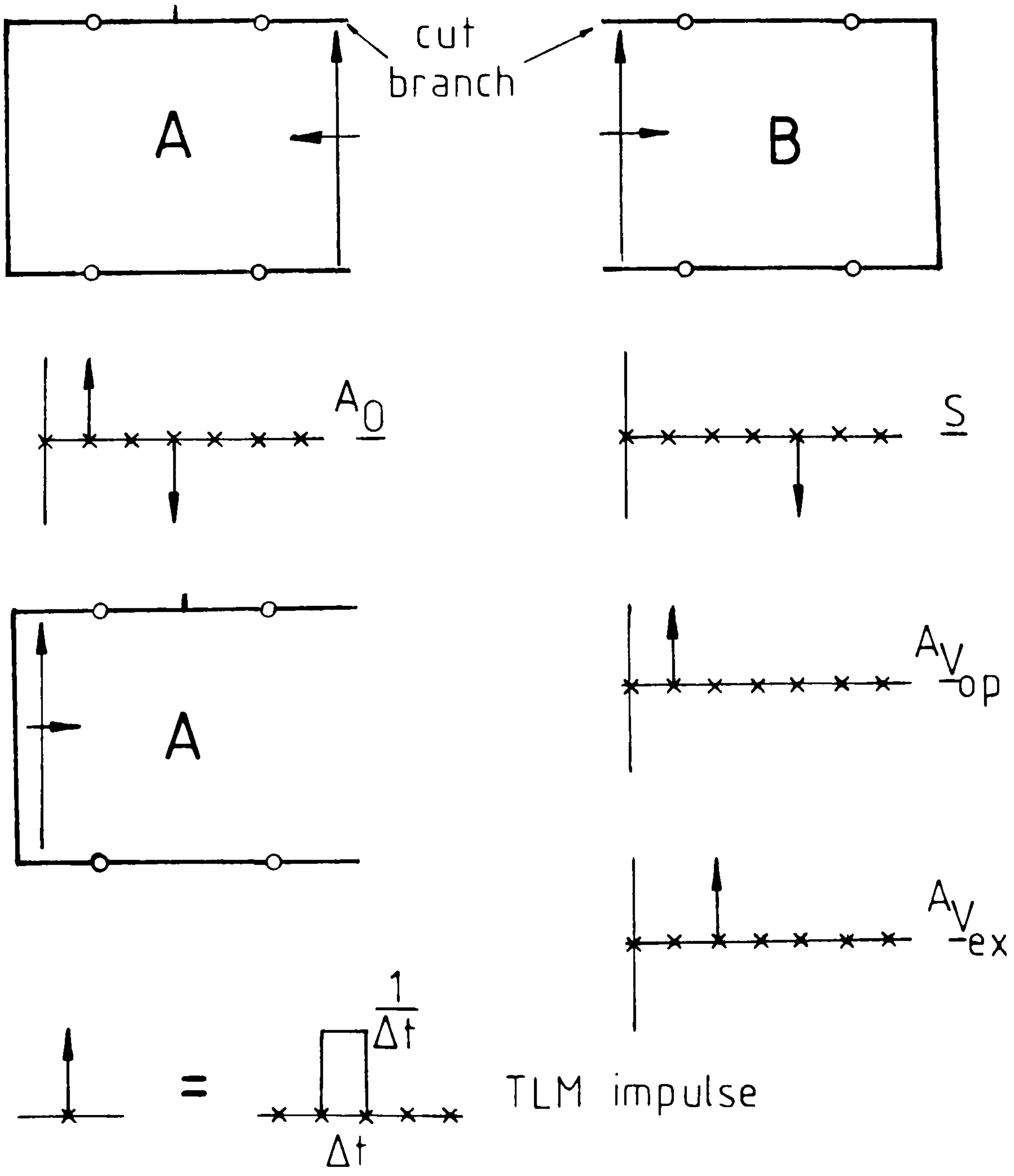

need not contain source or output points). Figure 5.2 shows the impulse responses for the simple one-dimensional line. These impulse responses can be combined by use of the diakoptic joining process shown in figure 5.3. Note that although the form of this process differs slightly from (63,65,66) all are equally valid. [The sum of a convolution is identical to the convolution of a sum:

$$g_1(t) * h(t) + g_2(t) * h(t) \equiv (g_1(t)+g_2(t))*h(t)]$$

First the excitation to port response is used to obtain the initially reflected pulses from each substructure (a). These reflected pulses become incident pulses on another substructure (b). In general this connection can be described by a connection matrix $\underline{C}$:

$$\underline{V}^i = \underline{C}\underline{V}^r \qquad (5.1)$$

From Betts (85), if the impulse response is h(t), the response of the network to a function g(t) is given by:

$$r(t) = \int_{-\infty}^{\infty} h(\tau).g(t-\tau)d\tau$$

$$= h(t)*g(t) \qquad (5.2)$$

where the symbol '*' means 'convolved with'. Therefore the reflected voltage $\underline{V}^r$ in the diakoptic example is given by

$$_1\underline{V}^r = \underline{S} *_0 \underline{V}^i \qquad (5.3)$$

From figures 5.3b,c,d this discrete convolution is:

Figure 5·3 Diakoptic joining process

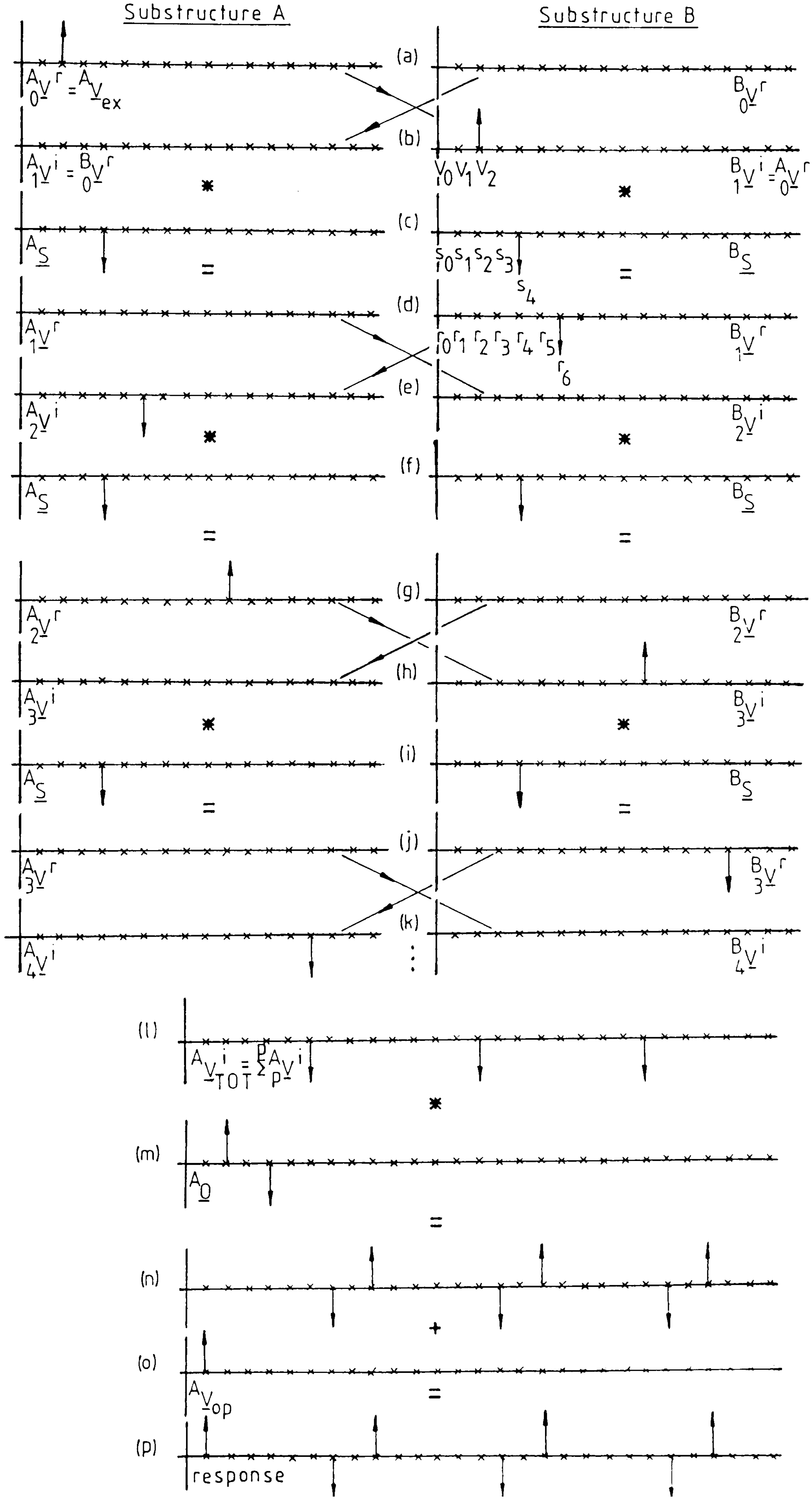

$$r_o = S_o V_o \Delta t \tag{5.4}$$

$$r_1 = (S_o V_1 + S_1 V_o)\Delta t \tag{5.5}$$

$$r_2 = (S_o V_2 + S_1 V_1 + S_2 V_o)\Delta t \tag{5.6}$$

or

$$r_n = \sum_{p=o}^{n} S_p V_{p-n} \Delta t \tag{5.7}$$

$\underline{V}^i$ at the next iteration can be obtained from $\underline{V}^r$ and $\underline{C}$ as above (e). The next reflected pulses are then obtained from the convolution with $\underline{S}$ (f,g) and so on.

Thus the process is:

$${}^{A}_{o}\underline{V}^{r} = {}^{A}\underline{V}_{ex} \; ; \quad {}^{B}_{o}\underline{V} = {}^{B}\underline{V}_{ex} \tag{5.8}$$

p=1

repeat:

$${}^{A}_{p}\underline{V}^{i} = {}^{B}_{p-1}\underline{V}^{r} \; ; \quad {}^{B}_{p}\underline{V}^{i} = {}^{A}_{p-1}\underline{V}^{r} \tag{5.9}$$

$${}^{A}_{p}\underline{V}^{r} = {}^{A}_{p}\underline{V}^{i} * {}^{A}\underline{S} \; ; \quad {}^{B}_{p}\underline{V}^{r} = {}^{B}_{p}\underline{V}^{i} * {}^{B}\underline{S} \tag{5.10}$$

p = p + 1

until p > iteration limit.

The total pulse stream incident on each substructure can be obtained by summing all the individual incident vectors thus:

$$ {}^{A}\underline{V}^{i}_{TOT} = {}^{A}_{o}\underline{V}^{i} + {}^{A}_{1}\underline{V}^{i} + {}^{A}_{2}\underline{V}^{i} + \ldots \quad (j,k,l) \qquad (5.11) $$

The output response, $\underline{R}$, can be evaluated by convolving the total pulse stream with the port to output vector $\underline{O}$ (l,m,n) and then adding the source to output vector (n,o) to give the complete response (p) which is the same as for no diakoptics (figure 5.1b). For two or three dimensional problems the form of the solution is more complex. Figure 5.4 shows a simple 2D problem with two cut transmission lines per substructure. In order to obtain the complete impulse response of the substructure it is necessary to find all possible responses to an impulse applied to each cut-branch in turn. For figure 5.4 the scattering matrix for substructure A contains four vectors:

i) ${}^{A}\underline{S}_{11}$, the response obtained from port 1 due to an impulse on port 1.

ii) ${}^{A}\underline{S}_{12}$, the response obtained from port 1 due to an impulse on port 2.

iii) ${}^{A}\underline{S}_{21}$, the response obtained from port 2 due to an impulse on port 1.

iv) ${}^{A}\underline{S}_{22}$, the response obtained from port 2 due to an impulse on port 2.

The scattering equation becomes:

$$ {}^{A}\underline{V}^{r}_{1} = {}^{A}\underline{V}^{i}_{1} * {}^{A}\underline{S}_{11} + {}^{A}\underline{V}^{i}_{2} * {}^{A}\underline{S}_{12} \qquad (5.12) $$

The output matrices and equations are similarly modified.

In both these simple examples there is only one approximating factor - the number of time-domain pulses included in each impulse response (time levels). In the one dimensional case 5 time levels completely described the response of the substructure but, in general, the response is usually infinitely long (but causal and decaying). This must be truncated to some practical length but, in doing so, some errors will be introduced into the final result. If sufficient time levels are used, for a lossy substructure, these errors will be minimised. In all cases where no further time or spatial approximations are made the final (complete) response will always be correct up to the time $p\Delta t$, where p is the number of joins completed. If there has been truncation of non-zero terms beyond the truncation time, $t = T\Delta t$, in the impulse responses then the maximum time which can be computed accurately is $T\Delta t$. Further joins $(p > T)$ will not give exact results beyond the truncation time.

5.3 Time-Domain Approximations

Usually TLM-diakoptics is used in a form similar to that depicted in figure 5.5. There are two substructures but each has been modelled using a different mesh coarseness. This means at the junction between the two substructures there are two types of approximation which have to be made: time and space. The space approximation techniques will be investigated in Chapter 6 where diakoptics will be used to develop pre-solved wire elements.

Figure 5·4 Simple 2D geometry

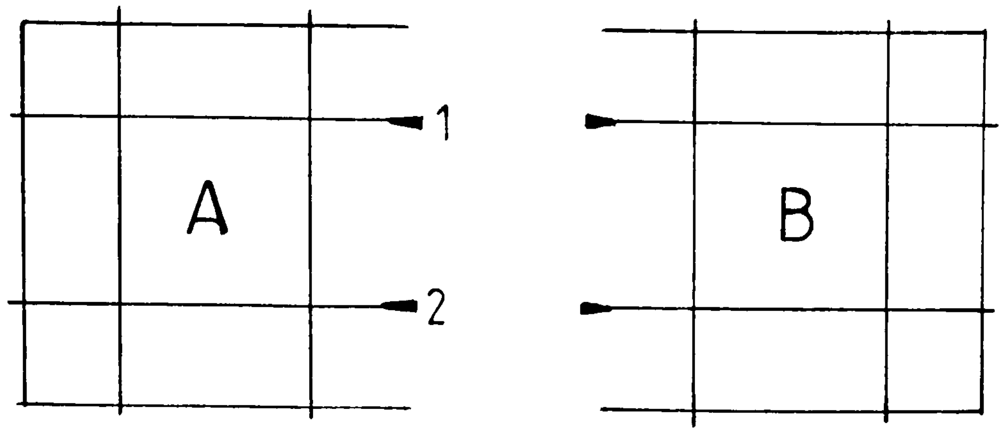

Figure 5·5 Unequal substructures

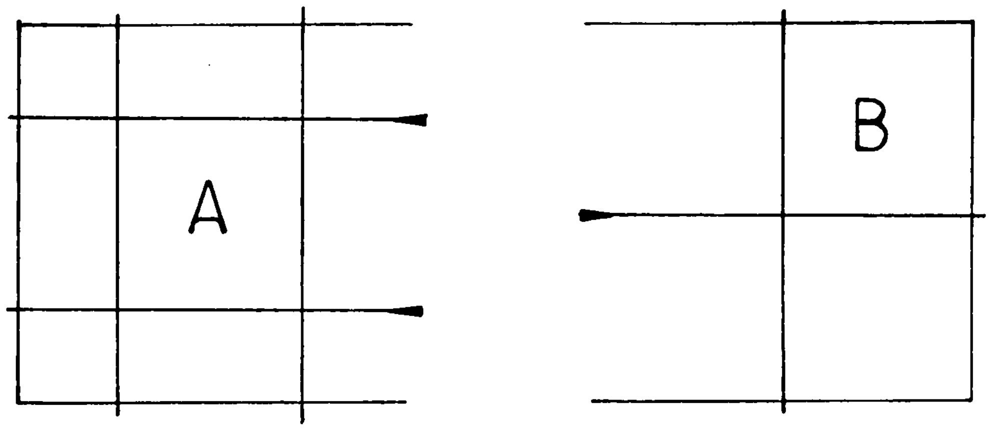

Figure 5·6 Time and frequency responses for unequal substructures

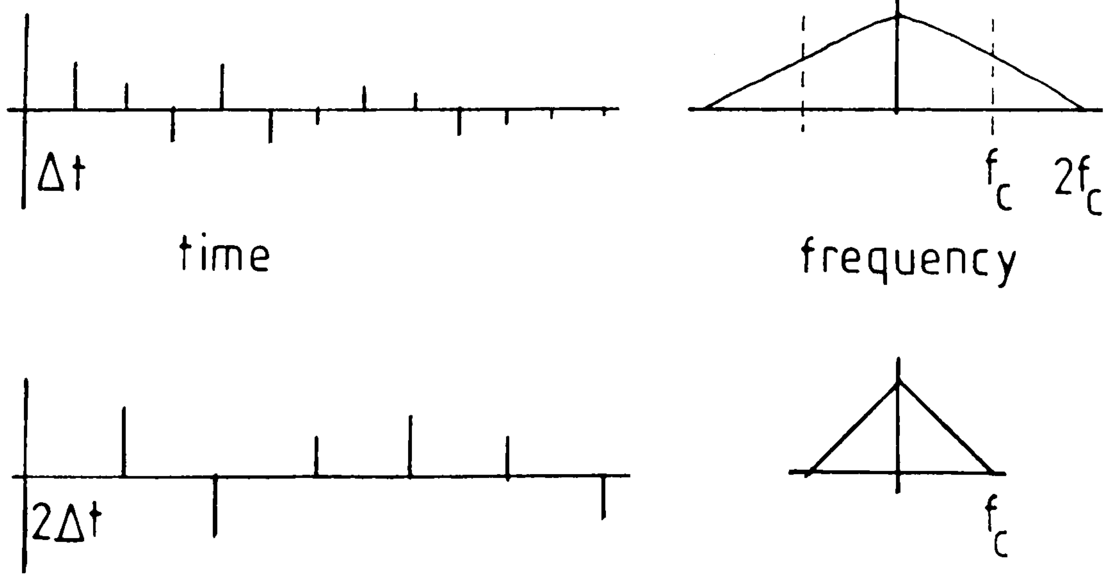

5.3.1 Filtering and Resampling

The time responses shown in figure 5.6 represent the impulse responses obtained from substructures solved with different mesh sizes. When these are joined together to obtain the final response there are two choices : the discrete convolutions can be performed either at the fine mesh time step or at the coarse mesh time step. For the former the coarse mesh response needs to be resampled at the fine mesh rate. This has the disadvantage that more data is created. The time taken to evaluate the convolved response is proportionally to the (number of terms)^2 (based on the number of multiplications required). The usual practice is to reduce the amount of data by resampling the fine mesh response at the coarse time step. Because the fine mesh response contains higher frequencies than the coarse mesh the sampling theorem requires that all frequencies above the Nyquist frequency (of the coarse mesh) be filtered out. This is to prevent aliasing. Failure to do this will cause large errors in the final output. However, in filtering the response, some of the benefits of using the fine mesh are lost.

A filtering function should have the following properties:

1) The filter should be a reasonable low-pass filter.
2) The filter should not introduce a phase delay - in resonance type problems this would

shift the position of the resonance.

3) The impulse response of the filter, when convolved with itself should give a (delayed) version of itself. Since, in the simple 1D example, an impulse convolved with an impulse gives an impulse the filtered quantities should also meet this condition. Furthermore since $\delta(t)*\delta(t) = \delta(t)$, where $\delta(t)$ is a unit impulse, $g(t)*g(t) = g(t)$, where $g(t)$ is the filtering function.

4) It would be preferable if the filtering function was causal.

Since the filtering function cannot be both causal and introduce no phase delay and since no phase delay is an important property, causality has been discarded. Examining property 3):

$$g(t) = g(t)*g(t) \tag{5.13}$$

or by the convolution theorem (85,86)

$$G(w) = G(w)G(w) \tag{5.14}$$

$$\Rightarrow G(w) = 1$$

This can either be interpreted as an impulse in the time-domain or if $G(w)$ is only valid up to the cut-off frequency of the filter, f_c, as an ideal filtering function in the time-domain (a $\sin(x)/x$ function). The time-domain function of this filter is given by (using the Inverse Fourier Transform)

$$g(t) = \frac{1}{2\pi} \int_{-2\pi f_c}^{2\pi f_c} 1.e^{jwt} dw \tag{5.15}$$

or
$$g(t) = 2f_c \frac{\sin(2\pi f_c t)}{2\pi f_c t} \tag{5.16}$$

Thus the ideal filtering routine in continuous form of the function f(t) will be:

$$r(t) = \int_{-\infty}^{\infty} \frac{\sin((t-\tau)2\pi f_c)}{(t-\tau)2\pi f_c} 2f_c f(\tau)d\tau \tag{5.17}$$

In discrete form this becomes:

$$r(i\Delta t_{out}) = \sum_{n=N_1}^{N_2} \frac{\sin((i\Delta t_{out}-n\Delta t_{in})2\pi f_c) 2f_c f(n\Delta t_{in}).\Delta t_{in}}{(i\Delta t_{out}-n\Delta t_{in})2\pi f_c} \tag{5.18}$$

where Δt_{in} is the fine mesh time step;

Δt_{out} is the coarse mesh time step;

and N_1 and N_2 are the limits of the convolution process.

From the sampling theorem (85)

$$f_c \leqslant \frac{1}{2\Delta t_{out}} \tag{5.19}$$

If the function in equation (5.18) is applied over infinite limits the impulse response at one time step would be correctly 'filtered and resampled' to give a non-causal response at the coarse time step.

However, it is necessary to truncate the infinite response of the filter at some limits (as suggested by equation 5.18) so that the discrete convolution can be performed. This truncation can lead to substantial errors in the filtered response. It has been usual to truncate the filtered response at $t = 0$ and $t = N_2\Delta t$ (equation 5.18). If the substructure under analysis gives scattered pulses close to $t = 0$ then the filtering function is drastically approximated by this truncation, as shown in figure 5.7. When the convolution process is repeated the shape of the pulse (which is a filtered, truncated impulse) is not preserved. The side lobes of the $\frac{\sin(x)}{x}$ function becomes larger with the number of convolutions performed and the total response is corrupted.

For the simple one-dimensional case shown in figure 5.1 the frequency response after 500 iterations is shown in figure 5.8a. Filtering and resampling the impulse responses of figure 5.2 with f_c=70 MHz (Nyquist = 75 MHz), $\frac{\Delta t_{out}}{\Delta t_{in}} = 2$ and truncating at $t = 0$ and $t = 100\Delta t$ gives the frequency response shown in figure 5.8b.

Examining only the first resonance at about 38 MHz shows that there is a clear error in the response. The time period covered by the diakoptic and non-diakoptic results is the same so the widths and heights of the resonances should be the same. Changing the bandwidth of the filter does improve the response as shown by figure 5.8c, although this is problem dependent (i.e. it is only true of a substructure where the impulse response is a delayed impulse. It is usual in 2D or 3D for the response to be more like figure 5.9).

Figure 5·7 Result of repeated convolutions of filtered response

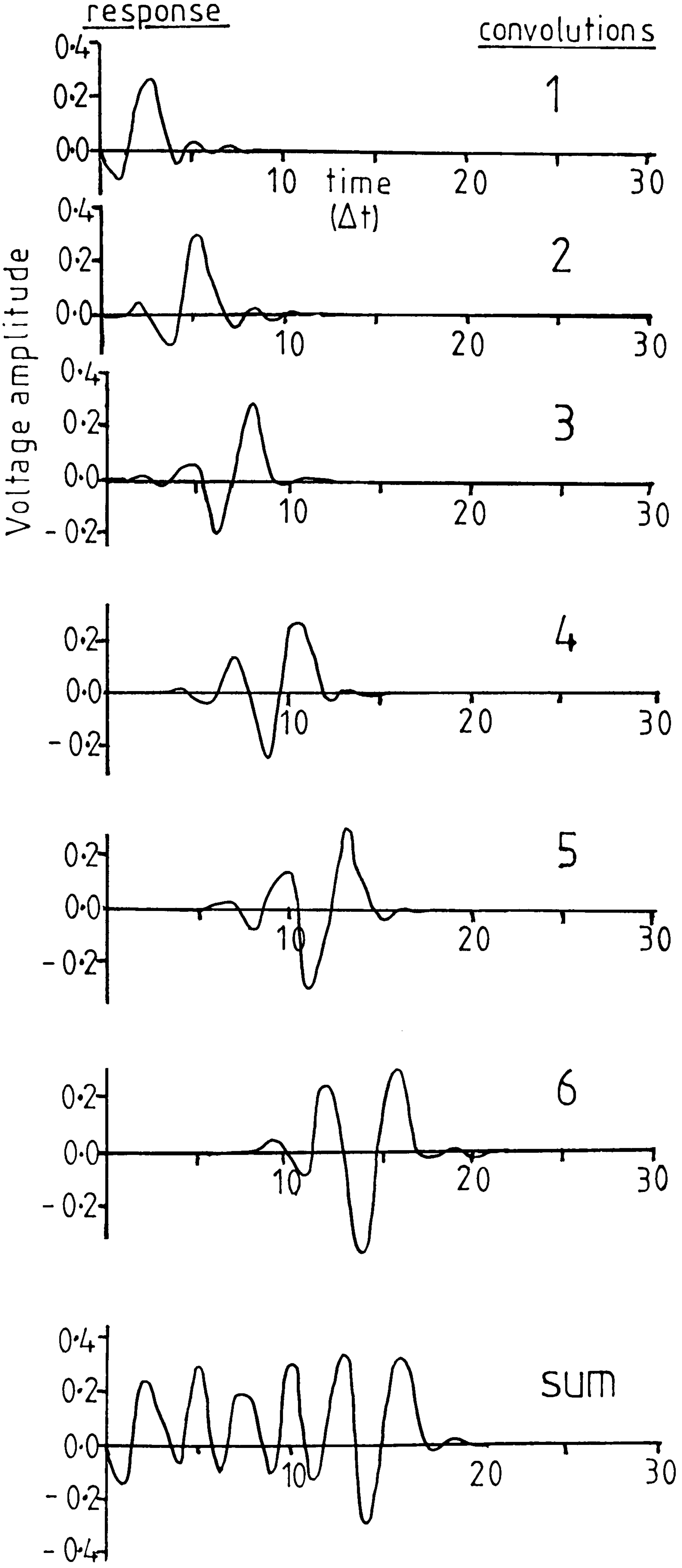

Figure 5·8 Frequency responses for 4m wire

a) No diakoptics

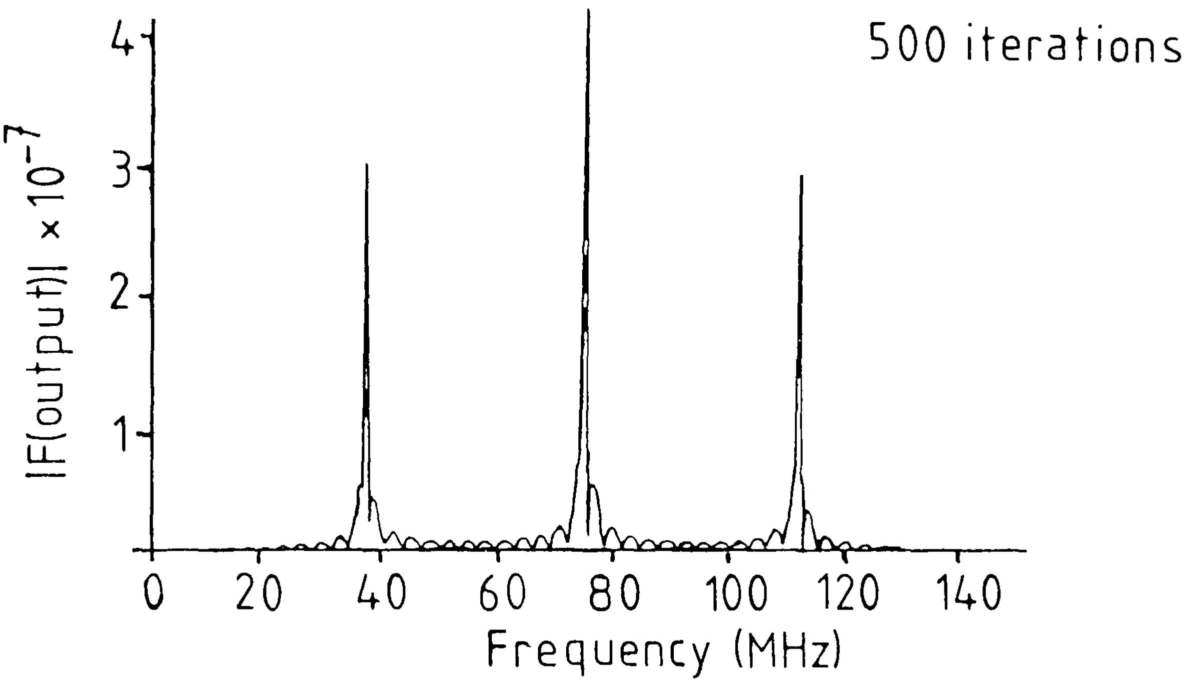

b) Time Domain Diakoptics (TDD)

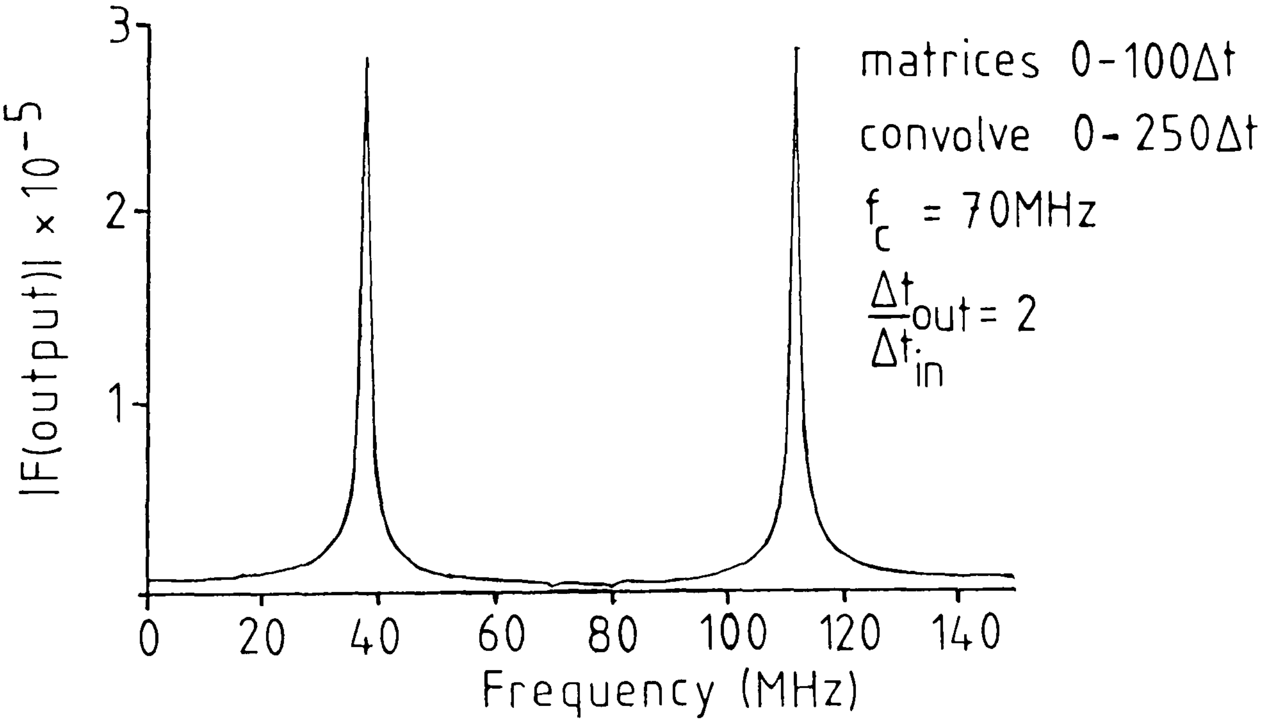

c) TDD

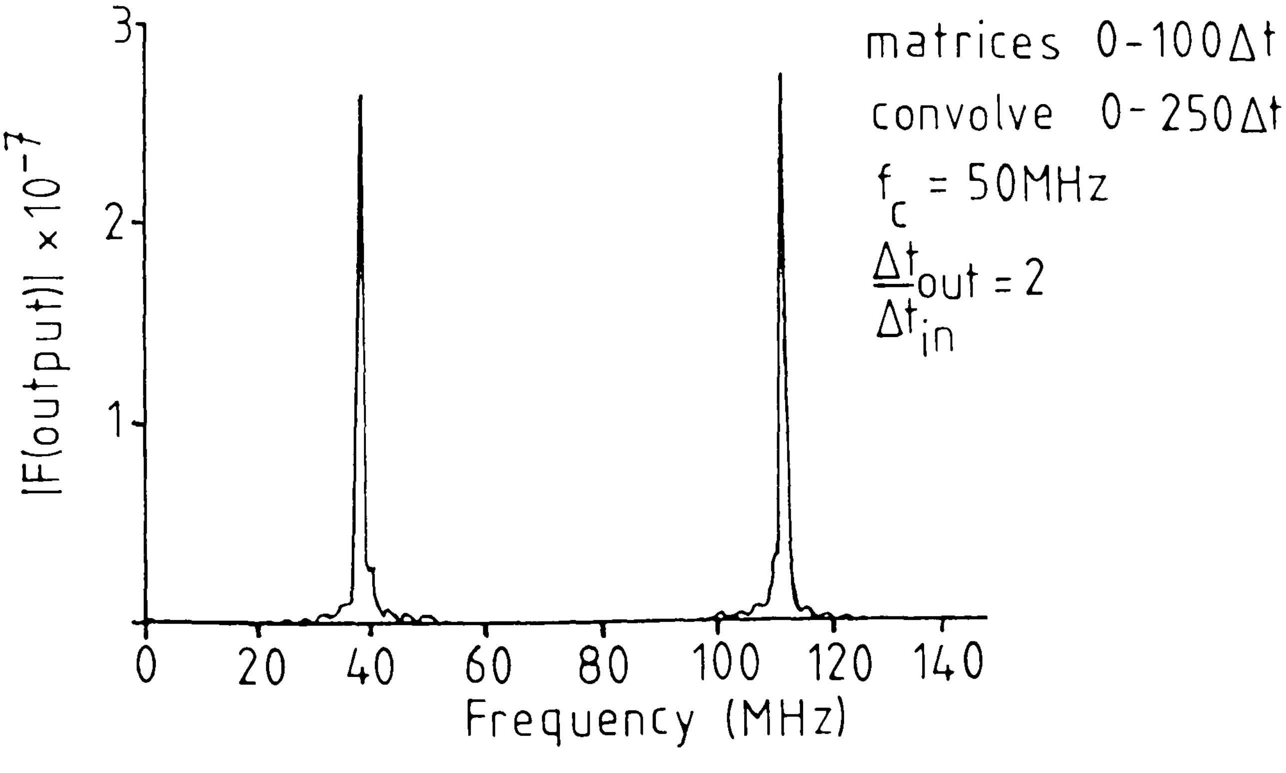

If the one-dimensional wire is made longer (e.g. 8m, 16m) and each substructure remains half the total length (4m, 8m) then the impulse response is effectively moved away from the $t = 0$. When filtering and resampling is applied to these impulse responses the accuracy of the joined (final) response improves with increasing wire length as demonstrated by figures 5.10 and 5.11.

Even if the filtered function is very finely sampled (figure 5.12a) the fact that it is truncated very near to the main peak does lead to considerable errors. The use of much fewer samples but with the peak much further away from zero (5.12b) leads to more accuracy.

The width of the filtered function and its positioning relative to time $t = 0$ are limited by the following factors:

i) The width is determined by the filter cut-off frequency, f_c, which, in turn, is related to the time step by $f_c \leqslant \frac{1}{2\Delta t_{out}}$.

ii) The geometry of the problem fixes the position of any peaks in the time responses.

In the wire geometries considered in Chapter 6 this results in peaks which are close to $t = 0$. This, combined with the fact that $\frac{\Delta t_{out}}{\Delta t_{in}} = 10$ means that significant portions of the filtered function will be truncated and errors are likely to occur in any convolved response.

In an attempt to reduce these truncation errors various windowing functions were applied to the filtered

Figure 5·9 Usual form of 2D or 3D response

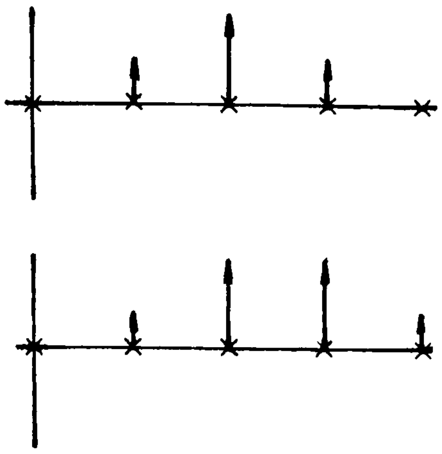

Figure 5·10 Frequency responses of 8m wire

a) No diakoptics

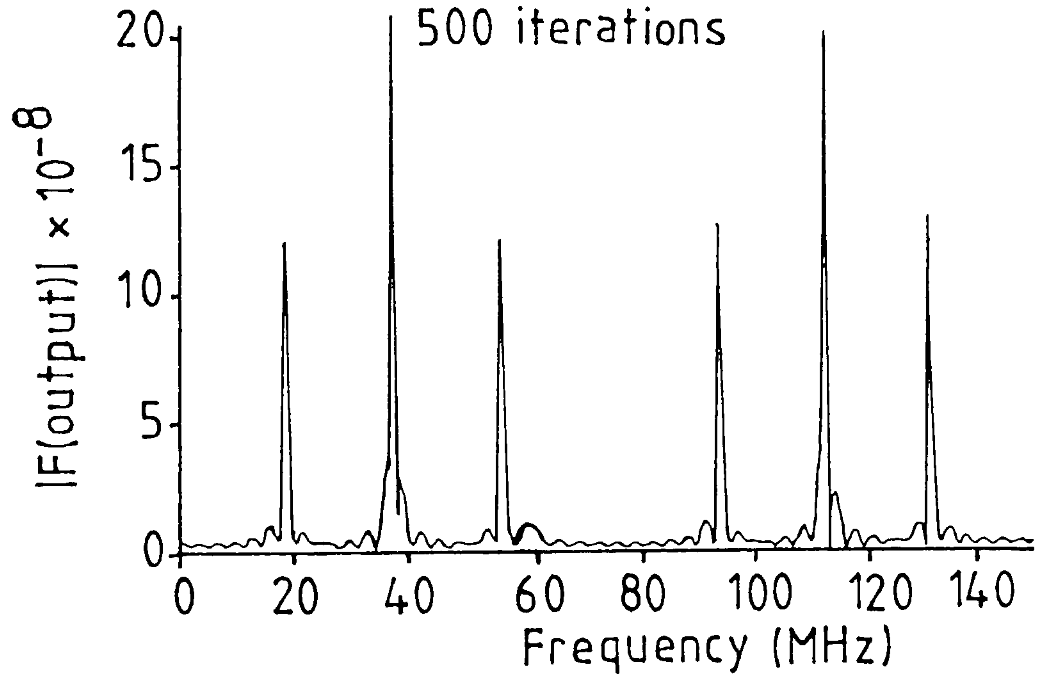

b) TDD

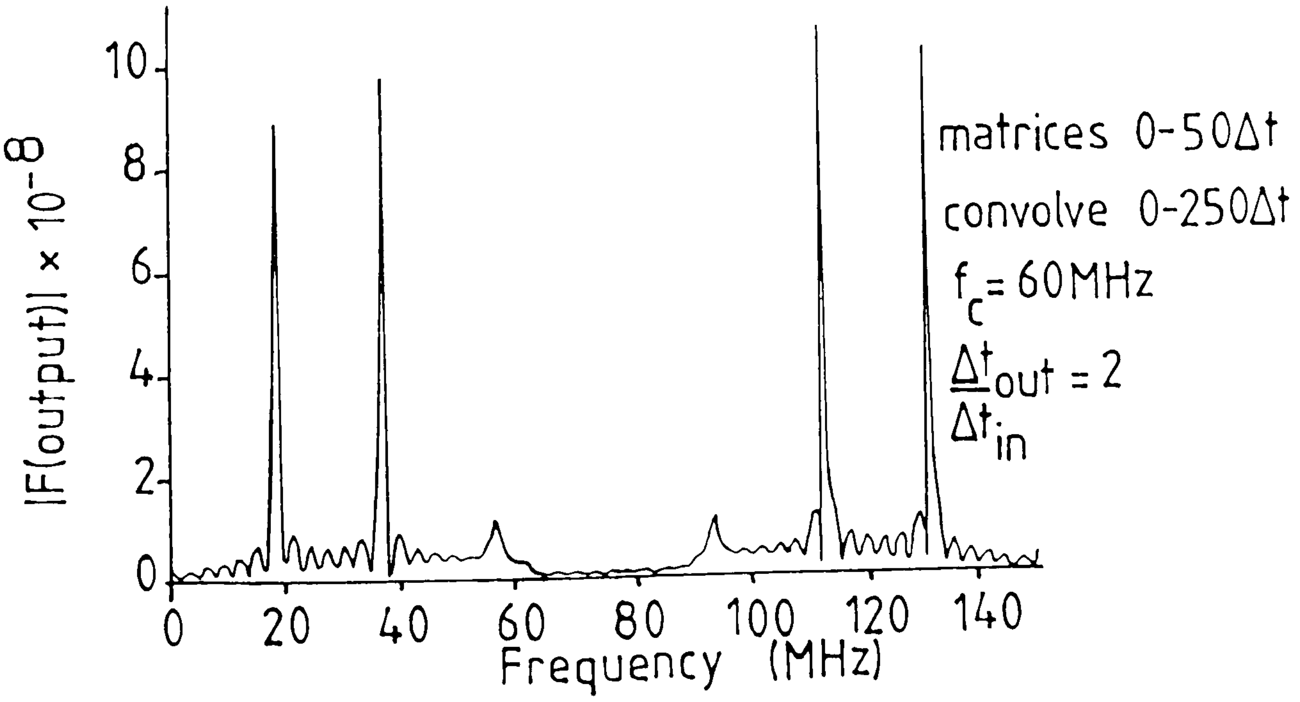

Figure 5·11 Frequency responses of 16m wire

a) No diakoptics

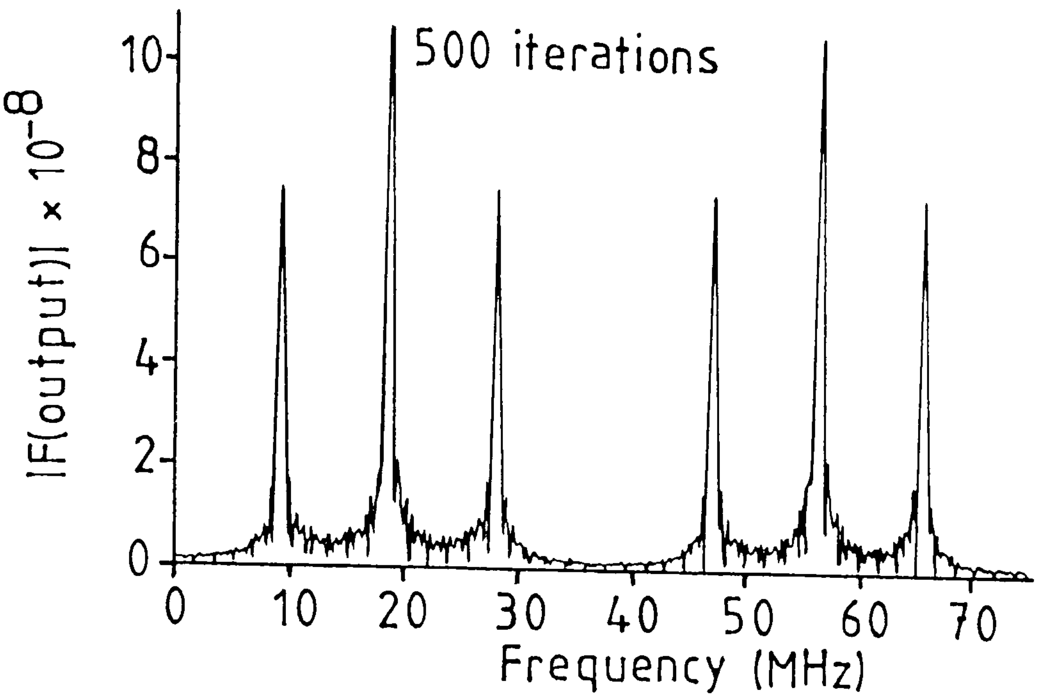

b) TDD

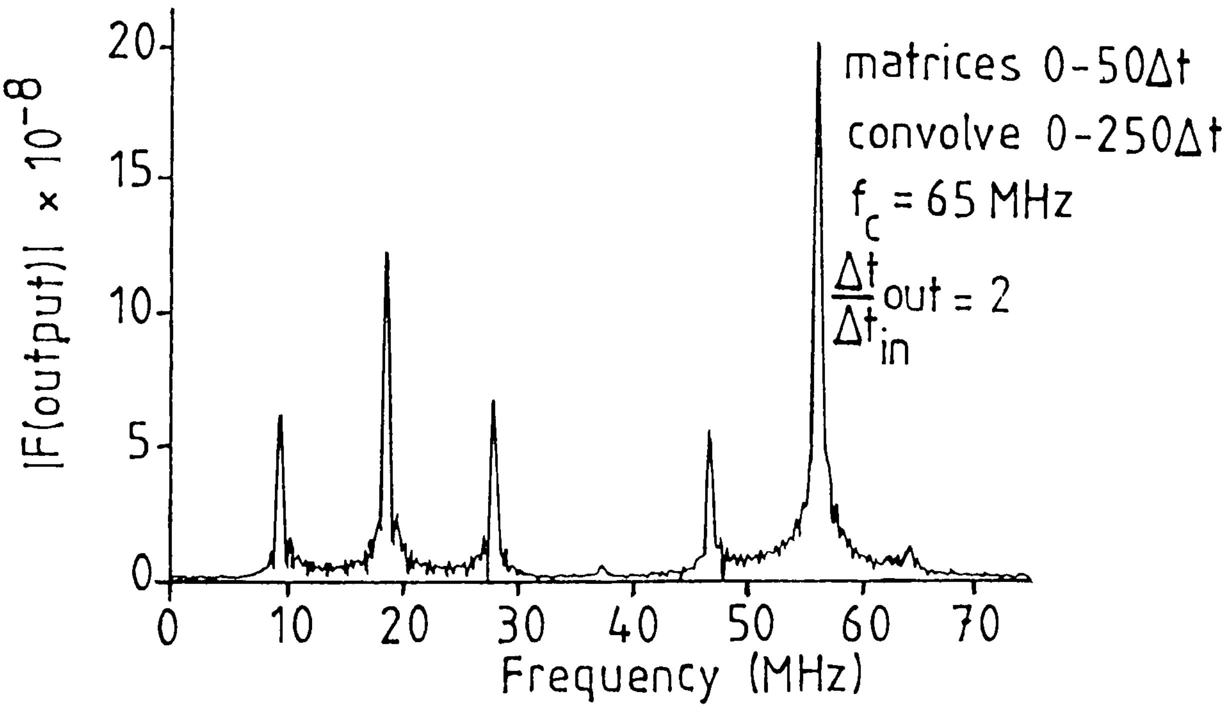

Figure 5·12 Sampled sin(x)/x function

a) Worse

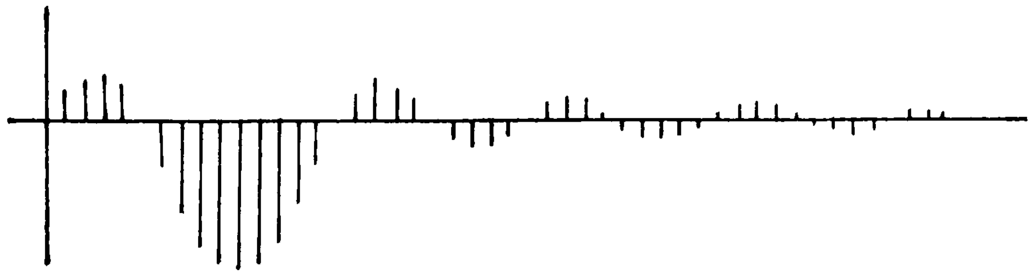

b) Better

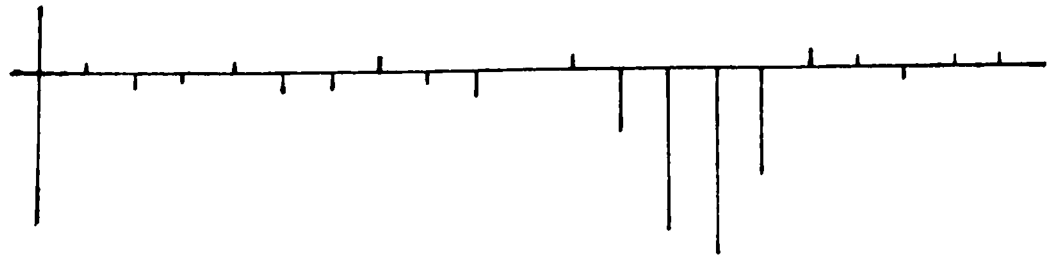

responses of the one-dimensional example. The following functions were tested:

Von Hann Raised Cosine (86,88)
Hamming Window (86,88)
Blackman Window (88)
Kalman Filter (87)

None of these functions significantly reduced the errors occurring due to truncation because it is the fact that truncation (in any form) is taking place near to $t = 0$ that is causing the errors.

One possible way of avoiding this problem is to include more of the filtered function in the response, i.e. truncate before $t = 0$. This is, of course, non-causal and the use of 'negative time' does lead to other errors.

Consider the frequency response of the previously used 4m long wire shown in figure 5.13a. If the impulse responses of the substructures are filtered and resampled and truncated at $\pm 100\Delta t_{out}$ then joined with convolutions performed over a **fixed** time window (i.e. the convolution is always performed over the range $-200\Delta t_{out}$ to $350\Delta t_{out}$) the result shown in figure 5.13b is obtained. This contains a number of errors: the resonance is at the wrong frequency and has the wrong amplitude. Figure 5.14 shows how this error occurs. If a time function has a length as shown (a) then after convolution with a similar function the result is defined over a time length twice as long (b).

Figure 5.13 Frequency responses of 4m wire

a) No diakoptics

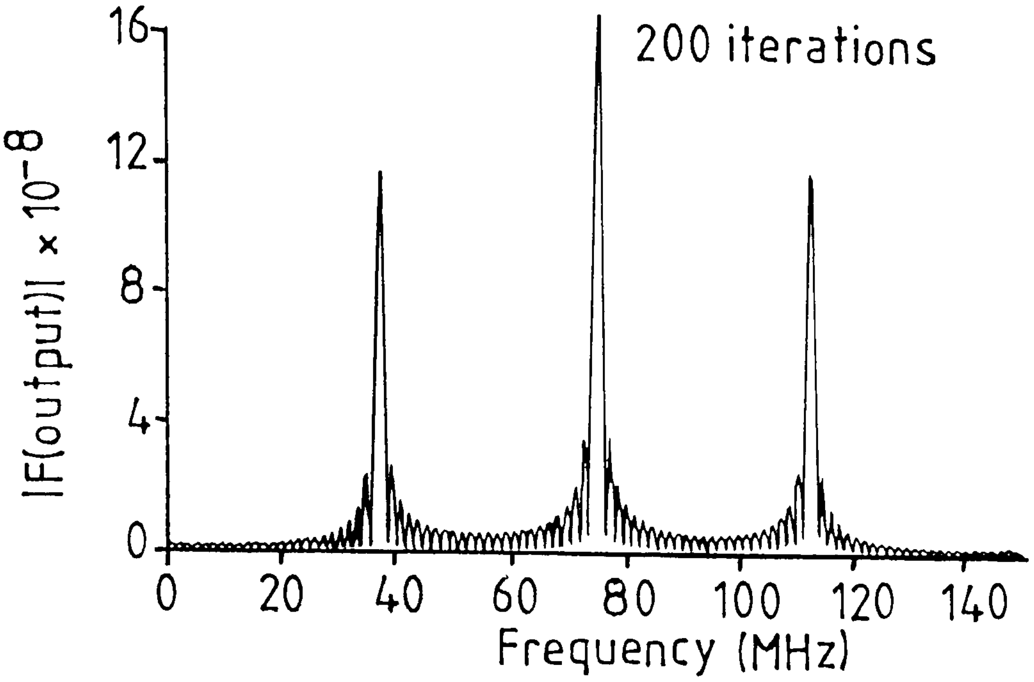

b) Incorrect use of 'negative time' in TDD

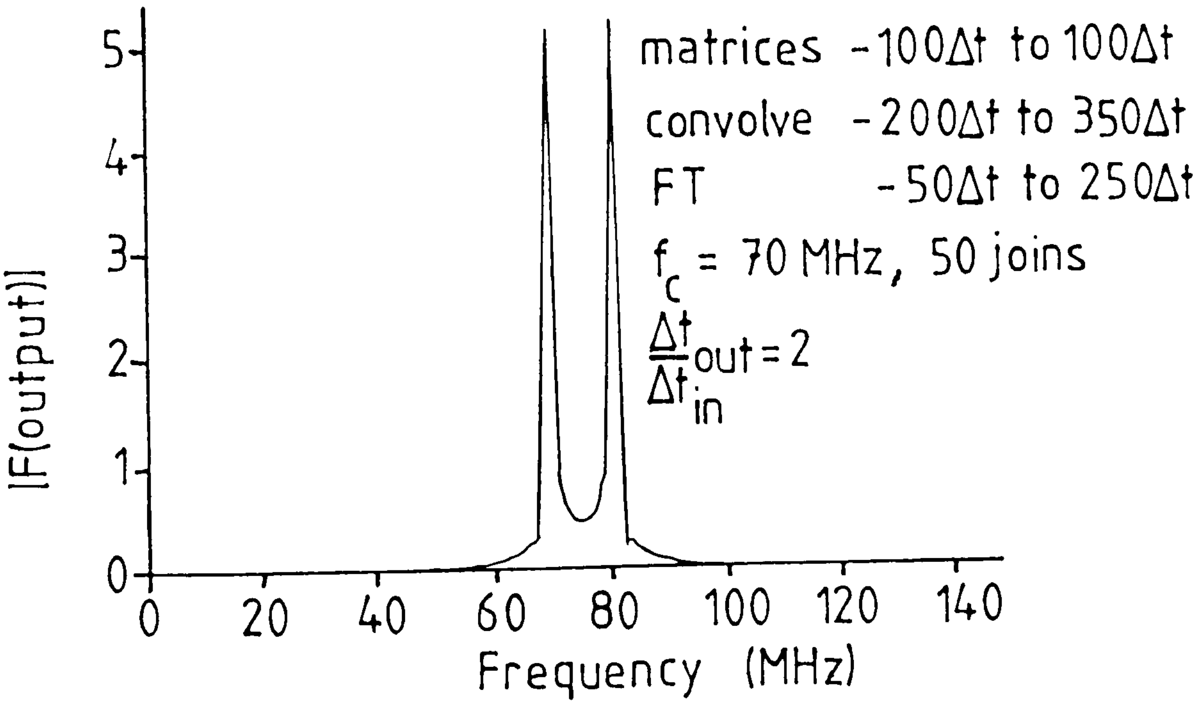

Figure 5·14 Effect of truncation on convolutions using 'negative time'

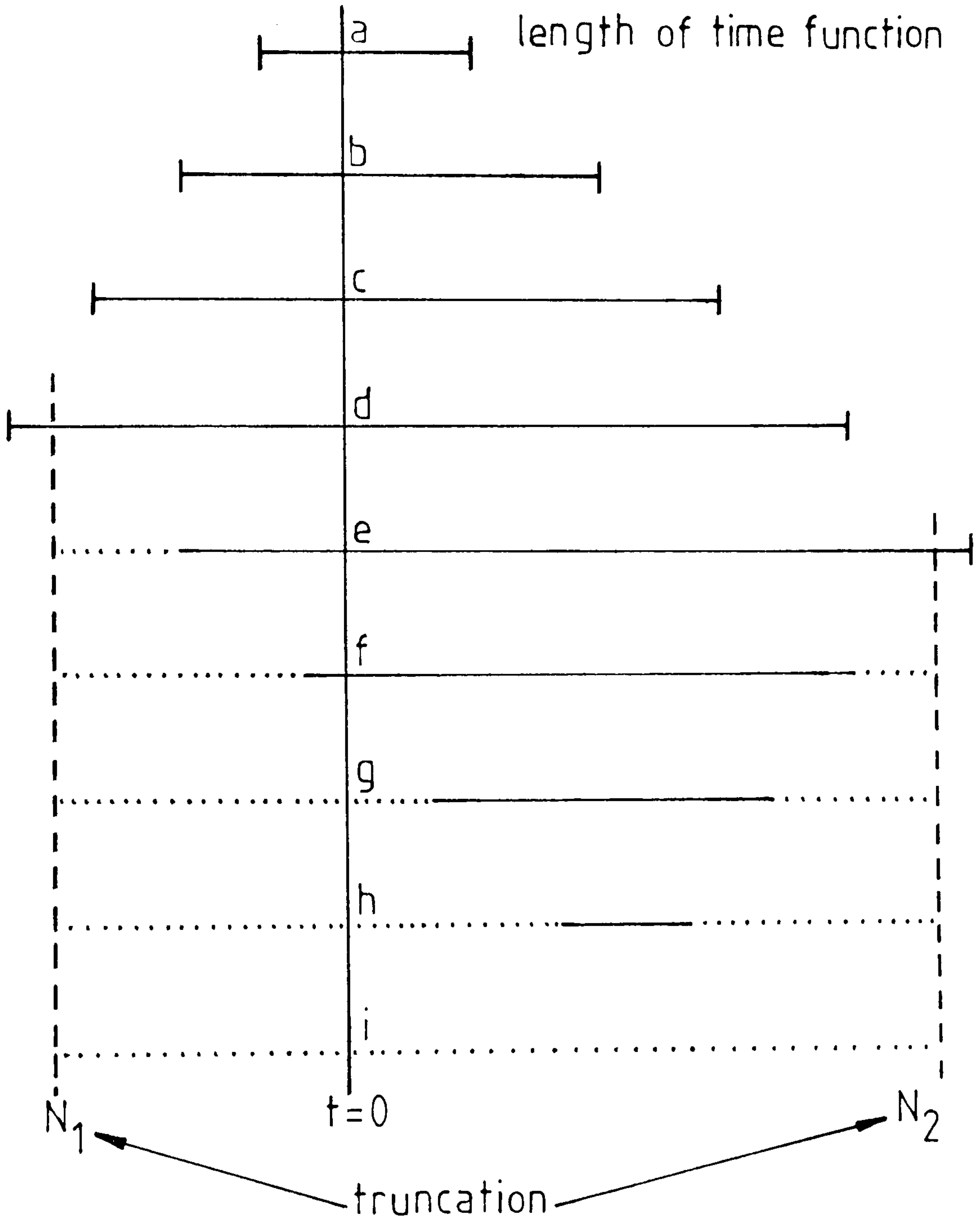

After n convolutions (n joins in the diakoptic process) the length of the function should be n x (original length). But at some stage (d) the process is truncated. At the next convolution, part of the data is missing and so the resulting output contains errors (...) at all points where a multiplication with this data is expected. This error occurs at both ends of the time window (f). At subsequent convolutions erroneous data is used to obtain the response. Therefore the errors extend further into the rest of the response until (i) all parts of the data are subjected to some deviation entirely due to the truncation of the convolution process. If the time-domain function naturally decays to zero at the truncation times then these errors will be small. But for a sin (x)/x function this decay is not fast enough to prevent serious errors occurring as was shown in figure 5.13b.

To reduce the errors described above it is necessary to convolve over all the available data always. In doing this, the length of the time response becomes larger with the number of convolutions performed. If this is done, results like those shown in figure 5.15 can be obtained. These frequency responses show that the first resonance is at the same frequency, width and amplitude as the no diakoptic solution. However, there are unexpected peaks of incorrect widths to be resonances located near to the cut-off frequency of the filter. After investigating further conditions where the cut-off frequency and the truncation times were varied (60 MHz $\leqslant f_c \leqslant$ 75 MHz,

Figure 5·15 Corrected use of 'negative time' in TDD for 4m wire

a)

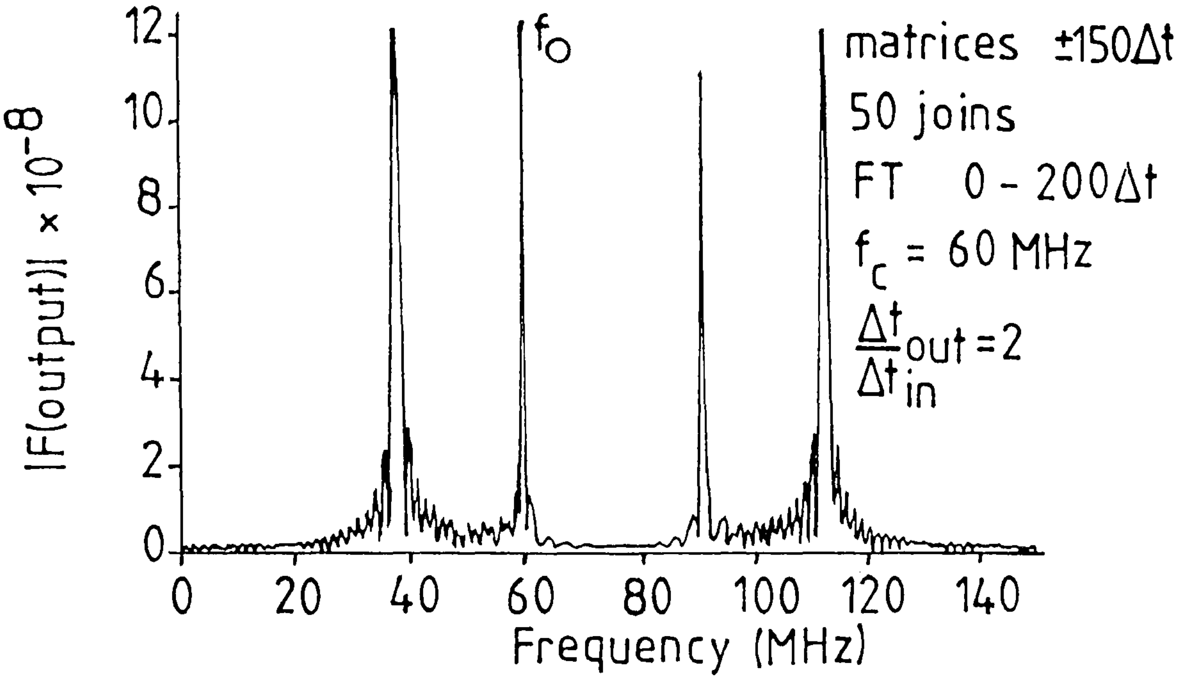

Empirically $f_o = f_c - \frac{1}{2T}$

2T = window size (eg −25Δt to 25Δt = 50Δt)

b)

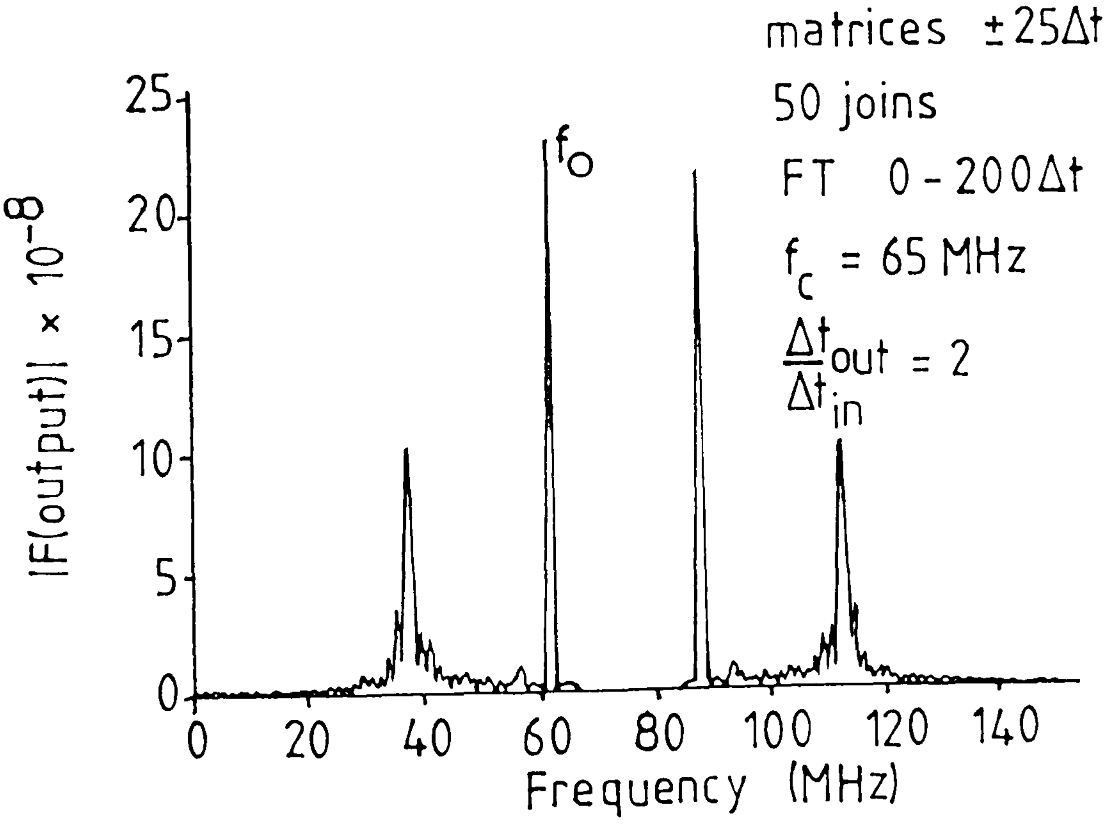

truncation ± 75 Δt, ± 100Δt, ± 150Δt) the expected resonances were found to be correct always. The unexpected peak, at a frequency f_o, was empirically found to be:

$$f_o = f_c - \frac{1}{2T} \tag{5.20}$$

(where 2T is the window size, for ± 100Δt, $2T = 200\Delta t$). This unexpected peak probably occurs because there is still some truncation in the process. But because the original response has been truncated (usually by using a rectangular window) there are slight errors in the final response. Although these errors are minimised by the use of full length convolution, the frequency corresponding to the window $(\frac{1}{2T})$ is emphasised by each convolution. Thus the frequency response is only valid upto f_o (but note that as $T \to \infty$, $f_o \to f_c$).

5.4 Frequency Domain Diakoptics (FDD)

5.4.1 Modifications to the Process

In many applications the final result is required in the frequency domain. Therefore it may be simpler to actually perform the diakoptic joining in the frequency domain.

The convolution theorem states:

$$g(t)*h(t) \rightarrow G(w)H(w) \tag{5.21}$$

(where → means "Fourier Transforms to").

Thus it is possible to Fourier Transform the four characteristic matrices describing a substructure into complex frequency components. The diakoptic joining process for the simple one-dimensional case (equations (5.8) to (5.10)) becomes:

$$F({}^{A}_{o}\underline{V}^{r}) = F({}^{A}\underline{V}_{ex}); \quad F({}^{B}_{o}\underline{V}^{r}) = F({}^{B}\underline{V}_{ex}) \qquad (5.22)$$

$p = 1$

repeat

$$F({}^{A}_{p}\underline{V}^{i}) = F({}^{B}_{p-1}\underline{V}^{r}); \quad F({}^{B}_{p}\underline{V}^{i}) = F({}^{A}_{p-1}\underline{V}^{r}) \qquad (5.23)$$

$$F({}^{A}_{p}\underline{V}^{r}) = F({}^{A}_{p}\underline{V}^{i}) x F({}^{A}\underline{S}); \quad F({}^{B}_{p}\underline{V}^{r}) = F({}^{B}_{p}\underline{V}^{i}) x F({}^{B}\underline{S}) \qquad (5.24)$$

$p = p + 1$

until $p >$ iteration limit

where F(a) is the Fourier Transform of (a);

$$F(a)\Big|_{w=2\pi f} = \sum_{i=0}^{N} {}_{i}a e^{j2\pi f i \Delta t} . \Delta t \qquad (5.25)$$

and F(a) x F(b) is a termwise complex multiplication of the frequency responses.

The total frequency spectrum incident on a substructure is just the sum of all such spectra (given by equation (5.23)). The final frequency spectrum is then found by multiplying this total incident spectrum with the port to output matrix and adding the source to output thus:

$$F({}^{A}\underline{R}) \quad = \quad F({}^{A}_{p}\underline{V}^{i}_{TOT}) \times F({}^{A}\underline{O}) + F({}^{A}\underline{V}_{op}) \qquad (5.26)$$

5.4.2 Frequency Domain Diakoptics Applied to the One-Dimensional Case

Using the above method the simple one-dimensional line (figures 5.1 and 5.2) can be solved in the Frequency Domain. The resulting frequency responses can be compared with the no diakoptic solution shown in figure 5.13a. Figure 5.16a shows the response obtained using FDD with equal substructures. The response is identical to that shown in figure 5.13a. If unequal substructures are used, as shown in figure 5.16b the response of figure 5.16c is obtained. Again this is identical to that shown in figure 5.13a.

5.4.3 3D Results

The Frequency Domain Diakoptics can be used in three dimensions and a simple example is shown in figure 5.17. In this example both substructures have four cut transmission lines and therefore the sizes of the scattering matrices are:

$\underline{S}$	4 x 4
$\underline{O}$	1 x 4
$\underline{V}_{ex}$	1 x 4
$\underline{V}_{op}$	1 x 1

Figure 5·16 4m (1D) wire solved using FDD

a) Equal substructures

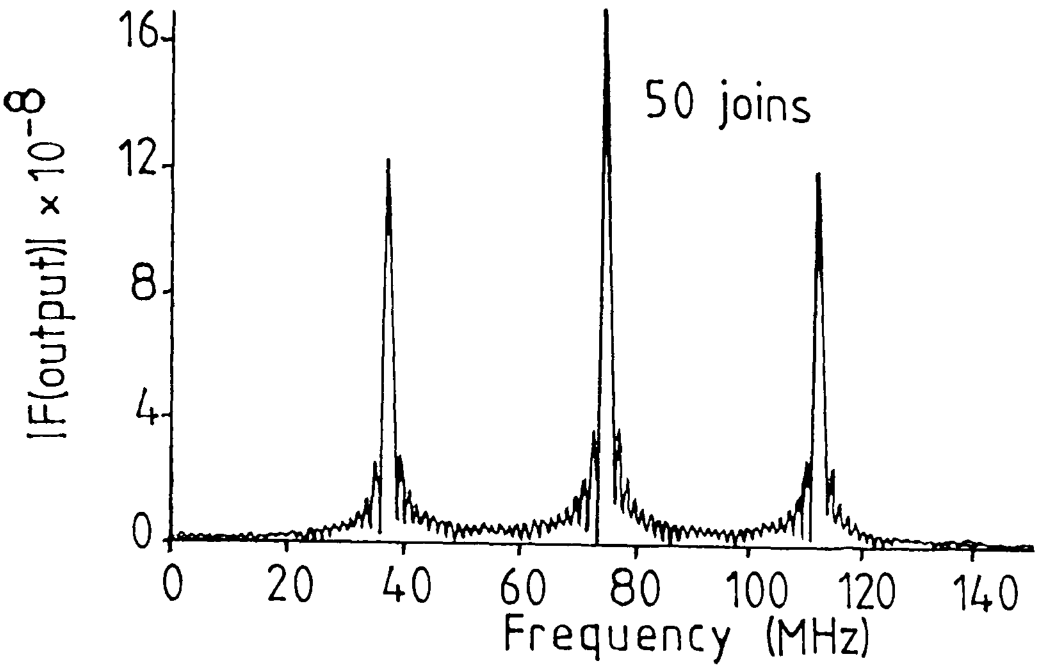

b) Description of unequal substructures

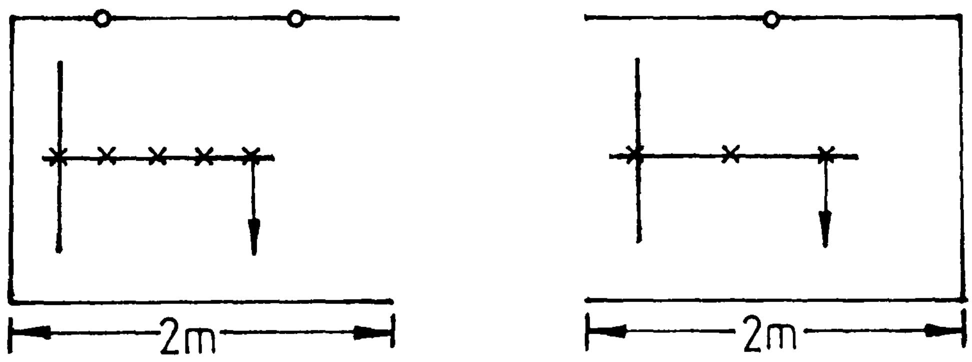

c) Unequal substructures

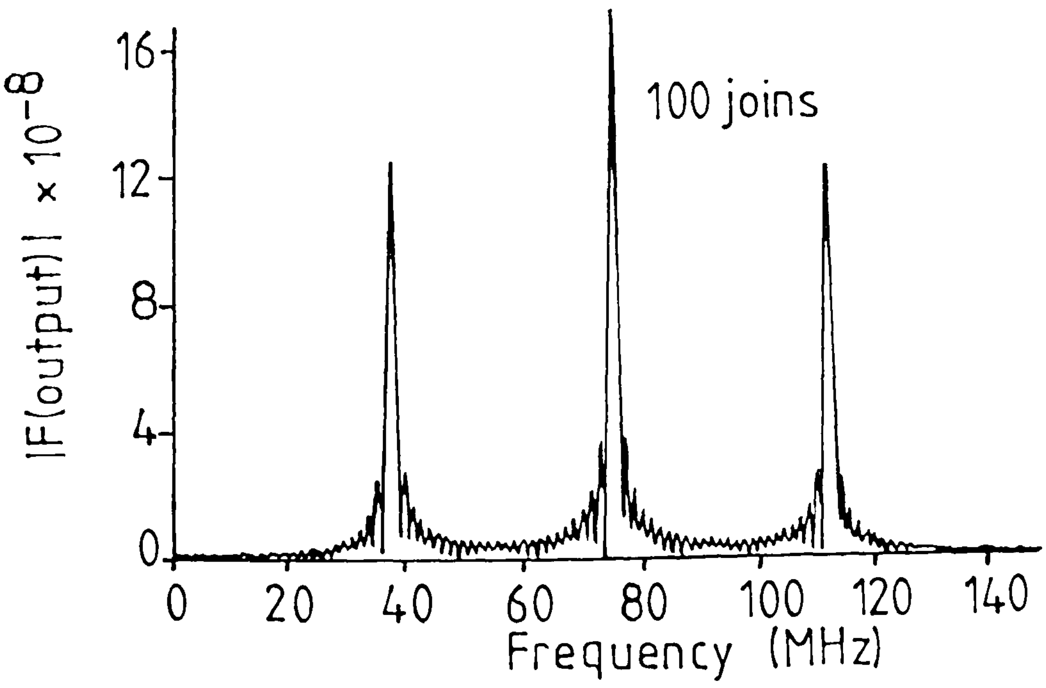

Figure 5·17 Geometry of 4×2×2 test cavity

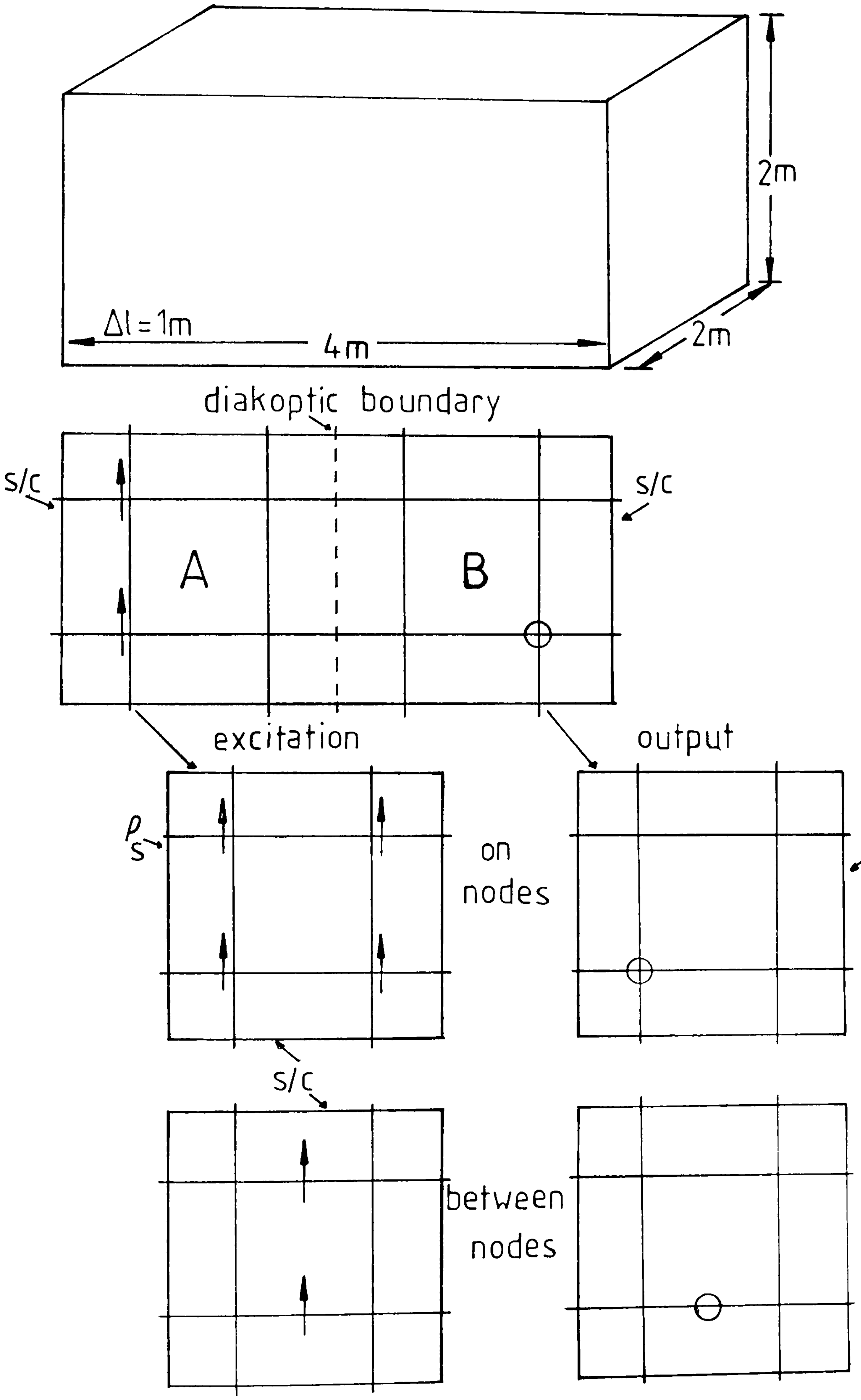

where each element of the matrix is a vector.

Using the excitation and output conditions shown in the figure the Frequency Domain, Time Domain and no diakoptic methods were compared. Figures 5.18, 5.19 and 5.20 show that some of the FDD results contain errors. Examination of the method and the suite of programs used to compute the results revealed no obvious mistakes. However, a difference was found in the way time and frequency domain results were evaluated. In the time domain the length of the time response increases with the number of joins, as shown earlier. The time response is only valid upto the time length of the original matrices. By truncating the final time-domain response and then Fourier Transforming the correct frequency response is obtained.

In FDD this process of an increasing time length is still happening even though the method proceeds in the Frequency Domain. The final frequency response therefore corresponds to a large time domain length, and all the terms beyond the time length used in the matrices contain errors. To remove these errors a time domain truncation is required. In the frequency domain this is a convolution with a sin(x)/x function. From figure 5.21 this function is:

$$G(w) = \int_{-T}^{T} 1.e^{-jwt}\,dt$$

$$= \frac{2T\ \sin(wT)}{wT} \qquad (5.27)$$

Figure 5·18 Frequency responses of figure 5·17 geometry- on nodes $\rho_s = o/c$

a) No diakoptics

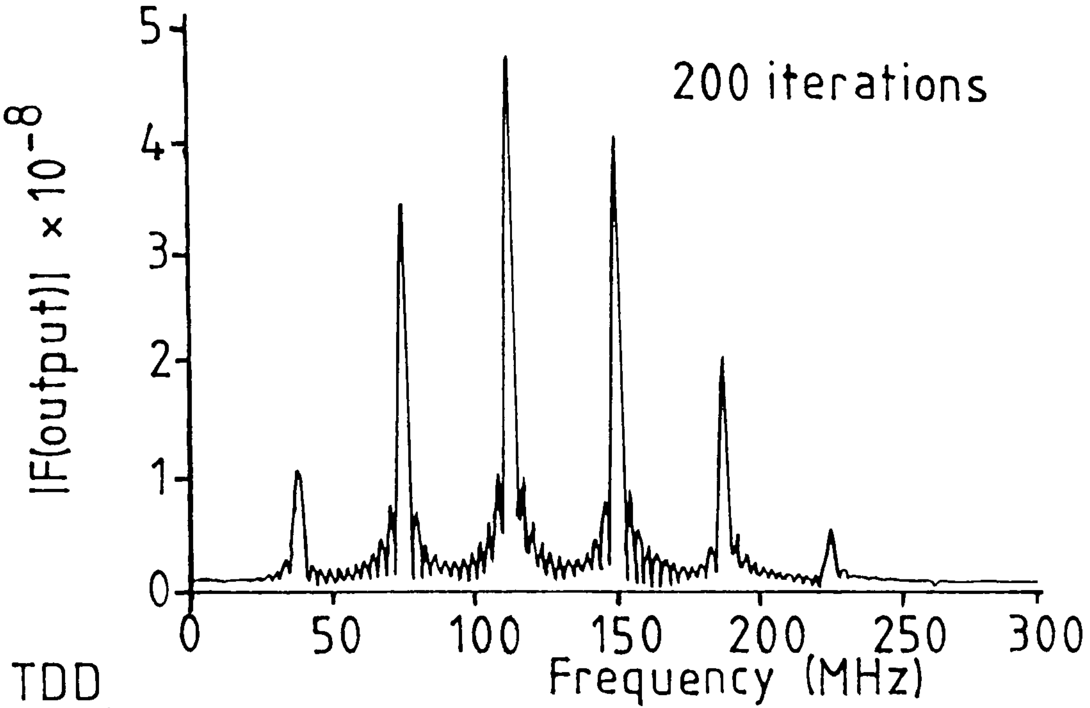

b) TDD

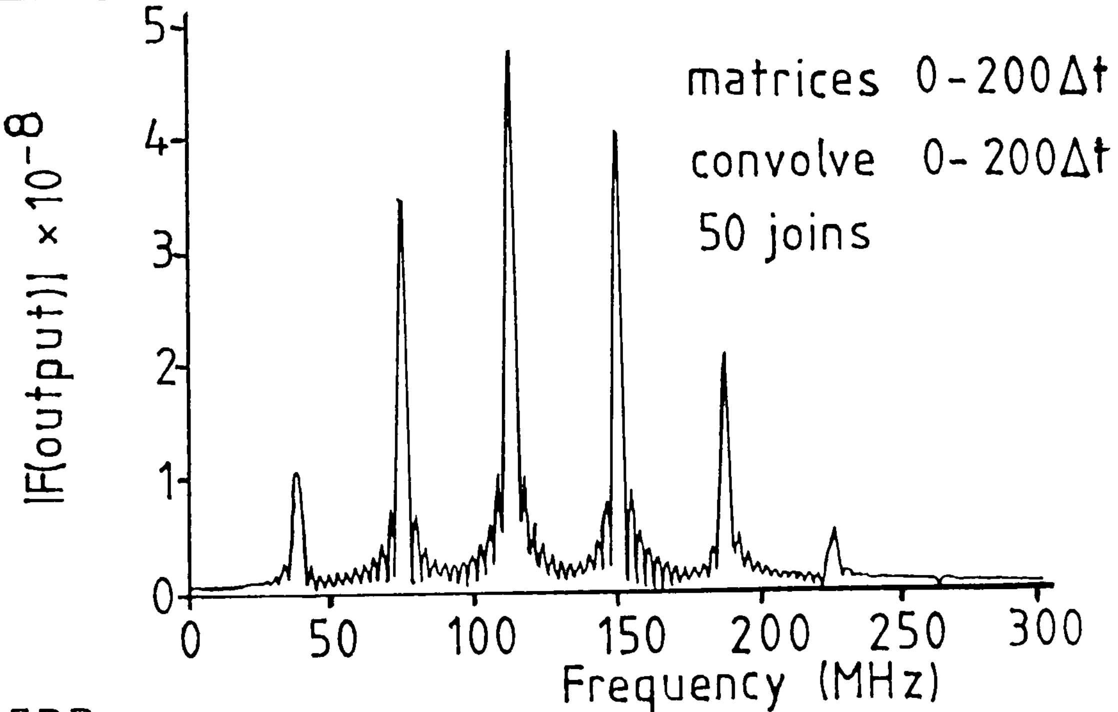

c) FDD

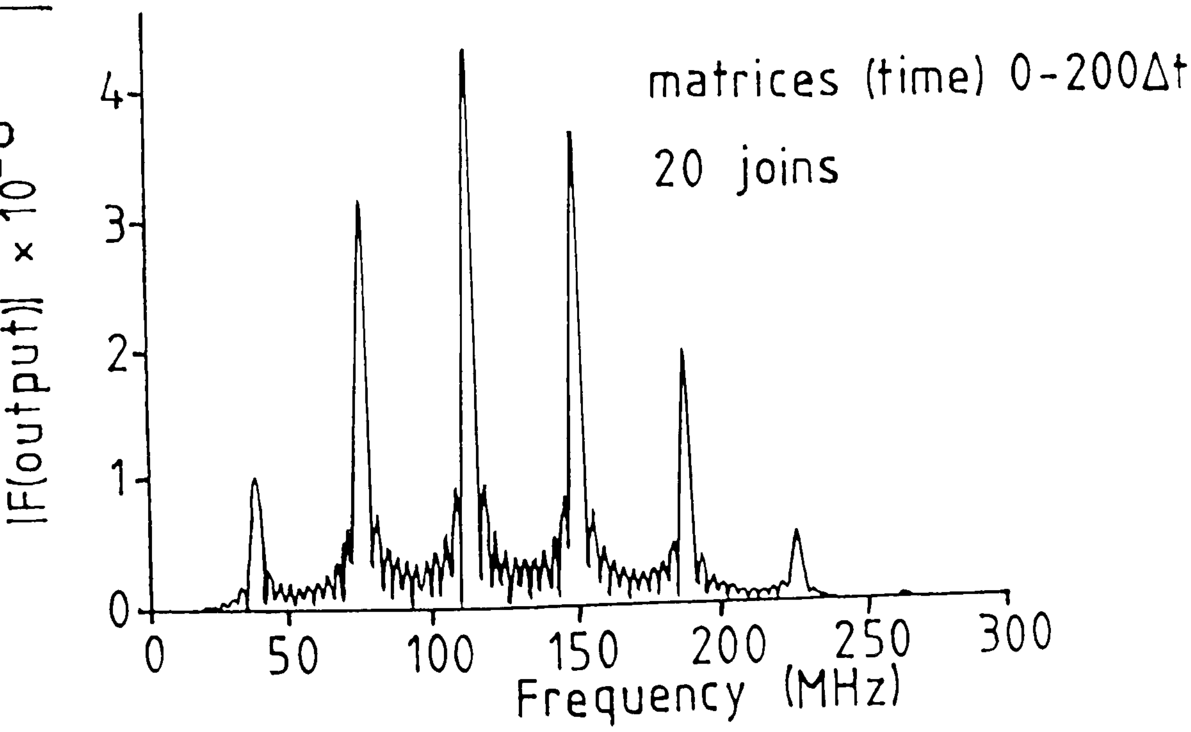

Figure 5·19 Frequency responses of figure 5·17 geometry - on nodes $\rho_s = s/c$

a) No diakoptics

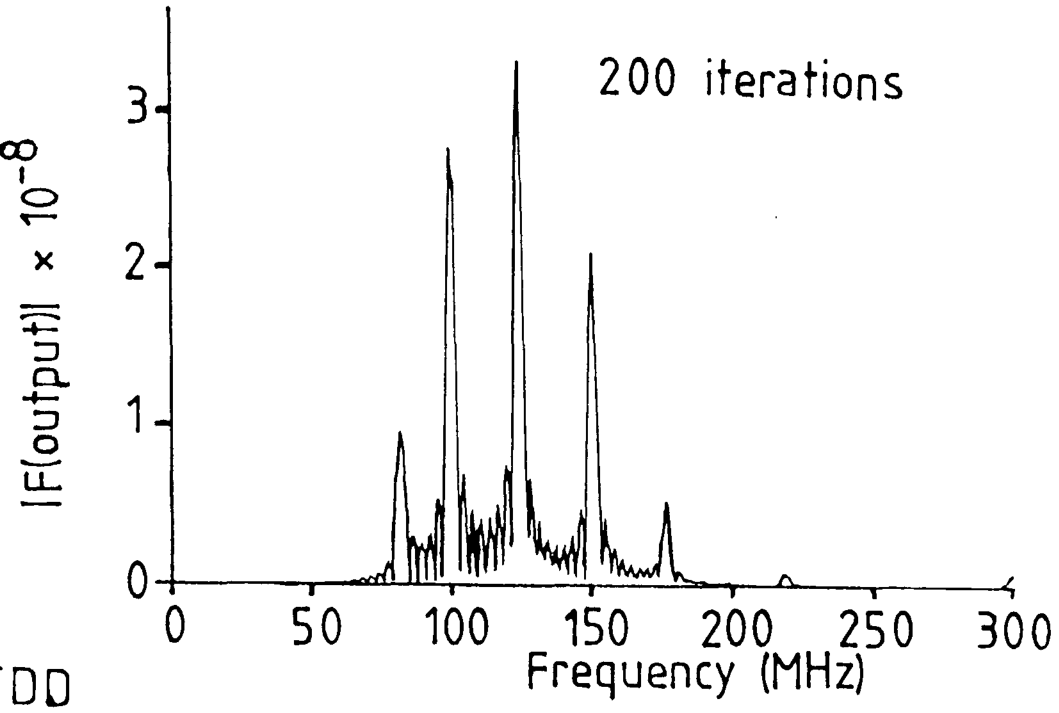

b) TDD

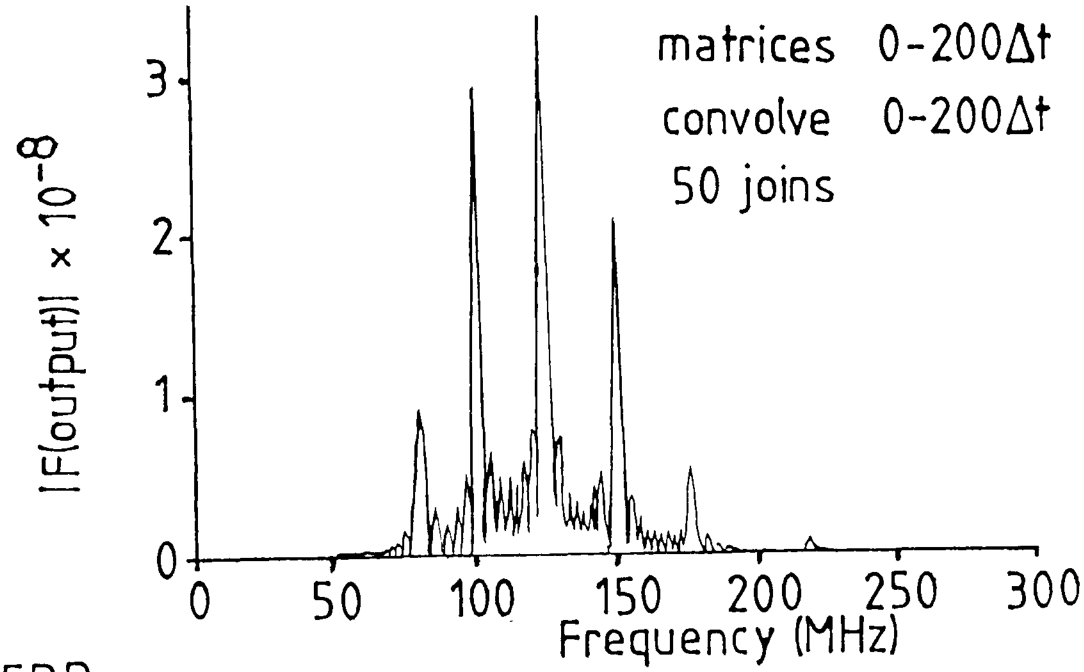

c) FDD

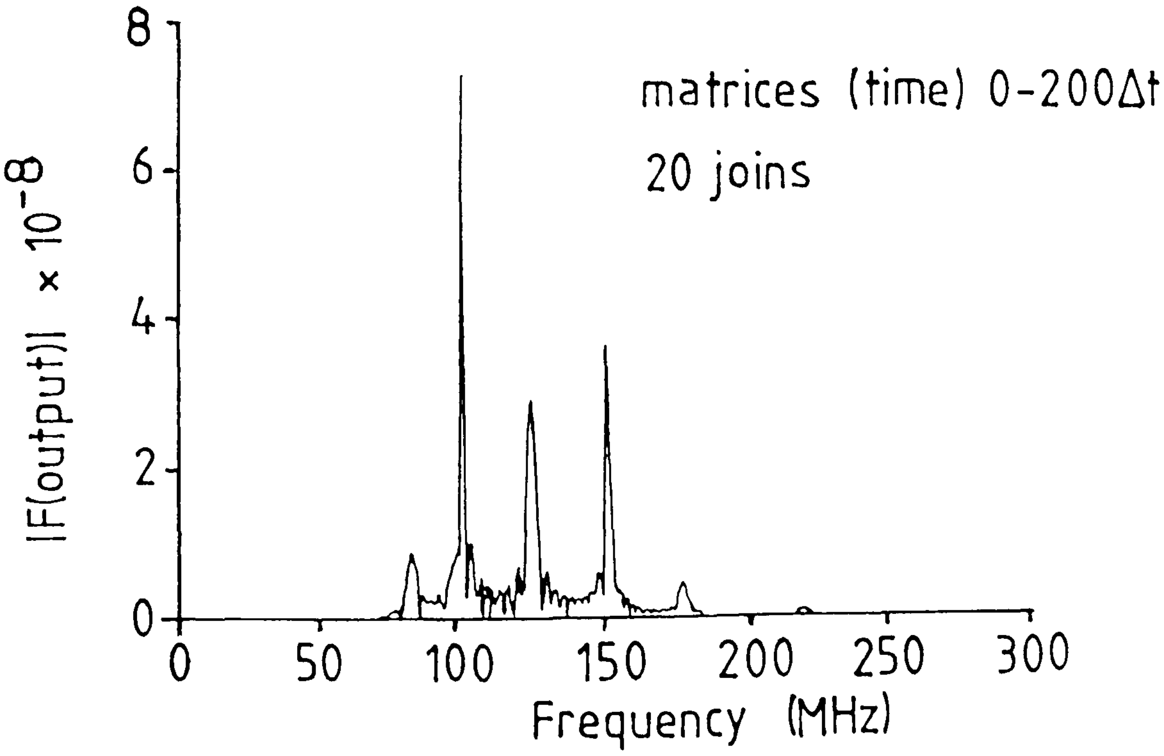

Figure 5·20 Frequency responses of figure 5·17 geometry-between nodes $\rho_s = s/c$

a) No diakoptics

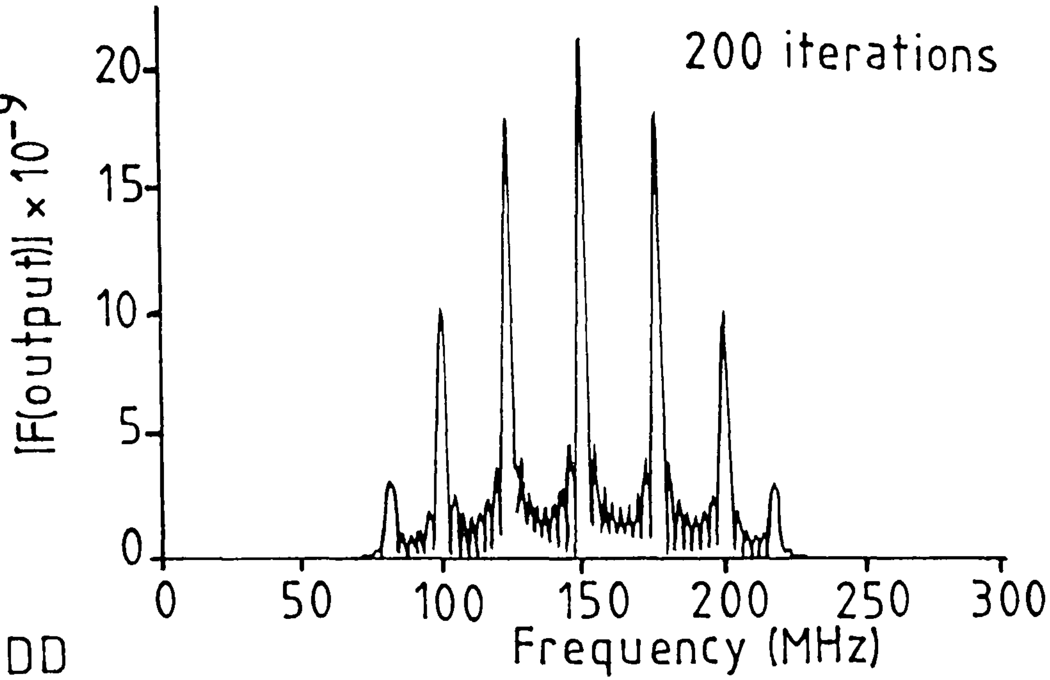

b) TDD

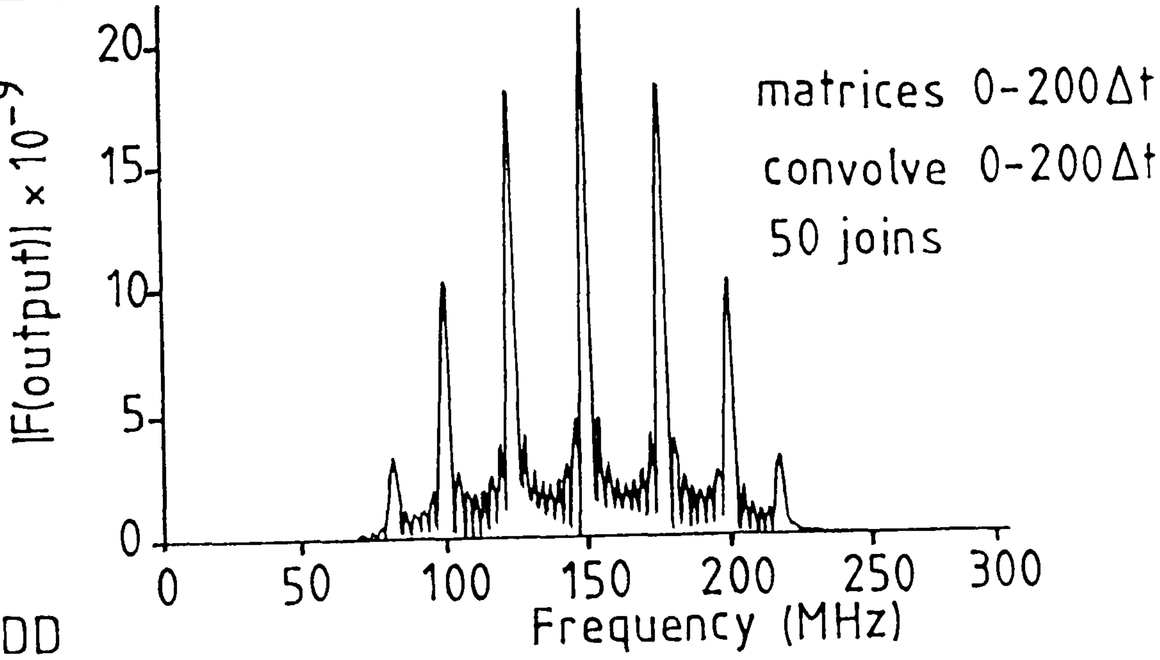

c) FDD

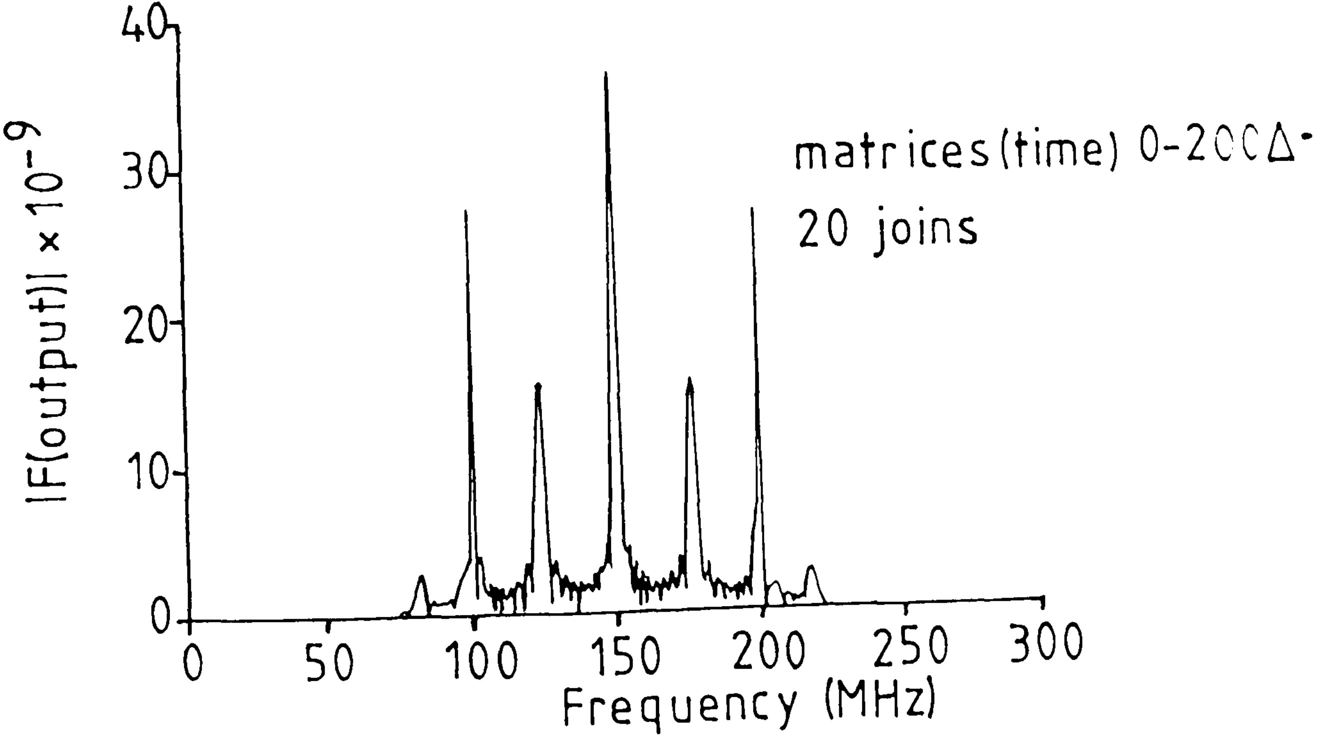

Figure 5·21 Time domain truncation

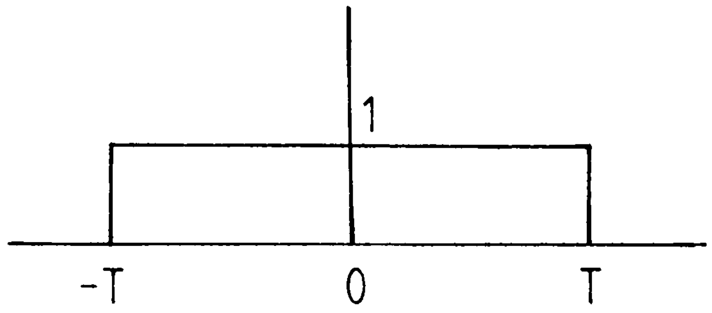

Figure 5·22 Geometry of 10×2×2 test cavity

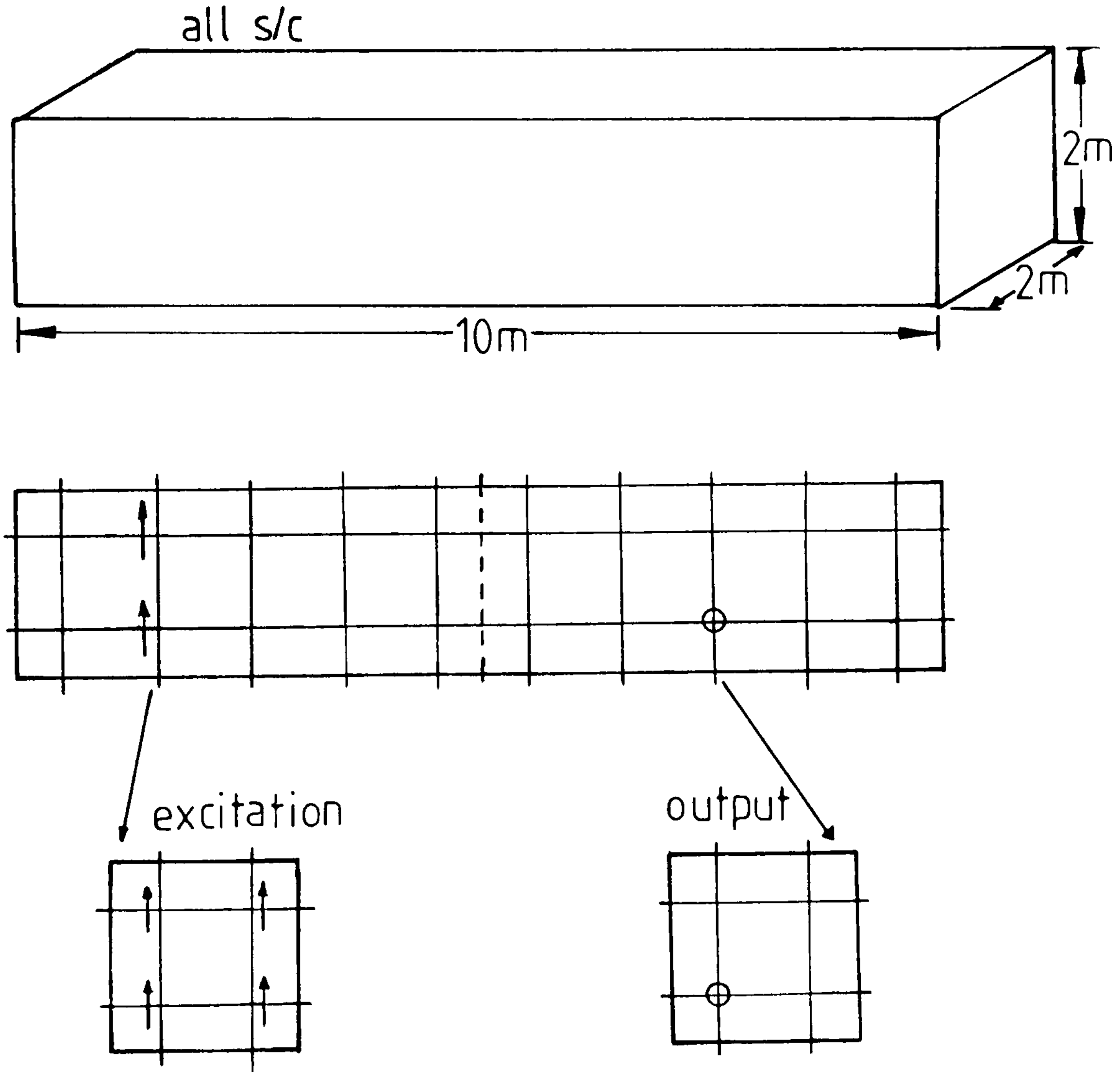

However, even using this time-domain truncation does not guarantee that the response is corrected as shown for the geometry in figure 5.22 by figure 5.23. The cause of this error is frequency domain aliasing, that is the frequency steps are too far apart. If the time length of the final response is examined it is equal to (time length of original matrices) x (number of joins). Therefore, from the sampling theorem:

$$\Delta f \leqslant \frac{1}{(\text{original time length})\text{x}(\text{number of joins})} \qquad (5.28)$$

When this condition was met, the correct results, as shown in figure 5.24 were obtained.

5.5 Discussion

The diakoptic method when used in TLM presents no problems providing no approximations are made. However, in most cases, approximations must be made. This applies even when the substructures are solved using the same mesh step. This is because some form of time domain truncation is always required. The joined result is only accurate up to this truncation point.

If different mesh sizes are used in different substructures then it is necessary for time and spatial approximations to be made. It is these time domain approximations which can lead to substantial errors in the diakoptic process. The use of filtering and resampling requires care. The truncation of the filtering near to

Figure 5·23 Frequency responses of figure 5·22 geometry

a) No diakoptics

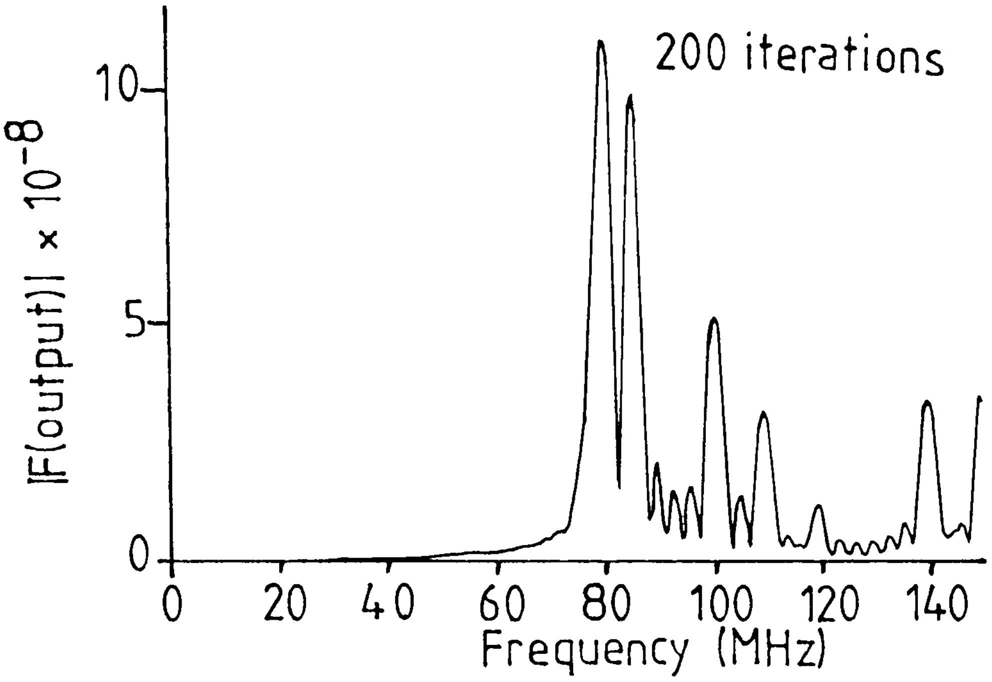

b) FDD

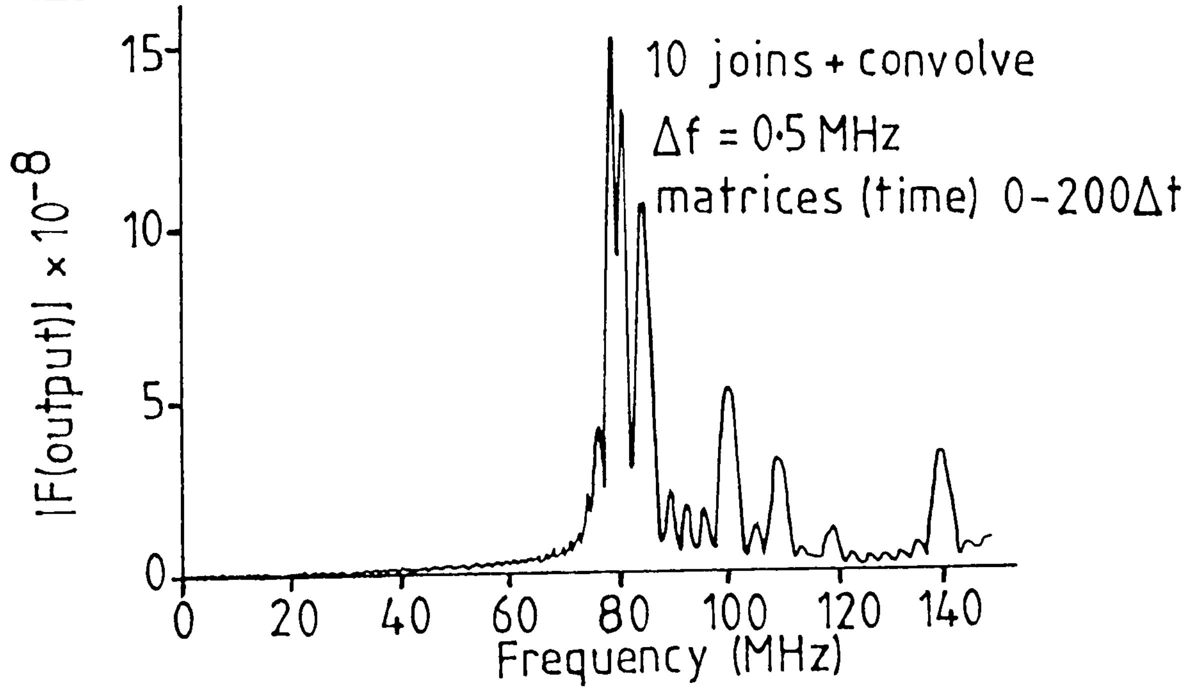

c) FDD

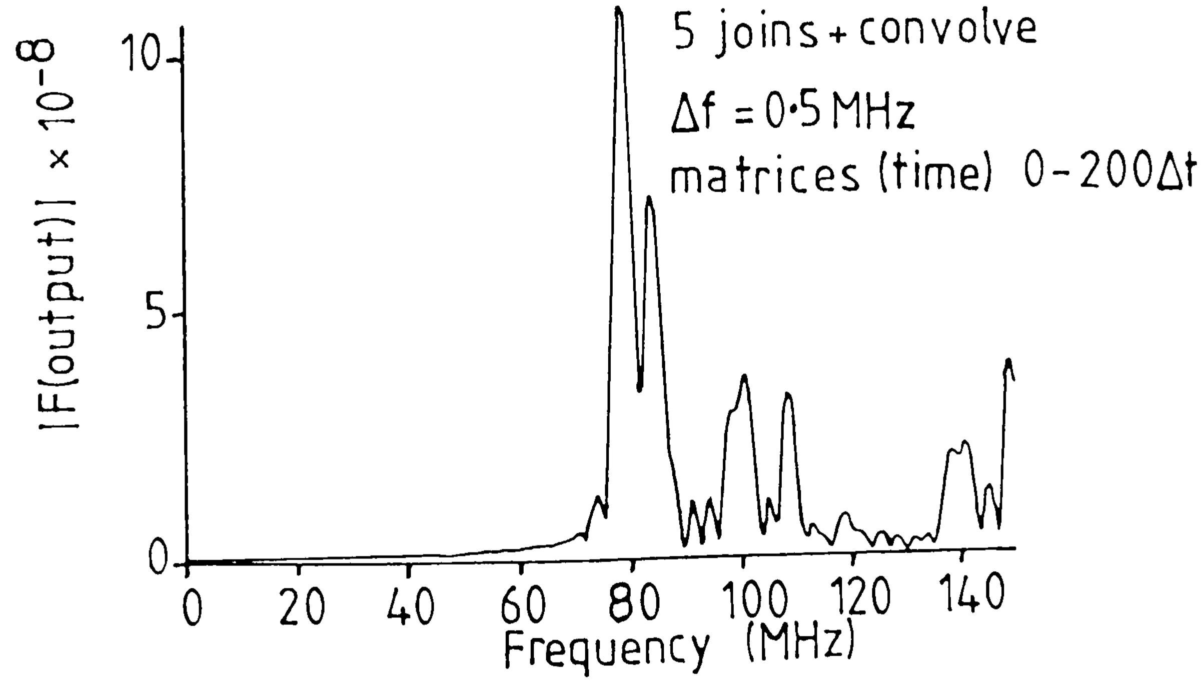

Figure 5·24 Frequency responses of figure 5·22 geometry - FDD

a)

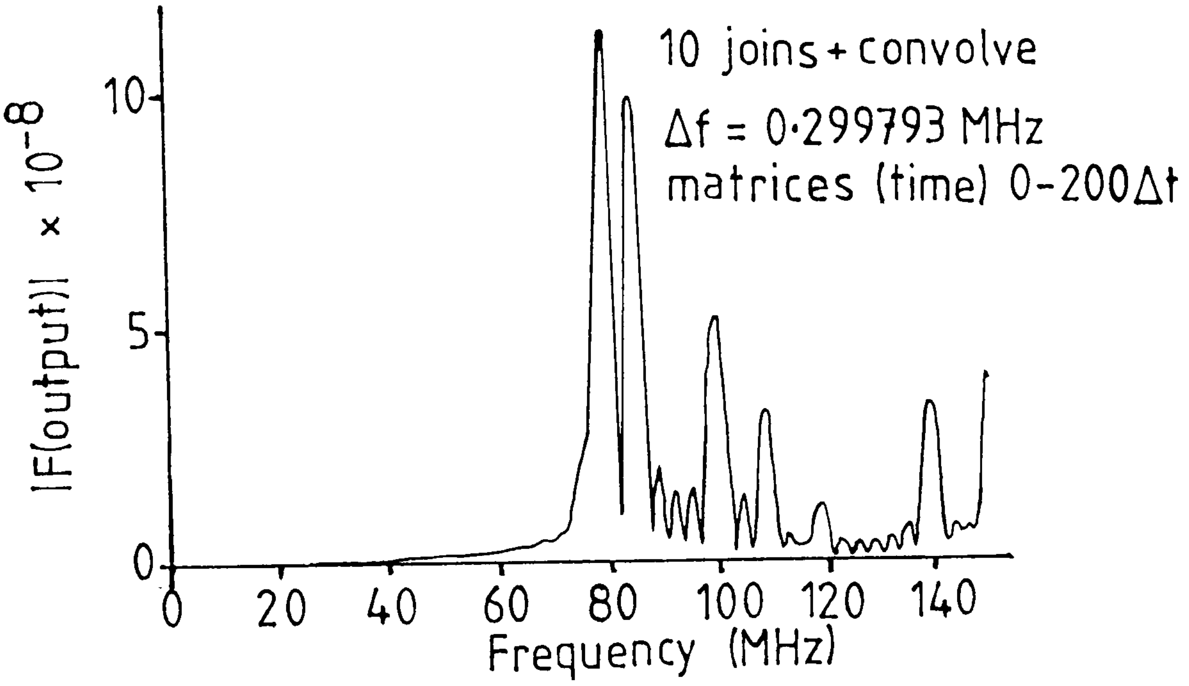

b)

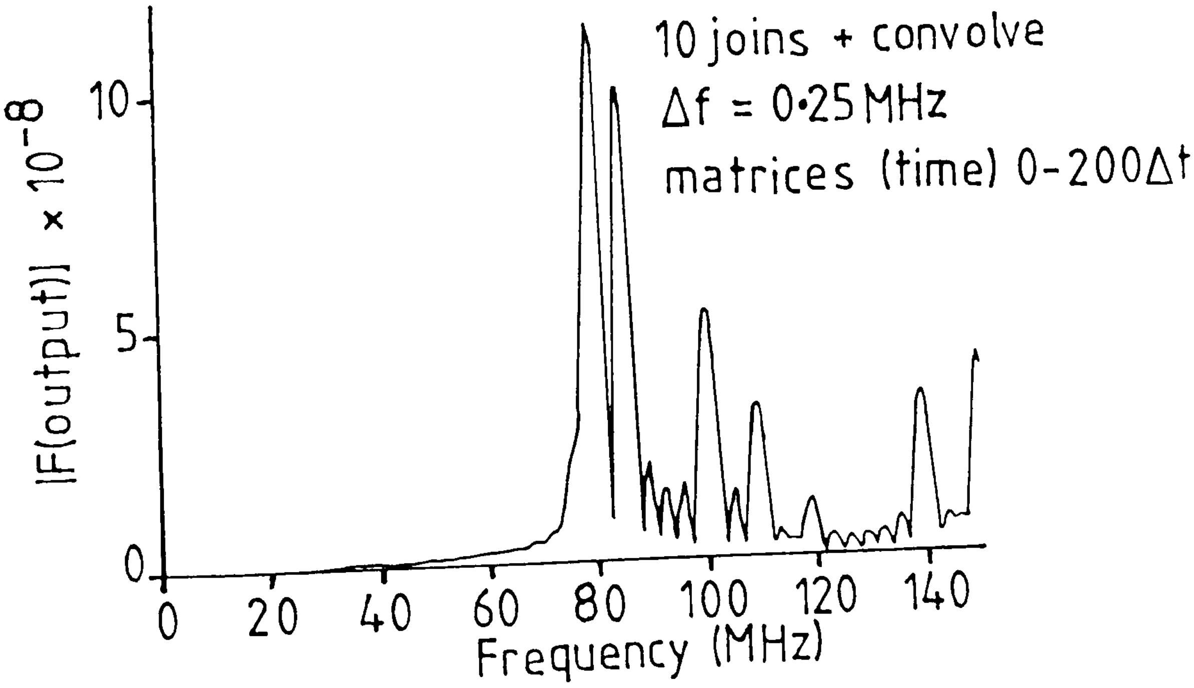

t = 0 should be avoided as this causes incorrect pulse shapes to be generated.

Caution is required when incorporating negative times into a convolution process. To reduce errors it is important to use **all** of the time domain information and avoid further truncation of the data. When this is done unexpected peaks will be found in the final response, although frequencies below the peaks are correct.

Frequency Domain Diakoptics has been developed. It is necessary to perform a time domain truncation on the frequency domain data obtained to remove inaccurate time terms. To achieve this the frequency response must be convolved with the Fourier Transform of a time domain truncation. This requires the frequency steps in the response to be much less than the Nyquist rate. The Fast Fourier Transform (FFT) is not suitable for transforming the time domain scattering matrices. This is because the FFT produces frequency steps at the Nyquist rate. Whilst this is correct for normal Fourier Transforms the problem with the FDD is that the Transform of the final response has a Nyquist rate much less than that of the matrices. Therefore a Discrete Fourier Transform (DFT) must be used. The DFT is a slow process as it uses convolutions and evaluates sines and cosines, but its frequency step can be freely chosen.

Figure 5.25 gives an indication of the execution time and storage required by the two forms of diakoptics.

Figure 5·25 Comparisons between TDD and FDD

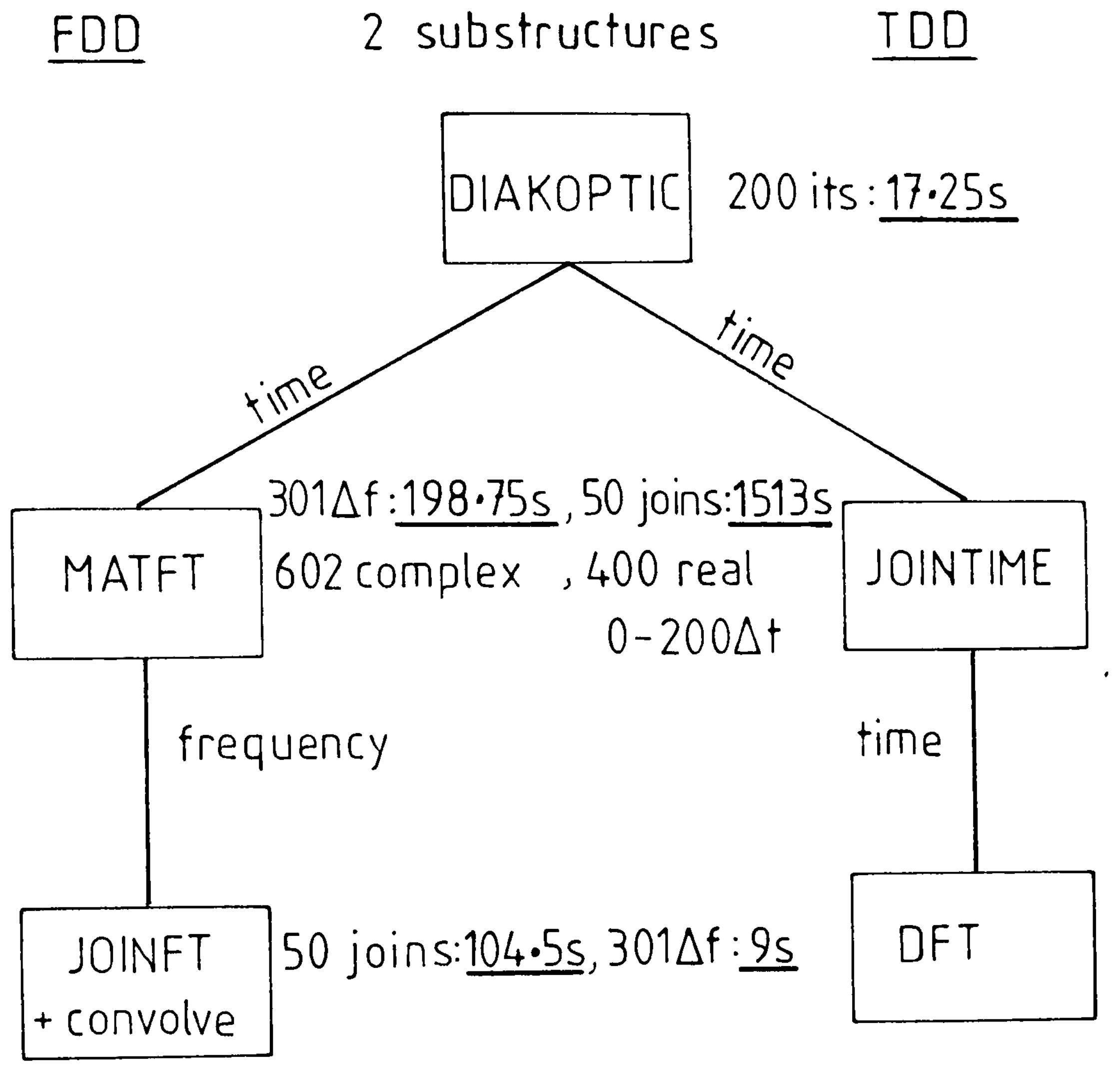

320·5s	Total time	1539·25s

Time required to solve and join one extra substructure (same size)

0·5 × (17·25 + 198·75)	0·5 × 17·25
+ 104·50	+1513 +9
= 212·50s	= 1530·63s

Times are for FORTRAN77 programs running on an ICL 2982 computer.

For the purposes of this comparison the time domain convolution is considered to apply always over all the truncated interval 0 to 200Δt. The example shows that for 301 frequency samples the FDD method executes more quickly than TDD. In fact for the number of joins performed FDD would take as long as TDD only when 1500 frequency steps are used. So, as a guide, if less than 1500 frequency steps will describe the final response, the FDD method will execute more quickly, otherwise the TDD method is better. This is only based on cases where the time step is the same in both substructures. If it is not then FDD is more promising, even if execution time is larger than TDD, as there are no errors introduced by the filter and resample process.

If the final result is required in the time domain FDD may be used without the time domain truncation. The final response is then Inverse Fourier Transformed but, from the sampling theorem, the time domain result will only be valid upto $t = 1/2\Delta f$.

5.6 Conclusions

The causes of errors in the time domain TLM implementation of diakoptics have been discovered and corrected.

Frequency Domain Diakoptics has been introduced and operating conditions defined.

Chapter 6 Pre-Solved Wire Elements

6.1 Introduction

The techniques introduced in Chapters 3, 4 and 5 can now be brought together to model wires of various radii smaller than half the space step ($\Delta\ell/2$).

A wire can be modelled on a fine mesh as shown in Chapter 3. Using the diakoptic techniques in Chapters 5 and 4 the wire can be solved in isolation and a multi-time-level scattering matrix obtained. The current induced into the wire can also be determined. This 'pre-solved wire element' can then be substituted for an ordinary node in a TLM model and the mesh solved using a hybrid form of diakoptic joining.

In this chapter the following aspects will be investigated: the generation of the scattering matrix ('impulse' response), the interface between the fine mesh and the coarse mesh (diakoptic boundary), the use of filtering and resampling, boundary conditions at the ends of the wire, (relatively) long wires and calculating the radius modelled by the wire.

6.2 Generating the Scattering Matrix

A wire and some of the surrounding space can be modelled as shown in figure 6.1a. This block models the same volume of space as the ordinary 3D node of figure 6.1b. To obtain the scattering matrix of this volume each face

Figure 6·1

a) Wire element

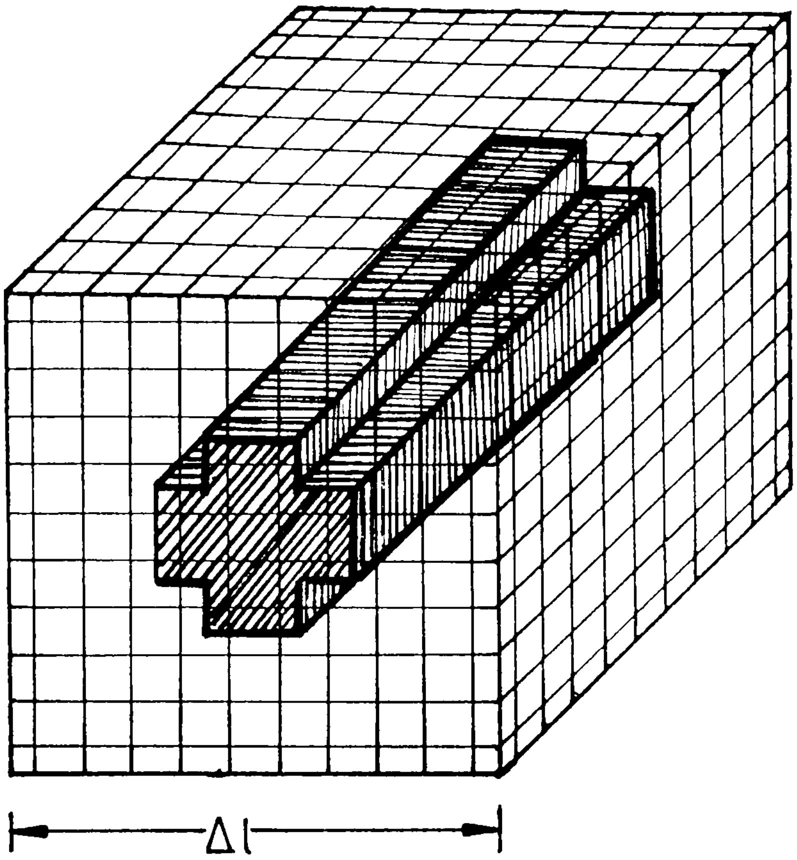

b) 3D node

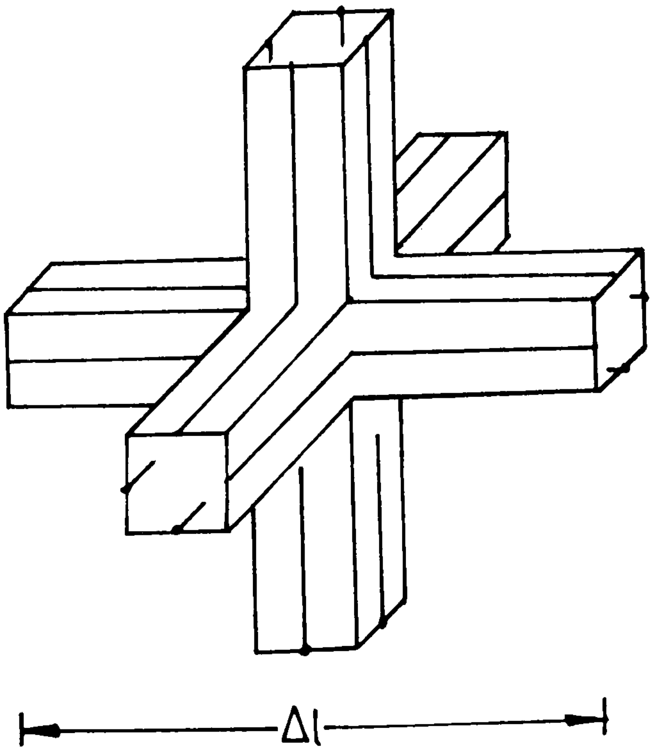

has to be impulsed in some way, remembering that the resulting impulse response is required at the coarse time step and must connect to one transmission-line on the adjacent node. This requires some form of spatial and time approximation. Space approximation will be investigated in section 6.3.

6.2.1 Time Approximations

TLM impulses on the coarse and fine meshes are shown in figure 6.2a, b. The impulse response of the wire element is required at the coarse time step and so the excitation of figure 6.2c was used to excite the wire element. The smaller bandwidth of this signal (compared with figure 6.2b) reduces any errors introduced by the filtering and resampling of pulses reflected from the wire element, as will be shown later in this chapter. Most of the results presented here use the excitation (c).

The reflected pulses occur at the fine mesh time step and so must be filtered and resampled using the 'ideal' filter described in Chapter 5. This filter introduces some errors into the response since it is impossible to store and use the scattering matrix with an infinite number of elements. In practice the scattering was truncated after 15 to 40 coarse time samples (that is the scattering matrix is defined from 0 to nΔt or Δt to nΔt depending on whether instantaneous reflection is allowed).

6.2.2 Scattering and Joining

A space and time approximated scattering matrix for a wire element has the form:

$$\underline{S} = \begin{bmatrix} \underline{S}_{1,1} & \underline{S}_{1,2} & \cdots & \underline{S}_{1,12} \\ \underline{S}_{2,1} & \underline{S}_{2,2} & \cdots & \underline{S}_{2,12} \\ \vdots & \vdots & & \vdots \\ \underline{S}_{12,1} & \underline{S}_{12,2} & \cdots & \underline{S}_{12,12} \end{bmatrix} \qquad (6.1)$$

Each term $\underline{S}_{i,j}$ is a time domain vector:

$$\underline{S}_{ij} = \begin{bmatrix} ({}_{o}S_{ij}) \\ {}_{1}S_{ij} \\ {}_{2}S_{ij} \\ \vdots \\ {}_{n}S_{ij} \end{bmatrix} \qquad (6.2)$$

${}_{k}S_{ij}$ represents the proportion of an impulse incident on port j which is reflected from port i at a time $k\Delta t$ (coarse mesh) later.

Rather than separately finding the scattering matrix of the coarse mesh geometry, (i.e. the rest of the geometry without the wire element) and subsequently joining the two substructures together, it is possible to join the wire element into the coarse mesh as the TLM routine proceeds. This has the following benefits:

Figure 6·2 Initial impulse

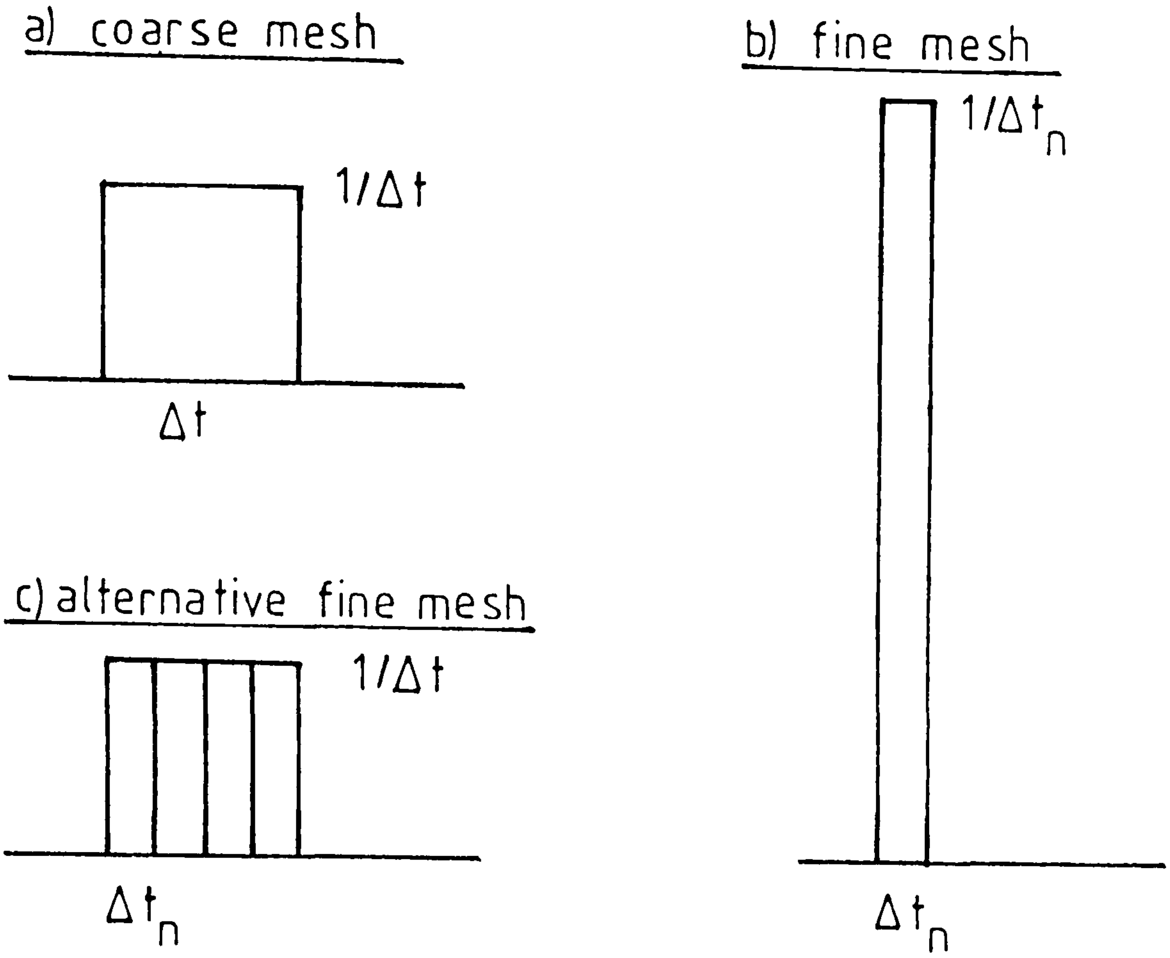

a) coarse mesh

b) fine mesh

c) alternative fine mesh

Figure 6·3 Simplified representation of a pre-solved wire element

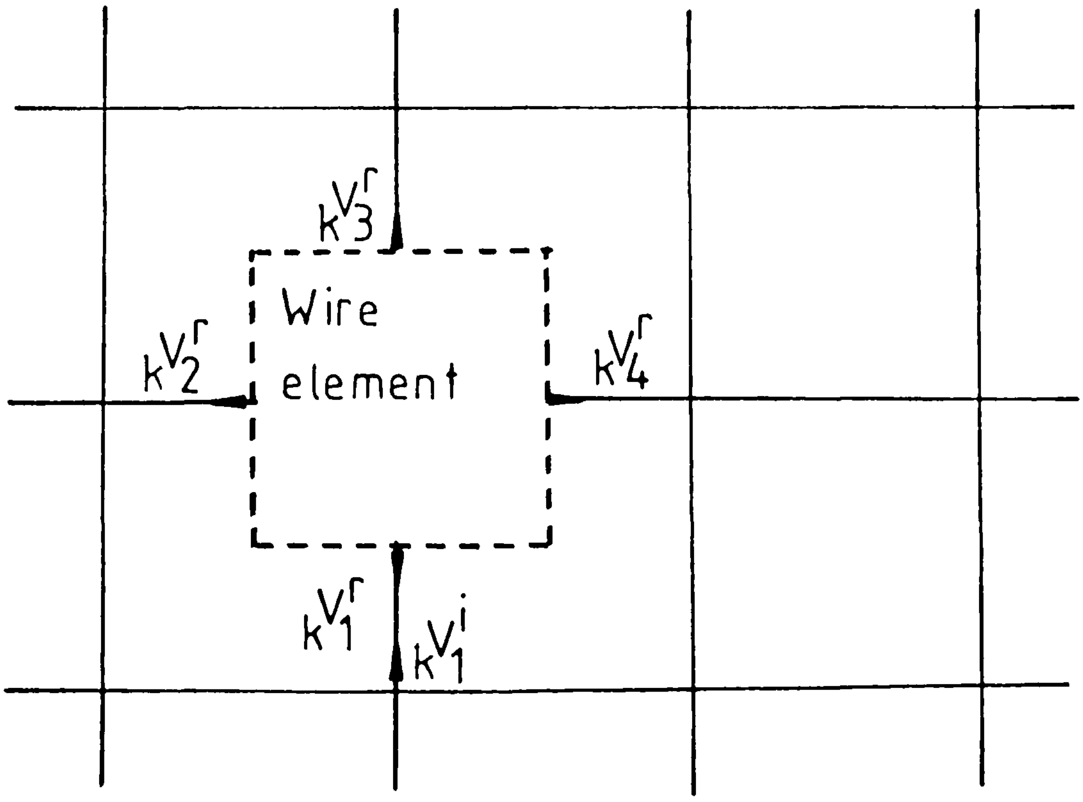

i) Only one set of scattering data need be stored (the wire). This can be important if the wire is composed of multiple elements making the scattering matrix of the coarse mesh large (at least 8 ports per wire element).

ii) Less computational effort is required. Computation of the coarse mesh scattering matrix plus the diakoptic joining process takes longer than joining as the coarse mesh routine proceeds.

iii) Less discrete convolutions need to be evaluated. Only the convolutions for finding the reflected pulses in the wire element are performed. Reflected pulses in the coarse mesh geometry are obtained by the normal TLM process.

Figure 6.3 shows a simplified representation of the wire element and the coarse mesh. Consider one impulse incident on the wire element as shown. From the scattering matrix the impulse relfected out of port (or line) 3 is :

$$ {}_kV^r_3 = {}_kV^i_1 \cdot {}_0S_{3,1} + {}_{k-1}V^i_1 \cdot {}_1S_{3,1} + {}_{k-2}V^i_1 \cdot {}_2S_{3,1} + \dots \qquad (6.3) $$

Generally when all lines are subjected to impulses $V_p{}^i$ then the response is:

$$ {}_kV^r_d = \sum_{p=1}^{12} \underline{S}_{p,d} * \underline{V}^i_p \quad . \qquad (6.4) $$

where '*' represents the convolution of the two vectors thus:

$$ {}_0S_{pd}\cdot{}_kV_p^i + {}_1S_{pd}\cdot{}_{k-1}V_p^i + {}_2S_{pd}\cdot{}_{k-2}V_p^i \cdots \qquad (6.5) $$

This can be simply programmed by the use of a storage vector for each reflected transmission-line. Figure 6.4 shows how the contents of one such vector are modified with time. Considering only one incident pulse (${}_kV_1^i$) the contents of this vector will be the products of ${}_kV_1^i$ and $\underline{S}_{11}$ (for more incident pulses than terms such as ${}_kV_p^i\cdot\underline{S}_{1p}$ will also be added to the vector). When all the vector contents have been evaluated the first term (${}_kV_1^i\cdot{}_0S_{11}$ in the figure) can be removed from the vector and this becomes ${}_kV_1^r$. All the other contents are then moved up the vector and the last term is set to zero. At the next iteration the ${}_{k+1}V_1^i$ products with $\underline{S}_{11}$ are added to the vector as shown and so on. The figure shows how ${}_{k+2}V_1^r$ is evaluated.

6.2.3 Outputs

The current (or any other electromagnetic parameter) can be calculated in a similar form. A scattering matrix relating initial impulse on each port to the output can be computed at the same time as the port to port scattering is obtained. Such a matrix has the form:

$$ \underline{O} = \begin{bmatrix} \underline{O}_{11} & \underline{O}_{12} & \cdots & \underline{O}_{1n} \\ \underline{O}_{21} & \underline{O}_{22} & \cdots & \underline{O}_{2n} \\ \vdots & & & \vdots \\ \underline{O}_{p1} & \cdots & \cdots & \underline{O}_{pn} \end{bmatrix} \qquad (6.6) $$

Figure 6·4 Simplified joining routine

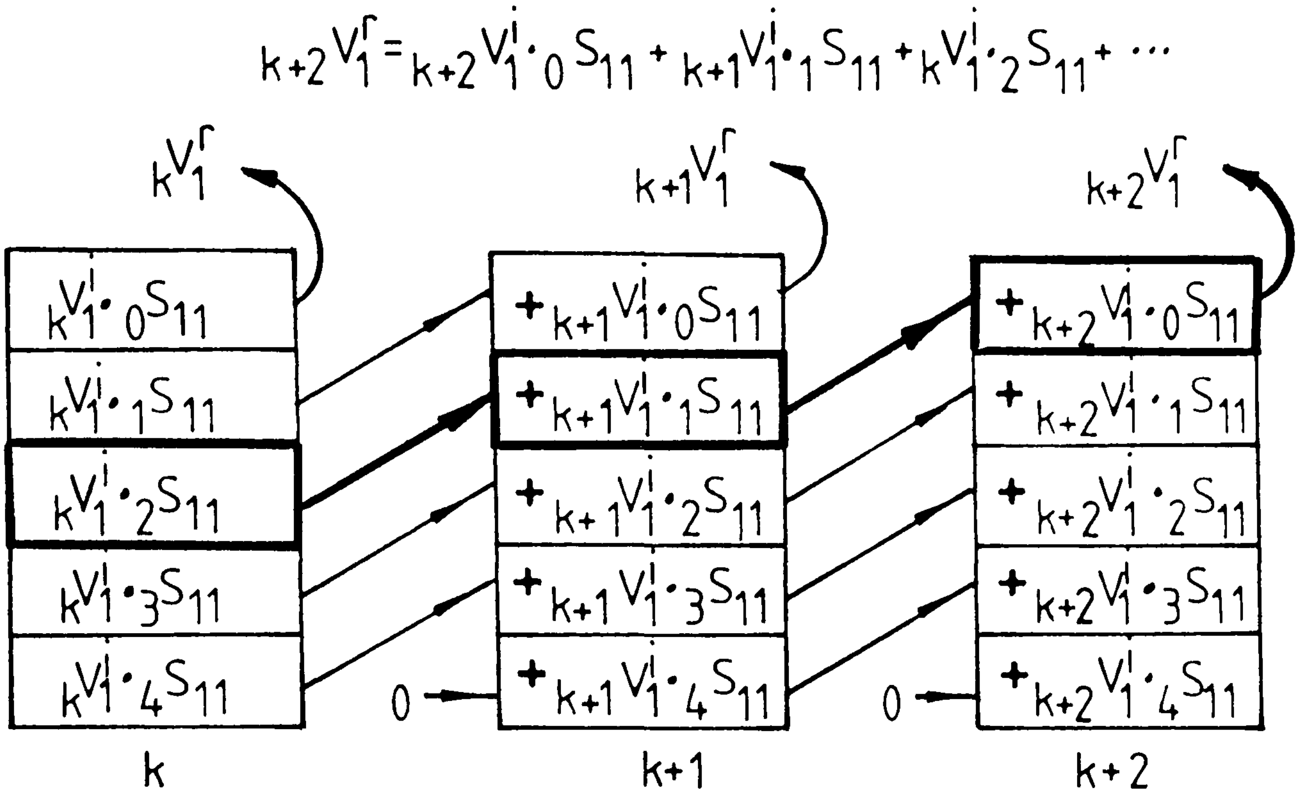

Figure 6·5 Simple averaging boundary

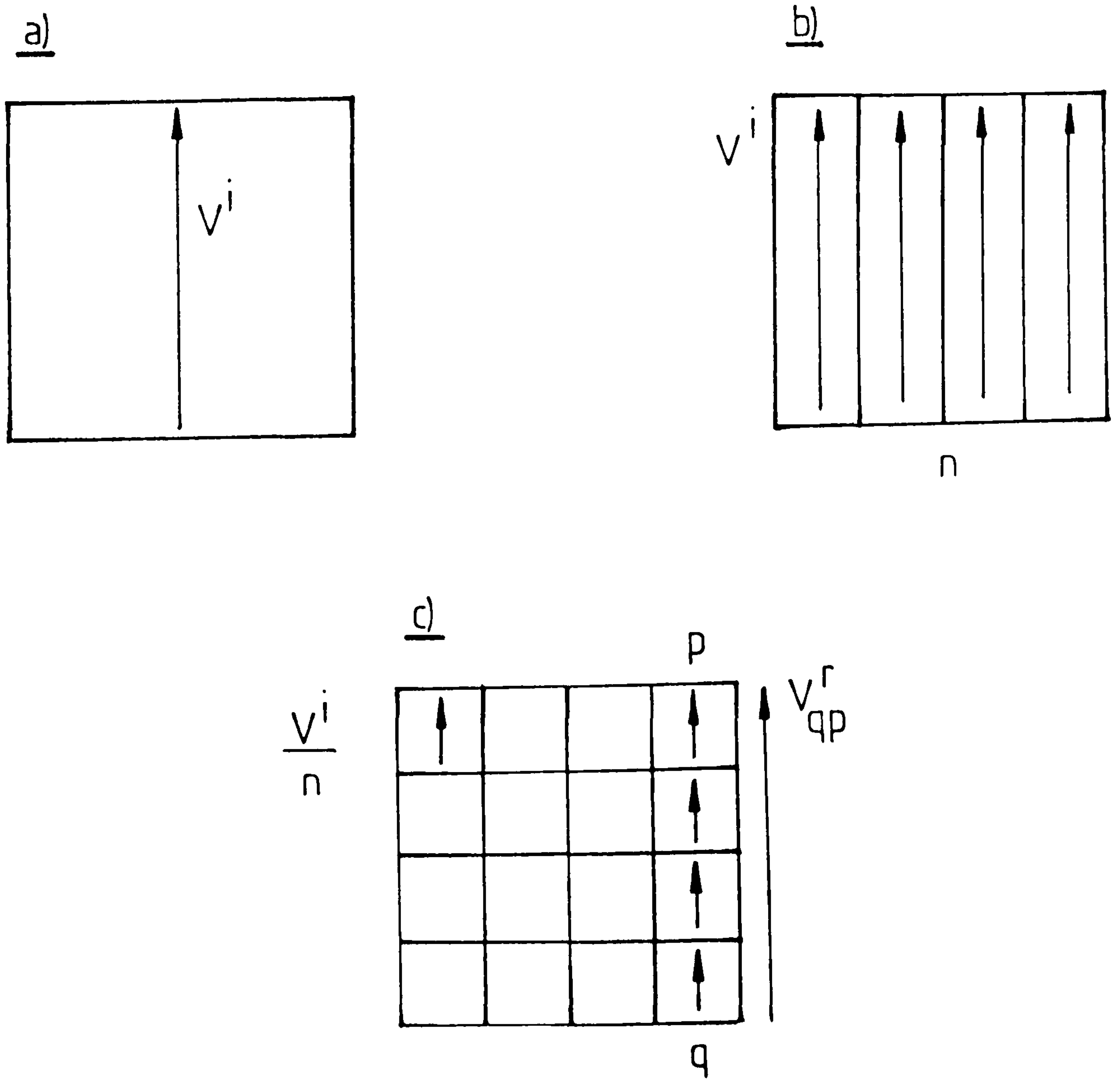

where $\underline{O}_{oj}$ is similar to $\underline{S}_{ij}$.

The current at iteration k is then

$$_k I_p = \sum_{j=1}^{12} \underline{O}_{pj} * \underline{V}_j^i \qquad (6.7)$$

where $\underline{O}$ is the port to output matrix as defined in Chapter 5.

6.3 Spatial Approximations

The n^2 transmission-lines emerging from the wire element need to be approximated by one joining transmission-line to allow a connection to the adjacent coarse mesh. Two space-approximation techniques were investigated : a simple averaging boundary (AVB) and a power conservation boundary (PCB).

6.3.1 Simple Averaging Boundary (AVB)

Figure 6.5a shows a voltage pulse, V^i, (from the coarse mesh) incident on the boundary. The voltage is considered to apply over the whole face and therefore the voltage may be regarded as made up of equal, discrete components on the fine mesh (6.5b). Since the impedance of each fine mesh transmission-line is the same this gives a voltage $\frac{V^i}{n}$ launched into each line (6.5c).

For pulses reflected from the fine mesh a voltage V^r_{qp} can be obtained which is the sum of the individual voltages:

$$V^{r}_{qo}(i) = \overset{j}{\Sigma} \; V^{r}_{ij} \qquad (6.8)$$

Using the parallel generator theorem the total reflected voltage will be

$$V^{r} = \frac{\overset{j\,i}{\Sigma\Sigma}}{n} V^{r}_{ij} \qquad (6.9)$$

If this scattering is viewed in matrix form then :

$$\begin{bmatrix} V^{r}_{o} \\ V^{r}_{1} \\ V^{r}_{2} \\ \vdots \\ V^{r}_{n^2} \end{bmatrix} = \begin{bmatrix} 0 & \frac{1}{n} & \frac{1}{n} & \cdots & \frac{1}{n} \\ \frac{1}{n} & 0 & 0 & \cdots & 0 \\ \frac{1}{n} & 0 & 0 & \cdots & 0 \\ \vdots & \vdots & \vdots & & \vdots \\ \frac{1}{n} & 0 & 0 & \cdots & 0 \end{bmatrix} \cdot \begin{bmatrix} V^{i}_{o} \\ V^{i}_{1} \\ V^{i}_{2} \\ \vdots \\ V^{i}_{n^2} \end{bmatrix} \qquad (6.10)$$

Collin (81) has shown that a lossless scattering matrix has the property :

$$\underline{S}.\underline{S}^{*T} = \underline{U} \qquad (6.11)$$

This ensures that power is conserved by the scatterer.

This condition is not observed by the matrix in equation (6.10) since,

$$\underline{S}.\underline{S}^{*T} = \begin{bmatrix} 1 & 0 & 0 & \cdots & 0 \\ 0 & \frac{1}{n^2} & \frac{1}{n^2} & \cdots & \frac{1}{n^2} \\ 0 & \frac{1}{n^2} & \frac{1}{n^2} & \cdots & \frac{1}{n^2} \\ \vdots & \vdots & \vdots & & \vdots \\ 0 & \frac{1}{n^2} & \frac{1}{n^2} & \cdots & \frac{1}{n^2} \end{bmatrix} \qquad (6.12)$$

and therefore the boundary is lossy. Charge is always conserved by this boundary but power is lost on the transformation from the fine mesh to the coarse mesh.

There is no electrical analogue to this process as there is no real physical connection between the coarse and fine meshes. If such a connection is made a power conservation boundary can be constructed.

6.3.2 Power Conservation Boundary (PCB)

In figures 6.6a and b it is required that the n^2 lines of (a) are physically connected to the one line in (b). To prevent instantaneous reflection of an incident pulse back into the coarse mesh (a) should appear matched to (b). If **all** transmission-lines have the same characteristic impedance (Z_0) then the joining network of figure 6.6c will achieve the aim. Note that, in general, although a pulse incident on the fine mesh will see a match, a reflected pulse will not, i.e. there will be internal reflection from the boundary. This may not be

Figure 6·6 Power conservation boundary

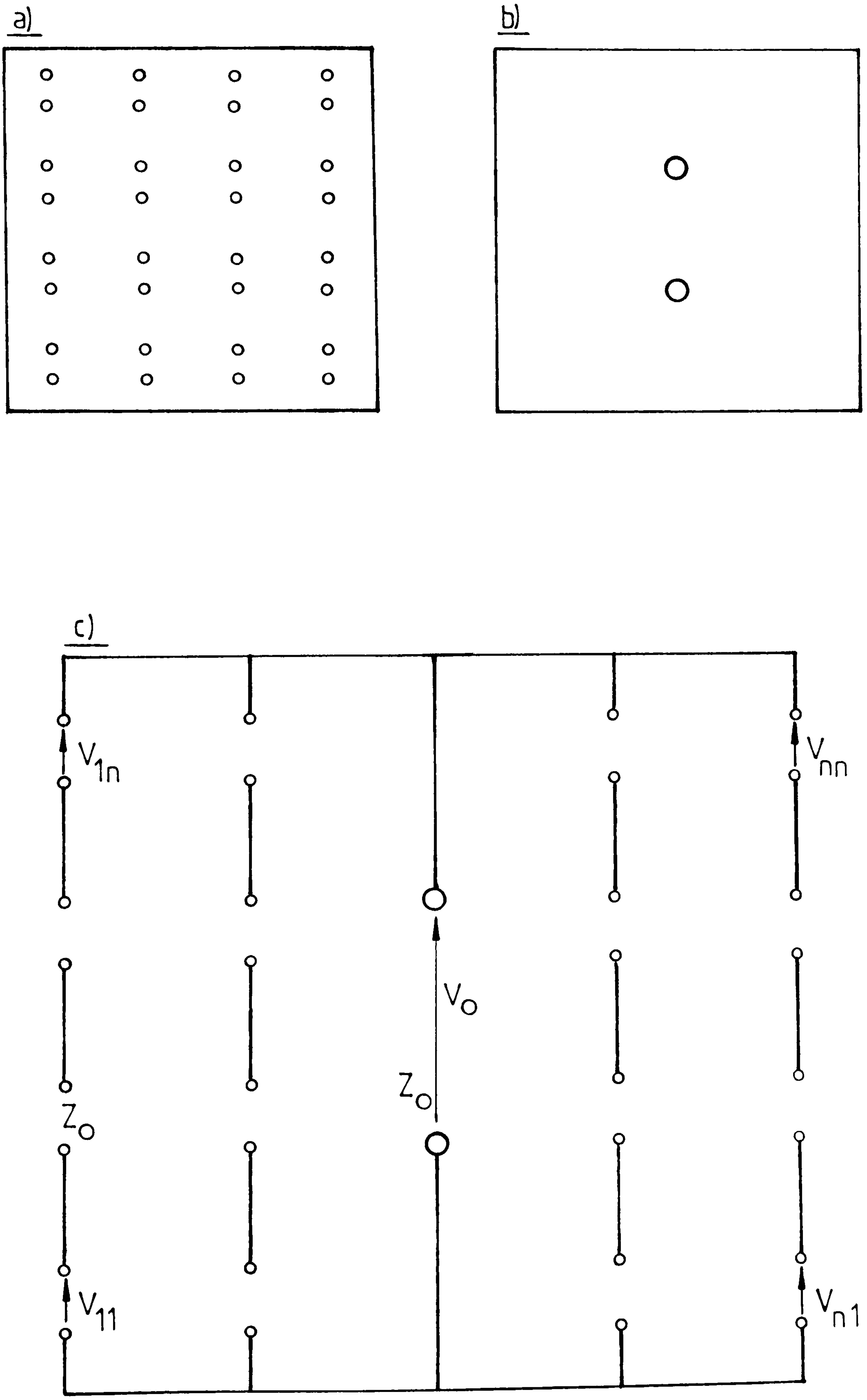

what is required by a diakoptic boundary as will be seen later. The very form of the PCB requires that the boundary itself has a square cross-section, otherwise the fine-mesh will not appear matched to the coarse-mesh.

6.3.2.1 The Scattering Matrix of the Power Conservation Boundary

Let V^i_{ij} be a voltage pulse incident on the boundary from the fine mesh transmission line (i,j).

V^r_{ij} be a voltage pulse reflected from the boundary into the fine mesh transmission-line (i,j).

V^i_o be a voltage pulse incident on the boundary from the coarse mesh.

V^r_o be a voltage pulse reflected from the boundary into the coarse mesh.

Consider the following possibilities:

(a) $V^i_{ij} = 0, \; V^i_o \neq 0$

The equivalent circuit of this condition is shown in figure 6.7a. The n^2 transmission present a total impedance of Z_o giving:

$$V = V^i_o \tag{6.13}$$

Thus, the reflected voltage V^r_o is:

$$V^r_o = V - V^i_o \equiv 0 \text{ (by definition)} \tag{6.14}$$

Figure 6·7 Power conservation boundary

Equivalent circuits

a) $V_{ij}^{i} = 0 \quad V_{o}^{i} \neq 0$

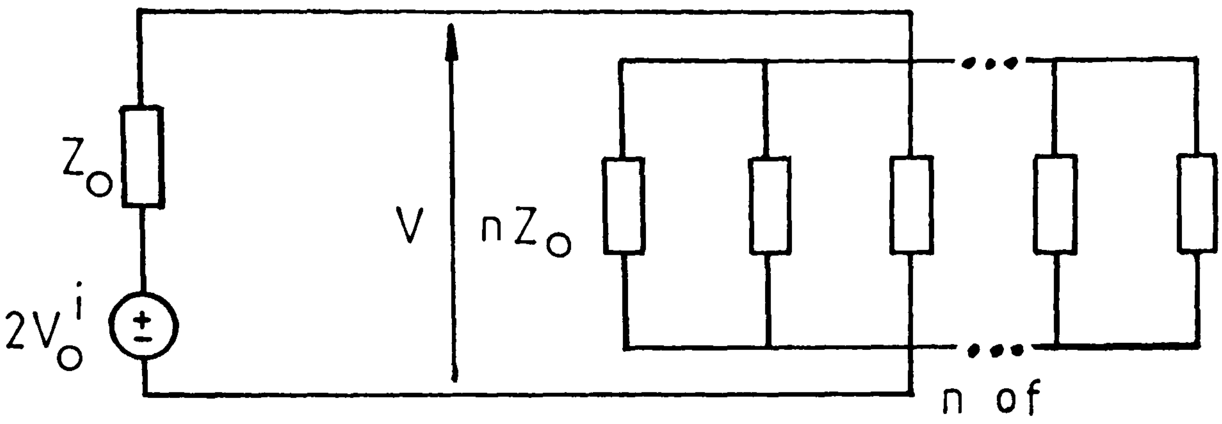

b) $V_o^i = 0 \quad V_{ab}^i \neq 0 \quad i \neq a$

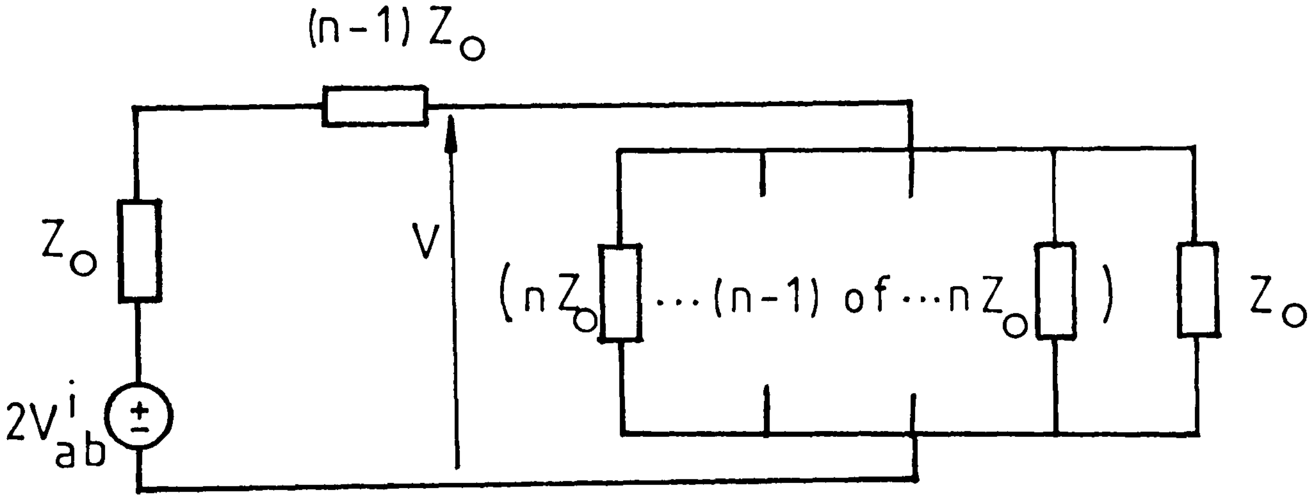

c) $V_o^i = 0 \quad V_{ab}^i \neq 0 \quad i = a$

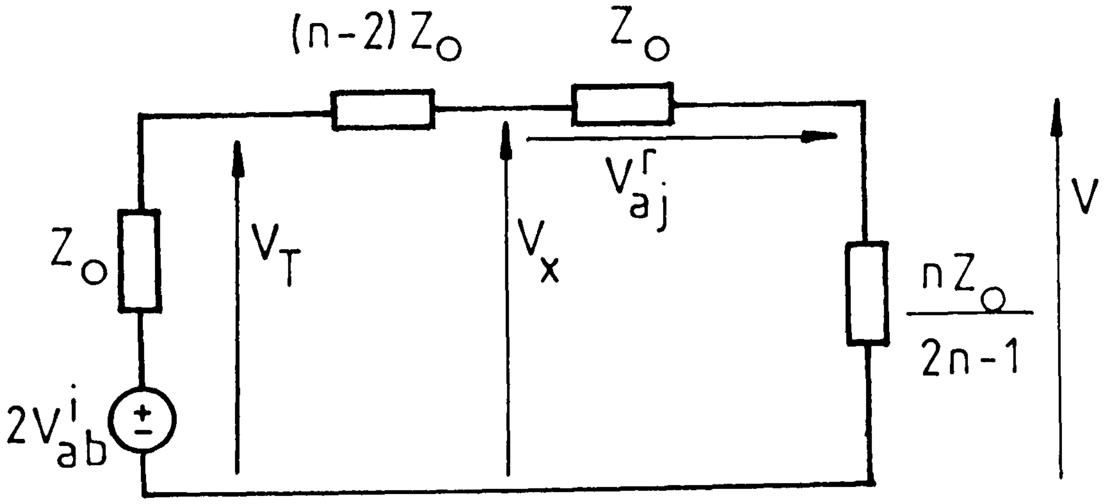

The voltage reflected into each fine mesh transmission-line is $\frac{V}{n}$ i.e.:

$$V^r_{ij} = \frac{V^i}{n} \text{ (as in the averaging boundary)} \qquad (6.15)$$

(b) $V^i_o = 0,\ V^i_{ij} = 0$ Except $V^i_{ab} \neq 0\ (i \neq a)$

(incident and reflected pulses on different vertical line. This has an equivalent circuit as shown in figure 6.7b).

$$V = \frac{2V^i_{ab}\ \frac{nZ_o}{2n-1}}{\frac{nZ_o}{2n-1} + nZ_o} = \frac{V^i_{ab}}{n} \qquad (6.16)$$

Therefore

$$V^r_o = \frac{V^i_{ab}}{n} \qquad (6.17)$$

and for $i \neq a$ $\quad V^r_{ij} = \frac{V^i_{ab}}{n^2} \qquad (6.18)$

(c) $V^i_o = 0,\ V^i_{ij} = 0,\ V^i_{ab} \neq 0\ (i = a,\ j \neq b)$

(incident and reflected pulse on same vertical line but not same transmission line).

The equivalent circuit is a modified version of figure 6.7b, shown in figure 6.7c.

$$V = \frac{V^i_{ab}}{n} \text{ from equation (6.16)}$$

$$V^r_{aj} = V - V_x \qquad (6.19)$$

The voltage V_x is given by :

$$V_x = \frac{2V^i_{ab}\left(Z_o + \frac{nZ_o}{2n-1}\right)}{(n-1)Z_o+\left(Z_o+\frac{nZ_o}{2n-1}\right)}$$

$$= V^i_{ab}\frac{(3n-1)}{n^2} \qquad (6.20)$$

Substituting into (6.19) gives

$$V^r_{aj} = \frac{1}{n^2}\, V^i_{ab}(1-2n) \qquad (6.21)$$

(d) Reflection on Same Transmission-Line (i=a, j=b)

Using the circuit of figure 6.7c

$$V_T = \frac{2V^i_{ab}\left[(n-1)Z_o + \frac{nZ_o}{2n-1}\right]}{Z_o+(n-1)Z_o + \frac{nZ_o}{2n-1}} \qquad (6.22)$$

with $V^r_{ab} = V_T - V^i_{ab}$ (6.23)

giving $V^r_{ab} = \left(\frac{n-1}{n}\right)^2 V^i_{ab}$ (6.24)

These can be rewritten in matrix form, which for a 3 x 3 face gives the equation (6.25) shown in figure 6.8. This matrix does have the property $\underline{S}.\underline{S}^{*T} = \underline{U}$ and therefore charge and power are conserved.

Using the parallel generator theorem the boundary voltage V can be defined as:

$$V = \frac{1}{n} \sum_{i=1}^{n} \sum_{j=1}^{n} V_{ij}^{i} + V_{o}^{i} \tag{6.26}$$

The total voltage reflected into the line (a,b) is given by:

$$V_{ab}^{r} = V_{ab}^{i} \frac{(n-1)^{2}}{n^{2}} + \sum_{\substack{j=1 \\ j\neq b}}^{n} V_{aj}^{i} \left(\frac{1-2n}{n^{2}}\right) + \sum_{\substack{i=1 \\ i\neq a}}^{n} \sum_{j=1}^{n} V_{ij}^{i} \frac{1}{n^{2}} + \frac{1}{n} V_{o}^{i} \tag{6.27}$$

Recognising that:

$$\sum_{\substack{j=1 \\ j\neq b}}^{n} V_{aj}^{i} = \sum_{j=1}^{n} V_{aj} - V_{ab}^{i} \tag{6.28}$$

and

$$\sum_{\substack{i=1 \\ i\neq a}}^{n} \sum_{j=1}^{n} V_{ij}^{i} = \sum_{i=1}^{n} \sum_{j=1}^{n} V_{ij}^{i} - \sum_{j=1}^{n} V_{aj}^{i} \tag{6.29}$$

allows the substitution of these equations and (6.26) into (6.27) to give:

$$V_{ab}^{r} = \frac{V}{n} - \frac{2}{n} \sum_{j=1}^{n} V_{aj}^{i} + V_{ab}^{i} \tag{6.30}$$

and

$$V_{o}^{r} = V - V_{o}^{i} \tag{6.31}$$

Figure 6·8 Power conservation boundary Scattering matrix

$$\begin{bmatrix} V_0 \\ V_{11} \\ V_{12} \\ V_{13} \\ V_{21} \\ V_{22} \\ V_{23} \\ V_{31} \\ V_{32} \\ V_{33} \end{bmatrix}^r = \frac{1}{n^2} \begin{bmatrix} 0 & n & n & n & n & n & n & n & n & n \\ n & (n-1)^2 & 1-2n & 1-2n & 1 & 1 & 1 & 1 & 1 & 1 \\ n & 1-2n & (n-1)^2 & 1-2n & 1 & 1 & 1 & 1 & 1 & 1 \\ n & 1-2n & 1-2n & (n-1)^2 & 1 & 1 & 1 & 1 & 1 & 1 \\ n & 1 & 1 & 1 & (n-1)^2 & 1-2n & 1-2n & 1 & 1 & 1 \\ n & 1 & 1 & 1 & 1-2n & (n-1)^2 & 1-2n & 1 & 1 & 1 \\ n & 1 & 1 & 1 & 1-2n & 1-2n & (n-1)^2 & 1 & 1 & 1 \\ n & 1 & 1 & 1 & 1 & 1 & 1 & (n-1)^2 & 1-2n & 1-2n \\ n & 1 & 1 & 1 & 1 & 1 & 1 & 1-2n & (n-1)^2 & 1-2n \\ n & 1 & 1 & 1 & 1 & 1 & 1 & 1-2n & 1-2n & (n-1)^2 \end{bmatrix} \cdot \begin{bmatrix} V_0 \\ V_{11} \\ V_{12} \\ V_{13} \\ V_{21} \\ V_{22} \\ V_{23} \\ V_{31} \\ V_{32} \\ V_{33} \end{bmatrix}^i$$

$n=3$

Figure 6·9 Wire-above-ground geometry

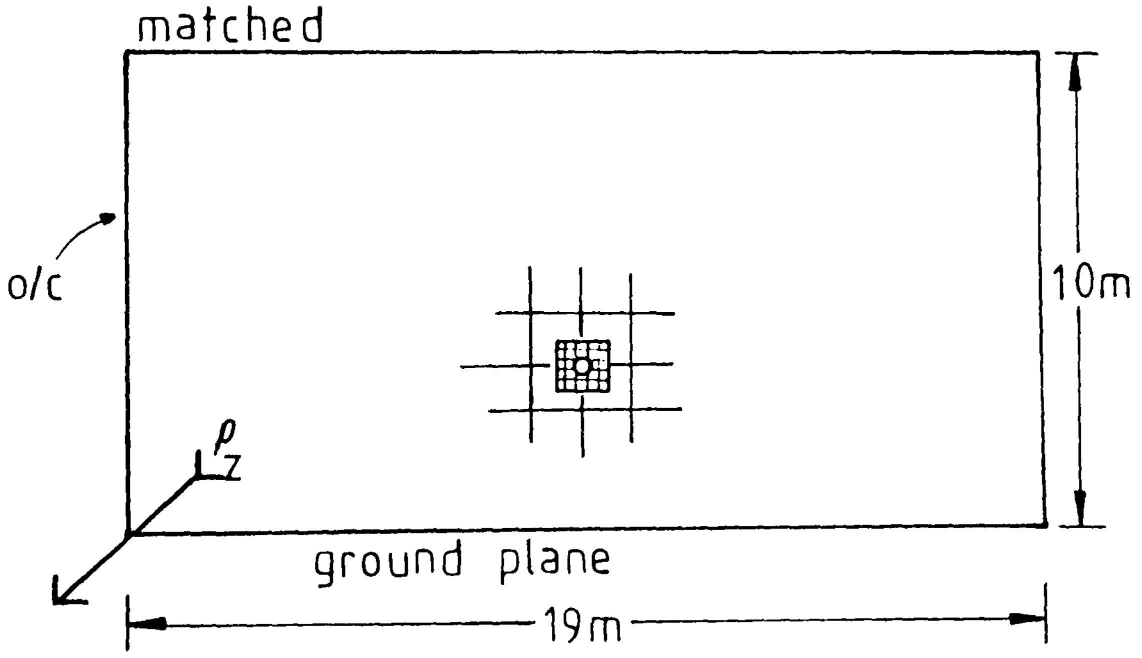

Equations (6.26), (6.30) and (6.31) allow for the efficient calculation of the scattering from this power conserving diakoptic boundary.

Although this boundary conserves power and charge the act of filtering and resampling the scattering matrix causes a loss of power and, when too few samples are used, charge.

6.4 The Use of the Pre-Solved Wire Element in Wire-Above-Ground and Resonant Cavity Geometries

The pre-solved wire element can be used in place of an ordinary 3D node in a wire-above-ground configuration as shown in figure 6.9, or in a resonant cavity geometry. For a wire-above ground the inductance and capacitance to ground can be obtained in the same way as for the models used in Chapters 3 and 4. From these calculations the inductance and capacitance radii can be obtained in the normal way. However, the capacitance model will be shown to contain further modelling errors when used with a pre-solved wire element.

For a resonant cavity geometry a slightly different excitation condition is required. Again, this is due to errors obtained in the excitation of the capacitance model. Two types of wire elements will be used in these models : 'single-slice' and 'long-wire' elements.

6.4.1 Single-Slice Geometries

6.4.1.1 Wire-Above-Ground

A wire of radius 0.167m is shown in figure 6.10. The scattering matrix of this geometry was obtained for several 'single-slice' conditions : that is the given cross-section extends 9 nodes into the figure, modelling a cubic space $\Delta\ell^3$ in the coarse mesh of figure 6.9. Firstly one PCB was connected to each face of the cube and the impulse of figure 6.2c used to obtain the scattering matrix. The resulting wire element was placed 3.5m above ground in the coarse mesh. The analytical value for the inductance to ground in this geometry is 7.47×10^{-7} Hm^{-1}, but this wire element models an inductance of 1049.80×10^{-7} Hm^{-1}, a very large error. (ρ_z in figure 6.9 is a short-circuit). The cause of this error is shown in figure 6.11. For an ordinary (matched) PCB with a short-circuit boundary next to it, in the coarse mesh, the voltage incident on the coarse mesh boundary is $\Sigma \frac{V^i}{n}$. This is then reflected from the coarse mesh boundary and distributed equally amongst all the transmission lines of the fine mesh (6.11a). The fine mesh description at the boundary has been lost because of the double averaging effect of the diakoptic boundary. This would be very noticeable if, for example, $V_1^i = +1$ and $V_4^i = -1$ in figure 6.11a (all other $V^i = 0$). $\Sigma \frac{V^i}{n}$ is then zero, therefore $V^r = 0$, thus nothing is reflected back into the fine mesh. If these transmission-lines were up against a short-circuit boundary then $V_1^r = -1$ and $V_4^r = +1$ would be expected.

Figure 6·10 Cross-section of 0·167m wire element

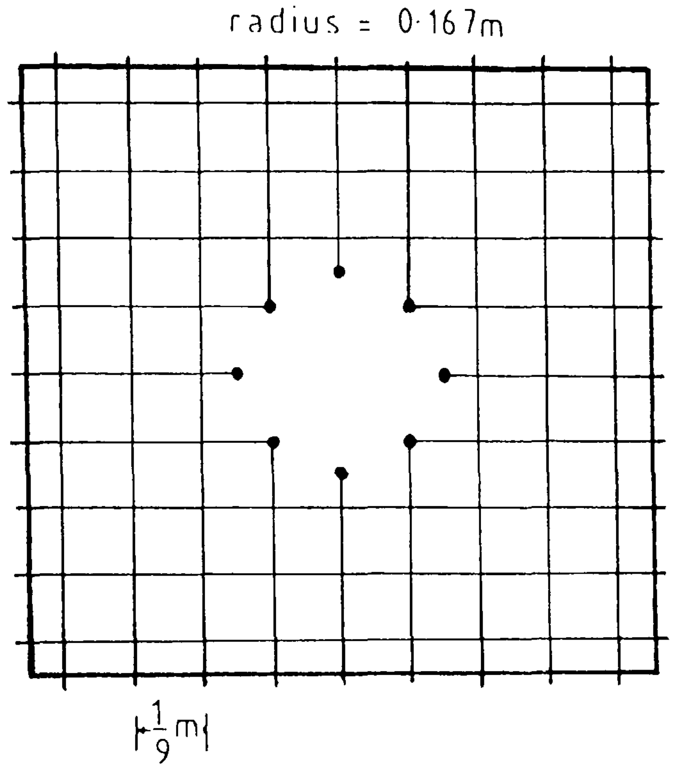

Figure 6·11 Terminating boundaries

a) matched

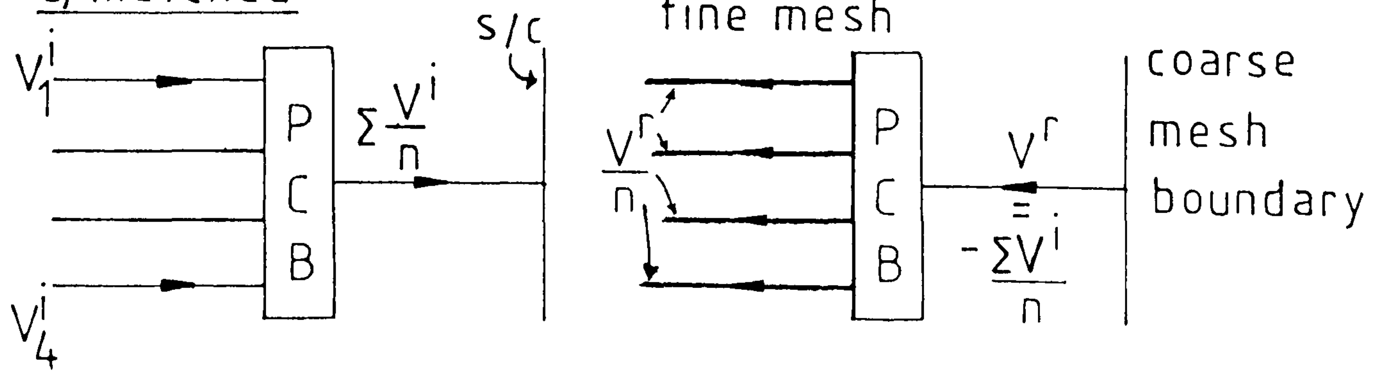

b) short-circuit

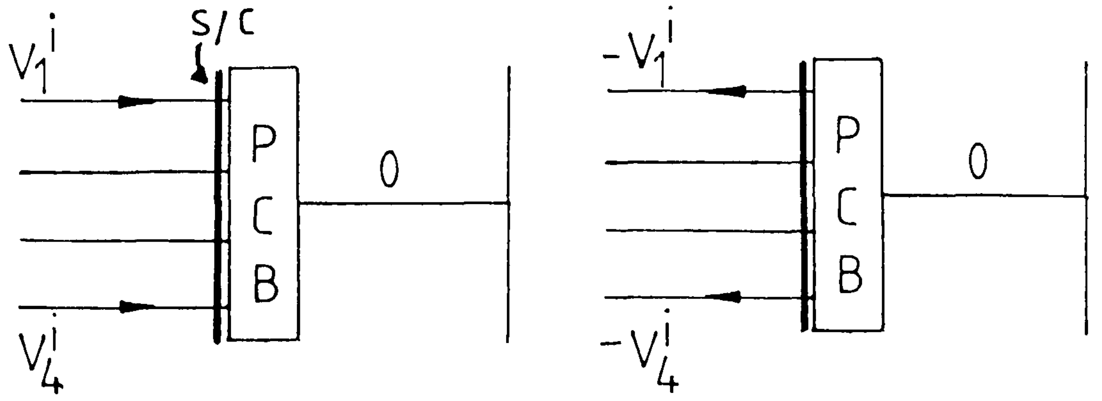

The correct model of the terminating boundary can be achieved by placing the short-circuit boundary inside the fine mesh as shown in figure 6.11b. Now the fine mesh description is preserved at the boundary because no averaging takes place. Further evidence for the need to include the termination within the element can be seen from the geometries and results detailed in figure 6.12. A wire with radius approximately 0.2m was subjected to a magnetic field excitation as shown. Three separate geometries were investigated:

i) a fine mesh ($\Delta \ell = 0.1$m) (figure 6.12a)
ii) a coarse mesh with pre-solved element containing PCB terminating boundaries (6.12b)
iii) as (ii) but wire-element has short-circuit terminations contained in the element

The current induced into the wire was computed (in the time-domain). The frequency response (obtained from the Fourier Transform of the current) is shown in figure 6.12c for all three geometries. The graph shows that the coarse mesh with PCB terminations does not compare well with the fine mesh solution. The inclusion of short-circuit terminations within the element improves the comparison - there is approximate agreement over the first 40 MHz. The main disadvantage of including terminating boundaries within the element is that generality is lost. Rather than having one element which models a wire of radius r with axis parallel to the x axis, a number of different elements

Figure 6·12 Wire model- end boundaries

a) Fine mesh geometry

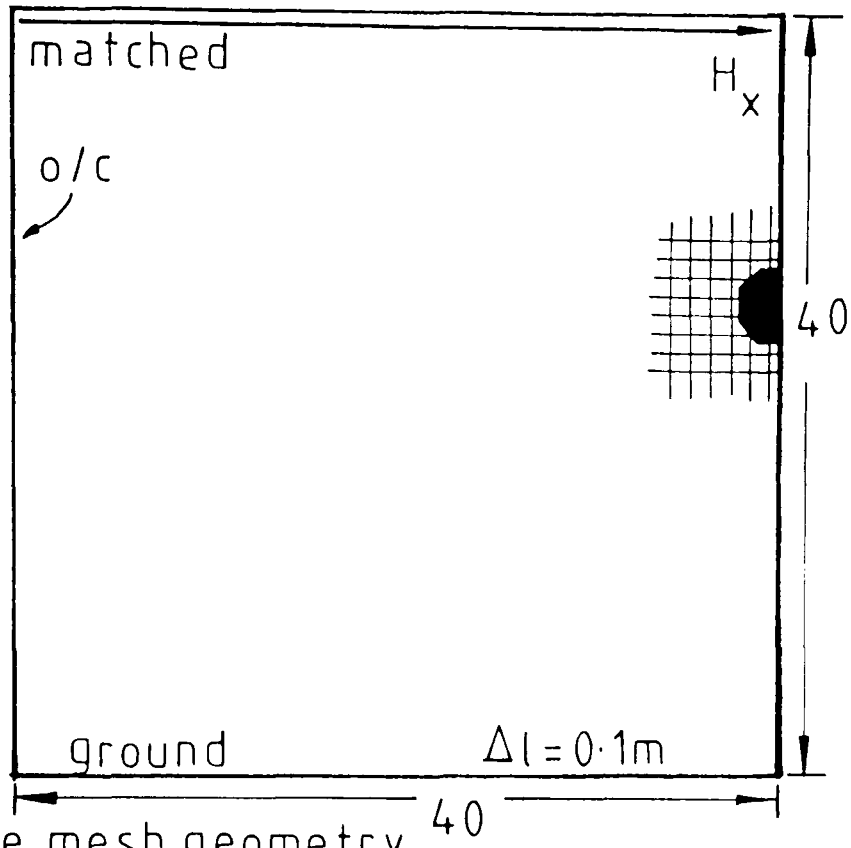

b) Coarse mesh geometry

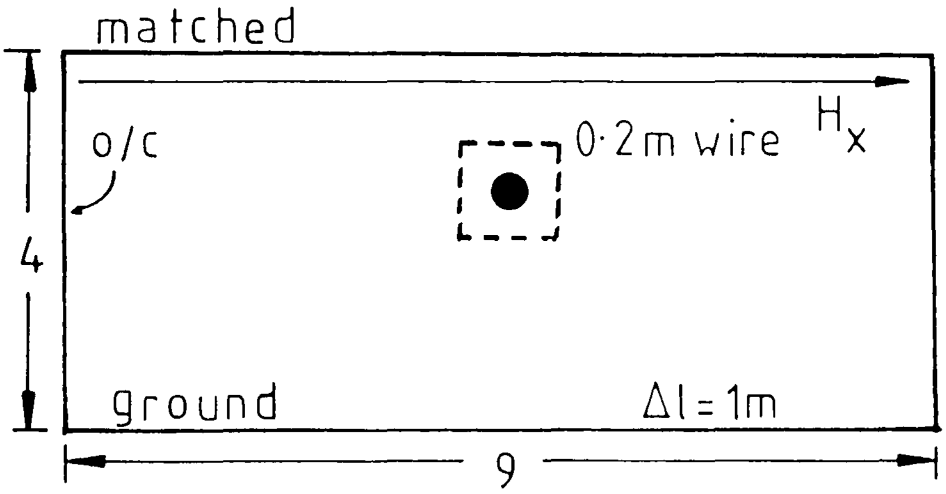

c) Frequency responses of above wire models

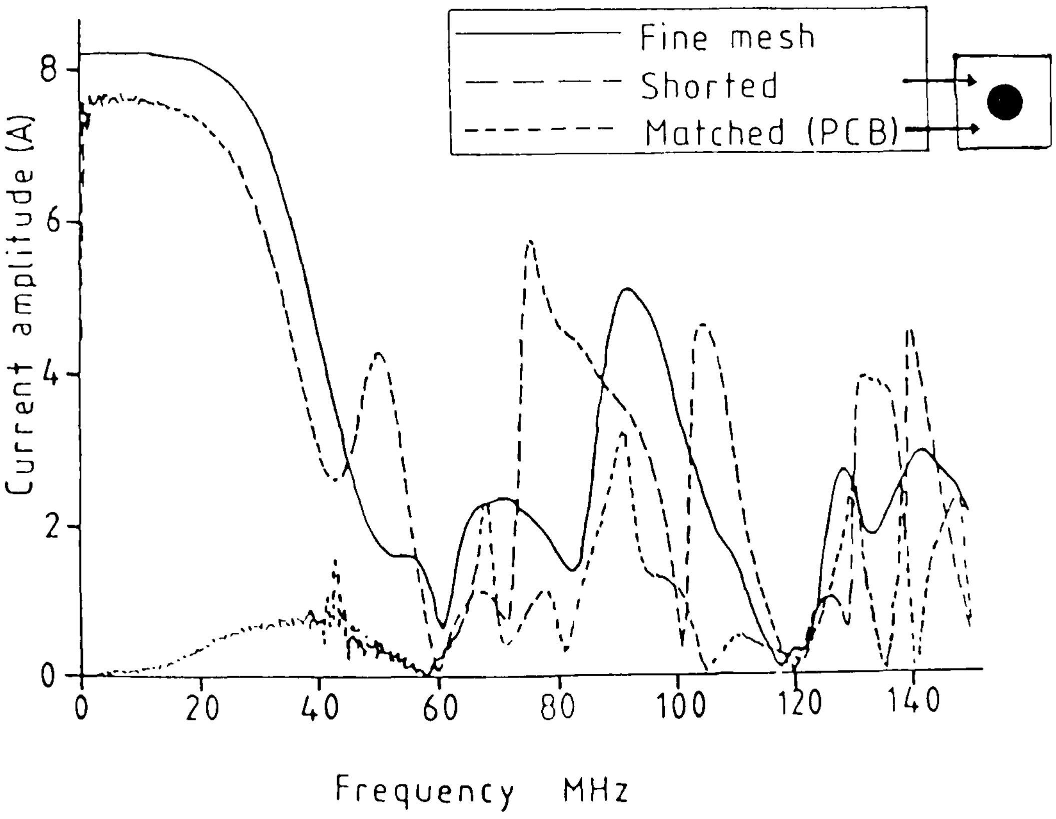

are required depending on what combination of terminating boundaries are required.

In an attempt to reintroduce generality into the element, it is possible to model the terminating boundaries by more than one PCB as suggested by figure 6.13. This averages the pulses scattered from the element over a smaller area. Two types of end boundaries were used: four PCB's and nine PCB's as shown in figure 6.13. Using these end boundaries in the element the results shown in Table 6.1 were obtained. It can be seen that as the element end boundaries are separated into smaller areas so the accuracy of the model improves. There are two important disadvantages with this type of element:

i) the scattering matrix of the element becomes larger;

ii) the execution time of both the scattering matrix generation and the coarse mesh geometry increases. Table 6.2 shows this increase.

These results are only for one wire element. For a wire of any appreciable length a number of such elements may be required.

At this point it is worth noting that all the results presented in this chapter are for the inductance model as defined in Chapter 3. When the capacitance calculation was attempted with a wire element geometry there was a problem exciting the model. In previous

Figure 6·13 Multiple terminating boundaries

a) one and 4 PCB's

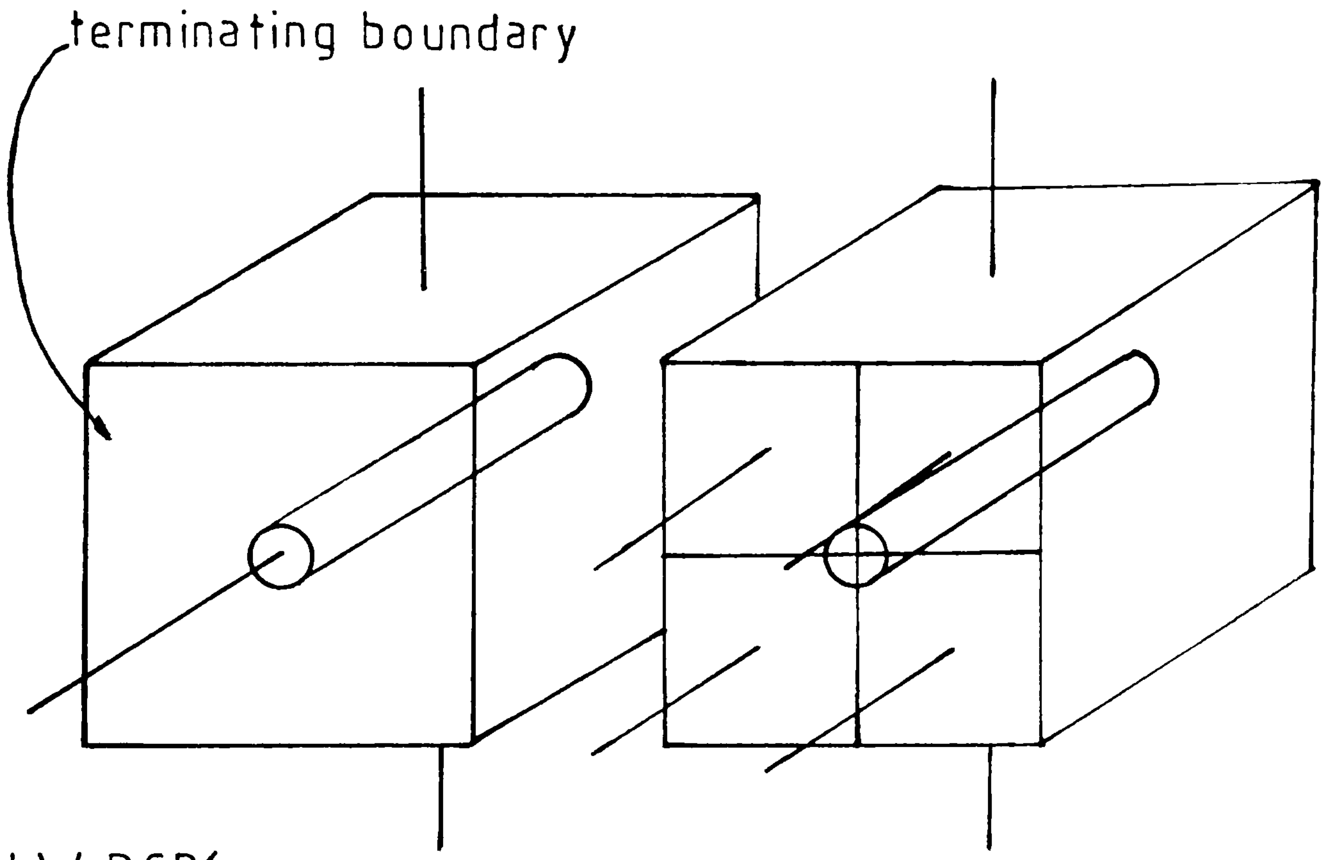

b) 4 PCB's

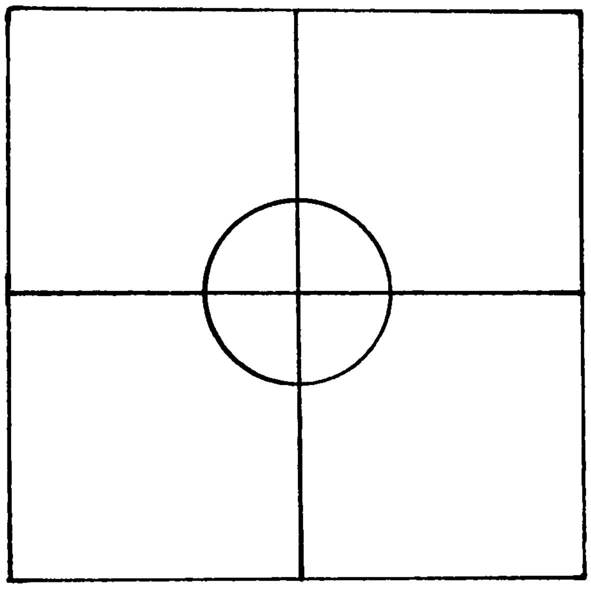

c) 9 PCB's

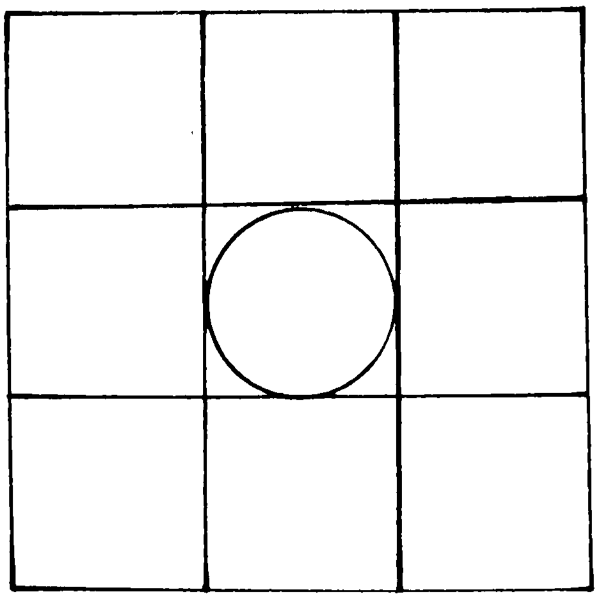

Table 6.1 Variation of the modelled radius with type of end boundary.

Single slice model, 0.167m radius wire 3.5m above ground, 500 iterations of coarse mesh. All wires solved for 200 iterations, filtered & resampled to 20 samples at the coarse time step. Excitation 6.2c

Description	Inductance $\times 10^{-7}$ (Hm^{-1})	%error
Analytic	7.474	-
1 PCB	1049.800	>>100
4 PCB	506.600	>>100
9 PCB	10.140	35.67
s/c end plane	8.129	8.06

Table 6.2 Comparison of execution time and storage requirements for multiple PCB end boundaries.

Description	Time for matrix calcn (s)	Time for w-a-g (s)	Matrix size (Kbytes)
No wire	-	23.5	-
1 PCB/short	472	38.0	22.5
4 PCB	980	70.1	90.0
9 PCB	1194	145.6	250.0

geometries the capacitance model has been excited by introducing a voltage between the wire and ground. With a pre-solved element geometry this means a voltage has to be placed between the ground and the position of the wire in the coarse mesh. A voltage also has to be placed between the boundary and the wire in the fine mesh. The boundaries A and B in figure 6.14 are pseudo-matched (PCB, although the same is true of AVB) and it can be shown that once a charge is placed at such a boundary then there is always a non-zero charge on the boundary. At all other points in the TLM mesh except the perfectly conducting boundaries the net charge at any point is zero. Thus this excitation across the diakoptic boundary is incorrect. When it was used it led to capacitance results which were always at least double the analytical result - but were quite often even less accurate. It has not been possible to derive an excitation technique for the capacitance model which does not leave a residual charge at the diakoptic boundary. For this reason no capacitance model results are presented.

The single-slice element (radius 0.2m) shown in figure 6.15 was used in the wire-above-ground geometry of figure 6.9. The termination boundaries (short-circuit planes) were included in the wire element. This time the type of excitation (figure 6.2b or 6.2c), type of diakoptic boundary (AVB or PCB) and height above ground of the wire were varied. Tables 6.3 and 6.4 show the results obtained. The excitation of figure 6.2b (one impulse on the fine mesh, Table 6.3) causes very large errors in the inductance model.

Figure 6·14 Charge left at diakoptic boundaries

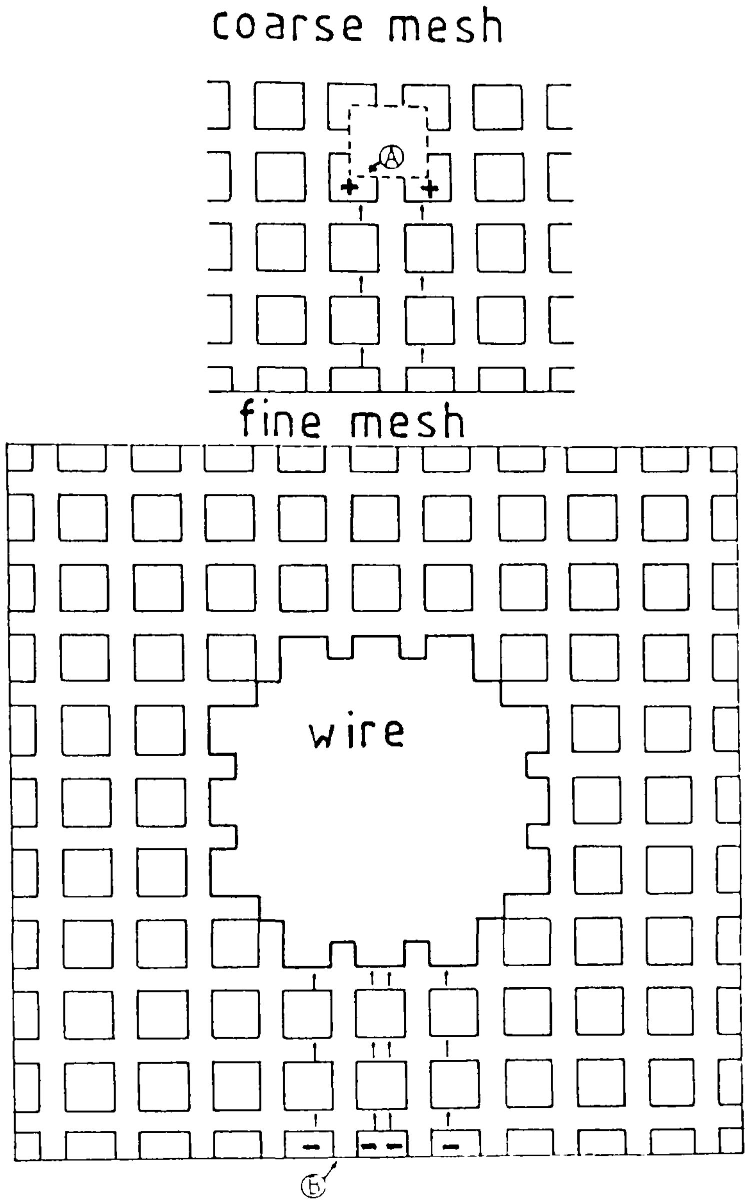

Figure 6·15 Cross-section of wire element

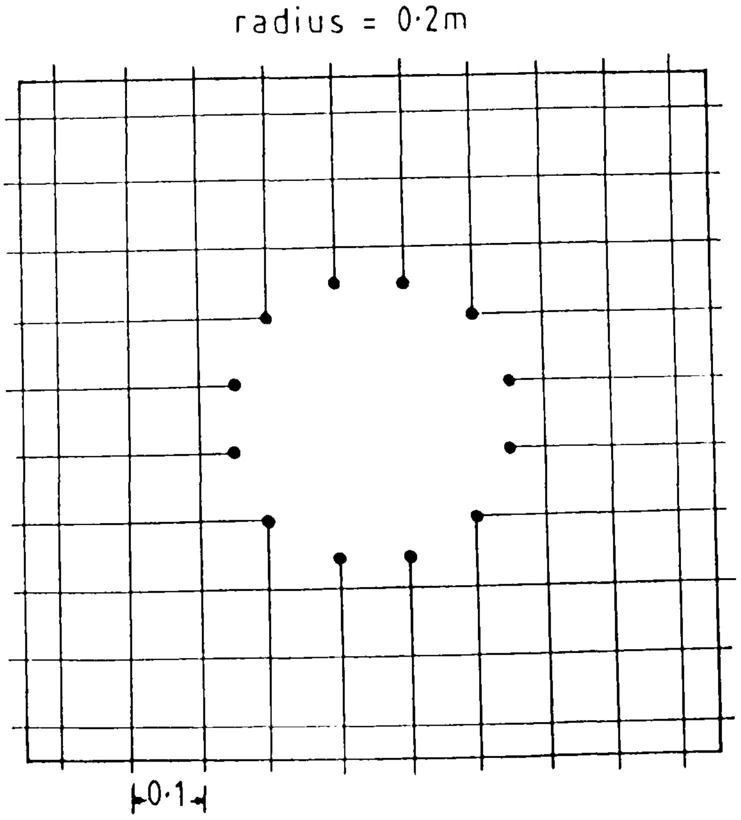

Table 6.3 Variation in flux, current and calculated inductance with height for a 0.2m wire (using short-circuit nodes in the description)

Single slice, power conservation boundaries, excitation 6.2b

Height (m)	Flux $\times \mu_0$	Current (A)	Inductance TLM $\times 10^{-7}$ (Hm^{-1})	Inductance Theoretical $\times 10^{-7}$ (Hm^{-1})
0.5	0.562×10^8	0.127×10^9	5.54	3.13
1.5	882.27	65.800	168.42	5.41
2.5	263.46	6.267	528.24	6.44
3.5	139.21	1.676	1044.09	7.11
4.5	91.81	0.701	1646.61	7.61
5.5	64.54	0.337	2403.00	8.01

Single slice, averaging boundaries, excitation 6.2b

Height (m)	Flux $\times \mu_0$	Current (A)	Inductance TLM $\times 10^{-7}$ (Hm^{-1})	Inductance Theoretical $\times 10^{-7}$ (Hm^{-1})
0.5	45.210	32.289	17.60	3.13
1.5	0.777	0.122	79.81	5.41
2.5	0.297	0.094	39.83	6.44
3.5	0.180	0.091	25.01	7.11
4.5	0.135	0.089	18.96	7.61
5.5	0.108	0.089	15.32	8.01

Table 6.4 Variation in inductance with height

for a 0.2m wire.

(using short-circuit nodes in the description)

Single slice, power conservation boundaries, excitation 6.2c

Height (m)	Inductance TLM x 10^{-7} (Hm^{-1})	Inductance Theoretical x 10^{-7} (Hm^{-1})	%error
0.5	7.98	3.13	155.95
1.5	8.81	5.41	62.89
2.5	7.60	6.44	18.08
3.5	7.89	7.11	10.96
4.5	8.45	7.61	11.05
5.5	9.07	8.01	13.19

Single slice, averaging boundaries, excitation 6.2c

Height (m)	Inductance TLM x 10^{-7} (Hm^{-1})	Inductance Theoretical x 10^{-7} (Hm^{-1})	%error
0.5	1.86	3.13	40.60
1.5	4.60	5.41	14.99
2.5	6.00	6.44	6.89
3.5	7.02	7.11	1.31
4.5	7.90	7.61	3.82
5.5	8.74	8.01	9.08

The most likely cause of this error is the (relatively) large high frequency components in the initial excitation. Later these have to be removed by an imperfect filter and resample routine which leads to large errors in the filtered response. If the alternative excitation of figure 6.2c is used the results of Table 6.4 are obtained. These show a much more accurate spread of results with the averaging boundary giving the best answers. The errors for a height of 0.5m are particularly large but this occurs when one diakoptic (matched) boundary is next to the perfectly conducting ground plane - i.e. the wire element is in contact with the ground. This is exactly the problem that occurred with the terminating boundaries above. If the ground plane is incorporated in the wire element it is likely that the error in the modelled radius will be reduced. [note that all non-diakoptic TLM wire models cannot model a wire $\frac{1}{2}\Delta\ell$ distant from any other wire or boundary].

Above a height of 3.5m the modelling errors become larger. This is where the closeness of the external boundaries, relative to the wire height, begins to take effect as in the previous models of Chapters 3 and 4.

6.4.1.2 Coaxial Geometry - Resonant Cavity Technique

The single-slice geometry is not really suitable for solution in a resonant cavity geometry as the length of the wire is too short. A number of single-slice elements can be connected end to end as shown in figure 6.16 to make up a longer wire. The terminating boundaries were included in

Figure 6·16 Long wire composed of single-slice elements

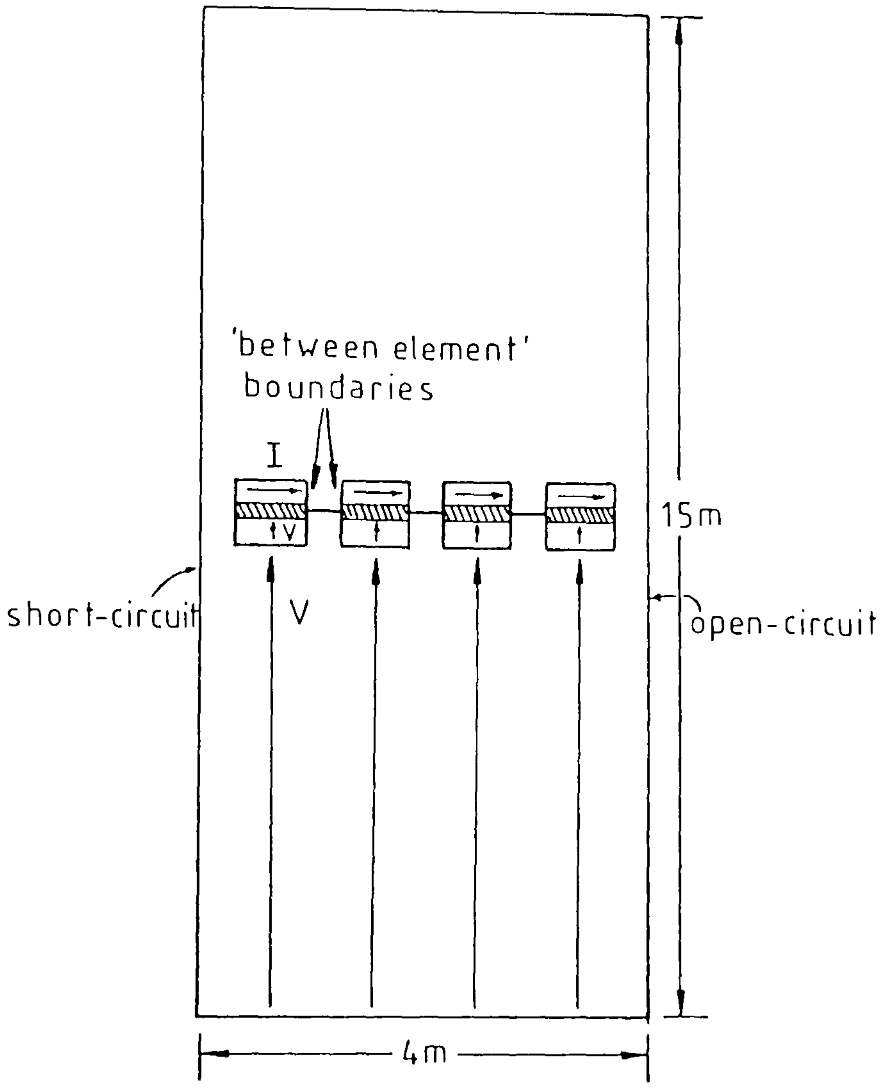

Figure 6·17 Long wire element

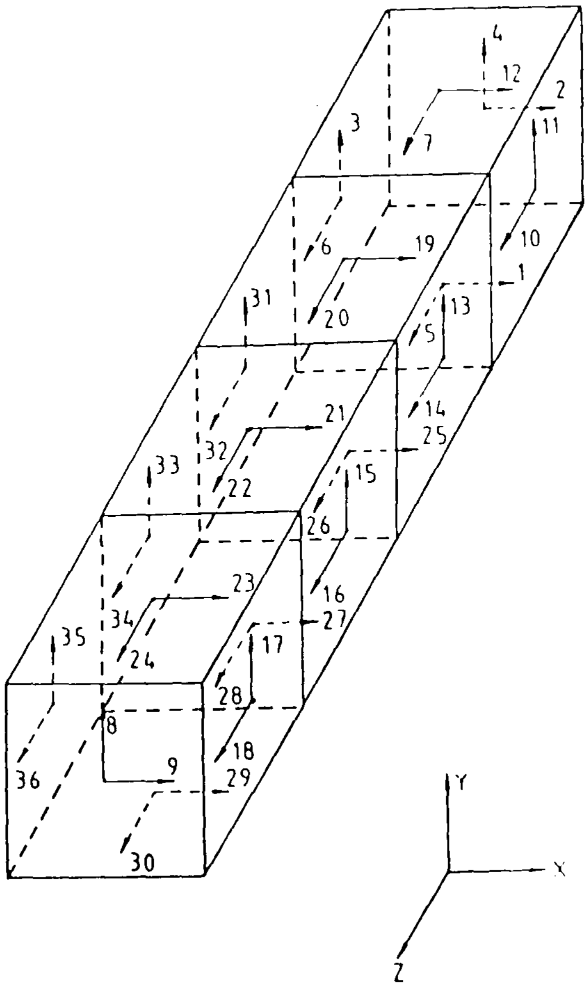

the wire element. However, there was a problem with the interconnection between adjacent wire elements. Initially matched (PCB) boundaries were used between elements. This did not produce a suitable model - the voltage and current resonances, previously obtained, for this type of geometry (Chapters 3 and 4), could not be located. The averaging of fields at the boundary between the wire elements seems to make the model lossy and corrupts the fine mesh field description between wire elements in a similar way to the terminating boundary problem described earlier (and in figure 6.11). In an attempt to reduce the losses and preserve field description open-circuit boundaries were included in the wire elements between the wire sections. This type of boundary was chosen pragmatically; the end of a free-wire is open-circuit, so try an open-circuit at the end of the wire element. This was non-physical when the elements were joined together and so does not provide a suitable model.

Connecting wire elements together using any of the standard boundaries (matched, open-circuit, short-circuit) proved to be an inaccurate model of a length of wire.

6.4.2 Long Wire Elements

Since it was not possible, using the method outlined in this chapter, to join wire elements together to form a long wire, a long wire element was developed. To achieve this a wire is modelled in a volume of space $4\Delta\ell \times \Delta\ell \times \Delta\ell$ (coarse mesh) as shown in figure 6.17. The figure shows the numbering of the transmission-lines in this configuration. In general there will be 4 + (length in $\Delta\ell$) x 8 transmission-lines for the long element. For a $4\Delta\ell$ long element, chosen for computational limitation only, there are 36 lines. It is envisaged that any length or complexity of wire could be pre-solved, the penalties being very large storage for the scattering matrix; large execution times to obtain and use the matrix and difficulty in defining the path of the wire in the coarse mesh.

Simple comparisons with the single-slice geometry were performed to establish that the method works using a wire above ground geometry. Later results will be obtained for the resonant cavity geometry.

6.4.2.1 Wire-Above-Ground

The previous 0.2m wire geometry of figure 6.15 was res-solved with z-dimension = $4\Delta\ell$ giving a pre-solved long-wire element. This element was then included, at various heights, in a $4\Delta\ell$ long version of the figure 6.9 geometry. Both types of diakoptic boundaries were tried, AVB and PCB. The flux and current for each model were calculated at zero frequency in the usual way.

These results were compared with those obtained from a single-slice (PCB) model and for a wire composed of short-circuit nodes (from Chapter 4 the radius of this wire in this geometry is 0.267 m). Table 6.5 and figure 6.18 summarise the results.

Table 6.5 Comparison of flux and currents at different heights using single-slice, long-wire and short-circuit node wire representations.

Excitation 6.2c, 500 iterations (20 samples)

Height	Single-slice & Long-wire (PCB)		Long-wire (AVB)		short-circuit node	
	flux ($\times\mu_0$ Hm^{-1})	current	flux ($\times\mu_0$ Hm^{-1})	current	flux ($\times\mu_0$ Hm^{-1})	current
(m)		(A)		(A)		(A)
0.5	0.646	1.018	0.025	0.174	0.25	1.691
1.5	0.120	0.171	0.060	0.167	0.25	0.475
2.5	0.098	0.162	0.076	0.161	0.25	0.559
3.5	0.099	0.157	0.086	0.156	0.25	0.481
4.5	0.102	0.152	0.094	0.151	0.25	0.428
5.5	0.107	0.148	0.101	0.147	0.25	0.387

Figure 6·18 Inductance vs height calculated from table 6·5

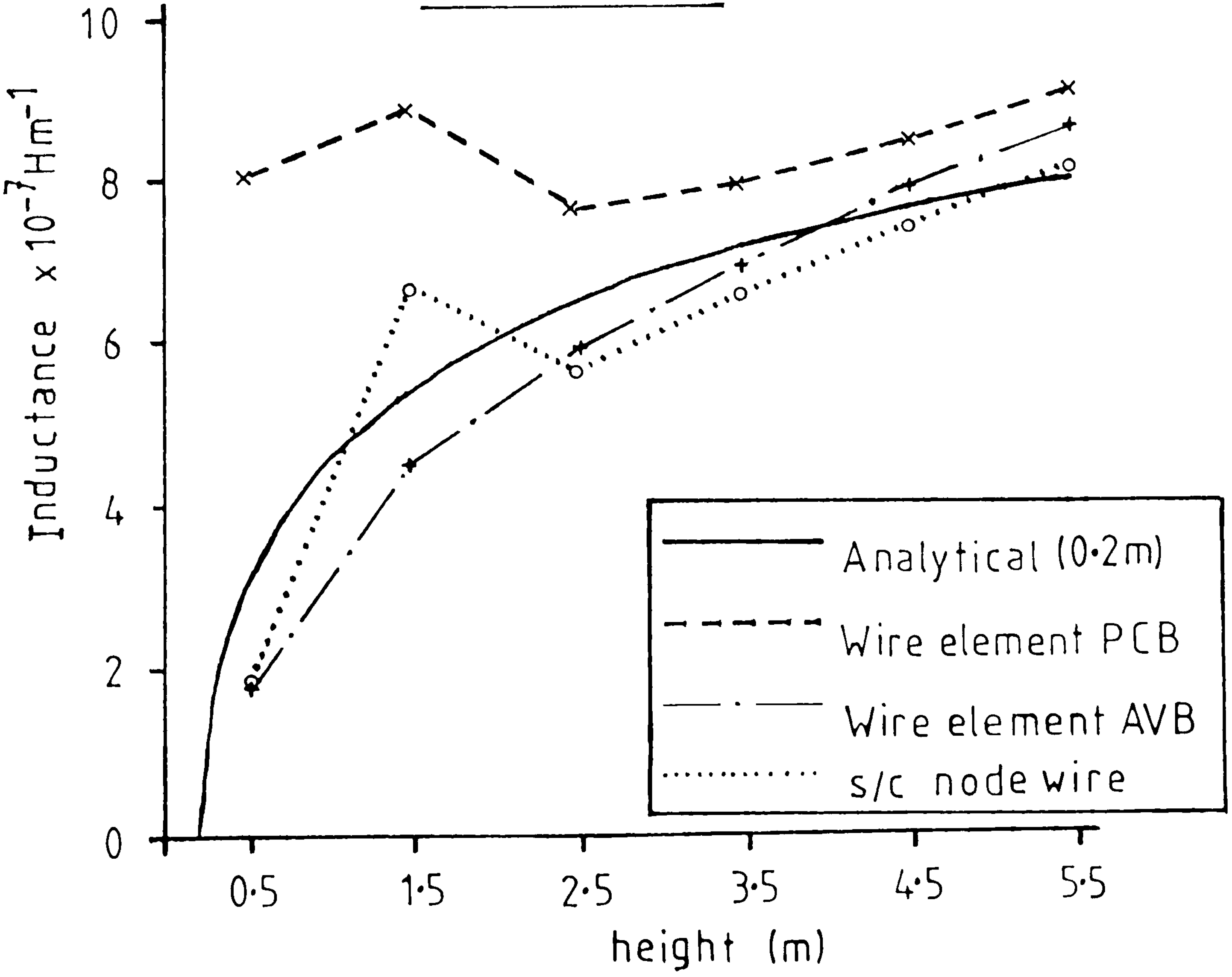

The long and short (PCB) wires provide identical results - verifying the long wire element model. But as can be seen from figure 6.18 and Table 6.6, where the inductances computed by the long-wire model are compared, that the PCB model gives inductances which are almost independent of the height. The AVB model, whilst not in total agreement with the analytical curve is the most accurate model, closely followed by the short-circuit node wire.

Table 6.7 shows how the errors in the long-wire (PCB) model can be reduced by using a matrix with 15 time samples per matrix element. With 40 samples per matrix element (not shown) the resulting inductances are almost identical to those of Table 6.6 (20 samples). For this reason most future results will use a matrix of 20 samples.

The reduction in error with 15 samples is somewhat odd. It seems unlikely that a reduction in information present will improve accuracy. What seems to be happening is that increasing the number of samples gives convergence to the wrong answer. The wire element does not, in the limit, model the correct radius. The matrix obtained with 15 samples therefore adds a truncation error to the modelling error. Fortunately, this has led to a cancellation in errors - giving improved accuracy.

Table 6.6 Variation of long-wire inductance and execution time with height for 20 samples.

Excitation 6.2c.

Height (m)	Inductance ($x10^{-7}$ Hm^{-1}) TLM PCB	TLM AVB	Analytic	%error PCB	%error AVB	Execution time (PCB) (s)
0.5	8.02	1.81	3.13	156.3	42.3	162
1.5	8.82	4.55	5.41	63.0	15.9	162
2.5	7.60	5.93	6.44	18.1	8.0	162
3.5	7.92	6.93	7.11	11.5	2.5	160
4.5	8.43	7.83	7.61	10.8	2.9	161
5.5	9.09	8.63	8.01	13.4	7.8	161
					Average	161
					No wire	73

Table 6.7 Variation of long-wire inductance and execution time with height for 15 samples.

Power Conservation Boundary, excitation 6.2c.

Height (m)	Inductance ($x10^{-7}$ Hm^{-1}) TLM	Analytic	%error	Execution time (s)
0.5	7.06	3.13	125.5	140
1.5	7.17	5.41	32.6	140
2.5	7.05	6.44	9.4	141
3.5	7.63	7.11	7.3	140
4.5	8.31	7.61	9.2	140
5.5	9.01	8.01	12.5	140
			Average	140

6.4.2.2 Coaxial Wire Geometries - Resonant Cavity Technique

The long wire element detailed above can be used in the coaxial geometry shown in figure 6.19. The terminating boundary conditions of short-circuit and open-circuit are included in the element. Thus the longest possible wavelength for a propagating wave is 16m as shown. Since the model contains diakoptic boundaries it is not possible to excite the wire in the usual way (Chapters 3, 4 and figure 6.20a). This is because of the problem, described earlier in this chapter, where a permanent charge is left at excitation points which cross the diakoptic boundaries. An alternative excitation, shown in figure 6.20b, was used for all long wire geometries. This injects a current into the short-circuit termination (the point where current is a maximum for a 16m wavelength).

Using the coarse mesh ($\Delta\ell$ = 1m) in the figure 6.19 geometry, three pre-solved long wire elements (radii = 0.167m, 0.2m using short-circuit nodes and 0.2m not using short-circuit nodes) were modelled. Power conservation and averaging boundaries were tested separately. The effect of including an instantaneous reflection term in the scattering matrix was also investigated.

Tables 6.8 to 6.13 show the radii obtained from a TLM computation for various iterations of the coarse mesh at four distances along the wire. A summary table is also shown in Table 6.14.

Figure 6·19 Geometry and wavelength for 4m wire element

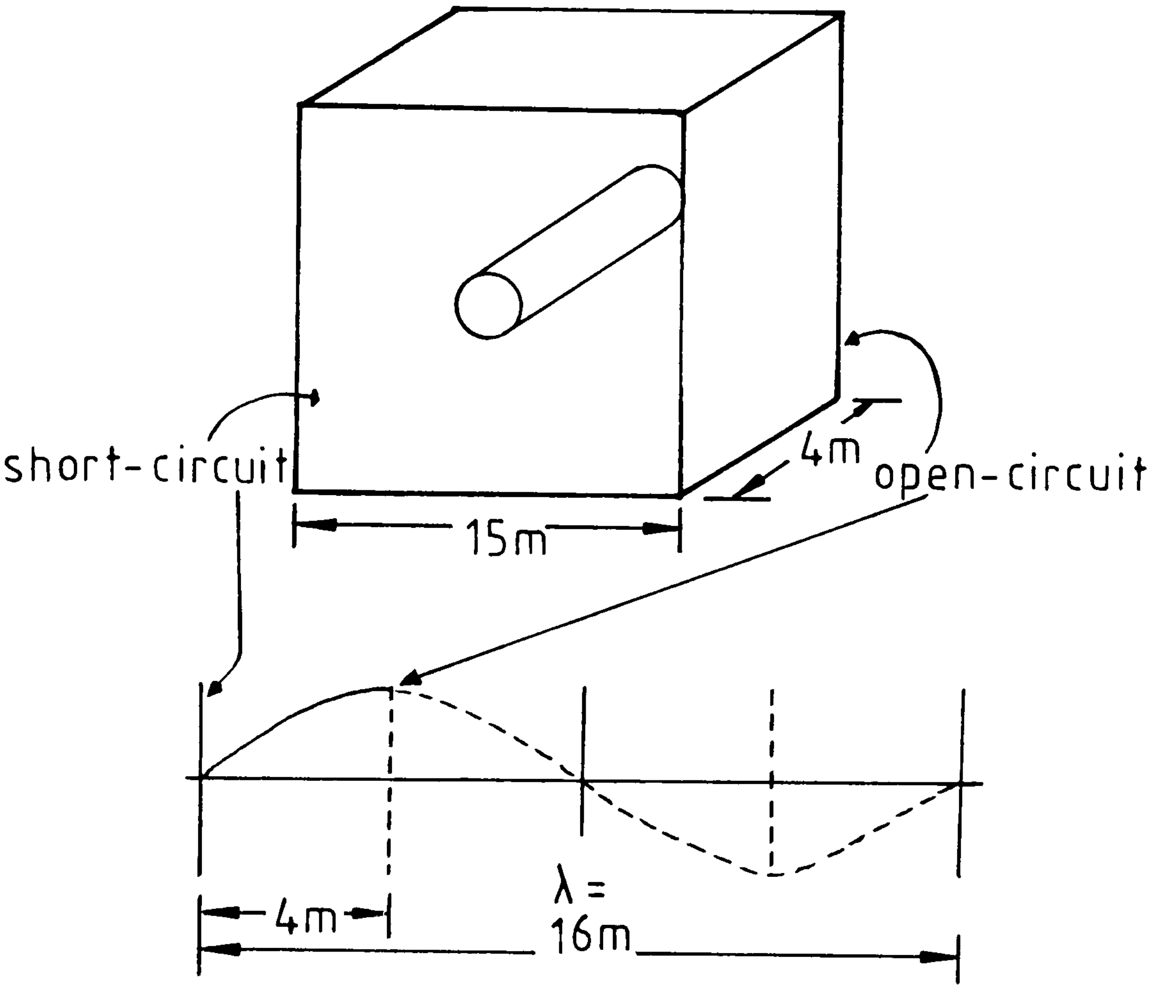

Figure 6·20 Excitation of wire elements

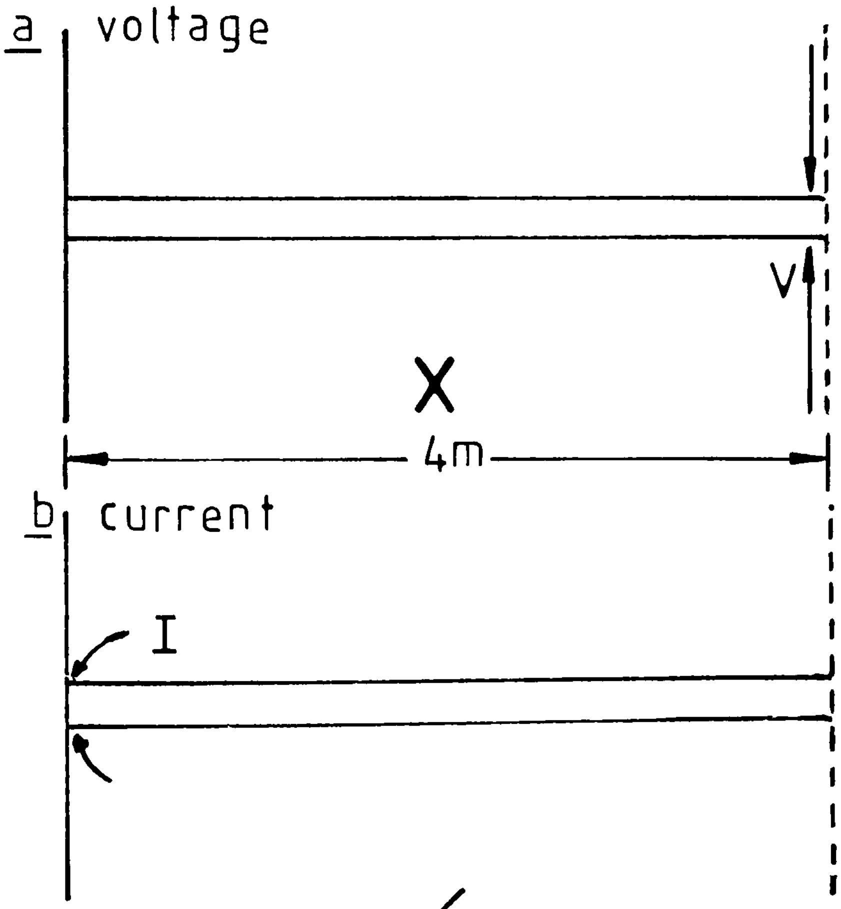

✓

Table 6.8 Modelled radius of 0.167m wire (figure 6.10)

Power Conservation Boundaries

Instantaneous scattering

Resonant frequency = 20.35 MHz , λ = 16m , velocity = $3.256x10^8$

Number of iterations	radii at			
	0.5m	1.5m	2.5m	3.5m
1500	0.282	0.282	0.282	0.282
1000	0.308	0.308	0.309	0.310
750	0.280	0.280	0.281	0.281
500	0.213	0.217	0.228	0.241

Average radius	0.274
error in average	64.07%

Non-instantaneous scattering

Resonant frequency = 19.70 MHz , λ = 16m , velocity = $3.152x10^8$

Number of iterations	radii at			
	0.5m	1.5m	2.5m	3.5m
1500	0.347	0.346	0.345	0.345
1000	0.342	0.340	0.338	0.339
750	0.412	0.413	0.409	0.405
500	0.332	0.336	0.336	0.333

Average radius	0.357
error in average	114.00%

Table 6.9 Modelled radius of 0.167m wire (figure 6.10)

Averaging Boundaries

Instantaneous scattering

Resonant frequency = 18.10 MHz , λ = 16m , velocity = $2.896\text{x}10^8$

Number of iterations	radii at			
	0.5m	1.5m	2.5m	3.5m
1500	0.259	0.255	0.252	0.252
1000	0.151	0.152	0.154	0.154
750	0.141	0.141	0.139	0.138
500	0.243	0.247	0.257	0.268
		Average radius		0.200
		error in average		19.87%

Non-instantaneous scattering

Resonant frequency = 17.35 MHz , λ = 16m , velocity = $2.776\text{x}10^8$

Number of iterations	radii at			
	0.5m	1.5m	2.5m	3.5m
1500	0.280	0.278	0.279	0.282
1000	0.239	0.228	0.219	0.219
750	0.224	0.227	0.221	0.210
500	0.221	0.215	0.202	0.187
		Average radius		0.233
		error in average		39.60%

Table 6.10 Modelled radius of 0.2m wire (figure 6.15)

Power Conservation Boundaries

Instantaneous scattering

Resonant frequency = 19.75 MHz , λ= 16m , velocity = $3.160\text{x}10^8$

Number of iterations	radii at			
	0.5m	1.5m	2.5m	3.5m
1500	0.376	0.376	0.376	0.376
1000	0.374	0.373	0.372	0.372
750	0.430	0.431	0.432	0.431
500	0.386	0.387	0.395	0.403
		Average radius		0.393
		error in average		96.56%

Non-instantaneous scattering

Number of iterations	radii at			
	0.5m	1.5m	2.5m	3.5m
1500	0.407	0.410	0.410	0.409
1000	0.412	0.413	0.414	0.412
750	0.424	0.426	0.426	0.423
		Average radius		0.416
		error in average		107.75%

Table 6.11 Modelled radius of 0.2m wire (figure 6.15)

Averaging Boundaries

Instantaneous scattering

Resonant frequency = 18.10 MHz , λ = 16m , velocity = $2.896\text{x}10^8$

Number of iterations	radii at			
	0.5m	1.5m	2.5m	3.5m
1500	0.305	0.301	0.298	0.299
1000	0.171	0.173	0.176	0.177
750	0.221	0.220	0.220	0.221
500	0.334	0.340	0.356	0.373
		Average radius		0.262
		error in average		30.78%

Non-instantaneous scattering

Resonant frequency = 17.35 MHz , λ = 16m , velocity = $2.770\text{x}10^8$

Number of iterations	radii at			
	0.5m	1.5m	2.5m	3.5m
1500	0.226	0.218	0.212	0.215
1000	0.250	0.220	0.220	0.220
750	0.244	0.242	0.233	0.222
500	0.243	0.235	0.214	0.192
		Average radius		0.225
		error in average		12.69%

Table 6.12 Modelled radius of 0.2m wire (figure 6.21)

Power Conservation Boundaries

Instantaneous scattering

Resonant frequency = 19.80 MHz , λ = 16m , velocity = 3.168x10^{8}

Number of iterations	radii at			
	0.5m	1.5m	2.5m	3.5m
1500	0.333	0.332	0.333	0.333
1000	0.347	0.346	0.346	0.345
750	0.382	0.383	0.382	0.380
500	0.335	0.338	0.337	0.332
		Average radius error in average		0.349 74.50%

Non-instantaneous scattering

Number of iterations	radii at			
	0.5m	1.5m	2.5m	3.5m
1500	0.352	0.354	0.355	0.354
1000	0.381	0.382	0.382	0.381
750	0.376	0.377	0.375	0.370
		Average radius error in average		0.370 84.96%

Figure 6·21 Cross-section of wire element

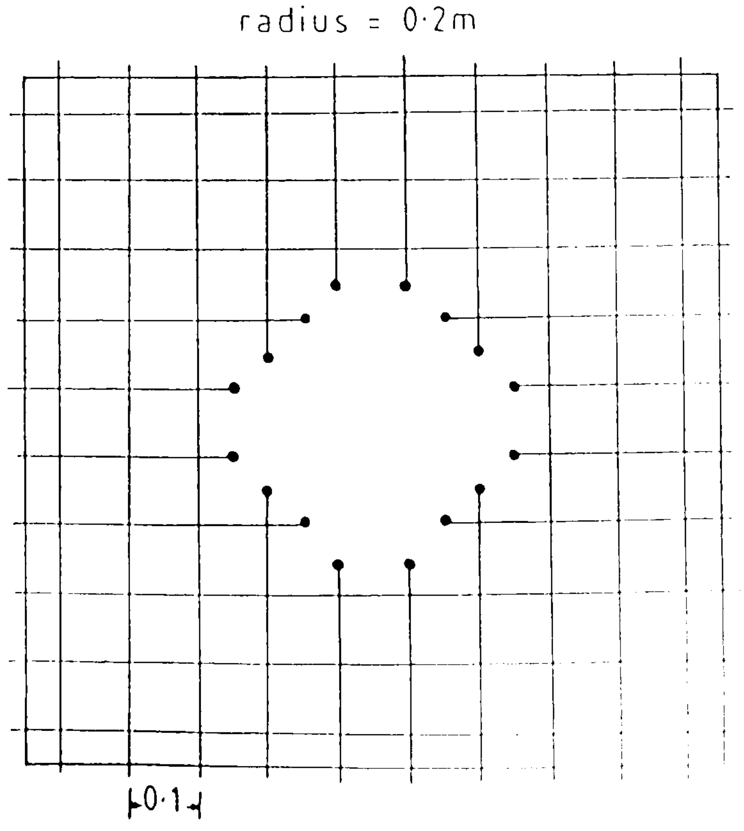

Table 6.13 Modelled radius of 0.2m wire (figure 6.21)

Averaging Boundaries

Instantaneous scattering

Resonant frequency = 17.35 MHz , λ = 16m , velocity = 2.776×10^{8}

Number of iterations	radii at			
	0.5m	1.5m	2.5m	3.5m
1500	0.227	0.225	0.225	0.226
1000	0.214	0.207	0.200	0.200
750	0.210	0.211	0.207	0.198
500	0.208	0.203	0.190	0.176
		Average radius		0.208
		error in average		3.97%

Non-instantaneous scattering

Resonant frequency = 17.40 MHz , λ = 16m , velocity = 2.784×10^{8}

Number of iterations		radii at		
	0.5m	1.5m	2.5m	3.5m
1500	0.301	0.308	0.313	0.315
1000	0.253	0.254	0.256	0.259
750	0.275	0.277	0.267	0.250
500	0.275	0.265	0.248	0.232
		Average radius		0.272
		error in average		35.88%

Table 6.14 Summary of wire element results.

Description	frequency (MHz)	velocity $\times 10^8$ (ms^{-1})	velocity % error	Average radius (m)	Average radius % error
0.167 PCBi*	20.35	3.256	8.608	0.274	64.07
0.167 PCBn*	19.70	3.152	5.139	0.357	114.00
0.167 AVi	18.10	2.896	-3.400	0.200	19.87
0.167 AVn	17.35	2.776	-7.403	0.233	39.60
0.2s+ PCBi	19.75	3.160	5.406	0.393	96.56
0.2s PCBn	-	-	-	0.416	107.75
0.2s AVi	18.10	2.896	-3.400	0.262	30.78
0.2s AVn	17.35	2.770	-7.603	0.225	12.69
0.2 PCBi	19.80	3.168	5.673	0.349	74.50
0.2 PCBn	-	-	-	0.370	84.96
0.2 AVi	17.35	2.770	-7.603	0.208	3.97
0.2 AVn	17.40	2.780	-7.269	0.272	35.88

* i = instantaneous scattering, n = non-instantaneous.
\+ description contains short-circuit nodes (figure 6.15)

Table 6.15 Variation in modelling accuracy with finer mesh.

a) Power Conservation Boundaries. Figure 6.2c excitation.

mesh description	frequency (MHz)	radius (m) range	radius (m) average	radius (m) theoretical
3 x 3	19.05	$0.412 < r < 0.541$	0.484	0.212
5 x 5	19.20	$0.218 < r < 0.280$	0.248	0.127
7 x 7	19.25	$0.118 < r < 0.222$	0.178	0.091
9 x 9	19.25	$0.018 < r < 0.206$	0.139	0.071
11 x 11	19.35	$0.010 < r < 0.169$	0.145	0.058

b) Averaging Boundaries. Figure 6.2c excitation.

mesh description	frequency (MHz)	radius (m) range	radius (m) average	radius (m) theoretical
3 x 3	17.35	$0.279 < r < 0.345$	0.309	0.212
5 x 5	17.50	$0.066 < r < 0.210$	0.139	0.127
7 x 7	17.50	$0.047 < r < 0.164$	0.102	0.091
9 x 9	17.50	$0.028 < r < 0.222$	0.100	0.071

All results using figure 6.2b excitation highly unstable.

Surprisingly, the averaging boundary gives consistently more accurate modelled radii when compared with the power conservation boundary. Generally, both boundaries give a error < 9% for the velocity of propagation. The use of instantaneous scattering reduces the modelled radius and improves the accuracy.

The PCB results give a modelled radius approximately double the desired radius. To determine whether this is due to the nearness of the side boundaries in the wire element, the simple wire geometries shown in figure 6.21a were pre-solved (with both types of diakoptic boundaries and both types of excitation). From the results obtained in Chapter 3 the radius of such wires should be $0.636\Delta\ell$. Table 6.15 shows that the increased number of nodes between the wire and the PCB does not reduce the error. For an AVB the average results are more accurate, but the range of results is much wider. In fact the results for AVB were very iteration dependent. For the 5 x 5 mesh description the overall average radius was 0.139m but this is the average for 2000, 1500, 1000 and 750 iterations. Taking each of these iterations in turn the approximate average radii are 0.07, 0.09, 0.2, 0.19 showing a clear distinction between high and low numbers of iterations. (Taking the average over 1000 and 750 iterations leads to $r = 0.198$m compared with the theoretical answer of 0.127m).

This sort of error occurs with both types of boundaries and is due to the filtering function used.

Figure 6·21a Simple wire geometries

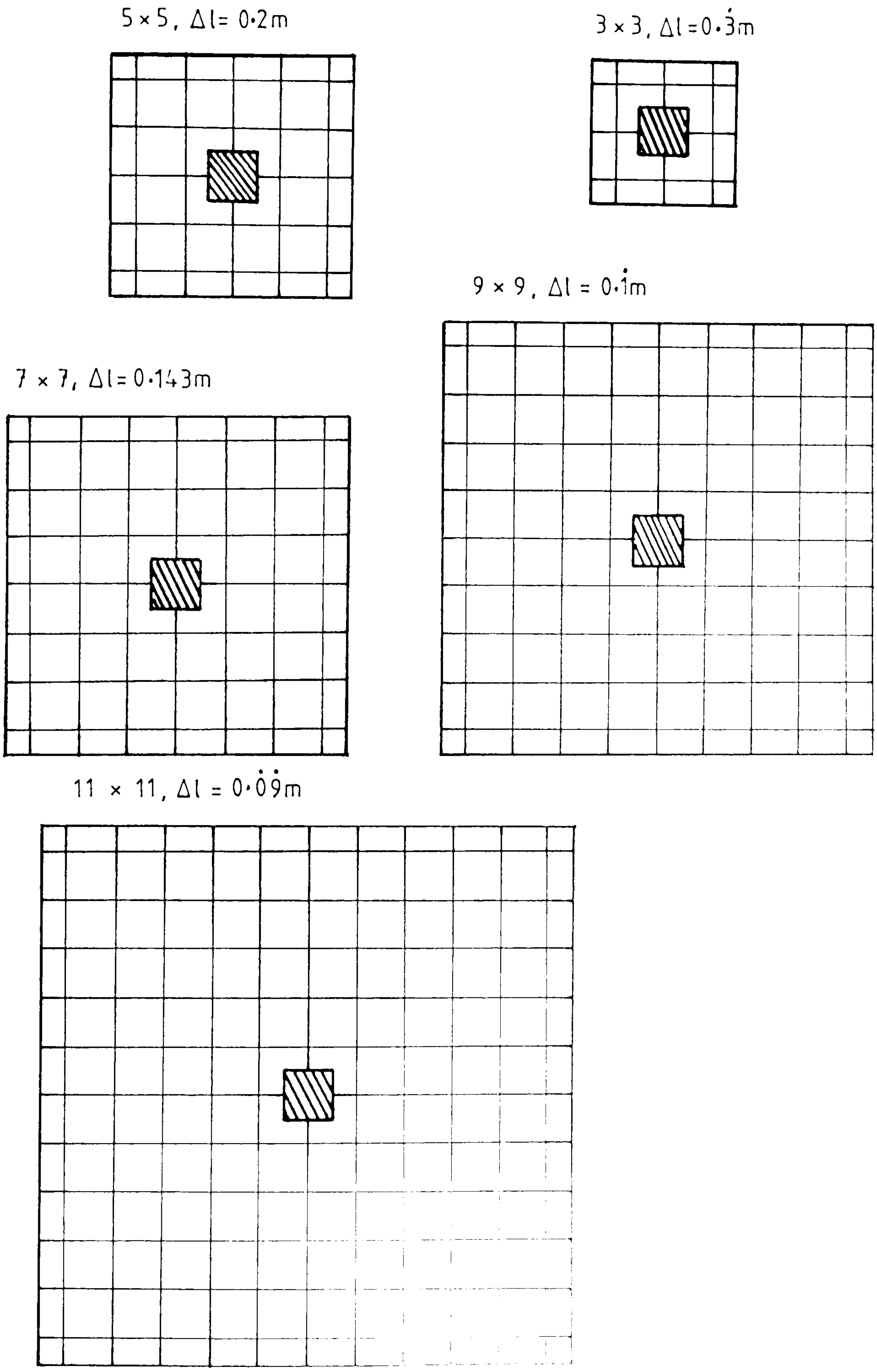

5×5, $\Delta l = 0{\cdot}2$m

3×3, $\Delta l = 0{\cdot}\dot{3}$m

9×9, $\Delta l = 0{\cdot}\dot{1}$m

7×7, $\Delta l = 0{\cdot}143$m

11×11, $\Delta l = 0{\cdot}\dot{0}\dot{9}$m

Since this is not ideal errors are introduced as explained in Chapter 5. For a low number of iterations (e.g. 500) of the coarse mesh this is not important but, as shown in figure 6.22, after 1500 iterations the predicted voltage has become unstable. At 3500 iterations a clear error is observed.

6.5 Discussion

Clearly neither the averaging nor the power conservation boundaries are entirely satisfactory. The actual averaging process is required so that the fine mesh can be connected to the coarse mesh. But the use of averaging (either boundary) reduces the accuracy of the model, particularly at the boundary. The averaging used is rather crude - 81 lines reduced to one for 0.167m or 100 to one for 0.2m wires. The use of multiple boundaries at the terminations does improve accuracy but requires much more work and storage. Including the terminating boundary in the wire element is by far the best solution to the problem.

Boundaries between wire elements are far more difficult to determine. An ideal solution would be to have no averaging at these boundaries. This can only be realistically achieved in the long wire element geometry (no boundary). Even this requires an excessive amount of computer resources to generate and store the scattering matrix.

Figure 6·22 Voltage observed with time (iterations) for wire element model

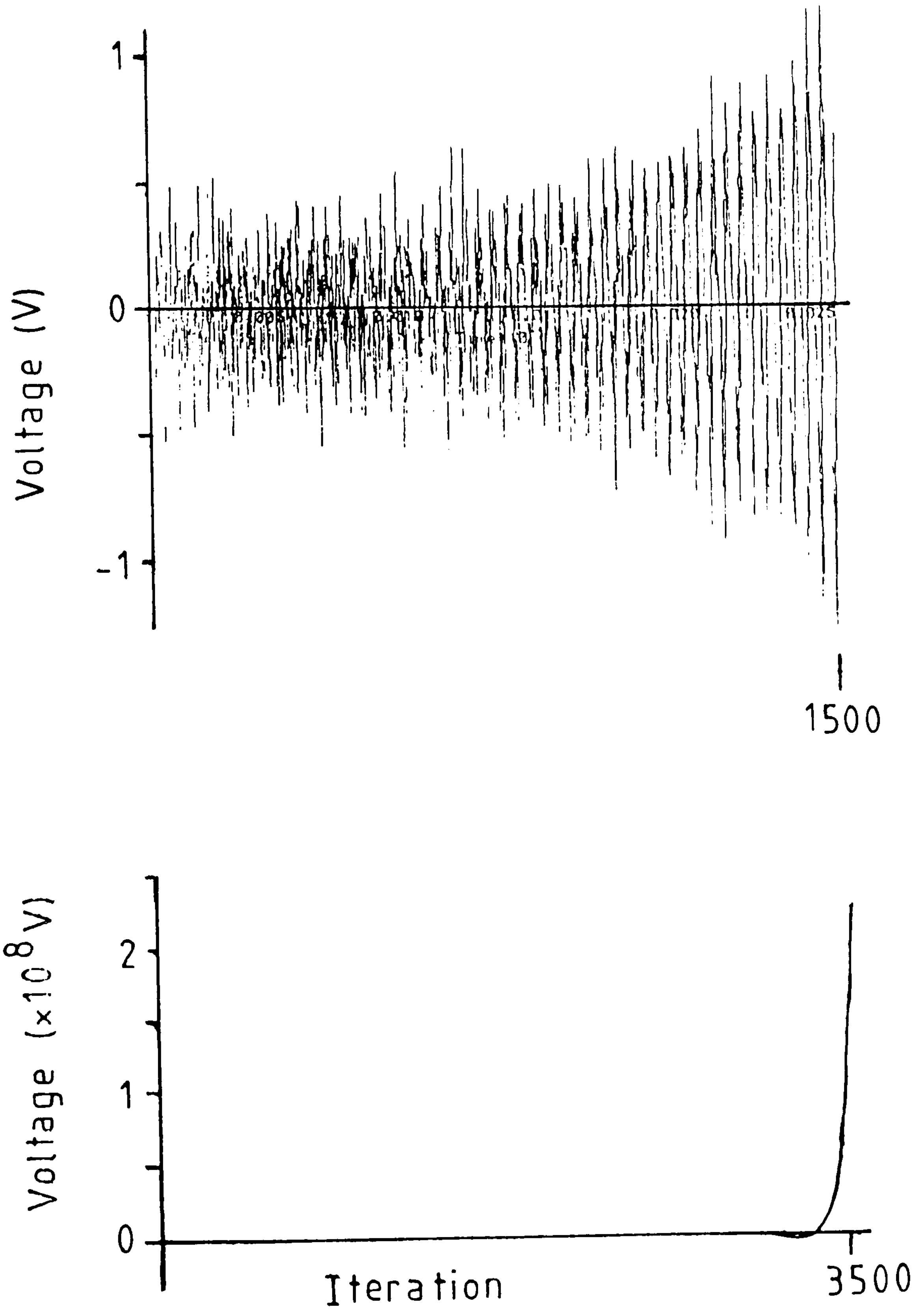

The averaging boundary is non-physical and lossy whilst the power conservation boundary enables propagation velocities larger than light. It is the very nature of the PCB that causes the problem. The free-space conditions are not observed by the boundary because there are reflections back into the fine-mesh from the boundary, as shown in figure 6·23a. Thus $\varepsilon_2 \neq 1$, which changes the modelled radius. Also a wave propagating at an angle to the wire axis will be partially reflected by the PCB (figure 6.23b). When the scattering matrix of such a wire element is computed and then filtered using the standard low-pass filter (Chapter 5) more information about a pulse incident at A is available at B instantly (which is clearly incorrect) than is the case for an averaging boundary (6.23c).

For the averaging boundary $\varepsilon_2 = 1$ and so the modelled radius is more accurate. The velocity of propagation will be less than light because information is lost by the boundary. This is particularly true of directional information of oblique waves (although this is also true of the PCB).

The use of instantaneous scattering gives a more accurate result. This is because one extra, significant, term previously truncated from the filtered impulse response defining the scattering matrix of the element has been included.

Frequency Domain Diakoptics has not been used for pre-solved elements because, for each node modelled, a

Figure 6.23 Reflections from diakoptic boundaries

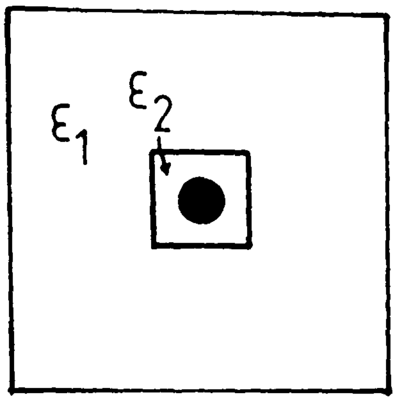

b) PCB ($\varepsilon_2 \neq \varepsilon_1$)

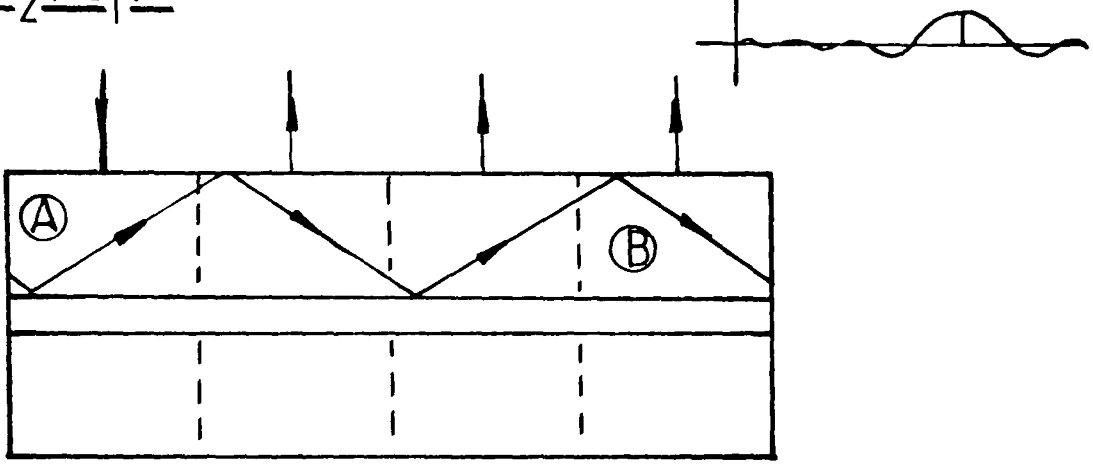

c) Averaging boundary ($\varepsilon_2 = \varepsilon_1$)

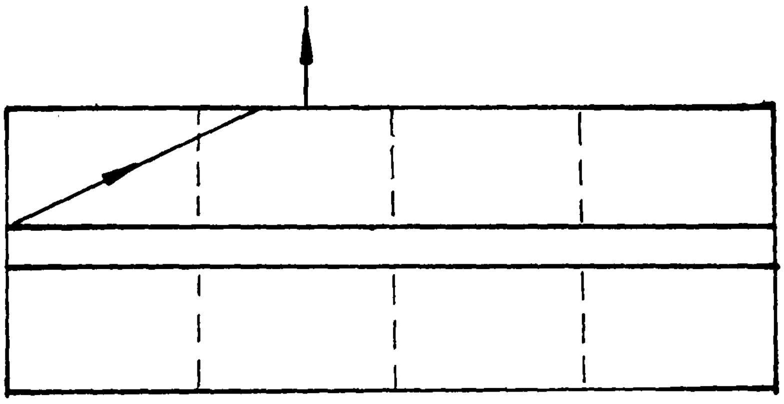

12 x 12x(number of frequency steps) matrix would be required. This was far too large to be stored (677 Kbytes approximately).

6.6 Conclusions

Whilst it is possible to model variable radii using a pre-solved element technique it can be difficult to predict what radius is being modelled.

Terminating boundaries are best included in the wire element.

The averaging diakoptic boundary gives the best balance of accurate radius and realistic velocity of propagation.

Long wire elements, whilst requiring large computational effort, are considerably more accurate than many single-sliced elements joined together.

Chapter 7 Comparisons Between the Currents Predicted by the Different TLM Models

7.1 Introduction

The purpose of this chapter is to compare the currents predicted by the different TLM models (Chapters 2, 3,4 and 6).

Firstly, the short-circuit node wire was compared with the 1D solution for a simple infinite wire-above-ground geometry.

Next the same two models were compared for a wire of varying length terminated by non-zero loads. A $\Delta\ell \times \Delta\ell$ (single node) wire was also compared with the 1D solution for a terminated line of fixed length.

Finally, the long wire element, short-circuit node and 1D models were compared for a short wire in a cavity.

7.2 Short-Circuit Node and 1D

7.2.1 Single-Slice

Figure 7.1a shows the 3D geometry used for these comparisons. The excitation was a magnetic field impulse at the position shown. This effectively models a plane wave incident on the wire from above.

The geometry was solved in two separate ways.

First, the short-circuit node was included in the model and the current induced computed using a TLM 3D solver.

Figure 7·1 Single-slice (infinite wire) geometry

a) 3D model

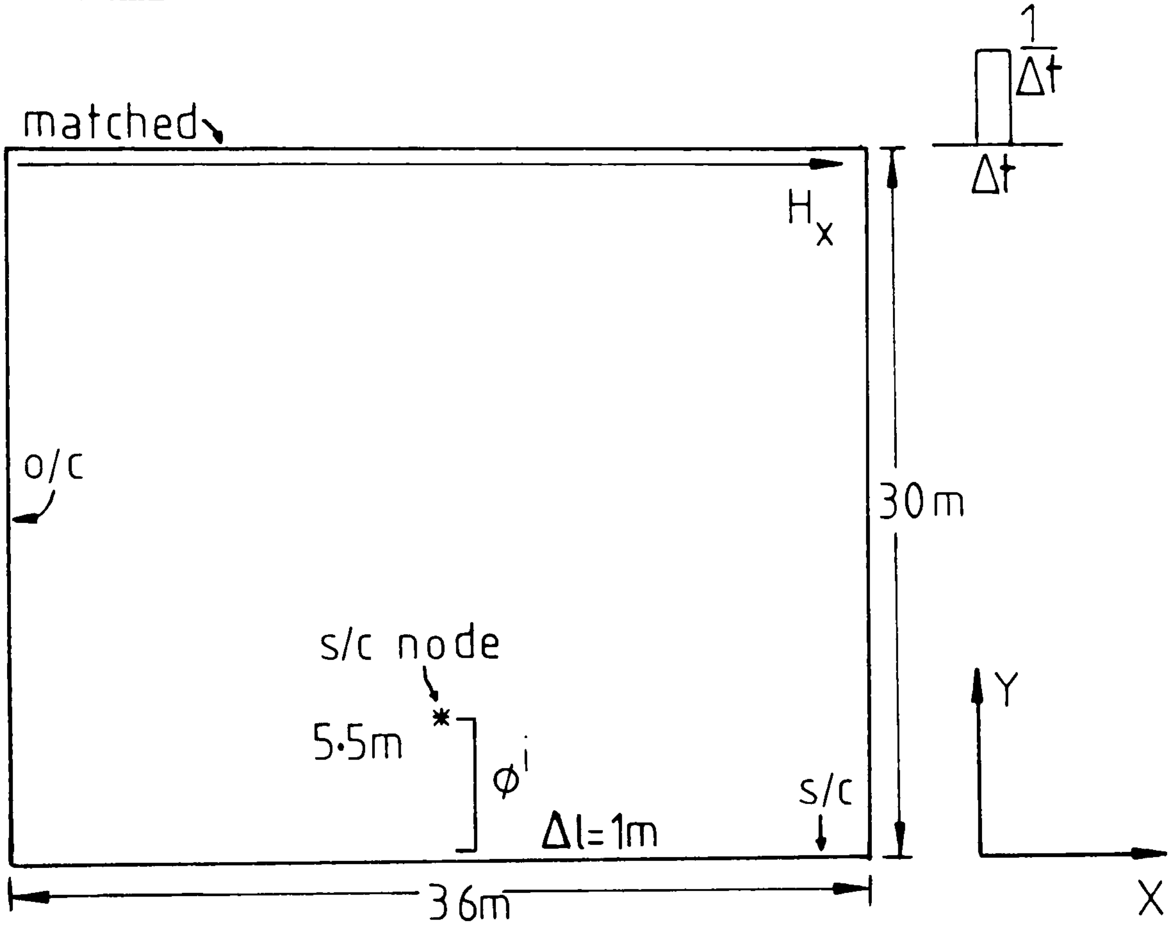

b) 1D model

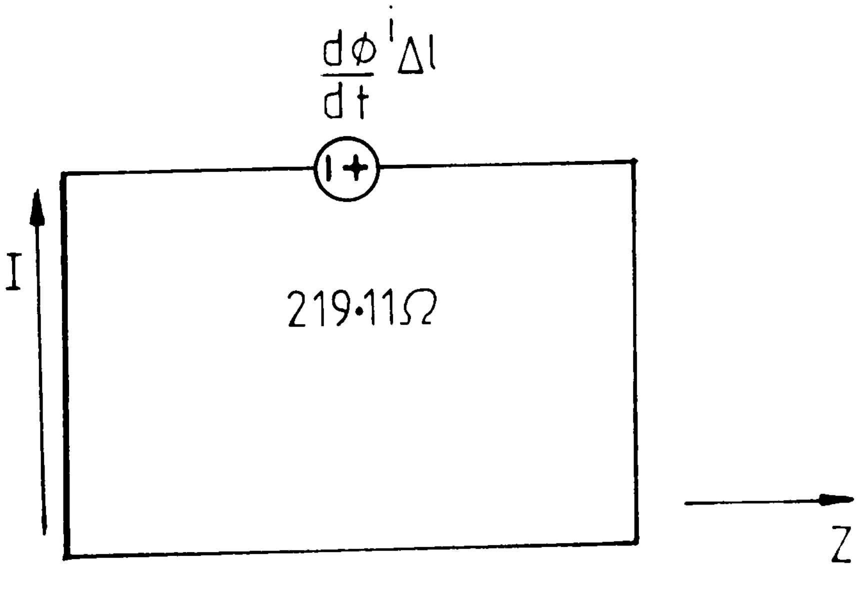

Secondly, the short-circuit node was removed from the 3D model. The incident flux and voltage between the wire position and the ground plane (as a function of time) were then obtained from a separate use of the 3D solver. These flux and voltage responses were differentiated numerically and then filtered and resampled at twice the original time step (to convert from the 3D time step, $\Delta t_{3D} = \Delta \ell/2c$, to the 1D time step, $\Delta t_{1D} = \Delta \ell/c$).

Using the techniques of Chapter 4, the impedance of the wire to ground for the short-circuit node can be obtained from a separate 3D solution of the problem with current excited directly. This gave an impedance of 219.11Ω. With the flux, voltage and impedance the simple 1D model shown in figure 7.1b was used to calculate the current flowing in the short-circuit load. Figures 7.2a and b show the time and frequency domain comparisons between the two methods.

There is reasonable similarity between the 1D and 3D responses. In the time domain, the widths of the responses are equal, the slight delay in the 1D solution being caused by the differentiating and filtering routines. The 3D solution does show the addition of oscillations which are unlikely to be entirely due to TLM noise - that is oscillations at the time step. This oscillation seems to correspond with the peak in the frequency domain at 213 MHz, or $\lambda \simeq 1.4$m. This wavelength cannot be due to a wire resonance but it may be due to some complex resonance between the wire and the outer boundaries of the 3D geometry. The frequency domain responses show broad agreement upto 150 MHz (which is the

Figure 7·2 Comparisons between the 1D and 3D methods for figure 7·1 geometry

a) Time Domain

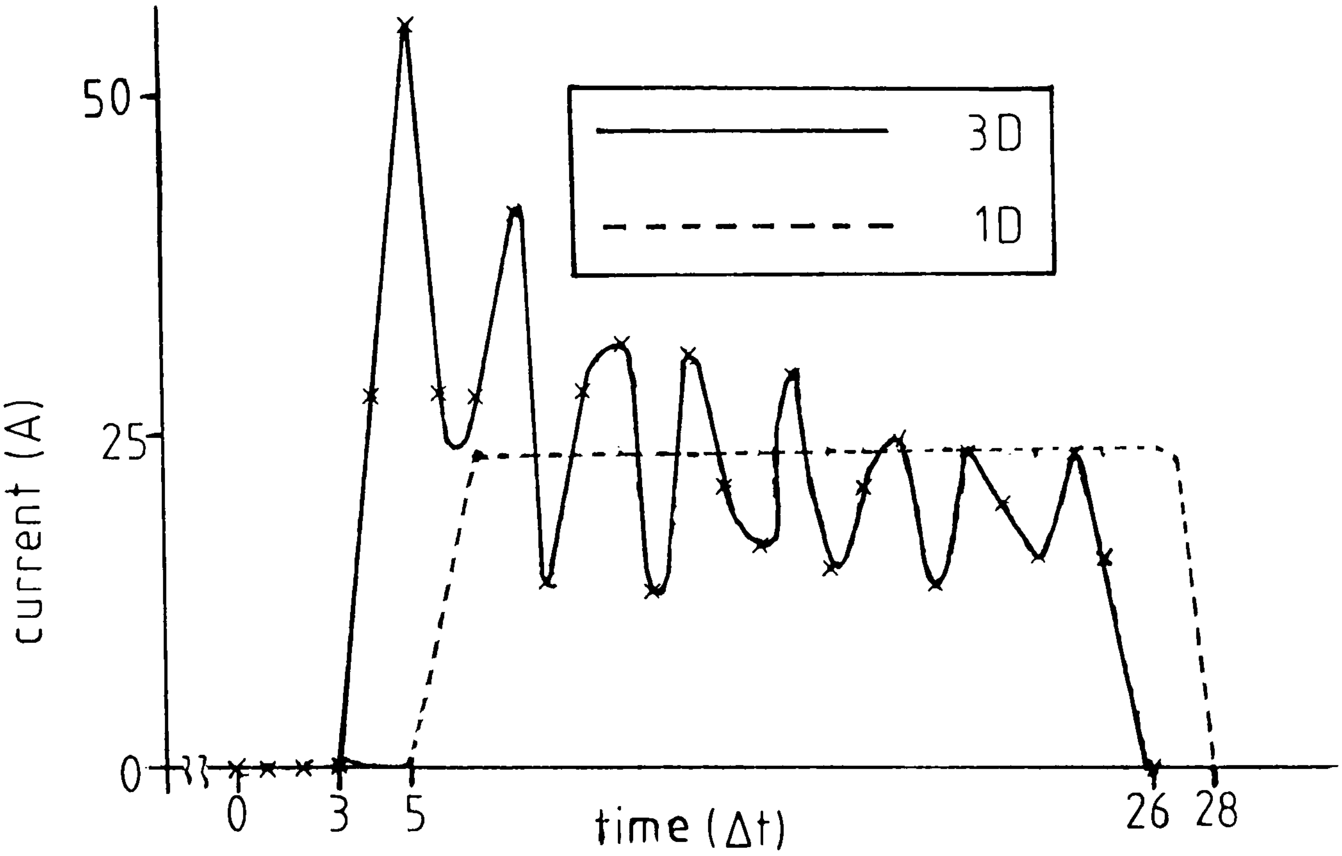

b) Frequency Domain

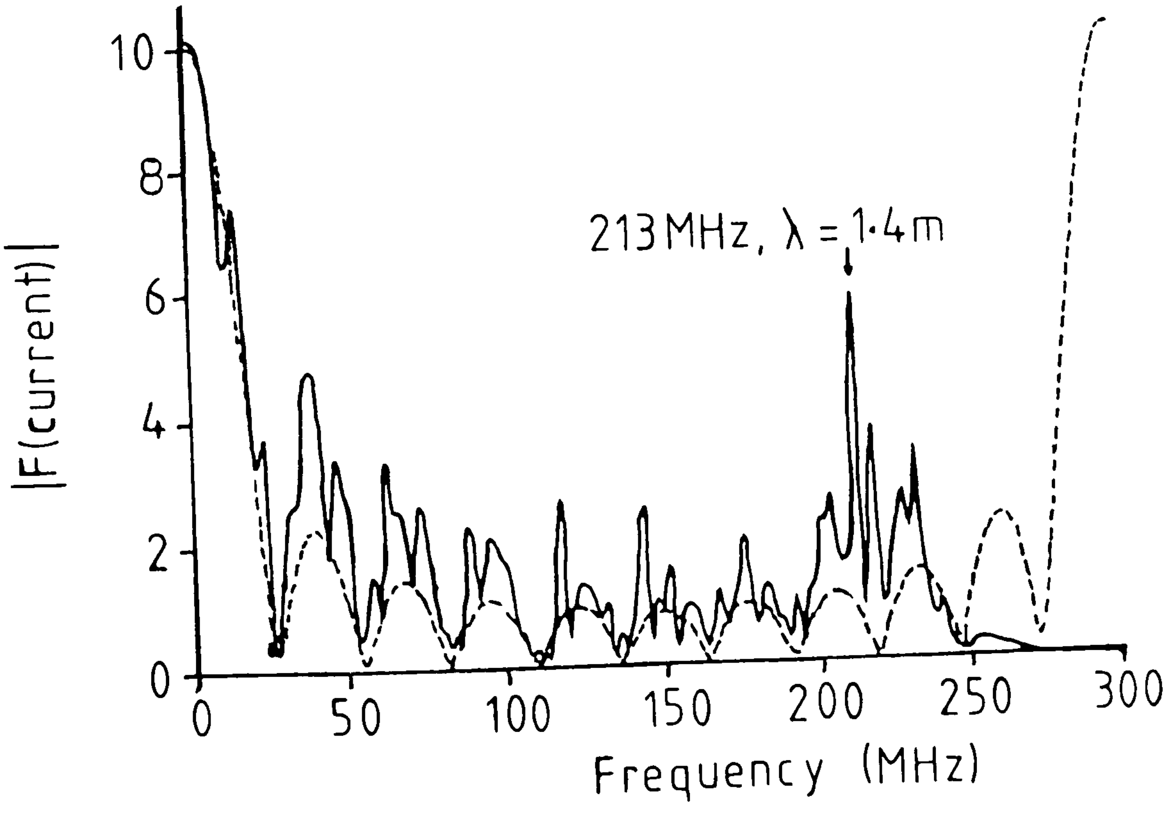

filter cut-off frequency (Nyquist) for the 1D solution). The global minima of the two responses occur at the same frequencies whilst the maxima do not. In addition there are local minima in the 3D solution. The frequencies of these maxima and local minima (in 3D) again do not correspond to any wire resonance nor do they correspond to multiples of the wire to ground length. To test whether these maxima and minima are connected with complex wire to outer boundary resonances, short wires with terminations were investigated.

7.2. Short Wires with Terminations

The short wire geometry is shown in figure 7.3. For the 1D solution the flux and voltage were calculated in the same way as for the previous section, the only difference being the circuit components of the 1D model itself, as shown in figure 7.3b. In the 3D model the 50Ω terminating loads were modelled by imperfectly conducting sheets as shown. The reflection and transmission coefficients of these sheets (ρ,τ) were chosen to model the 50Ω loads in the way indicated by figure 7.3c. To simulate the same condition for the 1D model the same reflection coefficient must characterise the load terminating the wire. Thus a reflection of -0.7657 is again required. Since the characteristic impedance of the 1D line is different to that of free space (201.67Ω not 376.73Ω) the 1D load corresponds to a $50 \times \frac{201.67}{376.73} = 26.77\Omega$ load, as shown in figure 7.3b.

The comparison between the 1D and 3D methods for this geometry are shown in figure 7.4. The difference between the global minima is caused by obtaining the incident flux over

Figure 7·3 4m terminated wire geometry

a) 3D

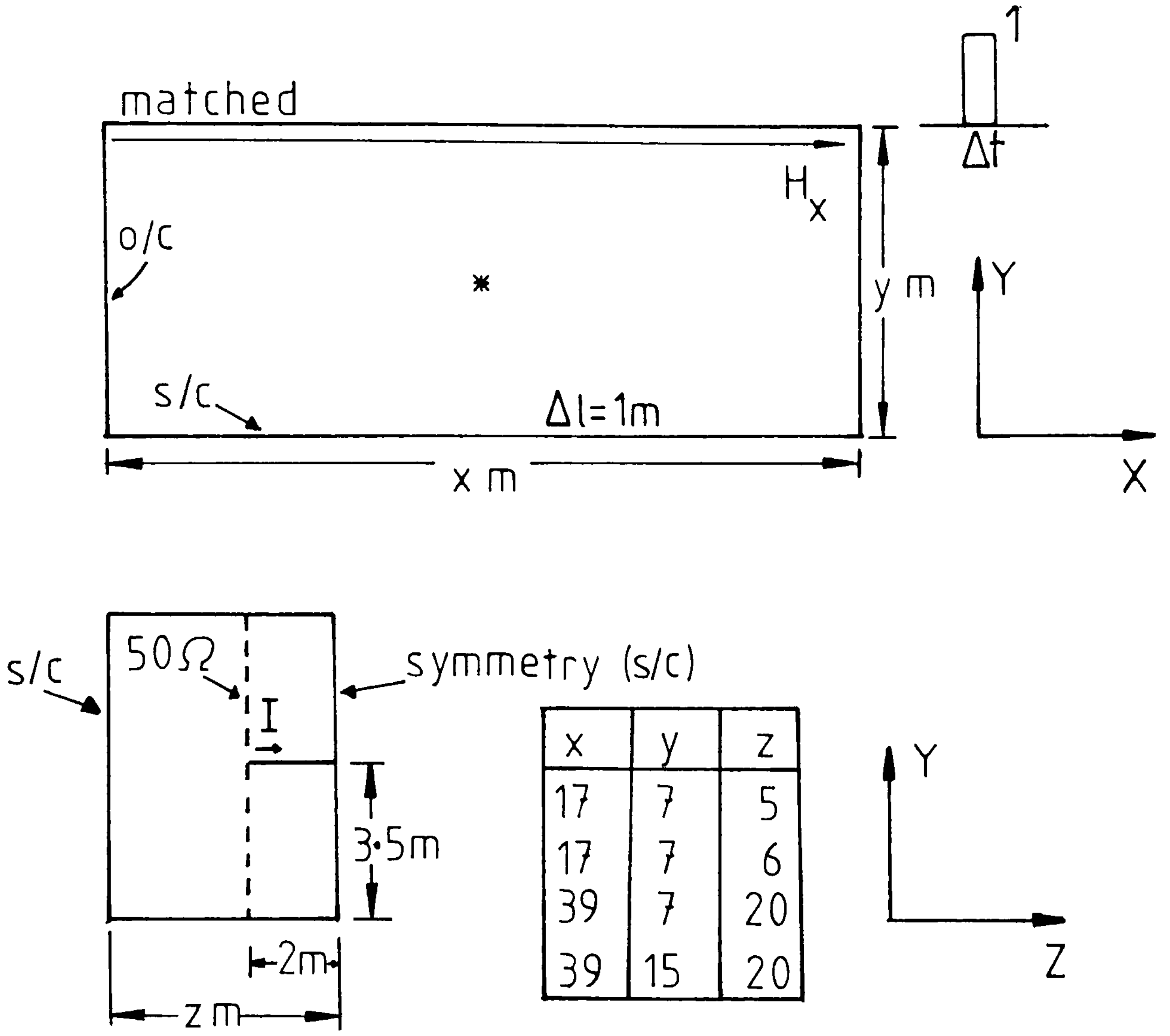

x	y	z
17	7	5
17	7	6
39	7	20
39	15	20

b) 1D

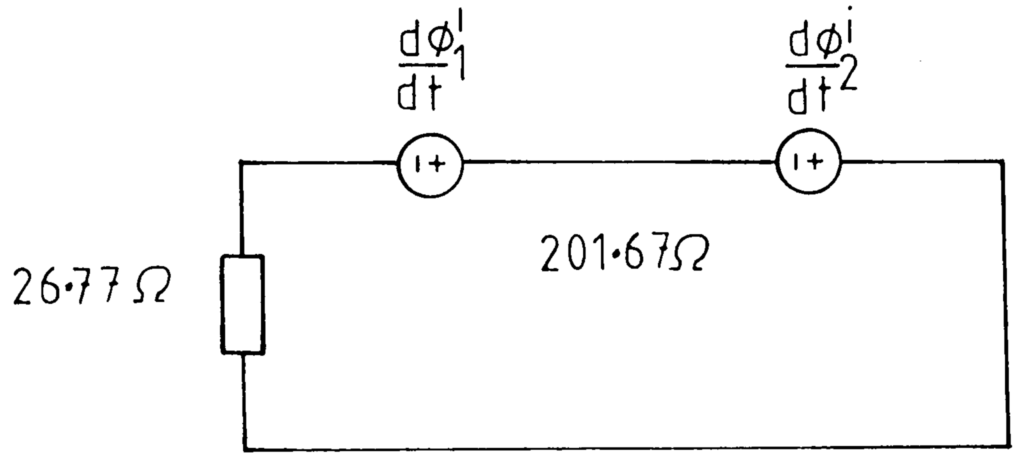

c) 3D load

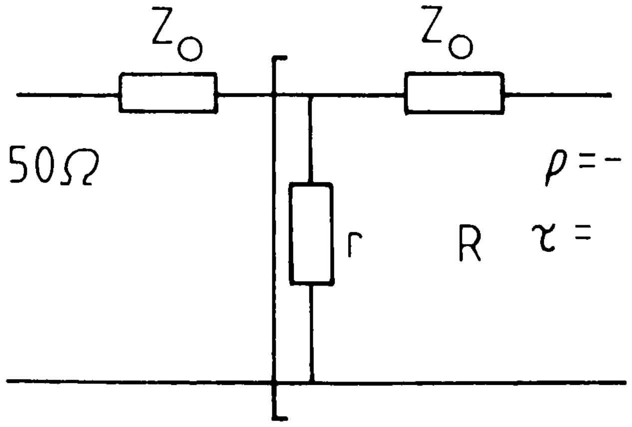

$R = \frac{r Z_0}{r + Z_0} = 50\Omega$

R $\rho = -0{\cdot}7657$

$\tau = 0{\cdot}2343$

Figure 7·4 Frequency comparison between the 1D and 3D methods for figure 7·3 geometry

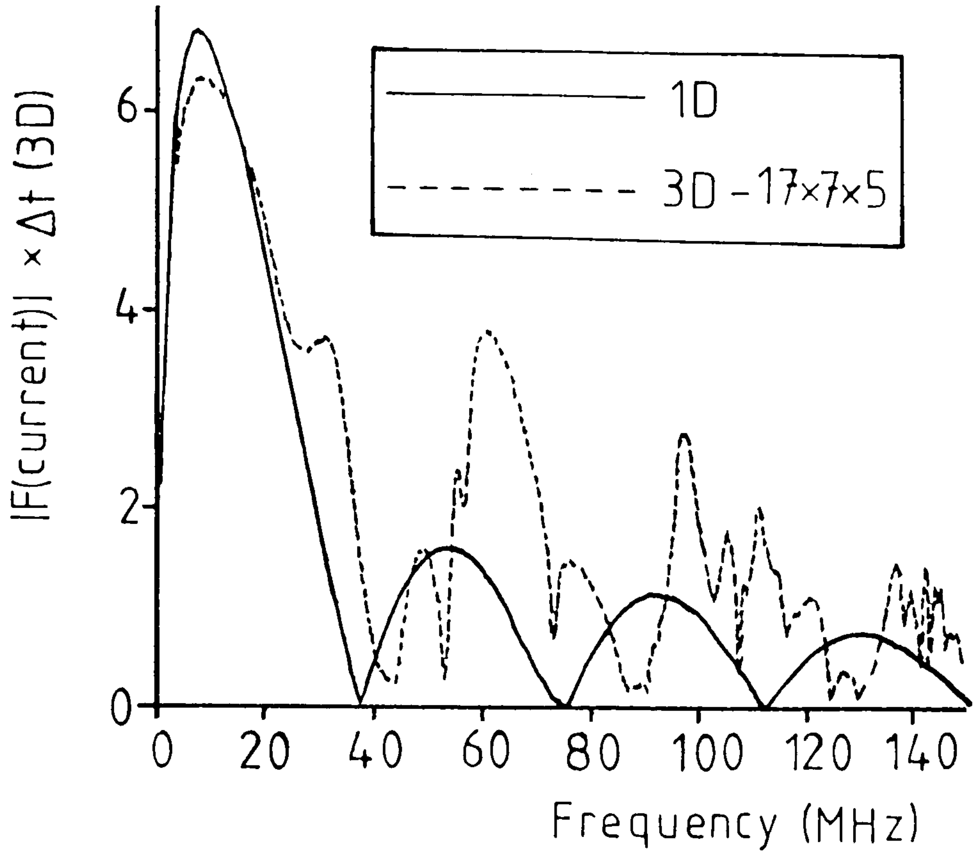

Figure 7·5 Slight variation to 3D geometry

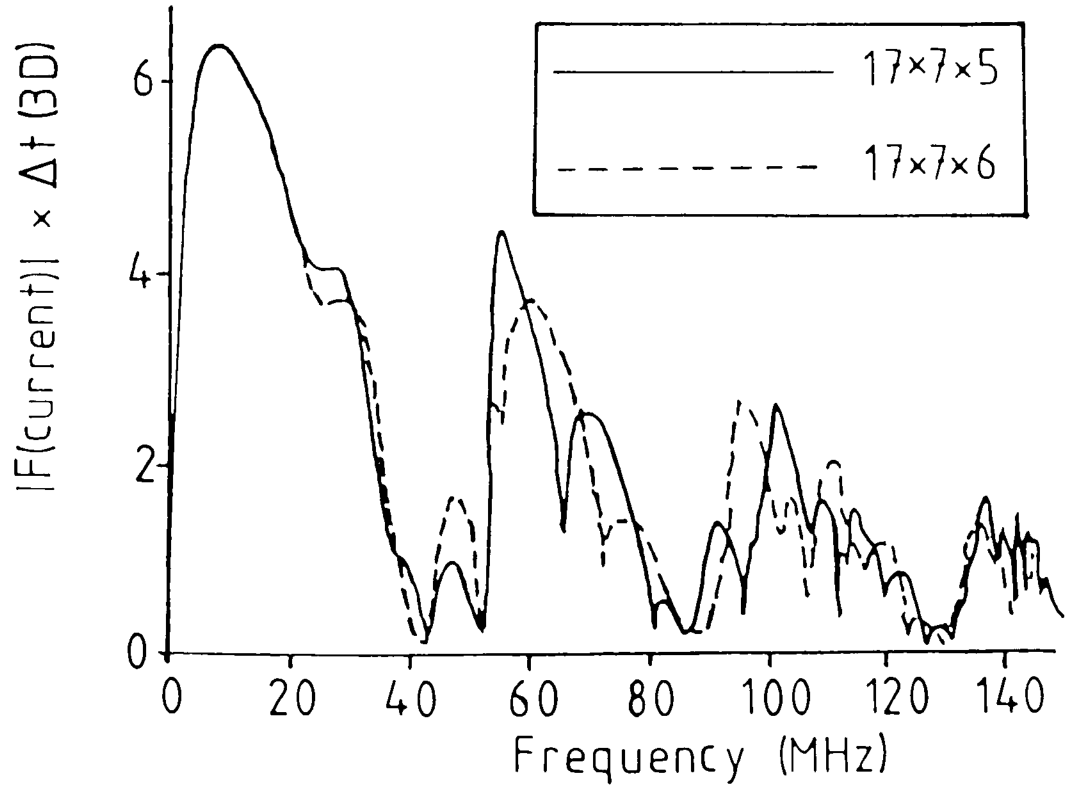

4m between the wire position and ground, rather than the actual distance of 3.5m. Again there are additional local minima on the 3D response. To find out whether these minima are dependent on the position of the external boundaries the geometry was changed slightly.

If the outer (z) boundaries are moved 1m further away from the wire then the spectrum changes as shown by figure 7.5. A small change in the outer geometry has made noticeable changes to the frequency spectrum. Some of the maxima and minima have changed amplitude and position.

By enlarging the outer geometry still further the spectrum becomes figure 7.6. This clearly shows that the local minimum at approximately 30 MHz has been removed, just by making the TLM workspace larger.

For a very large workspace still containing the same wire geometry the frequency spectrum of figure 7.7 was obtained. Extra local minima and maxima appear on the on the spectrum in the range 0-40 MHz and there is a sharp increase in amplitude around 52 MHz but the response between 85 and 130 MHz is much more like the 1D result than the previous geometries.

The 1D solution does not vary with the movement of any of these external boundaries (except for the top boundary) which only causes a time delay in the current induced). For a perfectly conducting wire above an infinite ground plane the fault lies with the 3D solution. As shown above the 3D TLM mesh must form a finite workspace (e.g. 39 x 15 x 20 nodes). At the edge of this workspace boundary conditions must be introduced as shown in Chapter 3. In order to model an infinite ground plane open-circuit boundaries were placed as shown in figure 7.3. This effectively models a multiple

Figure 7·6 Large variation in 3D geometry

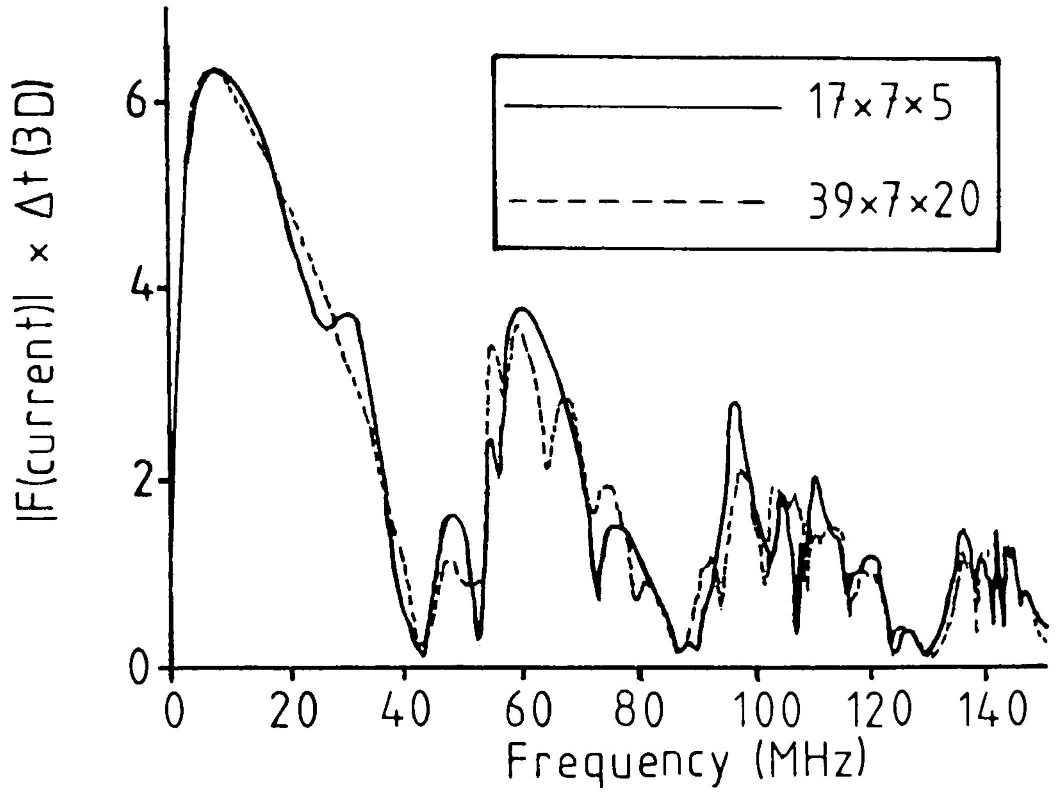

Figure 7·7 Largest 3D geometry for 4m wire

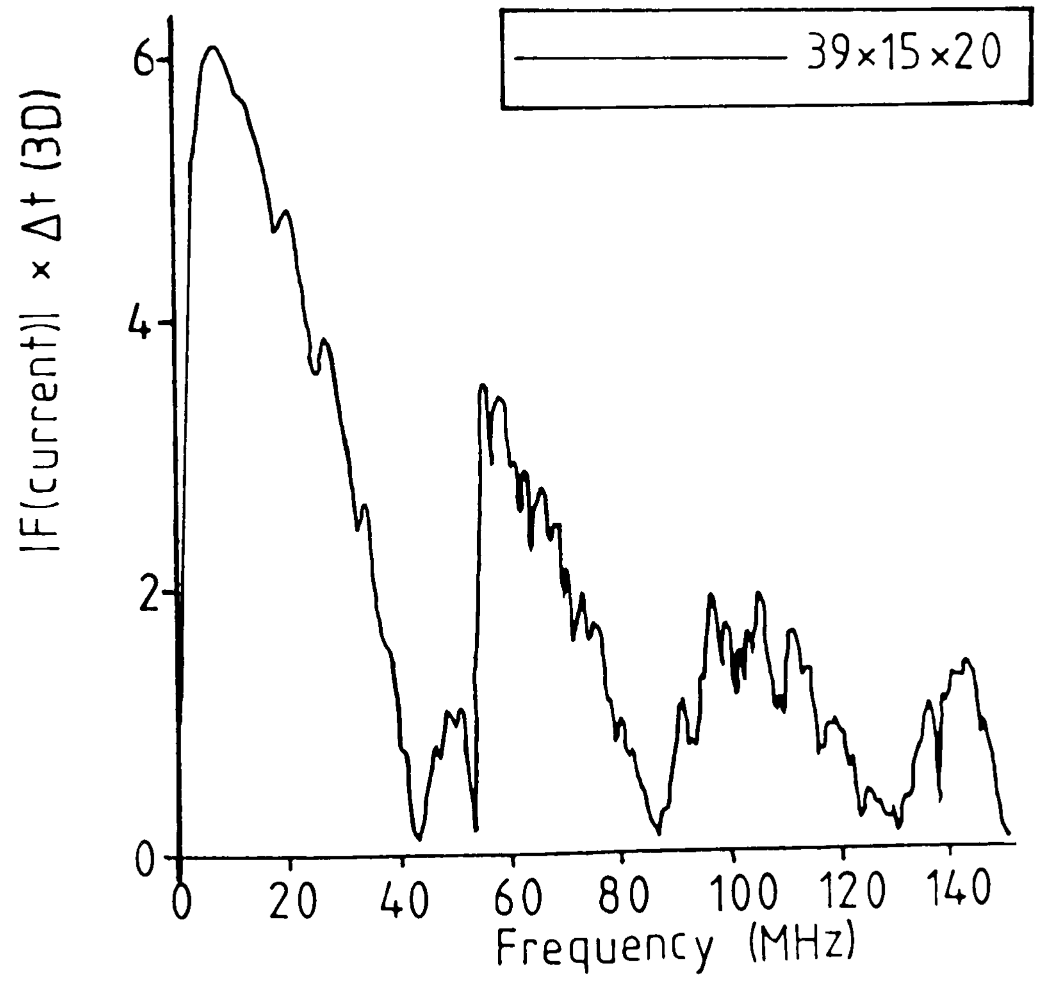

wire geometry and it is likely that the additional minima (and maxima) on the 3D responses will be due to this.

Since for this (figure 7.3) geometry, with wire of length 4m, the minima due to flux and wire length considerations will all correspond to multiples of 4m the length of the wire was increase to 6m as shown in figure 7.8. The loading conditions were identical to those for the previous example. Figure 7.9 shows the 1D and 3D frequency responses obtained and the predicted frequencies for flux and wire resonance conditions. The 1D method computes these frequencies accurately but the 3D methods do not. The low frequency comparison is very good with both spectra agreeing up to about 25 MHz.

An even longer terminated wire of 16m in length is shown in figure 7.10. Again the wire is excited by a magnetic field as shown. The resulting frequency responses obtained by the 1D and 3D methods are shown in figure 7.11. Although the general trend of the results is similar there are two noticeable features - there seems to be a shift in the maximum and minimum frequencies (in the 3D case), and the 3D solution has a higher amplitude. These effects are most likely caused by two factors:

i) The flux calculation for the 1D model was calculated over the incorrect distance. This would cause the 1D amplitude to be wrong.

Figure 7·8 6m wire geometry (3D)

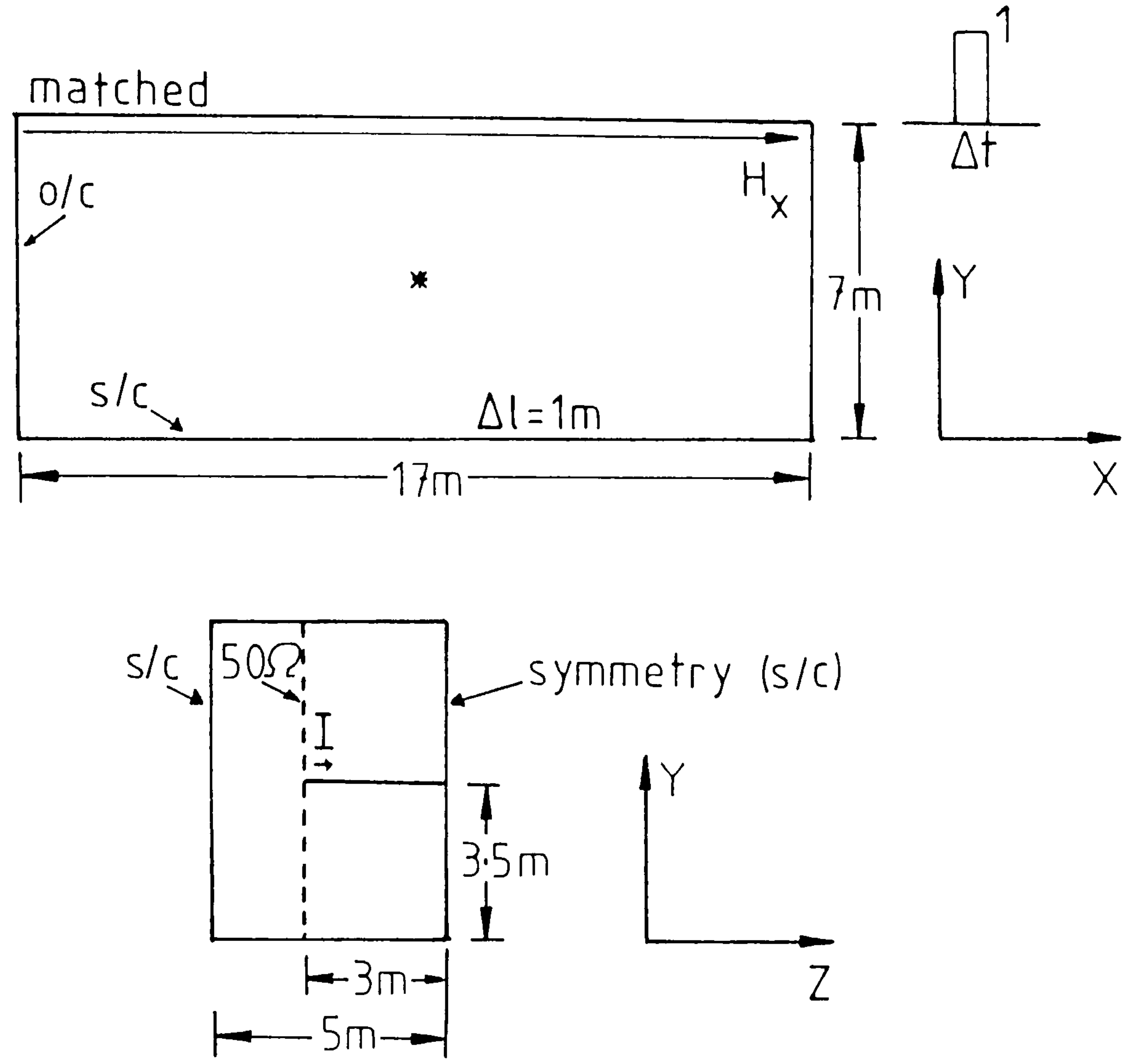

Figure 7·9 Frequency comparison between 1D and 3D methods for above geometry

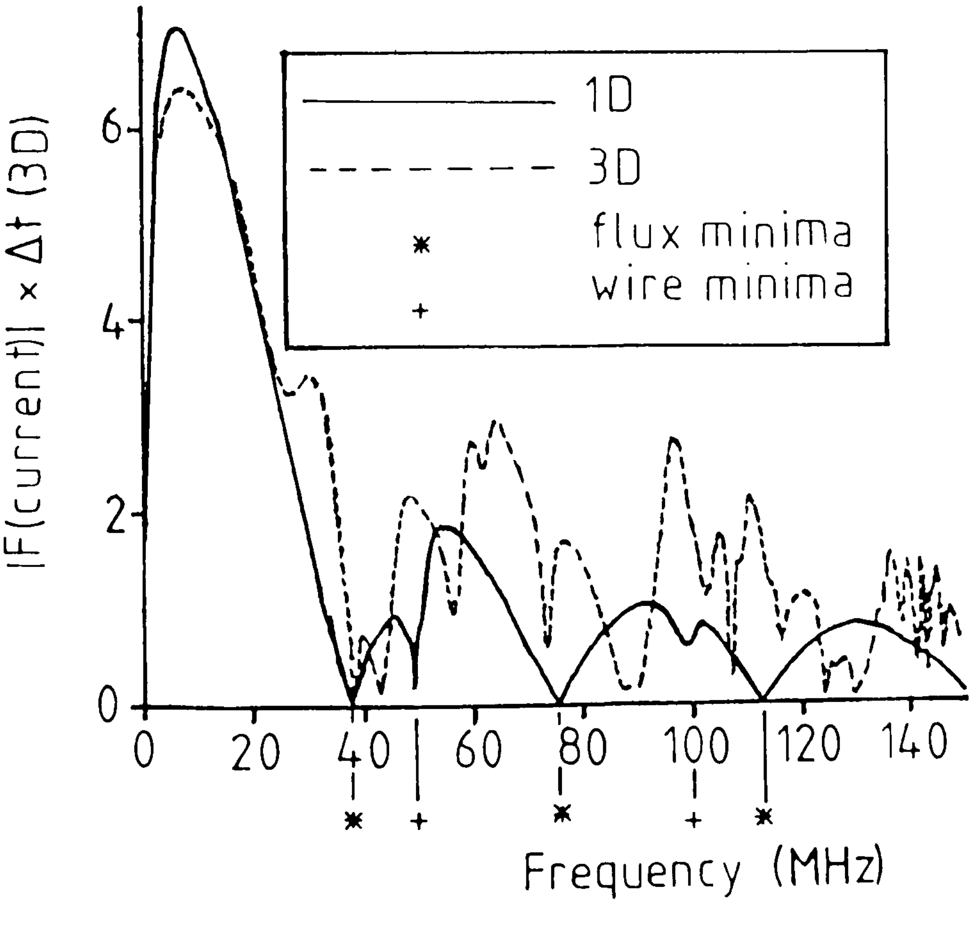

Figure 7·10 16m wire geometry (3D)

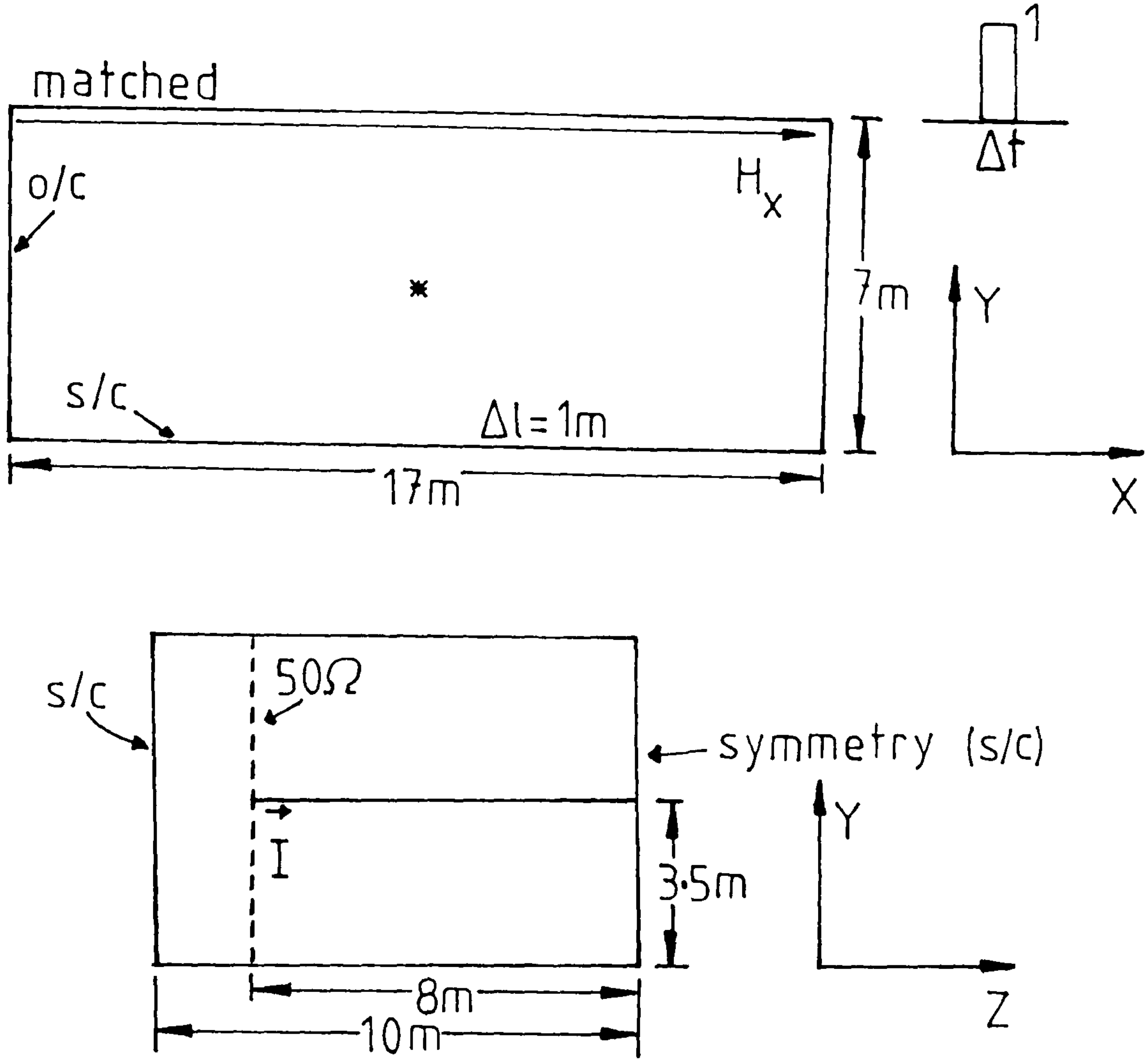

Figure 7·11 Frequency comparison between 1D and 3D methods for above geometry

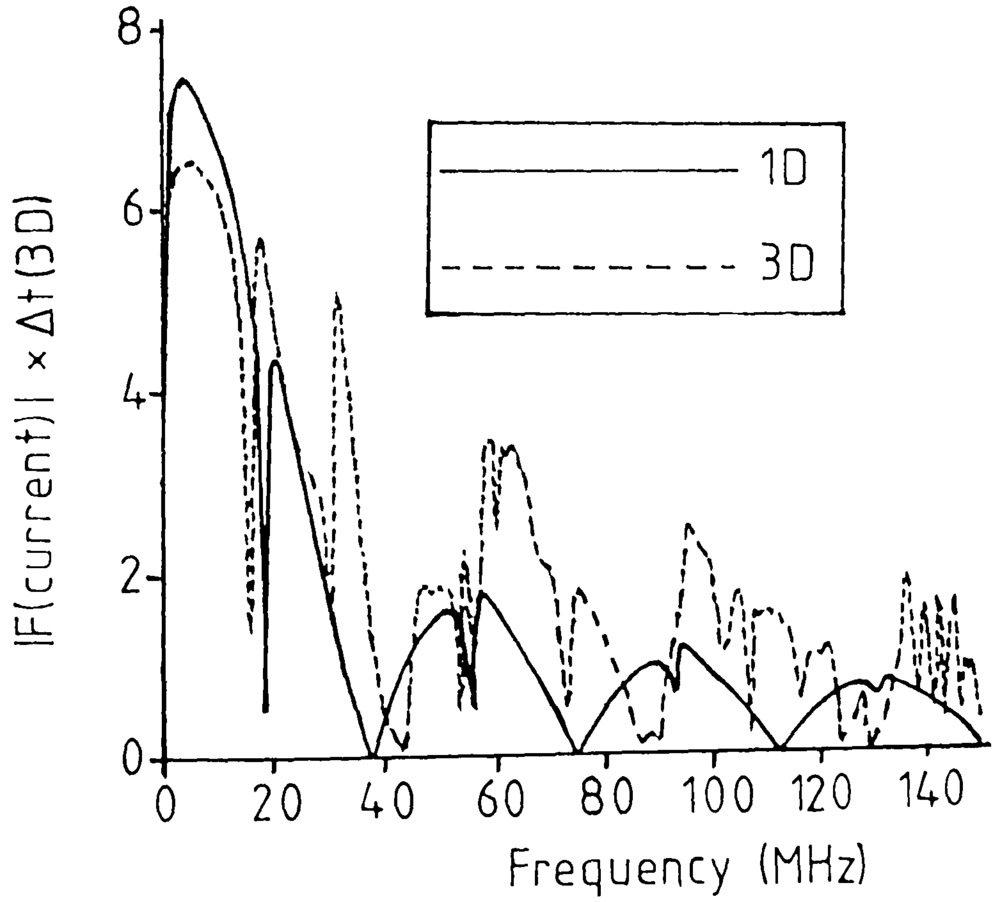

ii) The electrical length of the 3D wire is different from its physical length - that is energy radiates beyond the wire terminations, something which cannot happen in the 1D model.

For the flux calculation a 3D model without a wire was used. The incident flux between the wire position and ground is required but the TLM model can only obtain the magnetic fields (hence flux) over a discrete distance (to the nearest $\Delta\ell/2$). The height of the wire was 3.5m and so the flux can be obtained over $3.5\Delta\ell$. This is only correct for a thin wire approximation. For a wire of radius $0.2\text{m} \leqslant r \leqslant 0.5\text{m}$ (i.e. a short-circuit node) then the height over which the incident flux should be calculated is (h-r) as shown by figure 7.12. Since this was not possible (unless $h-r = n\Delta\ell$) the nearest discrete length was taken. This does cause some discrepancies between the methods.

A short-circuit node wire can hardly be described as 'thin', and this will also lead to differences between the two methods. The 3D TLM model solves Maxwell's equations, and by implication in the vicinity of the wire:

$$\oint_{\ell} \underline{H}.d\underline{\ell} = I + \int_{S} \frac{\partial \underline{D}}{\partial t} . d\underline{S} \qquad (7.1)$$

but the 1D thin wire approximation assumes (Chapter 2):

$$\oint_{\ell} \underline{H}.d\underline{\ell} = I \qquad (7.2)$$

Figure 7·12 Heights for flux calculation

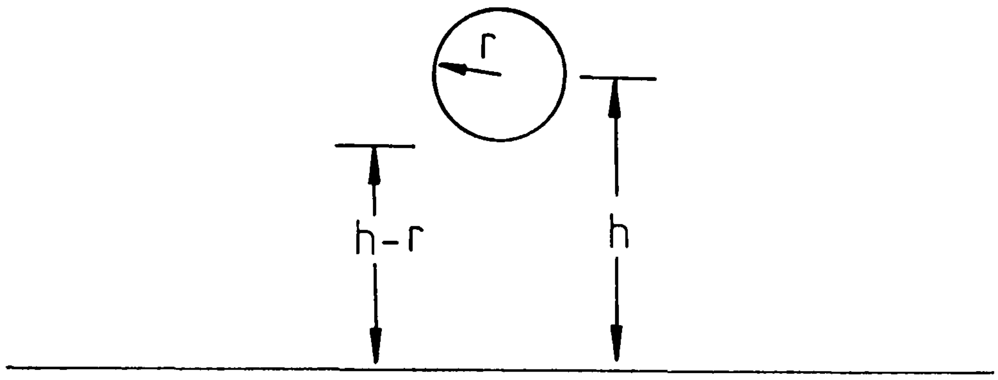

Figure 7·13 16m (Δl × Δl) wire geometry

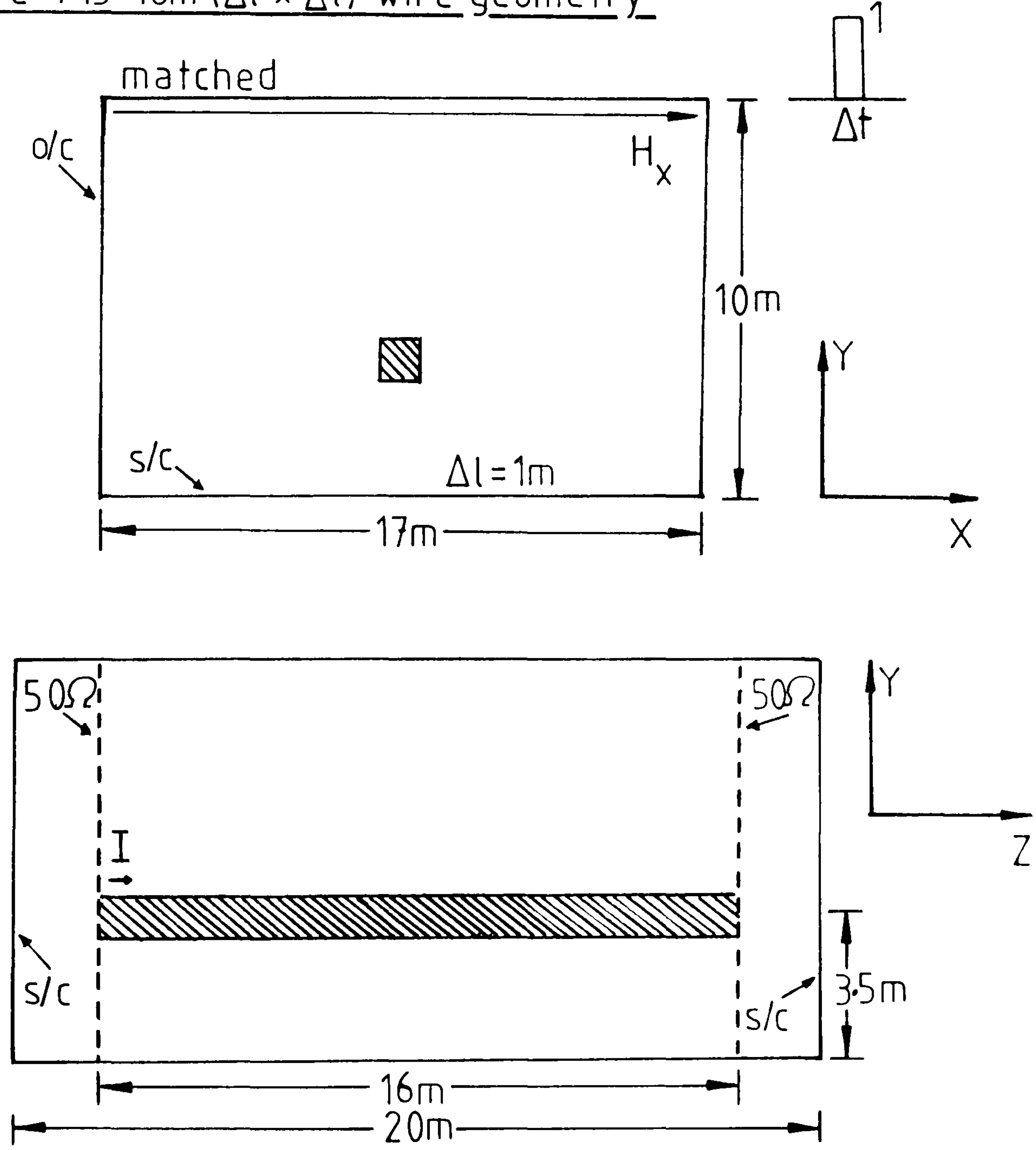

The terminating loads in the 1D model are lumped resistors which apply the load at a point. In 3D the loads are imperfectly conducting plates defined in terms of reflection and transmission coefficients. This means energy does penetrate the load and so the electrical length of the wire (i.e. the points where, for the longest wavelength resonance, the voltage between the wire and ground is zero) is longer than the physical length.

All these factors will cause discrepancies between the two methods.

7.3 Single Node ($\Delta\ell$ x $\Delta\ell$) Wires and 1D

To avoid problems with incorrect flux calculations the $\Delta\ell$ x $\Delta\ell$ wire shown in figure 7.13 can be used as the 3D model. The incident flux and voltage for the 1D model can be confidently calculated over $3\Delta\ell$ and then used in the normal way. The impedance of the wire to ground was found using equations (3.2) and (3.3) Chapter 3 and $Z = \sqrt{\frac{L}{C}}$. For this single node wire the radius of the wire was found to be 0.636m (Chapter 3) and the height is 3.5m. This gives an impedance of 143.32Ω for the 1D model. The loads at each end of the wire were 50Ω which were modelled in 3D as indicated in the previous section. This gives a 1D load of 19Ω.

Figure 7.14a shows the comparison between the 1D and 3D methods if the 1D flux is obtained over 3.5m rather than 3m. Whilst the results are generally similar there is

Figure 7·14 Frequency comparisons between 1D and 3D methods for figure 7·13 geometry

a) Flux calculated over 3·5m

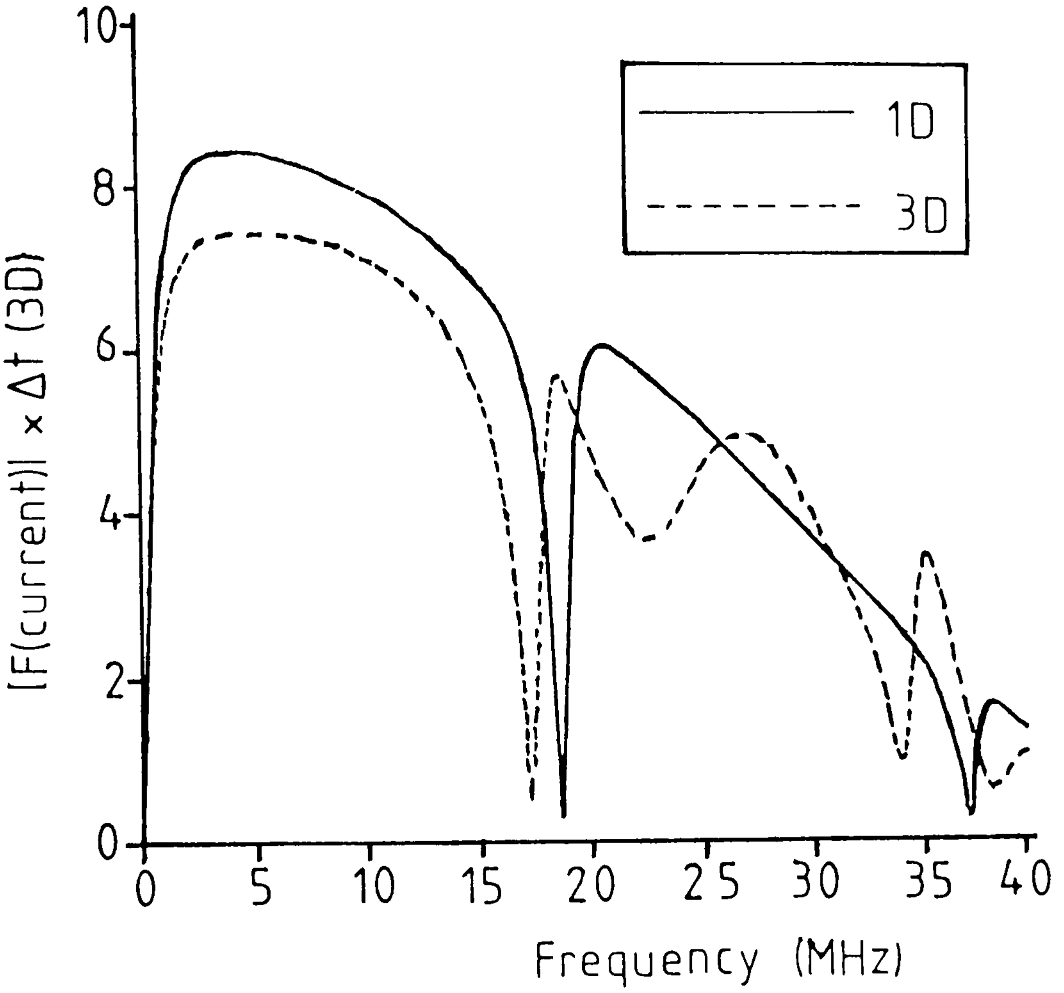

b) Flux calculated over 3m

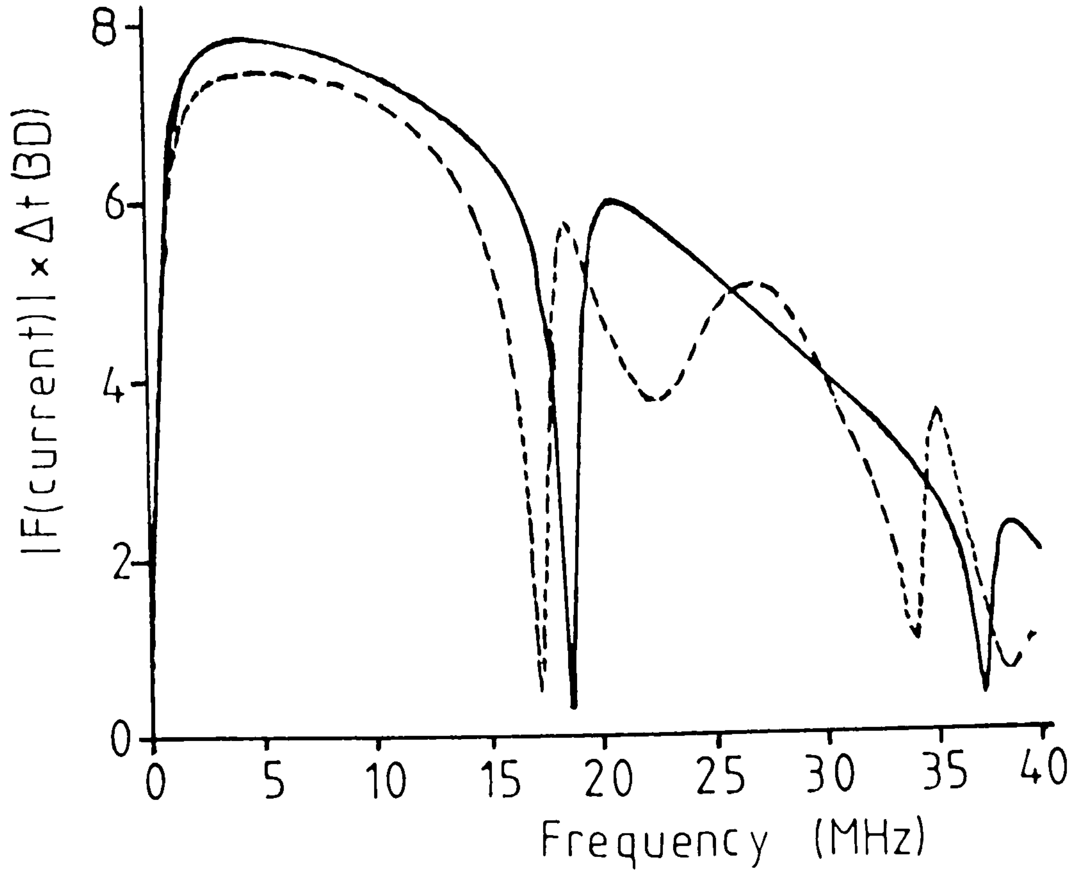

a frequency shift and a difference in amplitude. When the flux is obtained over 3m the results shown in figure 7.14b are calculated. This time the amplitudes are in good agreement but there still is a frequency shift. Examination of the first minimum shows that for the 1D model the frequency is 18.7 MHz which corresponds to a wavelength of 16m. For the 3D case it was found (Chapter 3) that the velocity of propagation for a wave on this model is 2.82×10^8 ms^{-1}. From the figure the frequency of the first minimum is approximately 17.2 MHz. Thus the wavelength λ is

$$\lambda = \frac{2.82 \times 10^8}{17.2 \times 10^6} = 16.39\text{m}$$

This suggests that in the 3D wire model shown in figure 7.13, the electrical length of the wire extends 0.20m beyond the physical ends of the wire. This is not an unreasonable observation as there is radiation beyond the wire termination which effectively lengthens the wire at different frequencies.

7.4 Comparison Between 1D, Short-Circuit Node and Long Wire Elements in an EMP Environment

The 1D, short-circuit node and long wire elements were compared using six distinct geometries. The basic geometry is shown in figure 7.15. In the Z-dimension the problem is limited to 4m to accommodate the long wire element. The geometries considered were:

i) a wire above ground,

ii) a wire in an open box,

iii) a wire in a closed box with aperture.

An additional variation to each geometry was the inclusion of a discontinuity at the base of the problem as shown by figure 7.15biv.

In all cases a magnetic field impulse was used to excite the problem as shown in figure 7.15b. When the aperture geometries were used this excitation was above the aperture (i.e. outside the box). The time varying currents were obtained from all three models at a point 0.5m along the wire (at z = 0.5m). These currents were then convolved with the EMP waveform shown in figure 7.15a.

The 1D and wire element models were chosen to represent a wire of radius = 0.2m whilst the short-circuit node wire models a radius of approximately 0.56m (Chapter 4).

Figures 7.16a and b show the time-domain responses for a wire above ground with and without a discontinuity. With no discontinuity the 1D and short-circuit node models show reasonable agreement. The wire element has a more rapid decay rate than the other two models and to maximum amplitude is 2/3 of that of the short-circuit node.

A similar picture is obtained for the discontinuity geometry (7.16b). Here both the 1D and short-circuit node models show an increased oscillation after the initial rise, due to reflections from the discontinuity. The short-circuit node and 1D models preserve the (different) amplitudes of

Figure 7·15 Excitation and geometries for three model comparisons

a) EMP excitation

$$H(t) = 133\left(\exp(-3{\cdot}075\times10^{6}t)-\exp(-1{\cdot}852\times10^{8}t)\right)$$

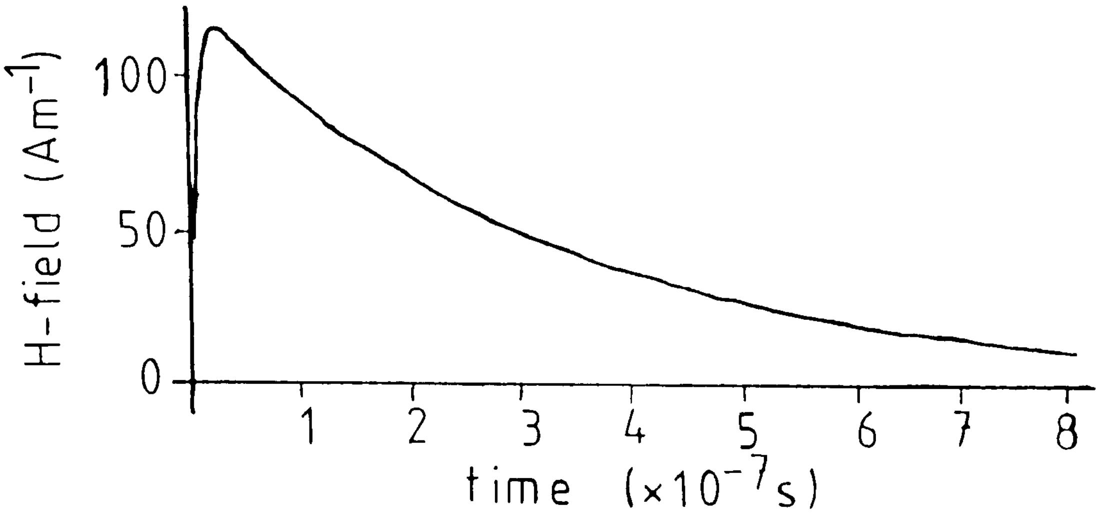

b) Geometry

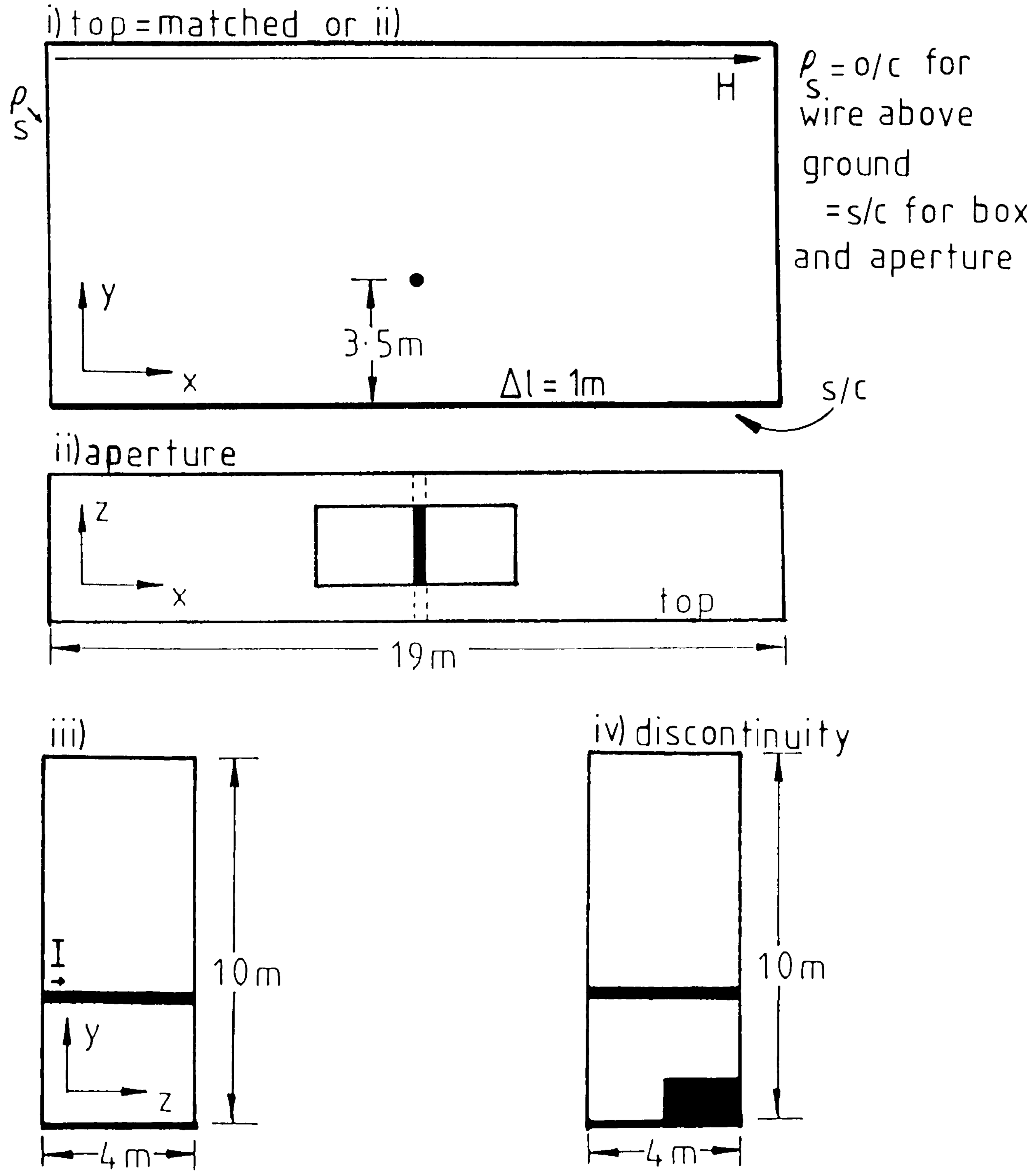

Figure 7·16 Comparisons between the three methods for wire-above-ground

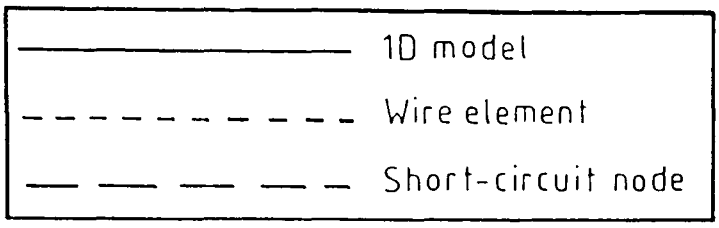

a) Without discontinuity

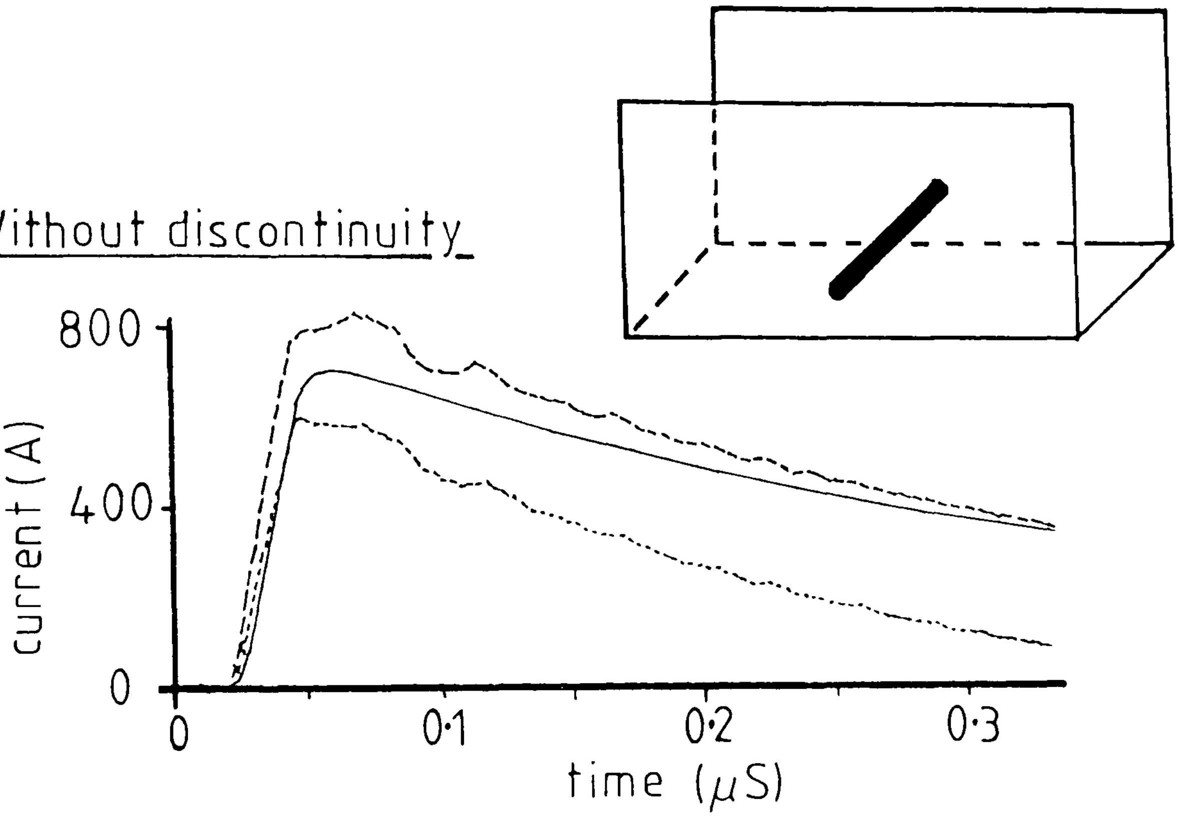

b) With discontinuity

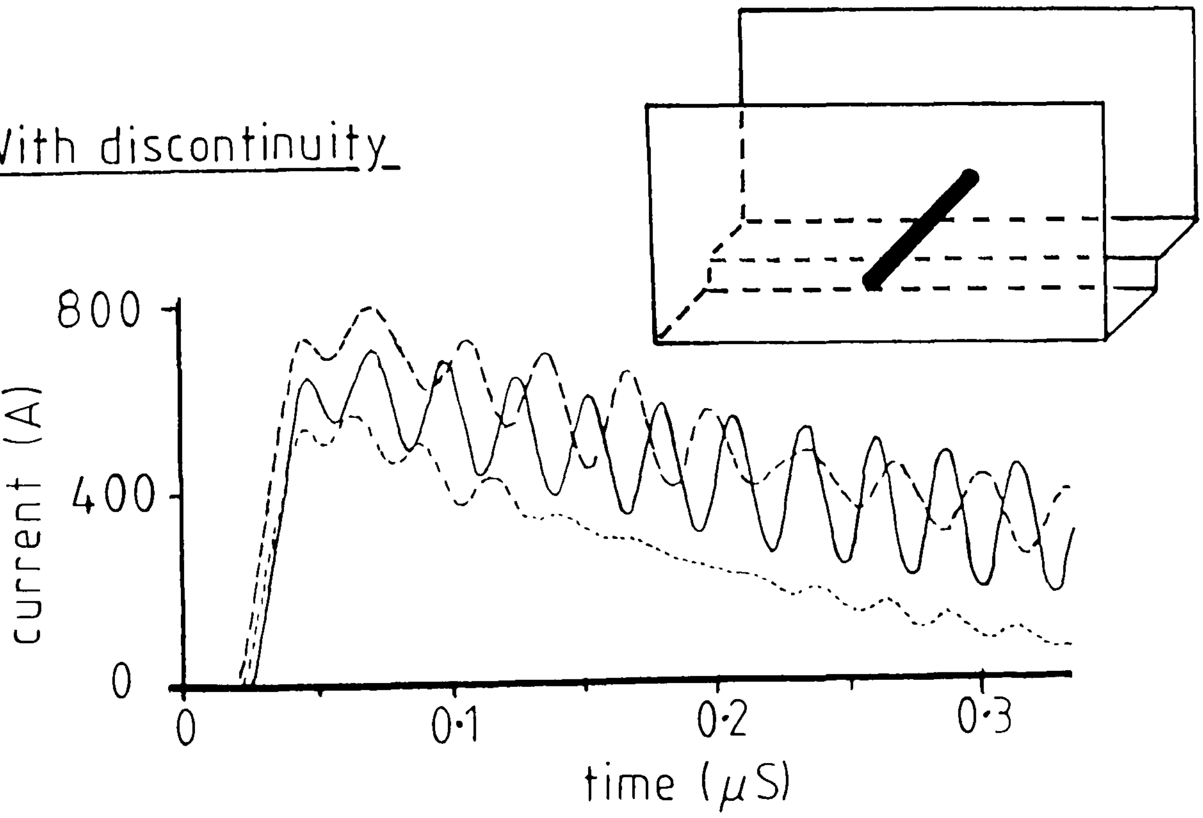

the oscillation whilst they are quickly damped out in the wire element model. Again the wire element also has a lower maximum amplitude. The time domain responses for a wire in an open box are shown in figure 7.17. With no discontinuity (a) the 1D and short-circuit node models exhibit similar but not identical waveforms. The wire element model has a slowly decaying response which is not the case for the other two models. With a discontinuity (b) all the methods predict an oscillating current after 0.05μs. The 1D and short-circuit node models maintain a constant average amplitude beyond this time whilst the wire element response decays. The frequency of oscillation is different in each model.

For the wire in a closed box with aperture (figure 7.18) there is more similarity between all the methods particularly over the first two cycles. This is true both without (a) and with (b) a discontinuity. In both cases the amplitudes of the first peaks are quite similar. Subsequent peaks and the zero crossings do show differences.

The differences between the three methods are caused by a number of factors:

i) as previously stated the radius of the short-circuit node is different from the other two methods.

ii) the pre-solved wire element is a lossy structure. The use of time and spatial averaging plus a truncation of samples used

Figure 7·17 Comparisons between the three methods for open box geometry

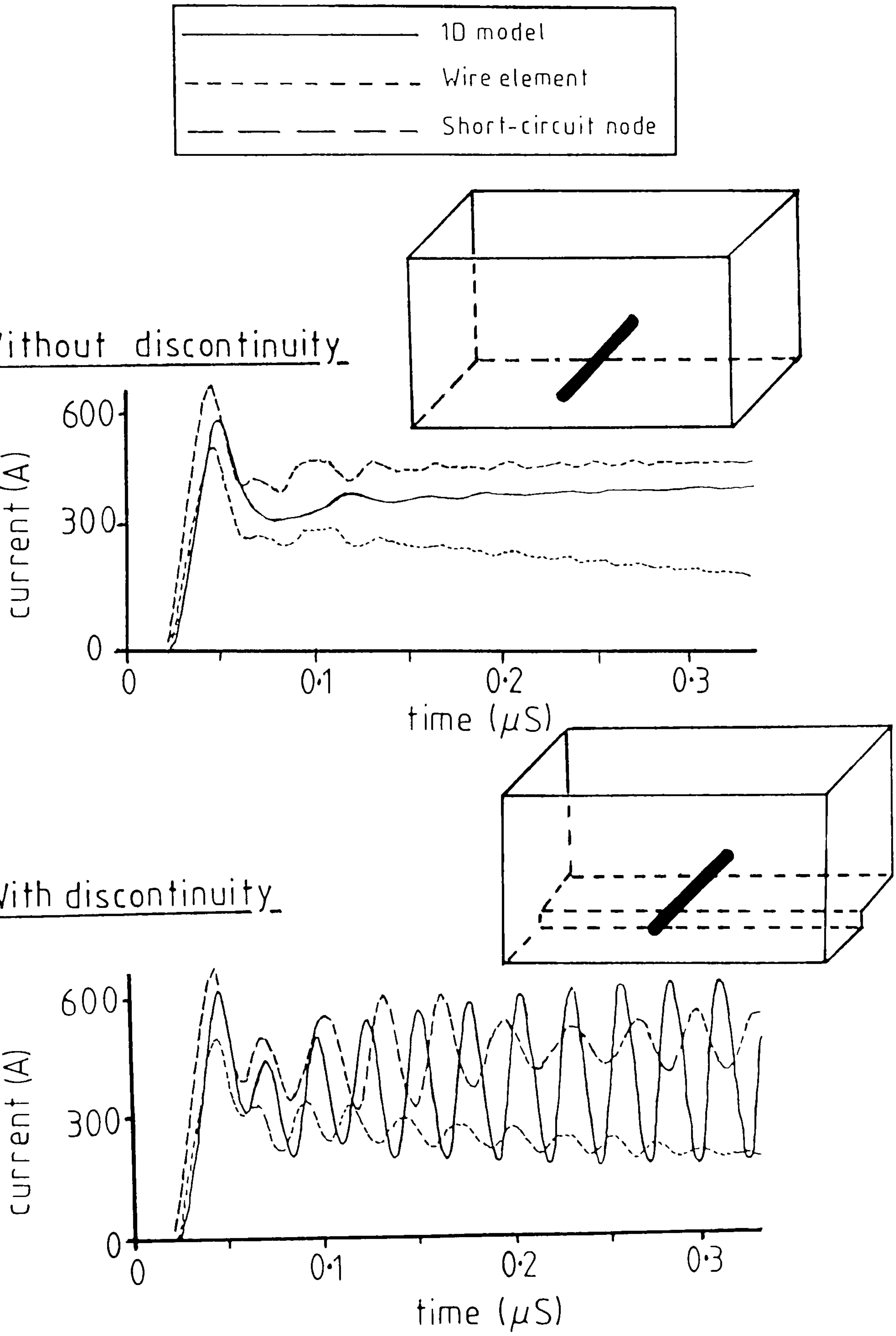

a) Without discontinuity

b) With discontinuity

Figure 7·18 Comparisons between the three methods for aperture geometry

a) Without discontinuity

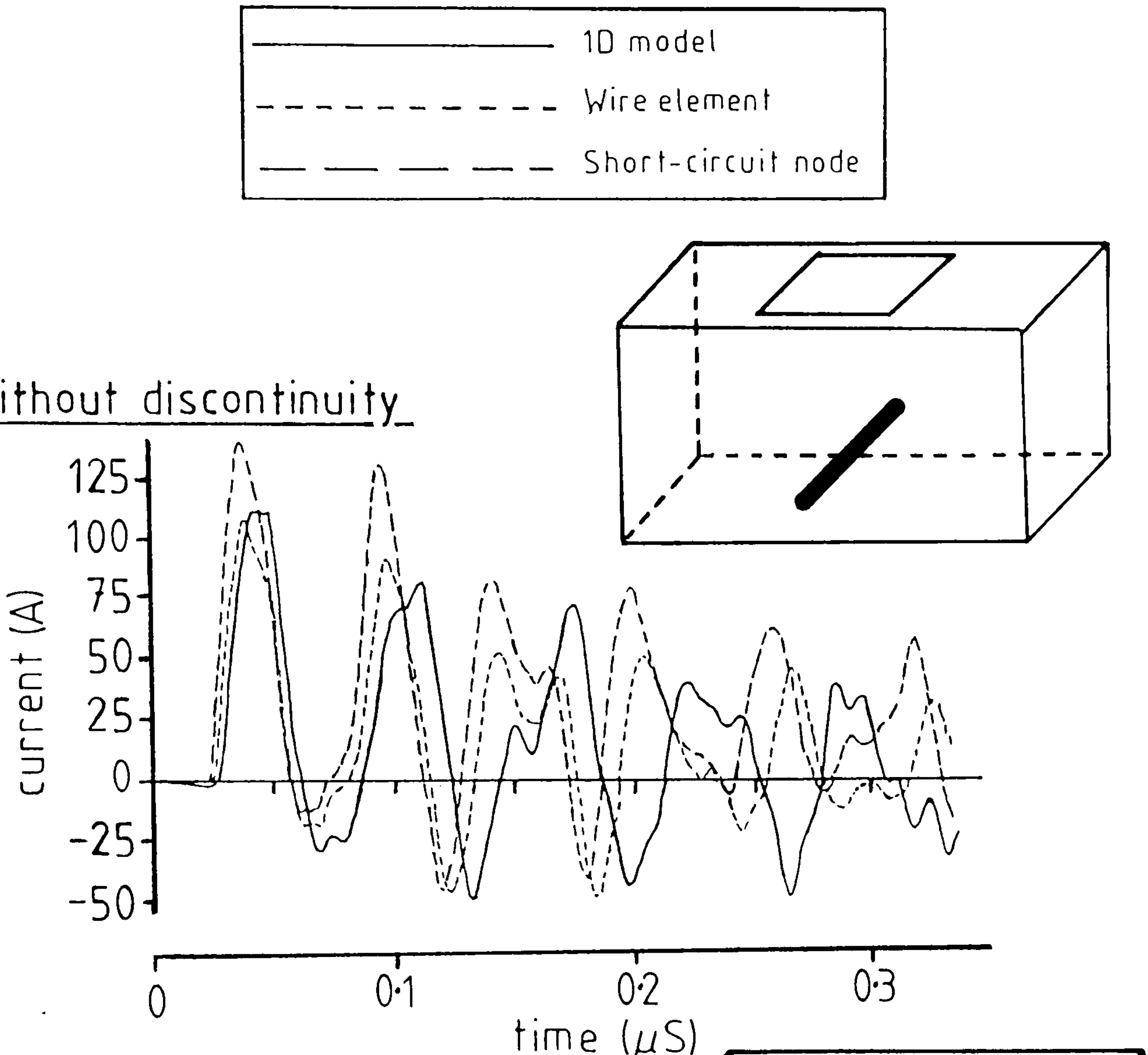

b) With discontinuity

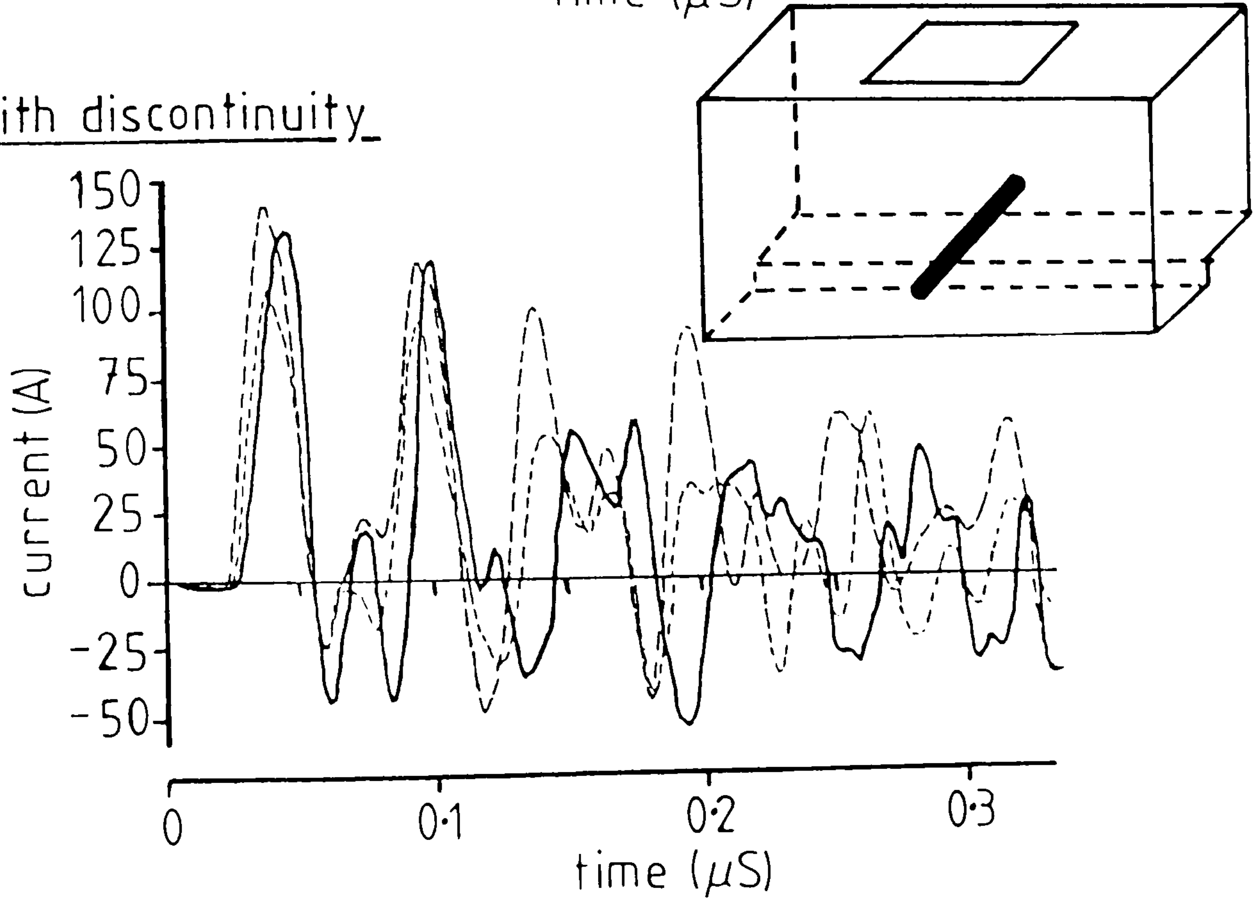

to describe the wire element ensure that power and charge are not conserved by the model.

iii) Incident flux and voltage for the 1D model are calculated over a discrete distance. This implies either a thin wire or a single node ($\Delta\ell$ x $\Delta\ell$) wire as previously stated. If the calculation implies a single node wire then the $\int_S \frac{\partial \underline{D}}{\partial t} \cdot dS$ term in Maxwell's equation should have been included. For the 1D solutions in this section the flux and voltage were calculated over 3m - so the wire is not thin.

iv) No common mode current was calculated for the 1D results. Hence the field solutions compute total current but only differential mode current is available from the 1D model.

Despite the differences mentioned above there is a reasonable similarity between the three methods. This is especially true when it is noted that the coupling into the wire is calculated in completely different ways by the 1D and field solutions.

7.5 Conclusions

Reasonable comparisons have been made between the various TLM wire models.

The differences between the methods result from a number of causes:

i) Field solutions require outer boundaries to the TLM workspace which can introduce non-physical resonances.

ii) Wire terminations in the field solutions generally radiate energy beyond the end of the wire. This means the electrical length of a wire is longer than its physical length.

iii) The 1D method calculates the differential mode current in a thin wire. The field solutions calculate the total current in a non-thin wire.

iv) The incident flux and voltage were calculated over a discrete distance which was different from the actual distance required.

v) Averaging in time and space makes the wire element lossy.

Chapter 8 Further Discussion and Overall Conclusions

8.1 Discussion

Three methods of describing wires in a TLM simulation of an electromagnetic field problem have been investigated. These are:

i) A one dimensional approach

ii) A fine mesh description of the wire - including the short-circuit node.

iii) Pre-solved wire elements using diakoptic techniques.

Ideally, with infinite computing resources, the currents and voltages coupled into wires could be modelled on a very fine TLM mesh where the wire radii and inter wire distances determine the mesh spacing. Chapter 3 showed that if the mesh is sufficiently fine then an accurate radius and velocity of propagation of waves on the wire can be computed. Practically, a very fine mesh could not be used since too many computer resources (i.e. storage and execution time) are required. If errors both in the radius and velocity of propagation of up to 10% can be allowed then it is possible to use a coarser mesh description. The coarsest descriptions of a wire in the 3D TLM models are the short-circuit node or a $\Delta\ell \times \Delta\ell$ (single node) wire. This limits the coarsest mesh to that which gives the wire radius equal to $0.5\Delta\ell$ (approx.). However there is a further condition that there must be at least one (preferably more) TLM nodes between the wire(s) and any other metal object modelled (otherwise a discrete plane rather than two wires (say) would be modelled). It was demonstrated in Chapters 3 and 4 that such crudely described wires can be used and that the resulting measured parameters contain about 10% error. There is still a problem. In any practical geometry the wire radius is very much smaller than any other dimension. If this is the case then the 3D single node wire model may still be computationally too demanding. Chapter 4 showed that it was not possible to reduce the effective radius of the short-circuit node by the addition of stub transmission lines to the geometry. Thus for a non-diakoptic 3D field approach there are computational rather than geometric difficulties in modelling wires.

Different radii wires could be modelled using the pre-solved element technique (Chapter 6). With this only the wire is solved on a fine mesh. The scattering matrix which defines the way the wire interacts with the rest of the space is inaccurate when time and space approximations to the data are made. This can cause instability when the model is used. The main difficulty with the use of pre-solved wire elements comes from the need to join many elements together to form a length of wire and to include terminating boundaries. As was shown in Chapter 6, there was a need for the terminating boundaries to be included in the wire element. Although this does not cause a problem it does remove complete generality from the wire element. The difficulty occurs when adjacent wire elements are connected together. Because of the crude spatial approximation techniques used at these boundaries much of the fine mesh description was lost (by averaging 100 or 81 fine mesh transmission lines to one line on the coarse mesh).

One way of avoiding the above problem was to extend the length of the wire element to $4\Delta\ell$ long. Such a wire element was pre-solved and the matrix obtained used to model a wire in a 3D field solution. Again this model is lossy in such a way that the computed current becomes unstable after about 750 iterations - in the same way that the time domain approximations used in the diakoptic method in Chapter 5 caused the time response to become unstable.

For low iterations and the averaging diakoptic boundary, the pre-solved $4\Delta\ell$ element gave a reasonable prediction of the current.

In order to pre-solve even longer wires a sufficient number of time-domain samples are required to model a wave propagating the length of the wire (i.e. the transit time of the wire). If L is the length of the wire element then at least 2L samples are required plus a margin of error (say 12) giving (2L + 12) samples. The matrix size also increases as a function of $(4 + 8L)^2$ to describe the port to port scattering. So just to describe the wire, the storage required is approximately:

$$(4 + 8L)^2 \ (2L + 12) \text{ storage units}$$

and for L = 4 and 8 bytes per storage unit this becomes

202.5 Kbytes

It is clear that, since the storage requirements vary with L^3, longer wires require considerably more store and computational effort to find the scattering matrix than the shorter wires. It is likely that a wire of any appreciable length will have storage requirements which exceed that for a non-diakoptic fine mesh. For example consider a fine mesh geometry containing a wire which is 30 x 20 x 40 nodes. This gives 24000 storage elements. Now assume that with a wire element the same space can be modelled using 6 x 4 x 8 nodes, (1/5th size) with the long wire element on the longest (8) length. The total storage required will be:

$$(4 + 8 \times 8)^2(2 \times 8 + 12) + 6 \times 4 \times 8 = 129644 \text{ elements,}$$

over 5 times more storage than the fine mesh. This along with the errors obtained using wire elements makes this technique unsuitable for long wires.

If single wire elements could be used the storage requirements would be reduced dramatically. What is required is some form of boundary between adjacent elements that provides a reasonable connection. As shown in Chapter 6 neither a matched nor an open-circuit boundary are suitable for this purpose. It may be that the non-physical use of a short-circuit boundary or the continuation boundary (57) would improve the model, but this seems unlikely.

A special case of a pre-solved wire element is the short-circuit node - as seen by one of the derivations in Chapter 4.

The methods discussed so far are capable of modelling the total current flowing in the wire - or with difficulty in the load. The 1D method allows for the calculation of the differential mode current in thin wires and their terminations easily. To calculate this current the incident flux and voltage between the two wire positions has to be obtained and differentiated. This can be achieved in a number of ways:

i) By analysis. Examine the geometry and calculate what the incident flux and voltage are (e.g. see the comparisons with the RADC method in Chapter 2).

ii) Use an electromagnetic solver (e.g. TLM) to obtain the incident terms and differentiate numerically (as in Chapter 7).

iii) Use the solver to find the incident terms but interpolate the results for smaller distances between wires.

Difficulty can arise when a wire is put into some complicated geometries. Figure 8.1a shows that for a wire close to two short-circuit boundaries the geometry is really that of a multiple wire geometry. The problem cannot be solved using the existing technique but may be soluable using a modified form of the 1D model (i.e. the multiconductor model presented by PAUL (30)).

Figure 8·1 Wire close to boundaries

a) Effective geometry when wire close to two boundaries

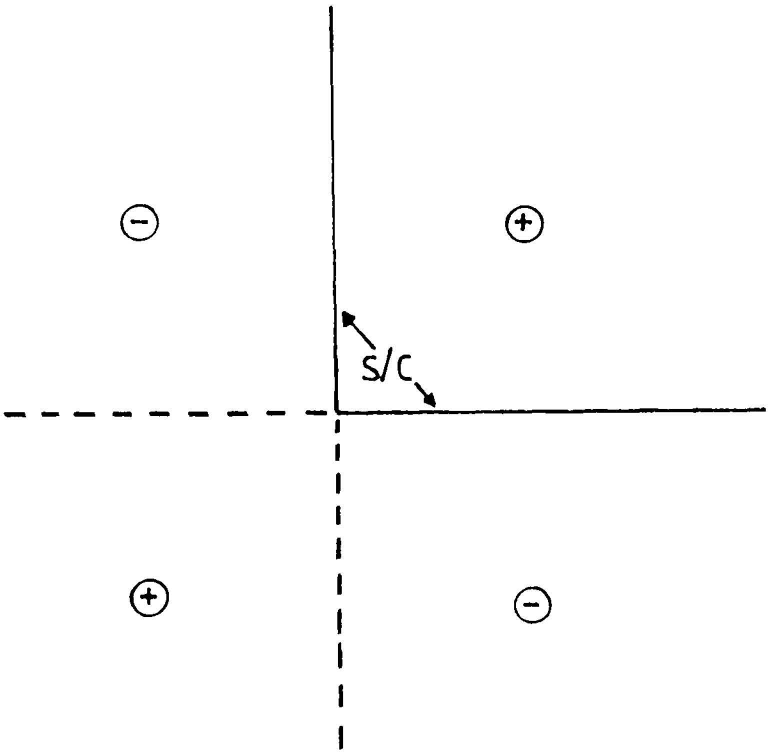

b) Close to one boundary

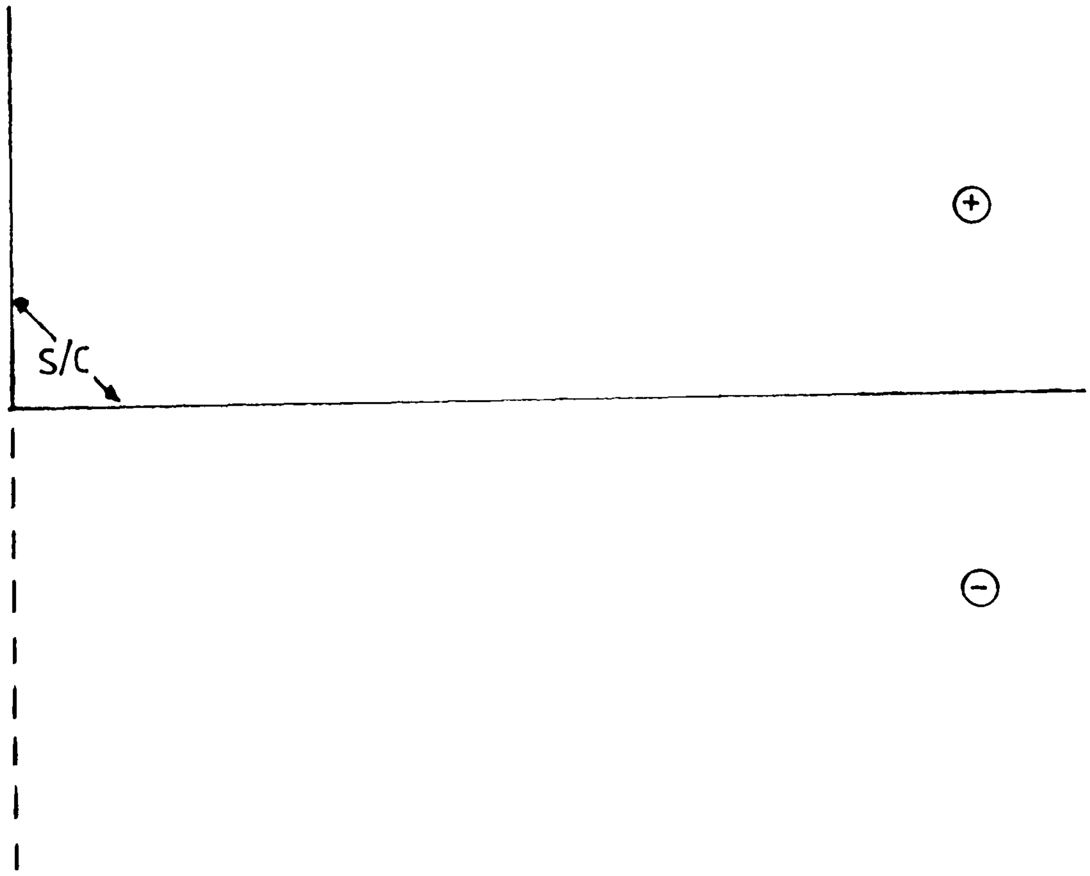

However if the wire is close to one plane but relatively distant from others (as in figure 8.1b) then the dominant modes are those between the two closest wires - and other modes can be ignored. In the frequency domain versions of this method (e.g. (7)) the following conditions are enforced:

i) the wire radius is thin

ii) the distance above ground/between wires is small compared with the wavelength of a mode of propagation.

In the TLM version this latter condition can be relaxed slightly as the method correctly calculates the time-domain flux variation between the two wires, although modes of propagation other than TEM will not be modelled by the transmission-line equations. The frequency methods excite all frequencies with the same amplitude (i.e. an impulse in the time domain) which implies that the pair of wires are close together with respect to any wavelengths of interest. In the TLM version it is possible to calculate, in the time domain, the actual time response of the flux (which in the frequency domain will not be linear). The 1D transmission line equations still correctly model the TEM propagation of the induced voltages and currents. In this way one of the limitations of the 1D (frequency domain) method has been reduced. Also, as shown in Chapter 2 it is possible to introduce non-linear loads into the 1D-TLM method, something which cannot be done in the frequency domain.

The comparisons between methods in the previous chapter has shown that, even with the problems described above there is reasonable similarity between the resulting currents. A justifiable question to ask is which method provides the best model for a given situation?

Probably the easiest and most versatile method to use is the 1D model (Chapter 2). It is very simple to operate but at present has three main drawbacks:

i) the thin wire approximation.
ii) it only computes the differential mode.
iii) it does not compute any re-radiation effects.

The total current in the 1D wire model may be computed by using the so-called antenna mode equations (1). It is probably not necessary to do this though, since it is the current flowing through the load (i.e. the differential mode) that is required.

The other, 3D, solutions whilst giving reasonable results for the geometries chosen can be quite clumsy and inefficient to use. For example, it would not have been easy to use a 3D field model to obtain the current flowing in the non-linear load as used in Chapter 2. Firstly the geometry is too large - the wire radius would fix the space step of the model at a maximum of 2.5mm giving at least 4000 x 40 x 1 nodes. Secondly, there is some difficulty in modelling linear loads in a field solution. Non-linear loads may be extremely complicated to model.

The 3D pre-solved wire elements, whilst being an interesting concept, do contain such large approximations at the boundary between elements and in the filtering of the time-domain data that the use of such a model could only be recommended for short wires and short time durations.

Fine mesh field solutions may be suitable for long thick wires (or cable looms) running between well shielded pieces of equipment. However, the differences between the inductance and capacitance forms of the TLM mesh (shunt and series nodes in 2D) can lead to velocities of propagation less than the velocity of light. This may not be such a problem since real wires are lossy and the velocity of propagation on these wires will be less than the velocity of light. But the size of radii which can be modelled is limited by the mesh size and since practical wires have radii <1 cm in geometries of the order of metres the amount of storage required could be large.

Multiconductor wire solutions exist for the 1D type of solution (24-43) and this model could be extended to model these.

The wire-element model could also be used to model multiple wires - but in the current state of development it can not be recommended.

8.2 Conclusions

Four wire models have been developed which allow the voltages and currents induced to be calculated. Three of these models are different forms of 3D TLM electromagnetic field solutions. The fourth model is a one dimensional model which allows the computation of the differential mode current in a thin wire. All the 3D solutions depend on a physical representation of the wire. The minimum radius that can be modelled is approximately half the TLM mesh spacing. This effectively requires a very fine mesh step implying a very large TLM workspace.

The 1D model is the easiest and most computationally efficient model to use. It could be modified to allow multiconductor wires to be solved. Non-linear loads can be modelled.

Chapter 9 References

1. LEE, K.S.H. (Editor): "EMP Interaction, Principles, Techniques and Reference Data (A compleat concatenation of technology from the EMP Interaction Notes) EMP Interaction 2-1", University of New Mexico/AFWL, December 1980.
2. COOK, R.: "Introduction to Electro-Magnetic Environments", Paper presented at "An Introduction to the Electromagnetic Environments", Society of Environmental Engineers, Imperial College, London, February 1984.
3. GIBBONS, W.: "Electromagnetic Compatibility of Automotive Electronics". Paper presented at "An Introduction to the Electromagnetic Enviroments", Society of Environmental Engineers, Imperial College, London, February 1984.
4. LITTLE, P.F.: "The Coupling of Lightning Fields into Aircraft and Cables", AGARD Lecture Series No. 110, Atmospheric Electricity - Aircraft Interaction, June 1980, pp 8-1 to 8-14.
5. SCHARFMAN, W.E., VANCE, E.F. and GRAF, K.A.: "EMP Coupling to Power Lines". IEEE Trans. Vol. EMC-20, No. 1, February 1978, pp 129-135.
6. TAYLOR, C.D.: "External Interaction of the Nuclear EMP with Aircraft and Missiles", IEEE Trans. Vol. EMC-20, pp 64-76.
7. ABRAHAM, R.T. and PAUL, C.R.: "Basic Technology

Advancement for C^3 Systems - Coupling of Electromagnetic Fields onto Transmission Lines : A Comparison of the Transmission Line Model and the Method of Moments", Rome Air Development Center Report RADC-TR-82-286, Vol. IVA, November 1982.

8. PERALA, R.A., RUDOLPH, T. and ERIKSEN, F.: "Electromagnetic Interaction of Lightning with Aircraft", IEEE Trans. Vol. EMC-24, No. 2, May 1982, pp 173-203.

9. BEVENSDEE, R.M., BRITTINGHAM, J.N., DEADRICK, F.J., LEHMAN, T.H., MILLER, E.K. and POGGIO, A.J.: "Computer Codes for EMP Interation and Coupling", IEEE Trans. Vol. EMC-20, No. 1, February 1978, pp 156-165.

10. HARRINGTON, R.F.: "Field Computation by Moment Methods", Macmillan, New York, 1968.

11. HARRINGTON, R.F.: "Matrix Methods for Field Problems", Proc. IEEE, Vol. 55, No. 2, February 1967, pp 136-149.

12. MAUTZ, J.R. and HARRINGTON, R.F.: "Radiation and Scattering from Bodies of Revolution", Appl. Sci. Res. 20, June 1969, pp 405-435.

13. SILVESTER, P.P. and FERRARI, R.L.: "Finite Elements for Electrical Engineers", Cambridge University Press, 1983.

14. BREAKALL, J.K., BURKE, G.J. and MILLER, E.K.: "The Numerical Electromagnetic Code (NEC)", Conference proc. Eletromagnetic Compatibility 1985, Zurich, March 1985, pp 301-308.

15. BOAS, M.L.: "Mathematical Methods in the Physical Sciences", Wiley and Sons, 1966, Chapter 11.

16. TESCHE, F.M.: "On the Analysis of Scattering and Antenna Problems Using the Singularity Expansion Technique", IEEE Trans. Vol. AP-21, No. 1, January 1973, pp 53-62.

17. UMASHANKAR, K.R., SHUMPERT, T.H. and WILTON, D.R.: "Scattering by a Thin Wire Parallel to a Ground Plane Using the Singularity Expansion Method", IEEE Trans. Vol. AP-23, No. 2, March 1975, pp 178-184.

18. VAN BLARICUM, M.L. and MITTRA, R.: "A Technique for Extracting the Poles and Residues of a System Directly from its Transient Response", IEEE Trans. Vol. AP-23, No. 6, November 1975, pp 777-781.

19. SANDER, K.F. and REED, G.A.L.: "Transmission and Propagation of Electromagnetic Waves", Cambridge University Press, 1978.

20. LEE, K.S.H.: "Two Parallel Terminated Conductors in External Fields", IEEE Trans. Vol. EMC-20, No. 2, May 1978, pp 288-295.

21. SMITH, A.A.: "A More Convenient Form of the Equations for the Response of a Transmission Line Excited by Non Uniform Fields", IEEE Trans., Vol. EMC-15, pp 151-152, August 1973.

22. SCHLESSINGER, L.: "Currents Induced by a Plane Wave on an Infinite Wire Above a Flat Earth", IEEE Trans. EMC-17, No. 3, August 1975, pp 156-158.

23. BATES, C.P. and HAWLEY, G.T.: "A Model for Currents and Voltages Induced Within Long Transmission Cables by an Electromagnetic Wave". IEEE Trans. Vol. EMC-13, No. 4, November 1971, pp 18-31.

24. BECHTOLD, G.W. and KOZAKOFF, D.J.: "Transmission Line Mode Response of a Multiconductor Cable in a Transient Electromagnetic Field". IEEE Trans. Vol. EMC-12, No. 1, February 1970, pp 5-11.

25. MARK, K.D.: "Propagation Modes, Equivalent Circuits and Characteristic Terminations for Multiconductor Transmission Lines with Inhomogeneous Dielectrics". IEEE Trans. Vol. MTT-21, No. 7, July 1973, pp 450-457.

26. PAUL, C.R.: "Efficient Numerical Computation of Frequency Response of Cables Illuminated by an Electromagnetic Field", IEEE Trans. Vol. MTT-22, April 1974, pp 454-457.

27. PAUL, C.R.: "Useful Matrix Chain Parameter Identities for the Analysis of Multiconductor Transmission Lines", IEEE Trans.Vol. MTT-23(9), pp 756-760.

28. CLEMENTS, J.C., PAUL, C.R. and ADAMS, A.T.: "Computation of the Capacitiance Matrix for Systems of Dielectric Coated Cylindrical Conductors", IEEE Trans. Vol. EMC-17, November 1975, pp 238-248.

29. PAUL, C.R. and FEATHER, A.E.: "Computation of the Transmission Line Inductance and Capacitance Matrices from the Generalised Capacitance Matrix", IEEE Trans. Vol. EMC-18(4), 1976, pp 175-183.

30. PAUL, C.R.: "Frequency Response of Multiconductor Transmission Lines Illuminated by an Electromagnetic Field", IEEE Trans. Vol. EMC-18(4), 1976, pp 183-190.

31. PAUL, C.R.: "Solution of the Transmission Line Equations for Three Conductor Lines in Homogeneous Media", IEEE Trans. Vol. EMC-20(1), 1978, pp 216-222.

32. BEECH, W.E. and PAUL, C.R.: "Basic Technology Advancement for C^3 Systems - Prediction of Crosstalk Flatpack Coaxial Cables", Rome Air Development Center Report RADC-TR-82-286, Vol. IVf, December 1984.

33. HARRISON, C.W.: "Generalized Theory of Impedance Loaded Multiconductor Transmission Lines in an Incident Field", IEEE Trans. Vol. EMC-14, No. 2, May 1982, pp. 56-63.

34. Taylor, C.D. and CASTILLO, J.P.: "On Electromagnetic-Field Excitation of Unshielded Multiconductor Cables", IEEE Trans. Vol. EMC-20, No. 4, November 1978, pp 495-500.

35. AGRAWAL, A.K., LEE, K-M., SCOTT, L.D. and FOWLES, H.M.: "Experimental Characterisation of Multiconductor Transmission Lines in the Frequency Domain", IEEE Trans. Vol. EMC-21, No. 1, February 1979, pp 20-27.

36. AGRAWAL, A.K., FOWLES, H.M. and SCOTT, L.D.: "Experimental Characterisation of Multiconductor Transmission Lines in Inhomogeneous Media Using Time Domain Techniques", IEEE Trans. Vol. EMC-21, No. 1, February 1979, pp 28-32.

37. AGRAWAL, A.K., PRICE, H.J. and GURBAXANI, S.H.: "Transient Response of Multiconductor Transmission Lines Excited by a Nonuniform Electromagnetic Field. IEEE Trans. Vol. EMC-22, No. 2, May 1980, pp119-129.

38. PRICE, H.J. and AGRAWAL, A.K.: "The Response of a Transmission Line Illuminated by Lightning-Induced Electromagnetic Fields", IEEE Trans. Vol. EMC-22, No. 3, August 1980, pp 150-156.

39. GIRI, D.V., TESCHE, F.M. and CHANG, S-K.: "The Transverse Distribution of Surface Charge Densities on Multiconductor Transmission Lines", IEEE Trans. Vol. EMC-21, No. 3, August 1979, pp 220-227.

40. ter HASEBORG, J.L., TRINKS, H. and STURM, R.: "Coupling and Propagation of Transient Currents on Multiconductor Transmission Lines". Conference Proceedings, EMC 1985, Zurich, March 1985, pp 273-277.

41. TAYLOR, C.D. and CASTILLO, J.P.: "On the Response of a Terminated Twisted-Wire Cable Excited by a Plane-Wave Electromagnetic Field", IEEE Trans. Vol. EMC-22, No. 1, February 1980, pp 16-19.

42. GIRI, D.V., CHANG, S-K. and TESCHE, F.M.: "A Coupling Model for a Pair of Skewed Transmission Lines", IEEE Trans. Vol. EMC-22, No. 1, February 1980, pp 22-28.

43. PAUL, C.R. and BUSH, D.R.: "Radiated Fields on Interconnected Cables", Conference Proceedings. International Conference on EMC, September 1984, University of Surrey, IERE Publ. No. 60, pp 259-264.

44. YEE, K.S.: "Numerical Solution of Initial Boundary Value Problems Involving Maxwell's Equations in Isotropic Media", IEEE Trans. Vol. AP-14, No. 3, May 1966, pp 302-307.

45. MEREWETHER, D.E.: "Transient Currents Induced on a Metallic Body of Revolution by an Electromagnetic Pulse", IEEE Trans. Vol. EMC-13, No. 2, May 1971, pp 41-44.

46. HOLLAND, R.: "THREDE: A Free-Field EMP Coupling and Scattering Code", IEEE Trans. Vol. NS-24, No. 6, December 1977, pp 2416-2421.

47. HOLLAND, R., SIMPSON, L. and KUNZ, K.S.: "Finite-Difference Analysis of EMP Coupling into Lossy Dielectric Structures", IEEE Trans. Vol. EMC-22, No. 3, August 1980, pp 203-209.

48. HOLLAND, R. and SIMPSON, L.: "Implementation and Optimisation of the Thin-Strut Formalism in THREDE", IEEE Trans. Vol. NS-27, No. 6, December 1980, pp 1625-1630.

49. HOLLAND, R. and SIMPSON, L.: "Finite-Difference Analysis of EMP Coupling into Thin Struts and Wires", IEEE Trans. Vol. EMC-23, No. 2, May 1981, pp 88-97.

50. ZIMMERMAN, W.R.: "Demonstration of a Time-Domain Integrated Electromagnetic-Field Circuit-Analysis Program", IEEE Trans. Vol. EMC-26, No. 4, November 1984, pp 201-206.

51. WILLIFORD, C.F. and HEBERT, J.L.: "Comparison of Absorbtion and Radiation Boundary Conditions in a Time-Domain Three-Dimensional Finite-Difference Code". International Aerospace and Ground Conference on Lightning and Static Electricity, Ohio, June 1986, pp 44-1 to 44-10.

52. JOHNS, P.B.: "On the Relationship Between TLM and Finite-Difference Methods for Maxwell's Equations", To be published in IEEE Trans. MTT. (1986).

53. PALADIAN, F., PLUMEY, J.P., ROUBERTOU, D. and FONTAINE, J.: "Response of a Single-Conductor Overhead Wire Illuminated by an Inhomogeneous Plane Wave", Conference Proceedings, EMC 1985, Zurich, March 1985, pp 279-282.

54. THIELE, G.A. and NEWHOUSE, T.H.: "A Hybrid Technique for Combining Moment Methods with Geometrical Theory of Diffraction", IEEE Trans. Vol. AP-23, No. 1, January 1975, pp 62-69.

55. THIELE, G.A. and CHAN, G.K.: "Application of the Hybrid Technique to Time Domain Problems", IEEE Trans. Vol. EMC-20, No. 1, February 1978, pp 151-155.

56. KRON, G.: "Equivalent Circuit of the Field Equations of Maxwell-I", Proc. IRE, May 1944, pp 289-299.

57. JOHNS, P.B. and BEURLE, R.L.: "Numerical Solutions of 2-Dimensional Scattering Problems Using a Transmission-Line Matrix". Proc. IEE Vol. 118, No. 9, September 1971, pp 1203-1208.

58. JOHNS, P.B.: "Application of the Transmission-Line-Matrix Method to Homogeneous Waveguides of Arbitrary Cross-Section", Proc. IEE Vol. 119, No. 8, August 1972, pp 1086-1091.

59. JOHNS, P.B.: "The Solution of Inhomogeneous Waveguide Problems Using a Transmission-Line Matrix", IEEE Trans. Vol. MTT-22, No. 3, March 1974, pp 209-215.

60. AKHTARZAD, S. and JOHNS, P.B.: "Generalised Elements for TLM Method of Numerical Analysis", Proc. IEEE Vol. 122, No. 12, December 1975, pp 1349-1352.

61. AKHTARZAD, S. and JOHNS, P.B.: "Solution of Maxwell's Equations in Three Space Dimensions and Time by the TLM Method of Numerical Analysis", Proc. IEE, Vol. 122, No. 12, December 1975.

62. AKHTARZAD, S. and JOHNS, P.B.: "Three-Dimensional Transmission-Line Matrix Computer Analysis of Microstrip Resonators", IEEE Trans. Vol. MTT-23, December 1975, pp 990-997.

63. BREWITT-TAYLOR, C.R. and JOHNS, P.B.: "On the Construction and Numerical Solution of Transmission-Line and Lumped Network Models of Maxwell's Equations", Int. Journ. for Numerical Meth. in Eng., Vol. 15-30, 1980, pp 13-30.

64. JOHNS, P.B. and O'BRIEN, M.: "Use of the Transmission-Line Modelling (TLM) Method to Solve Non-Linear Lumped Networks", The Radio and Electronic Engineer, Vol. 50, No. 1/2, pp 59-70, Jan/Feb 1980.

65. JOHNS, P.B. and AKHTARZAD, K.: "The Use of Time Domain Diakoptics in Time Discrete Models of Fields", Int. Journ. for Numerical Methods in Engineering. Vol. 17, (1981), pp 1-14.

66. JOHNS, P.B. and AKHTARZAD, K.: "Time Domain Approximations in the Solution of Fields by Time Domain Diakoptics", Int. Journ. for Numerical Methods in Eng., Vol. 18, (1982), pp 1361-1373.

67. JOHNS, P.B. and MALLIK, A.: "Prediction of the Shielding Effect of Carbon Fibre Composite Material Using TLM with Diakoptics", Conference Proceedings, International Conference on EMC, September 1984, University of Surrey, IERE Publ. No. 60, pp 51-55.

68. JOHNS, P.B. and MALLIK, A.: "EMP Response of Aircraft Structures Using Transmission-Line Modelling", Conference Proceedings, EMC 1985, Zurich, March 1985, pp 387-389.

69. MALLIK, A., CHRISTOPOULOS, C. and THOMSON, J.M.: "Prediction of Skin Currents Flowing on a Lynx Helicopter Due to a Simulated Lightning Strike", International Aerospace and Ground Conference on Lightning and Static Electricity, Ohio, June 1986, pp 14-1 to 14-7.

70. HOEFER, W.J.R.: "The Transmission-Line Matrix Method - Theory and Applications", IEEE Trans. Vol. MTT-33, No. 10, October 1985, pp 882-893.

71. JOHNS, P.B.: "New Symmetrical Condensed Node for Three-Dimensional Solution of Electro-magnetic-Wave Problems by TLM", Electr. Letters. Vol. 22, No. 3, January 1986, pp 162-164.

72. JOHNS, P.B.: "A Symmetrical Condensed Node for the TLM Method", paper submitted to IEEE Trans. MTT. (1986).

73. ALLEN, R., MALLIK, A. and JOHNS, P.B.: "Numerical Results for the Symmetrical Condensed TLM Node", paper submitted to IEEE Trans. MTT. (1986).

74. KRAUS, J.D.: "Electromagnetics - Third Edition", McGraw-Hill, 1984.

75. BURDEN, R.L. and FAIRES, J.D.: "Numerical Analysis - Third Edition", Prindle, Weber and Schmidt, Boston 1985.

76. BREWSTER, D.C.: "EMP Induced Currents in Internal Loads in Simplified Models of an Aircraft or Missile - Final Report on Contract A81a/1802", Marconi Research Centre, April 1983.

77. JOHNS, P.B. AKHTARZAD, K. and RAHHAL, Y.: "Numerical Simulation of Interference in Aircraft Due to Electromagnetic Fields", Paper presented at Conference on Electromagnetic Compatibility, University of Southampton, IERE Conf. Proc. No. 47, September 1980, pp 295-299.

78. MALLIK, A., JOHNS, P.B. and NAYLOR, P.: "Computer Simulation of Fields for Electromagnetic Compatibility (EMC) Design". Paper presented at Conference "An Introduction to the Electromagnetic Environments", Society of Environmental Engineers, Imperial College, London, February 1984.

79. PARTON, J.E. and OWEN, S.J.T.: "Applied Electromagnetics", Macmillan 1975.

80. FRANKEL, S.: "Multiconductor Transmission Line Analysis", Arteck, 1978.

81. COLLIN, R.E.: "Foundations for Microwave Engineering", McGraw-Hill.

82. BANDLER, J.W., JOHNS, P.B. and RIZK, M.R.M.: "Transmission-Line Modelling and Sensitivity

Evaluation for Lumped Network Simulation and Design in the Time Domain", Journal of the Franklin Institute, Vol. 304, No. 1, July 1977, pp 15-32.

83. KRON, G. " Diakoptics", MacDonald, London 1963.

84. BRAMELLER, A., JOHN, M.N. and SCOTT, M.R.: "Practical Diakoptics for Electrical Networks", Chapman and Hall, London, 1969.

85. BETTS, J.A.: "Signal Processing, Modulation and Noise", Hodder and Stoughton, 1980.

86. HAMMING, R.W.: "Digital Filters", Prentice-Hall, 1977.

87. BOZIC, S.M.: "Digital and Kalman Filtering", Edward Arnold, 1979.

88. LAM, H.Y-F.: "Analog and Digital Filters - Design and Realization", Prentice-Hall, 1979.

89. JOHNS, P.B.: "Ideal Transformers and Gauge Transformations in Lumped Network Models of Electromagnetic Fields" , IEE Proc., Vol. 129, Pt. A, No. 6, August 1982, pp 381-386.

90. NAYLOR, P.: "Variable Mesh-Size and Circular TLM", M.Sc. Thesis, University of Nottingham, 1982.

91. AMER, A.: "The Condensed Node TLM Method and its Application to Transmission in Power Systems", Ph.D. Thesis, University of Nottingham, 1980.

Appendix A A Summary of the Transmission-Line Matrix

A1 Introduction

This appendix briefly summarises the TLM method (in two dimensions) and shows what equivalences are made between the transmission-line model and Maxwell's equations. There are two forms of the TLM method in two dimensions: shunt mesh and series mesh. Each assumes no field variation in the third dimension.

A2 Shunt Mesh (TM Modes)

Figure A1a shows the propagation of a typical transverse magnetic wave in two dimensions. It has components of magnetic field only in the plane of the 2D space and electric field only perpendicular to the space. Hence $H_z = E_x = E_y = 0$ in this case. Maxwell's equations applied to such a propagation yield (19):

$$\frac{\partial E_z}{\partial x} = \mu\frac{\partial H_y}{\partial t} \qquad \text{(A1)}$$

$$\frac{\partial E_z}{\partial y} = -\mu\frac{\partial H_x}{\partial t} \qquad \text{(A2)}$$

$$-\frac{\partial H_x}{\partial y} + \frac{\partial H_y}{\partial x} = \varepsilon\frac{\partial E_z}{\partial t} \qquad \text{(A3)}$$

These combine to give

$$\frac{\partial^2 E_z}{\partial x^2} + \frac{\partial^2 E_z}{\partial y^2} = \mu\varepsilon\frac{\partial^2 E_z}{\partial t^2} \qquad \text{(A4)}$$

Figure A1 Resolving the fields

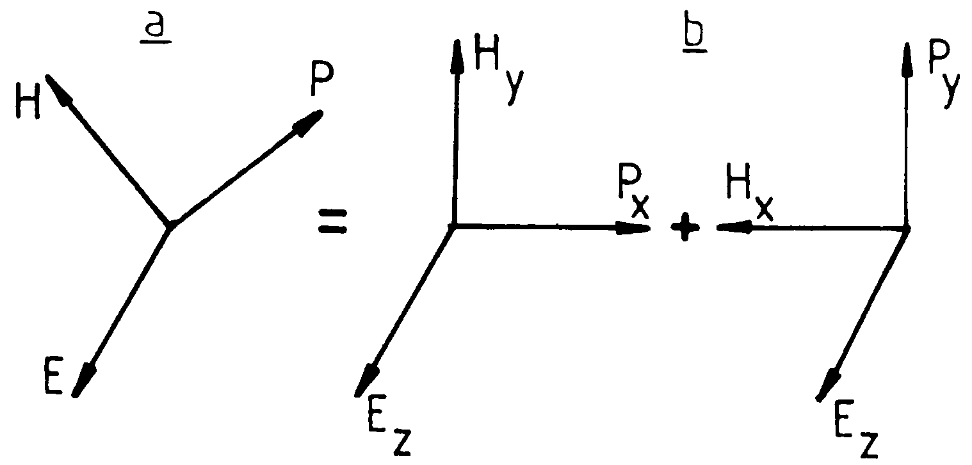

Figure A2 Equivalent network

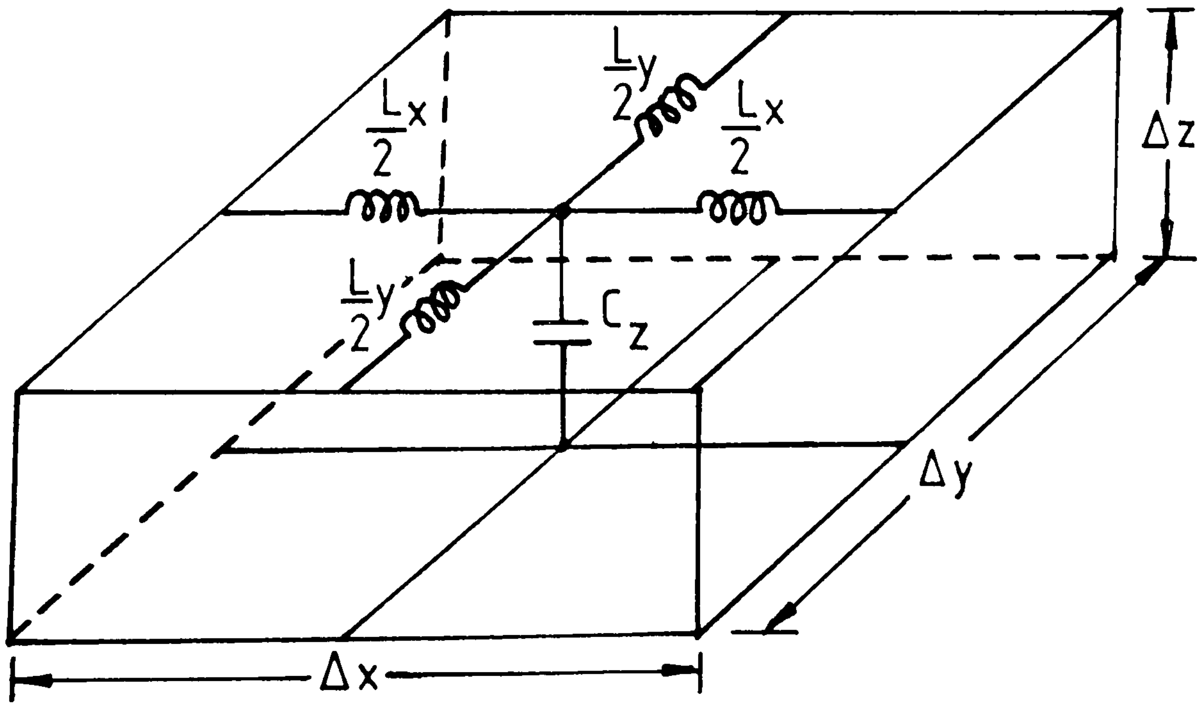

It was proposed by Johns and Beurle (57) that the lumped network shown in figure A2 models the equation (A4).

To verify this consider a plane wave propagating along an interconnected mesh of such primitive networks (figure A3a). This can be reduced to a one-dimensional problem if open-circuit boundaries are introduced as shown (figure A3b). The lumped network then becomes (figure A3c). From (19) the transmission-line equations for a distributed network similar to figure A3 would give:

$$\frac{\partial V_z}{\partial x} \Delta x = - L_x \frac{\partial I_x}{\partial t} \tag{A5}$$

$$\frac{-\partial I_x}{\partial x} \Delta x = C_z \frac{\partial V_z}{\partial t} \tag{A6}$$

differentiating (A5) wrt x:

$$\frac{\partial^2 V_z}{\partial x^2} \Delta x = - L_x \frac{\partial^2 I_x}{\partial x \partial t} \tag{A7}$$

and (A6) wrt time:

$$\frac{-\partial^2 I_x}{\partial x \partial t} \Delta x = C_z \frac{\partial^2 V_z}{\partial t^2} \tag{A8}$$

Substituting (A7) into (A8) gives:

$$\frac{\partial^2 V_z}{\partial x^2} \Delta x = L_x C_z \frac{\partial^2 V_z}{\partial t^2} \Delta x \tag{A9}$$

Similarly for propagation in the y-direction:

Figure A3 Plane wave

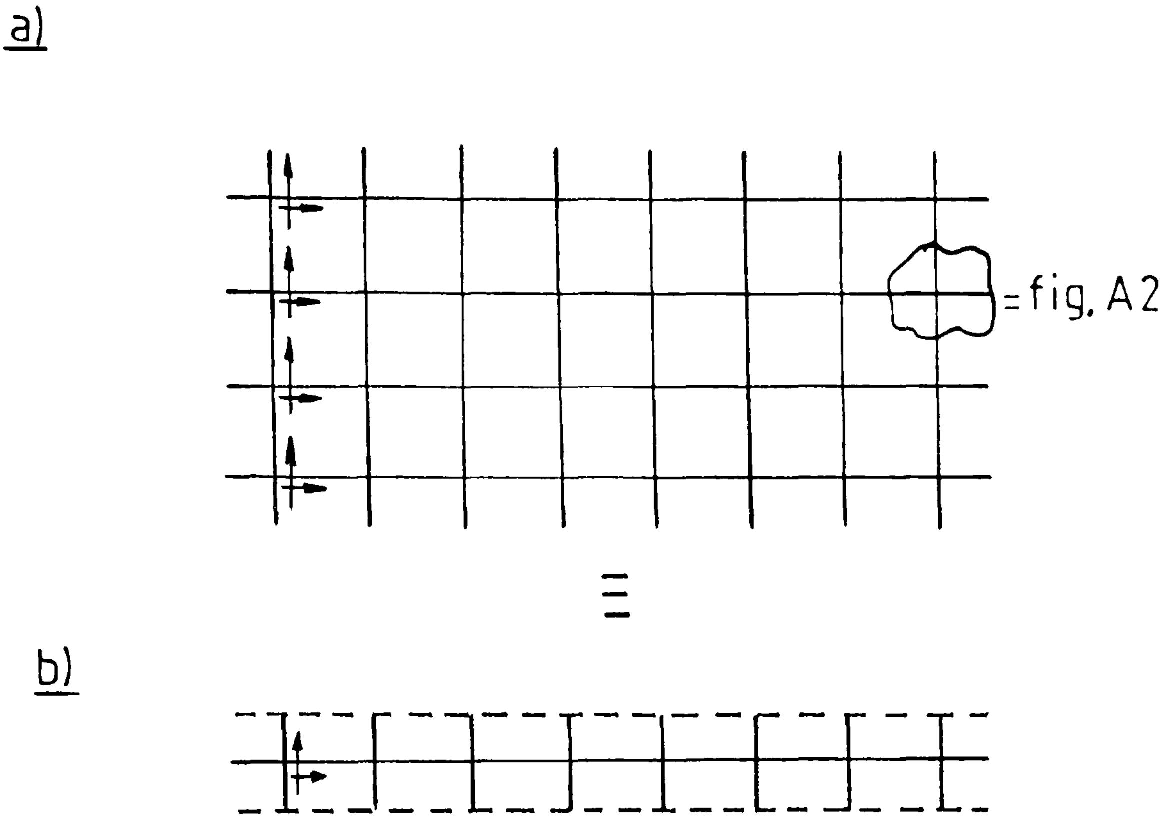

c) Lumped network

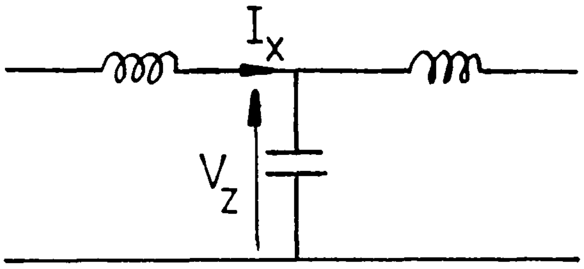

Figure A4 Intersecting transmission lines

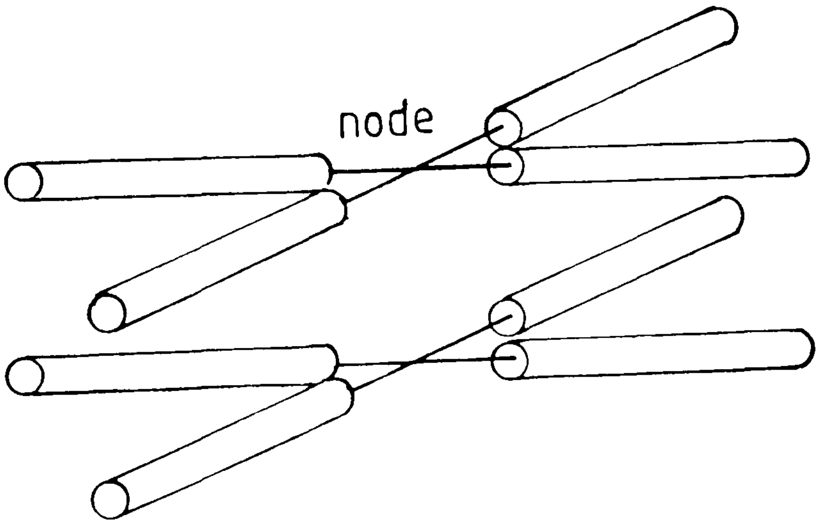

$$\frac{\partial^2 V_z}{\partial y^2}\,\Delta y \;=\; L_y C_z \frac{\partial^2 V_z}{\partial t^2}\,\Delta y \qquad \text{(A10)}$$

From Johns (89):

$$L_x = \mu\,\frac{\Delta x}{\Delta y}\,\Delta z \qquad \text{(A11)}$$

$$L_y = \mu\,\frac{\Delta y}{\Delta x}\,\Delta z \qquad \text{(A12)}$$

$$C_z = \varepsilon\,\frac{\Delta x \Delta y}{\Delta z} \qquad \text{(A13)}$$

Adding the two solutions (A9) and (A10) and making the substitutions (A11 - A13) gives:

$$\frac{\partial^2}{\partial x^2}\left(\frac{V_z}{\Delta z}\right) + \frac{\partial^2}{\partial y^2}\left(\frac{V_z}{\Delta z}\right) = \mu\varepsilon\frac{\partial^2}{\partial t^2}\left(\frac{V_z}{\Delta z}\right) \qquad \text{(A14)}$$

Also from (A5, A6, A11 - A13)

$$\frac{\partial}{\partial x}\left(\frac{V_z}{\Delta z}\right) = -\,\mu\frac{\partial}{\partial t}\left(\frac{I_x}{\Delta y}\right) \qquad \text{(A15)}$$

$$\frac{\partial}{\partial y}\left(\frac{V_z}{\Delta z}\right) = -\,\mu\frac{\partial}{\partial t}\left(\frac{I_y}{\Delta y}\right) \qquad \text{(A16)}$$

Comparing (A14 - A16) with (A1 - A3) requires that:

$$E_z = -\,\frac{V_z}{\Delta z} \qquad \text{(A17)}$$

$$H_x = -\,\frac{I_y}{\Delta x} \qquad \text{(A18)}$$

and $H_y = \dfrac{I_x}{\Delta y}$ (A19)

This shows that an interconnected network such as in figure A3 can model Maxwell's equations in 2D. However, when Maxwell's equations are made discrete by using the network errors are introduced. These errors are discussed fully by Johns and Beurle (57) and Brewitt-Taylor and Johns (89).

If the lumped network of figure A2 is now considered to be a pair of intersecting transmission lines (with $\Delta x = \Delta y = \Delta \ell$ and Δz is taken to be 1m, figure A4) then each branch of the network has the same impedance.

An impulse incident on one branch of the network will be scattered by the impedance discontinuity at the node (figure A5).

From the basic transmission-line premise that the voltage on a transmission-line is the sum of a forward and a backward travelling voltage waveform (19)

then $$V = V^i + V^r \tag{A20}$$

where V is the voltage at the node

V^i represents the voltage impulse incident on the node (the forward wave)

and V^r is the voltage reflected from the node (the backward wave).

From the Thêvenin equivalent circuit of the intersecting transmission-lines (figure A5):

$$V = \frac{2(V_1^i + V_2^i + V_3^i + V_4^i)\, Z/3}{4/3Z} \qquad \text{(A21)}$$

giving

$$V = \frac{V_1^i + V_2^i + V_3^i + V_4^i}{2} \qquad \text{(A22)}$$

from equation (A20) this gives (in matrix form):

$$\begin{bmatrix} V_1^r \\ V_2^r \\ V_3^r \\ V_4^r \end{bmatrix} = \tfrac{1}{2} \begin{bmatrix} -1 & 1 & 1 & 1 \\ 1 & -1 & 1 & 1 \\ 1 & 1 & -1 & 1 \\ 1 & 1 & 1 & -1 \end{bmatrix} \cdot \begin{bmatrix} V_1^i \\ V_2^i \\ V_3^i \\ V_4^i \end{bmatrix} \qquad \text{(A23)}$$

or

$$\underline{V}^r = \underline{S}.\underline{V}^i \qquad \text{(A24)}$$

where $\underline{S}$ is termed the SCATTERING MATRIX.

(However, it is usually more efficient to calculate the nodal voltage, equation A22, and then apply A20).

Different permittivities can be modelled by increasing the capacitance at the node in figure A2. This can be achieved by adding an extra open-circuit stub transmission-line at the node as shown in figure A6 and described by Johns in (59). The admittance of such a stub is

$$Y_s = \frac{2C}{\Delta t} \quad (82) \qquad \text{(A25)}$$

Figure A5 Thévenin equivalent circuit

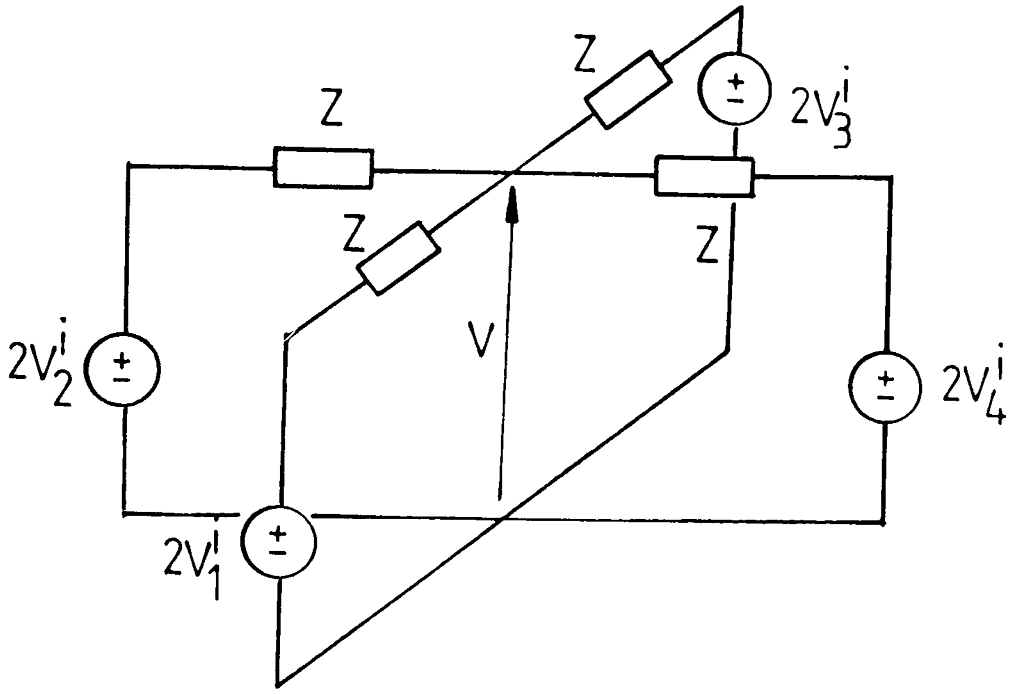

Figure A6 Shunt node with stub

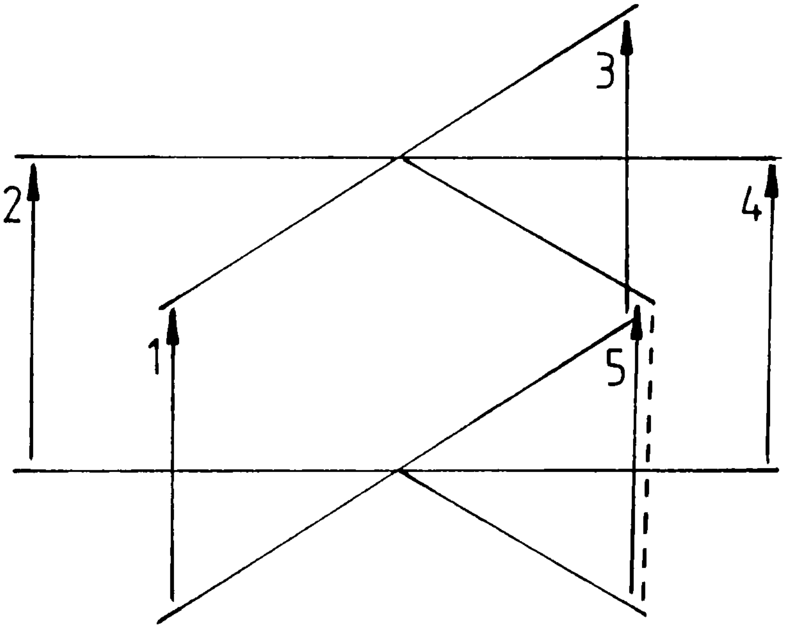

Figure A7 Joining

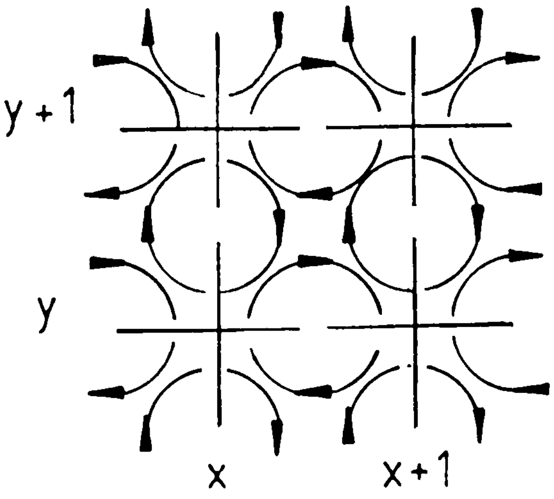

This can then be modelled using the scattering equation :

$$\begin{bmatrix} V_1^r \\ V_2^r \\ V_3^r \\ V_4^r \\ V_5^r \end{bmatrix} = \frac{1}{4Y_o+Y_s} \begin{bmatrix} -(2Y_o+Y_s) & 2Y_o & 2Y_o & 2Y_o & 2Y_s \\ 2Y_o & -(2Y_o+Y_s) & 2Y_o & 2Y_o & 2Y_s \\ 2Y_o & 2Y_o & -(2Y_o+Y_s) & 2Y_o & 2Y_s \\ 2Y_o & 2Y_o & 2Y_o & -(2Y_o+Y_s) & 2Y_s \\ 2Y_o & 2Y_o & 2Y_o & 2Y_o & Y_s-4Y_o \end{bmatrix} \cdot \begin{bmatrix} V_1^i \\ V_2^i \\ V_3^i \\ V_4^i \\ V_5^i \end{bmatrix}$$

(A26)

Reflected voltage pulses from one node then become incident pulses on adjacent nodes as suggested by figure A7.

Exceptions to this connection routine occur at 'internal boundaries', and 'external boundaries' as shown in figure A8. The figure shows the cases for perfectly conducting and open-circuit boundaries. Imperfectly conducting boundaries can be used and these are modelled by the use of reflection and transmission coefficients at a point mid-way between nodes as described in (59,90).

The 'output' equations (A17) - (A19) can be rewritten in terms of the incident voltages thus:

$$E_z = -\frac{\sum^{d} V_d^i}{2\Delta \ell} \qquad \text{(A27)}$$

Figure A8 Boundaries

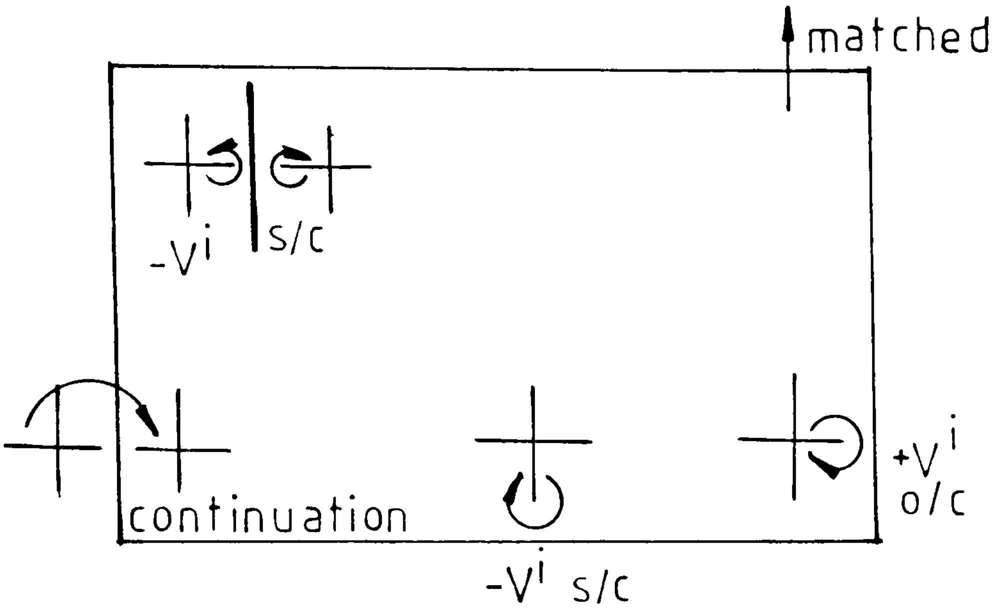

Figure A9 TLM routine

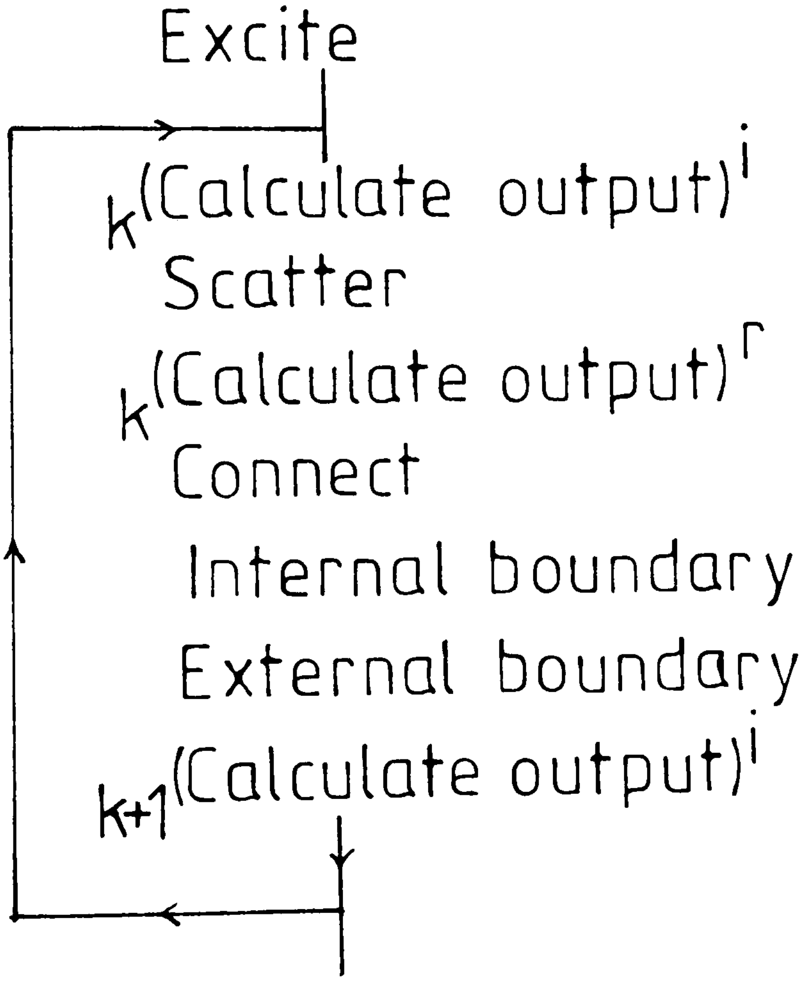

$$H_x = \frac{V_3^i - V_1^i}{Z_o \Delta\ell} \qquad (A28)$$

$$H_y = \frac{V_2^i - V_4^i}{Z_o \Delta\ell} \qquad (A29)$$

or reflected voltages :

$$E_z = -\frac{\overset{d}{\Sigma} V_d^r}{2\Delta\ell} \qquad (A30)$$

$$H_x = \frac{V_1^r - V_3^r}{Z_o \Delta\ell} \qquad (A31)$$

$$H_y = \frac{V_4^r - V_2^r}{Z_o \Delta\ell} \qquad (A32)$$

The complete routine can be summarised by figure A9. This shows the only valid positions for evaluating the output fields.

A3 Series Mesh (TE Modes)

For electric field only in the 2D plane and magnetic field perpendicular the alternative mesh (60) shown in figure A10 can be used.

Maxwell's equations for these conditions are :

$$\frac{\partial H_z}{\partial x} = -\varepsilon\frac{\partial E_y}{\partial t} \qquad (A33)$$

$$\frac{\partial H_z}{\partial y} = \varepsilon \frac{\partial E_x}{\partial t} \tag{A34}$$

$$\frac{\partial E_y}{\partial x} - \frac{\partial E_x}{\partial y} = -\mu \frac{\partial H_z}{\partial t} \tag{A35}$$

Combining to give:

$$\frac{\partial^2 H_z}{\partial x^2} + \frac{\partial^2 H_z}{\partial y^2} = \mu\varepsilon \frac{\partial^2 H_z}{\partial t^2} \tag{A36}$$

Following an argument similar to the shunt mesh yields :

$$\frac{\partial^2}{\partial x^2}\left(\frac{I}{\Delta z}\right) + \frac{\partial^2}{\partial y^2}\left(\frac{I}{\Delta z}\right) = \mu\varepsilon \frac{\partial^2}{\partial t^2}\left(\frac{I}{\Delta z}\right) \tag{A37}$$

with

$$\frac{\partial}{\partial x}\left(\frac{I}{\Delta z}\right) = \varepsilon \frac{\partial}{\partial t}\left(\frac{V_y}{\Delta y}\right) \tag{A38}$$

and

$$\frac{\partial}{\partial y}\left(\frac{I}{\Delta x}\right) = -\varepsilon \frac{\partial}{\partial t}\left(\frac{V_x}{\Delta x}\right) \tag{A39}$$

Thus $H_z = \frac{I}{\Delta z}$ (A40)

$$E_x = -\frac{V_x}{\Delta x} \tag{A41}$$

$$E_y = -\frac{V_y}{\Delta y} \tag{A42}$$

The scattering matrix for the series mesh, from the Thévenin equivalent circuit (figure A11) is:

Figure A10 Series node

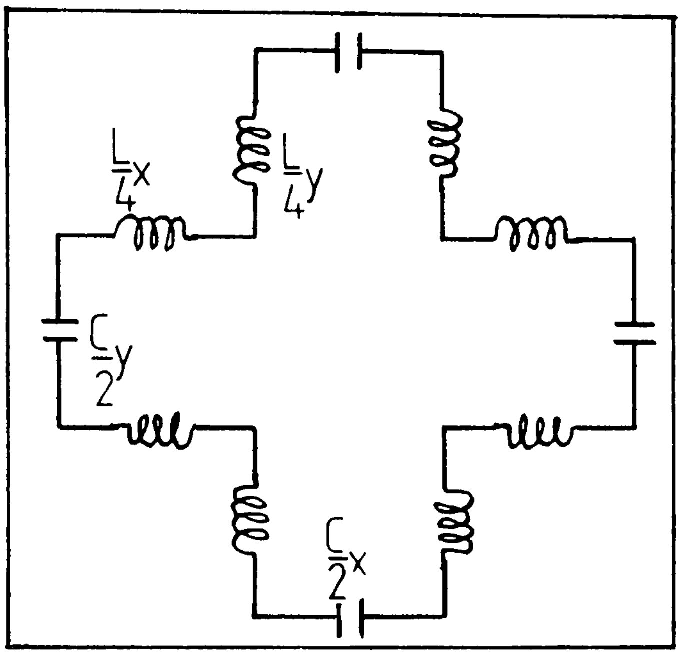

Figure A11 Thévenin equivalent circuit

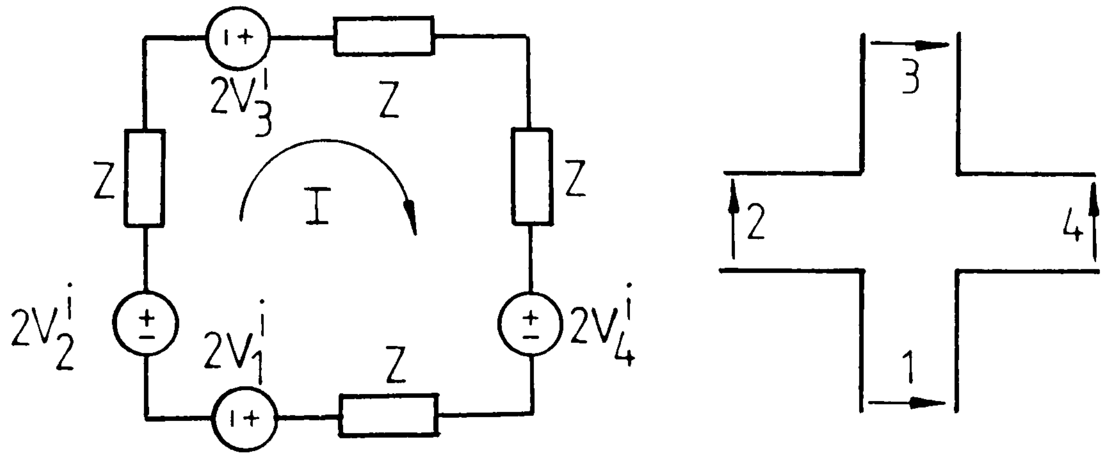

Figure A12 Series node with stub

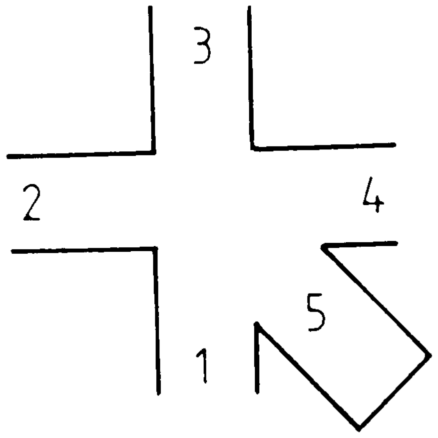

$$\begin{bmatrix} V_1^r \\ V_2^r \\ V_3^r \\ V_4^r \end{bmatrix} = \tfrac{1}{2} \begin{bmatrix} 1 & 1 & 1 & -1 \\ 1 & 1 & -1 & 1 \\ 1 & -1 & 1 & 1 \\ -1 & 1 & 1 & 1 \end{bmatrix} \cdot \begin{bmatrix} V_1^i \\ V_2^i \\ V_3^i \\ V_4^i \end{bmatrix} \qquad \text{(A43)}$$

Different permeabilities can be modelled using an additional short-circuit stub, as indicated in figure A12. The scattering matrix for the node is given by:

$$\begin{bmatrix} V_1^r \\ V_2^r \\ V_3^r \\ V_4^r \\ V_5^r \end{bmatrix} = \frac{1}{4Z_o+Z_s} \begin{bmatrix} 2Z_o+Z_s & 2Z_o & 2Z_o & -2Z_o & -2Z_o \\ 2Z_o & 2Z_o+Z_s & -2Z_o & 2Z_o & 2Z_o \\ 2Z_o & -2Z_o & 2Z_o+Z_s & 2Z_o & 2Z_o \\ -2Z_o & 2Z_o & 2Z_o & 2Z_o+Z_s & -2Z_o \\ -2Z_s & 2Z_s & 2Z_s & -2Z_s & 4Z_oZ_s \end{bmatrix} \cdot \begin{bmatrix} V_1^i \\ V_2^i \\ V_3^i \\ V_4^i \\ V_5^i \end{bmatrix}$$

(A44)

where $Z_s = \frac{2L_s}{\Delta t}$

and L_s is the inductance (of the stub). The connection and boundary routines are exactly the same as for the shunt mesh described above.

The equations A40 - A42 can be rewritten :

$$H_x = \frac{1}{2Z_o\Delta\ell}(V_1^i - V_2^i - V_3^i + V_4^i) \tag{A45}$$

$$E_x = -\frac{(V_1^i + V_3^i)}{\Delta\ell} \tag{A46}$$

$$E_y = -\frac{(V_2^i + V_4^i)}{\Delta\ell} \tag{A47}$$

or

$$H_x = \frac{1}{2Z_o\Delta\ell}(-V_1^r + V_2^r + V_3^r - V_4^r) \tag{A48}$$

$$E_x = -\frac{(V_1^r + V_3^r)}{\Delta\ell} \tag{A49}$$

$$E_y = -\frac{(V_2^r + V_4^r)}{\Delta\ell} \tag{A50}$$

A4 Time Step

If these meshes are used to model free space rather than space where $\varepsilon_r = 2$ (19) or $\mu_r = 2$ then the relationship between the mesh size and the time step is given by (90)

$$\frac{\Delta\ell}{\Delta t} = \surd 2c.$$

Appendix B Three Dimensional TLM

B1 Introduction

References (61) and (91) record the development and use of expanded and condensed asymmetrical nodes in the TLM process. More recently a new symmetrical condensed 3D TLM node has been developed (71,72,73). In this appendix TLM in 3D using the symmetrical condensed node will be briefly summarised.

B2 The Symmetrical Condensed Node

Figure B1 shows the symmetrical condensed node developed by Johns (71,72). There is no electrical network which describes the node and so the scattering matrix for the node has to be obtained by other means. Consider a pulse travelling towards the node as shown in figure B2. Associated with this pulse are the electric and magnetic fields as shown. By assuming that there is no field rotation, the possible scattering can be deduced from other ports containing E and H fields of the same polarisation and by noting left-right and top-bottom symmetry. Additional information can be obtained from similarities between this new node and the series and shunt nodes shown in Appendix A. For the example shown in figure B2

$$V_8 = aV_8 + b(V_3+V_{11}) + cV_4 + d(V_7-V_5) \qquad \text{(B1)}$$

where a, b, c and d are to be determined.

Figure B1 3D symmetrical condensed node

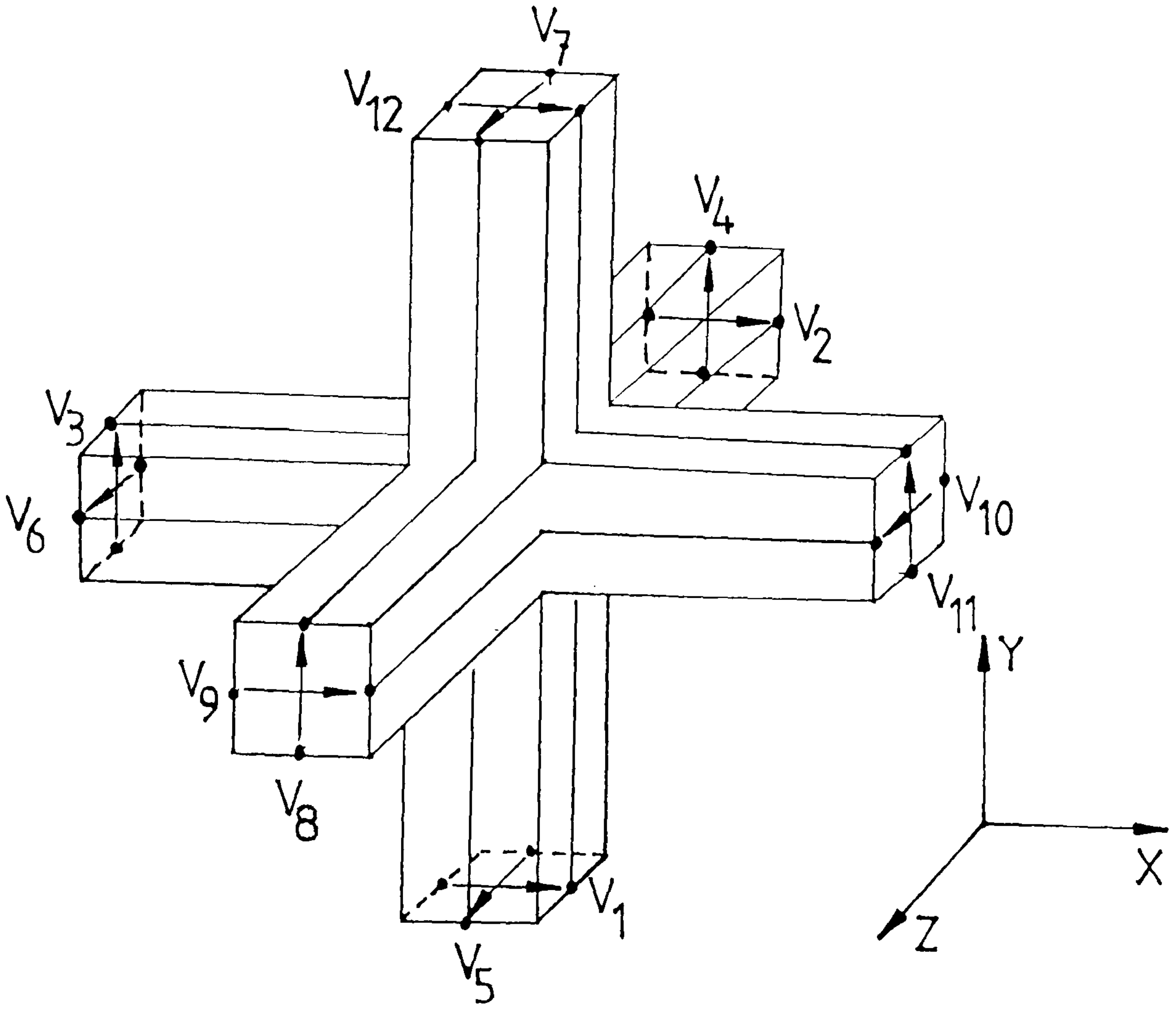

Figure B2 Scattering of an incident wave

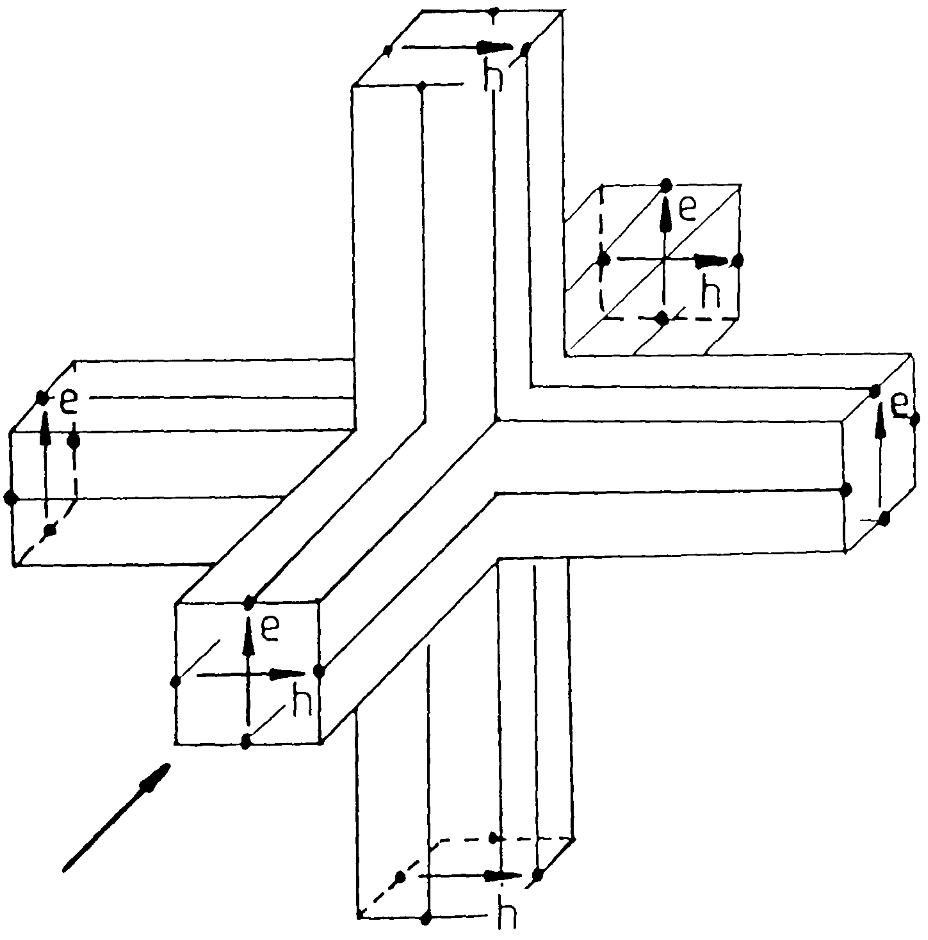

Extending this to all other ports gives the scattering matrix:

$$\underline{S} = \begin{bmatrix} a & b & d & 0 & 0 & 0 & 0 & 0 & b & 0 & -d & c \\ b & a & 0 & 0 & 0 & d & 0 & 0 & c & -d & 0 & b \\ d & 0 & a & b & 0 & 0 & 0 & b & 0 & 0 & c & -d \\ 0 & 0 & b & a & d & 0 & -d & c & 0 & 0 & b & 0 \\ 0 & 0 & 0 & d & a & b & c & -d & 0 & b & 0 & 0 \\ 0 & d & 0 & 0 & b & a & b & 0 & -d & c & 0 & 0 \\ 0 & 0 & 0 & -d & c & b & a & d & 0 & b & 0 & 0 \\ 0 & 0 & b & c & -d & 0 & d & a & 0 & 0 & b & 0 \\ b & c & 0 & 0 & 0 & -d & 0 & 0 & a & d & 0 & b \\ 0 & -d & 0 & 0 & b & c & b & 0 & d & a & 0 & 0 \\ -d & 0 & c & b & 0 & 0 & 0 & b & 0 & 0 & a & d \\ c & b & -d & 0 & 0 & 0 & 0 & 0 & b & 0 & d & a \end{bmatrix} \qquad (B2)$$

From the unitary condition (81)

$$\underline{S}.\underline{S}^{*T} = \underline{U} \qquad (B3)$$

For the above matrix, this gives

$$a^2 + 2b^2 + c^2 + 2d^2 = 1 \qquad (B4)$$

$$2ab + 2bc = 0 \qquad (B5)$$

$$2ad - 2cd = 0 \qquad (B6)$$

$$2ac + 2b^2 - 2d^2 = 0 \qquad (B7)$$

This gives $a = c = 0$

and $d = b = \pm \frac{1}{2}$

From the similarity with the series and shunt nodes

$$d = b = + \tfrac{1}{2}$$

and so the scattering matrix is:

$$\underline{S} = \frac{1}{2}\begin{bmatrix} 0 & 1 & 1 & 0 & 0 & 0 & 0 & 0 & 1 & 0 & -1 & 0 \\ 1 & 0 & 0 & 0 & 0 & 1 & 0 & 0 & 0 & -1 & 0 & 1 \\ 1 & 0 & 0 & 1 & 0 & 0 & 0 & 1 & 0 & 0 & 0 & -1 \\ 0 & 0 & 1 & 0 & 1 & 0 & -1 & 0 & 0 & 0 & 1 & 0 \\ 0 & 0 & 0 & 1 & 0 & 1 & 0 & -1 & 0 & 1 & 0 & 0 \\ 0 & 1 & 0 & 0 & 1 & 0 & 1 & 0 & -1 & 0 & 0 & 0 \\ 0 & 0 & 0 & -1 & 0 & 1 & 0 & 1 & 0 & 1 & 0 & 0 \\ 0 & 0 & 1 & 0 & -1 & 0 & 1 & 0 & 0 & 0 & 1 & 0 \\ 1 & 0 & 0 & 0 & 0 & -1 & 0 & 0 & 0 & 1 & 0 & 1 \\ 0 & -1 & 0 & 0 & 1 & 0 & 1 & 0 & 1 & 0 & 0 & 0 \\ -1 & 0 & 0 & 1 & 0 & 0 & 0 & 1 & 0 & 0 & 0 & 1 \\ 0 & 1 & -1 & 0 & 0 & 0 & 0 & 0 & 1 & 0 & 1 & 0 \end{bmatrix} \qquad \text{(B8)}$$

B3 Fields

The symmetrical condensed node allows the computation of all six electromagnetic field components at the node. These are:

$$E_x = -\frac{(V_1^r + V_2^r + V_9^r + V_{12}^r)}{2\Delta\ell} \qquad \text{(B9)}$$

$$E_y = -\frac{(V_3^r + V_4^r + V_8^r + V_{11}^r)}{2\Delta\ell}$$, shown in figure B3

(B10)

$$E_z = -\frac{(V_5^r + V_6^r + V_7^r + V_{10}^r)}{2\Delta\ell} \qquad \text{(B11)}$$

Figure B3 Electric field E_y.

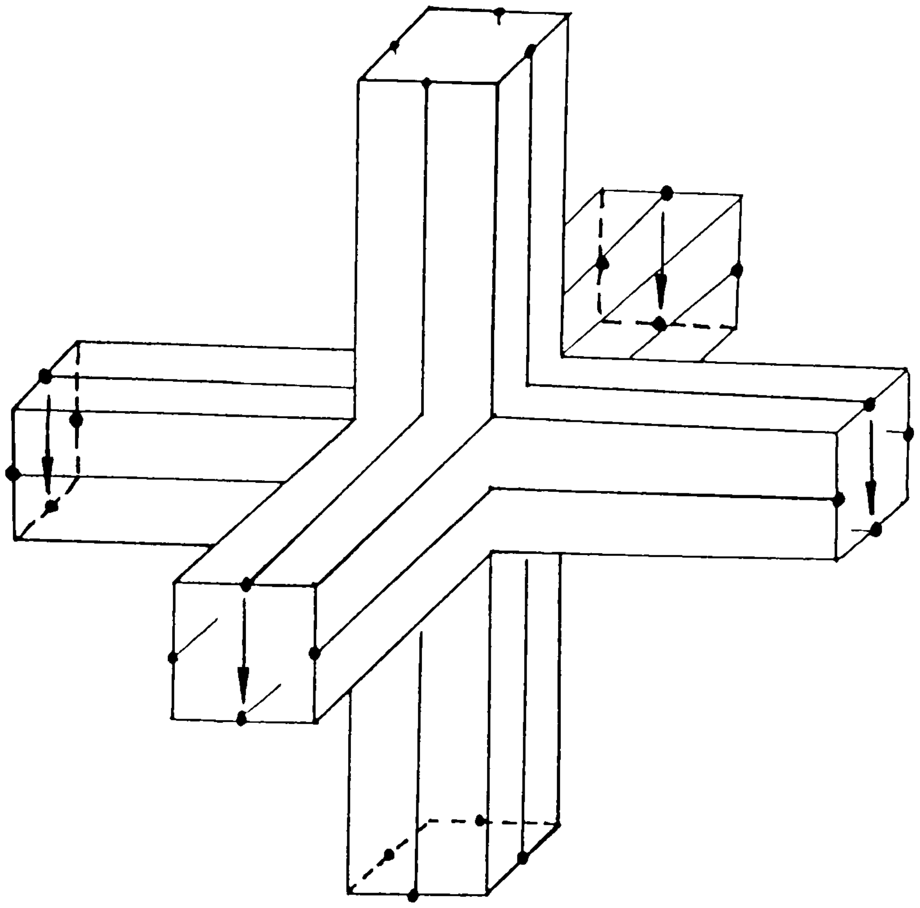

Figure B4 Magnetic field H_y.

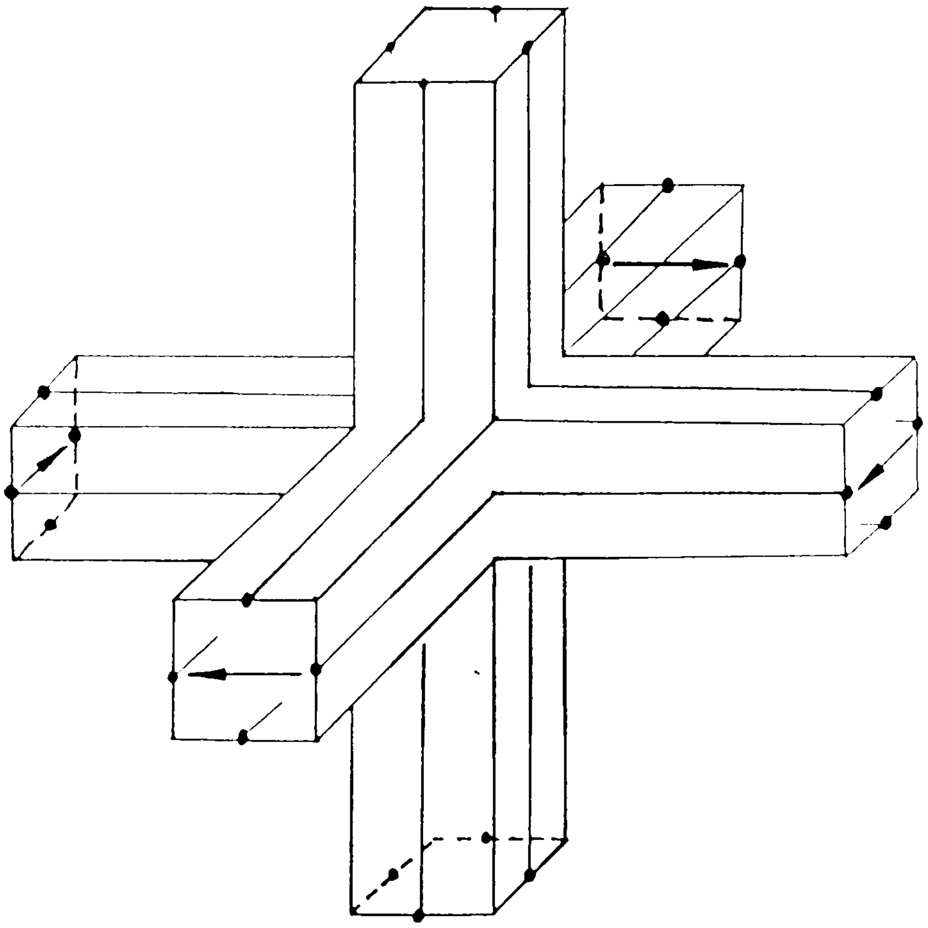

$$H_x = \frac{-V_4^r + V_5^r - V_7^r + V_8^r}{2Z_o\ \Delta\ell} \tag{B12}$$

$$H_y = \frac{V_2^r - V_6^r - V_9^r + V_{10}^r}{2Z_o\ \Delta\ell}$$, shown in figure B4 (B13)

$$H_z = \frac{-V_1^r + V_3^r - V_{11}^r + V_{12}^r}{2Z_o\Delta\ell} \tag{B14}$$

B4 Time Step

Examination of the scattering of this condensed node reveals that it takes two time steps for a pulse entering the node on port 1 (say) to appear on port 12. This means that a plane wave on the TLM mesh takes $2\Delta t$ to travel a distance $\Delta\ell$. Since a plane wave in free-space propagates at the velocity of light, c, $\Delta\ell$ and Δt are related by:

$$\frac{\Delta\ell}{\Delta t} = 2c \tag{B15}$$